SAPIENZA
UNIVERSITÀ DI ROMA

# Simulations of RF beam manipulations including intensity effects for CERN PSB and SPS upgrades


Istituto Nazionale di Fisica Nucleare (INFN) and "Sapienza" Universita di Roma

Dottorato di Ricerca in Fisica degli Acceleratori – XXXI Ciclo

Candidate

Danilo Quartullo
ID number 1201389

Thesis Advisors

Prof. Mauro Migliorati
Dr. Elena Shaposhnikova

Examiners

Dr. Elias Metral
Dr. Mikhail Zobov



February 2019

Thesis defended on 08 February 2019
in front of a Board of Examiners composed by:

Prof. Annalisa D'Angelo (chairperson)

Prof. Patrizio Antici

Prof. Roberto Senesi

---

**Simulations of RF beam manipulations including intensity effects for CERN PSB and SPS upgrades**

Ph.D. thesis. Sapienza – University of Rome



This thesis has been typeset by LaTeX and the Sapthesis class.

Version: February 11, 2019

Author's email: danilo.quartullo@cern.ch

*Dedicated to my parents.*

# Abstract

During Long Shutdown 2 (LS2, 2019-2021) all the injectors of the CERN LHC will undergo several upgrades to fulfill the requests of the LHC Injectors Upgrade (LIU) Project. Among them, an increase in luminosity of the LHC beam by a factor of ten and two respectively for proton and ion beams is expected. The upgrades of the CERN PSB, the first synchrotron in the LHC proton injection chain, will be significant. The injection and extraction beam energies will be increased respectively from 50 MeV to 160 MeV kinetic energy (via the new Linac4) and from 1.4 GeV to 2 GeV (using new magnet power supplies). The required beam intensities will be a factor of two higher for High-Luminosity LHC (HL-LHC) beams, and the currently used narrow-band ferrite RF systems will be replaced by broad-band Finemet® cavities. For ion beams instead, a fundamental upgrade will concern the CERN SPS, the LHC injector, where the Low Lever RF functionalities will be considerably enhanced to allow the interleaving of two batches in longitudinal phase space through momentum slip-stacking, aiming at halving the bunch spacing.

In order to predict future longitudinal beam stability and optimize complex RF manipulations both for PSB and SPS, longitudinal macro-particle simulations have been performed. Concerning the PSB, an accurate impedance model and a careful estimation of the space charge effects were included in simulations. Beam and cavity-based feedbacks were also taken into account. Controlled longitudinal emittance blow-up, currently obtained through phase modulation with a dedicated higher harmonic RF system, was achieved in measurements and simulations for the first time injecting RF phase noise in the main harmonic cavity, showing some advantages in using this new method. As for the SPS, the slip-stacking dynamics with collective effects has been studied in details aiming at optimizing the numerous parameters present and satisfying the stringent constraints on losses and bunch length at extraction. Beam quality issues were analyzed together with possible remedies. All simulations have been performed with the macro-particle longitudinal beam dynamics CERN BLonD code, after particular efforts have been spent to implement several algorithms for non ultra-relativistic energy machines (like the PSB) and for slip-stacking dynamics in order to easily optimize the large parameter space available. Benchmarks between BLonD, other codes and analytical formulas have been performed to study different approaches for induced voltage calculation and give some guidelines on the pros and cons of each of them.

## Acknowledgments

*It has been an honor for me to be guided by my CERN advisor Elena Shaposhnikova, who taught me how to be a competent researcher during my experience at CERN, firstly as a trainee and later as a PhD student. Her wisdom and brilliance are difficult to explain in words. I should thank her infinite times for the trust given to me when I arrived at CERN five years ago as a mathematician almost without knowing what an accelerator was. She has always been available along the years for explanations, insights and guidelines, without those this work would have been infinitely more difficult.*

*I will always be indebted to Mauro Migliorati, who accepted to be my university supervisor during my PhD. I still remember the joy I felt when he wrote me that I had passed the selection to enter the PhD course at Sapienza University of Rome and that he would have been my advisor. With his known competence in Accelerator Physics, Mauro provided immediate help and support whenever needed, giving me also the opportunity to work together during my PhD on some contributions on collective effects.*

*My most sincere thanks go to Dr. Elias Metral and Dr. Mikhail Zobov, who kindly accepted to review this thesis as referees. Their strong expertise in Accelerator Physics gives significant weight to their opinions on the present work.*

*When I first arrived at CERN, I could count on the precious and invaluable support given by few colleagues and friends in the RF group who I have been continuing working with during the following years. They are Theodoros Argyropoulos, Alex Lasheen, Juan Esteban Muller and Helga Timko. The BLonD code, which has been used extensively in this thesis and nowadays a reference software for longitudinal beam dynamics simulations, was initially developed by the five of us thanks to our strong collaboration and passion. I have also to thank in this respect my colleagues Hannes Bartosik, Kevin Li and Giovanni Rumolo from the CERN ABP group for the fruitful discussions on numerical issues and code implementation which preceded the conception of BLonD. My early efforts in code optimization would have been immensely larger without the precious support provided by my CERN colleague Danilo Piparo, one of the developers of the CERN ROOT code.*

*While my studies as a trainee at CERN were more focused on the BLonD development and optimization, my years as a PhD student dealt more with longitudinal beam dynamics studies for the CERN PSB and SPS.*

*Concerning the PSB, I have to thank firstly my current office mate Simon Albright. Our strong collaboration along the years aimed at understanding the complex longitudinal beam dynamics of the PSB machine has been very fruitful and productive. Thanks also to my colleague Vincenzo Forte, who I have been working with for some time on space charge studies and benchmarks between codes. I was able to increase my knowledge in Low Level RF (LLRF) feedbacks and RF operation thanks to useful discussions with my colleagues Maria Elena Angoletta, Philippe Baudrenghien, Heiko Damerau, Alan Findlay, Steven Hancock, Mauro Paoluzzi and Helga Timko, who were always available to exchange opinions and give interesting explanations. Finally I would like to show my deep appreciation to the persons in charge of the PSB operation whom I interacted with during my measurements in*

*the CERN Control Room. They are Gian Piero Di Giovanni, Klaus Hanke and Bettina Mikulec, without forgetting all the operators who were very kind and patient in satisfying my requests.*

*My studies on momentum slip-stacking for the CERN SPS ion beams would have been more challenging without the support of my colleagues Theodoros Argyropoulos and Alexandre Lasheen. In addition Philippe Baudrenghien and Thomas Bohl gave me important guidelines whenever needed. I have also to mention Joel Repond for his availability in providing me with the most updated SPS longitudinal impedance model, Hannes Bartosik for his valuable inputs to be used in the calculation of the longitudinal space charge contribution and Giovanni Rumolo, who gave me access to a private cluster helping me in the computationally expensive parameter scanning needed for my optimization studies. Thanks also to my colleague Konstantinos Iliakis who, in addition to generally contribute to the BLonD code optimization, helped me in speeding up the most numerically heavy routines needed for my slip-stacking simulations.*

*All the time spent in the RF/BR Section would have been surely less enjoyable without the regular coffee breaks at the CERN cafeteria in the 864 building and without the numerous lunches with my colleagues at the R3 restaurant. Apart from the names already mentioned, thanks to Rama, Fritz, Christine, Matthew, Maria, Toon, Thomas, Ivan, Markus, Jamie, Patrick, Branko, Aaron, Nasrin, Ezgi and Alessandro.*

*Last but not least, I have to thank my parents for their constant support during these five years at CERN. The home-made cakes prepared by my mother have become famous during coffee breaks and without any doubt they helped sometimes to alleviate challenging days at work.*

# Contents

# Chapter 1

# Introduction

## 1.1 The CERN Accelerator Complex

The European Organization for Nuclear Research, known as CERN, is the largest particle physics laboratory in the world [1]. CERN was founded in 1954 on the Franco-Swiss border near Geneva through a convention ratified by twelve countries in Western Europe. Nowadays CERN has 22 member states and this number is expected to increase in the future. CERN's main area of research is particle physics, or the study of the fundamental constituents of matter and the forces acting between them.

Figure 1.1 shows the present scheme of the CERN accelerator complex, which is a succession of machines accelerating particles to increasingly higher energies. The last element of this chain is the 27 km long Large Hadron Collider (LHC), where two counter-rotating proton and/or heavy ion beams are accelerated and brought into collisions inside the four detectors ATLAS, CMS, ALICE and LHCb. In addition to increasing the particles energy before the injection of the beam into the next machine in the chain, the major part of the accelerators in the complex have their own experiments.

Protons are obtained in the proton source, which is a bottle of hydrogen gas, through the application of an electric field aimed at stripping the hydrogen atoms of their electrons [2]. The linear accelerator Linac2, the first in the chain, accelerates the protons to a kinetic energy $E_{\mathrm{kin}}$ of 50 MeV. The beam is then injected into the Proton Synchrotron Booster (PSB), which accelerates the particles to 1.4 GeV kinetic energy, followed by the Proton Synchrotron (PS), where the beam reaches at flat top a momentum $p$ of 26 GeV/c. Then the protons are transferred into the Super Proton Synchrotron (SPS), where the momentum is increased up to 450 GeV/c. Finally the protons are sent to the two rings of the LHC. The two counter-rotating beams reach the maximum energy of 6.5 TeV per beam before colliding at the LHC experiments with a total energy of 13 TeV at the collision points.

The LHC lead-ion beams are created stripping away all the electrons from the lead isotope ${}^{208}_{82}\mathrm{Pb}$ [3], which has mass number $\mathrm{A_m} = 208$ and atomic number $\mathrm{Z_a} = 82$, corresponding respectively to the number of nucleons and protons in the isotope. Firstly, an ion source containing ${}^{208}_{82}\mathrm{Pb}$ isotopes is used to generate lead ions $\mathrm{Pb}^{29+}$ at 2.5 keV/u kinetic energy (u stands for nucleon). These ions are then

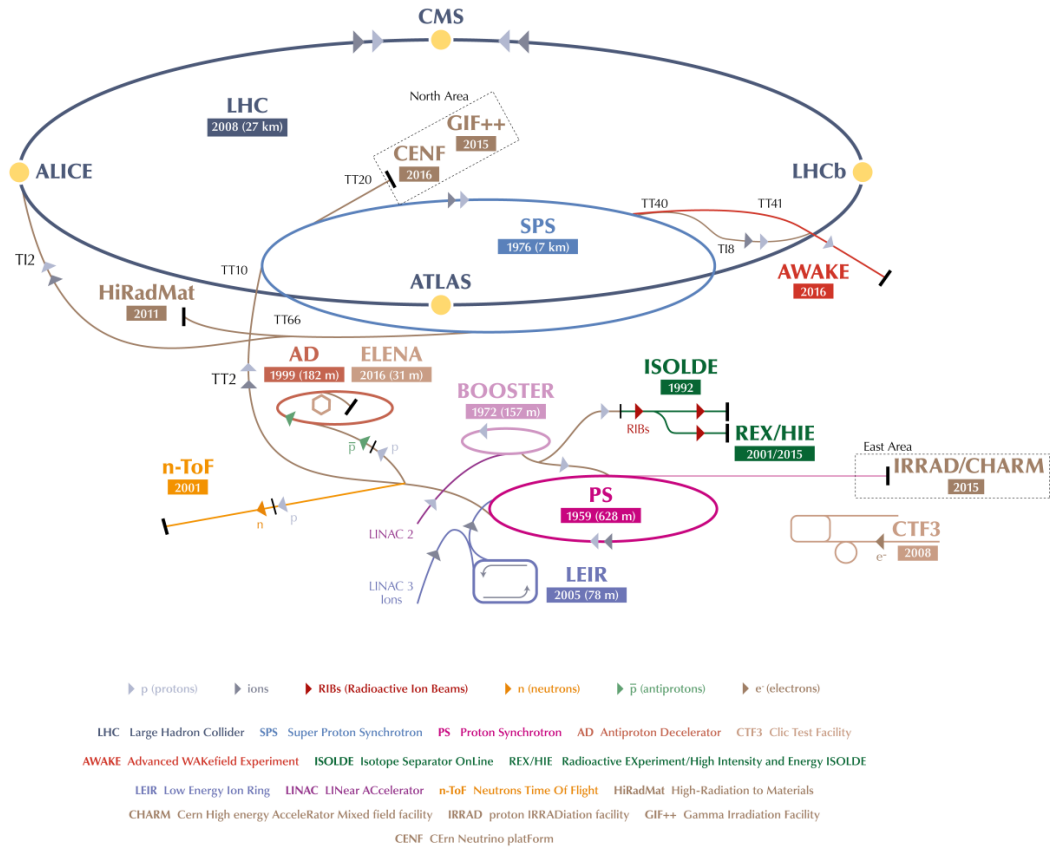


**Figure 1.1.** Scheme of the present CERN accelerator complex. The names of the accelerators and experiments are in capital letters. The year of construction, when available, is visible under those names. The length of the circular accelerators is also shown. The colored arrows in the scheme mark the type of accelerated particles and the direction of motion, see the legend. All the acronyms present in the scheme are explained in the legend as well (Copyright CERN 2016-2018).

accelerated in the Linac3 to a kinetic energy of 4.2 MeV/u. After hitting a stripping foil at the end of the Linac3 and becoming $Pb^{54+}$, the particles are injected into the Low Energy Ion Ring (LEIR) which increases their kinetic energy to 72.2 MeV/u, followed by the PS which pushes the kinetic energy to 5.9 GeV/u (17 $Z_a$GeV/c or 26 G$q$V/c, $q$ is the particle charge). The ions are then fully stripped to $Pb^{82+}$ in the PS-SPS transfer line before being injected into the SPS, where the kinetic energy is increased up to 176.4 GeV/u (450 $Z_a$GeV/c). Finally the particles are sent to the LHC where, analogously to the proton beam case, two counter-rotating beams are accelerated up to the maximum energy of 6.5 $Z_a$TeV per beam before colliding at the four interaction points with a center-of-mass energy of 13 $Z_a$TeV.

In order to evaluate the performance of the LHC up to now and understand the motivation for the studies presented in this thesis, some important physical quantities able to describe the "quality" of a beam have to be introduced.

## 1.2 Luminosity and Brightness Concepts

For two colliding beams the number of events per second $dR/dt$ can be defined as [4]

$$\frac{dR}{dt} \coloneqq \mathcal{L} \cdot \sigma_{\mathrm{p}}, \tag{1.1}$$

where $\sigma_{\mathrm{p}}$, measured in barn ($1\,\mathrm{b} = 10^{-24}\,\mathrm{cm}^2$), is the production cross section and represents a measurement of the probability that an event occurs. The instantaneous luminosity $\mathcal{L}$, measured in $\mathrm{cm}^{-2}\,\mathrm{s}^{-1}$, represents the ability of a particle accelerator to produce the required number of interactions. Let us consider two beams which collide head-on with the same Gaussian transverse distributions. If one assumes that they collide with a certain crossing angle without transverse offsets from their corresponding reference orbits, then the instantaneous luminosity is given by [4]

$$\mathcal{L} \coloneqq \frac{S_{\mathrm{f}} N_{\mathrm{b}}^2 f_{\mathrm{rev}} n_{\mathrm{B}}}{4\pi \sigma_x^* \sigma_y^*} = \frac{S_{\mathrm{f}} N_{\mathrm{b}}^2 f_{\mathrm{rev}} n_{\mathrm{B}} \beta_0 \gamma_0}{4\pi \sqrt{\beta_x^* \epsilon_{x,\mathrm{n}}} \sqrt{\beta_y^* \epsilon_{y,\mathrm{n}}}}, \tag{1.2}$$

where $N_{\mathrm{b}}$ is the number of particles in one colliding bunch, $n_{\mathrm{B}}$ is the number of bunches per beam, $f_{\mathrm{rev}}$ the revolution frequency of the particles, $\sigma_x^*$ and $\sigma_y^*$ the rms transverse beam sizes of one bunch at the collision point assuming negligible dispersions, $S_{\mathrm{f}} \leq 1$ is the so-called reduction factor which takes into account the impact of the crossing angle on the luminosity, $\beta_0$ and $\gamma_0$ are the relativistic Lorentz factor, $\beta_x^*$ and $\beta_y^*$ are the betatron amplitude functions at the collision point and $\epsilon_{x,\mathrm{n}} = \beta_0 \gamma_0 \epsilon_x$ and $\epsilon_{y,\mathrm{n}} = \beta_0 \gamma_0 \epsilon_y$ are the normalized 1-rms transverse emittances for one bunch (being $\epsilon_x$ and $\epsilon_y$ the so-called geometrical emittances). See Appendix A for more details on all the transverse-plane quantities used here.

Integrating both sides of Eq.(1.1) in a generic time interval $[0, T]$ we obtain the number of events of interest occurring in the chosen interval

$$R^{[0,T]} = \mathcal{L}_{\mathrm{int}}^{[0,T]} \cdot \sigma_{\mathrm{p}}, \tag{1.3}$$

where $\mathcal{L}_{\mathrm{int}}^{[0,T]}$ is the integrated luminosity in the interval $[0, T]$

$$\mathcal{L}_{\mathrm{int}}^{[0,T]} \coloneqq \int_0^T \mathcal{L}(t')dt'. \tag{1.4}$$

The instantaneous luminosity quickly decreases from its initial maximum value due to the protons consumed in the collisions [5]. This peak value cannot usually exceed some nominal quantity, due to limitations in accepting an arbitrarily high number of collision events at the experimental detectors (event "pile-up" constraints) and due to damaging energy deposition in the interaction-region magnets caused by the collisions. Therefore it can be useful to design a collider in such a way that the instantaneous luminosity remains constant with time ("leveled" luminosity) since, for a desired integrated luminosity, the peak luminosity with leveling will be considerably lower than the one ("virtual") without leveling.

It is important to note that, in Eq.(1.2), the parameters $S_{\mathrm{f}}$, $f_{\mathrm{rev}}$, $\beta_0$, $\gamma_0$, $\beta_x^*$ and $\beta_y^*$ depend exclusively on the collider itself, while $N_{\mathrm{b}}$, $n_{\mathrm{B}}$, $\epsilon_{x,\mathrm{n}}$, $\epsilon_{y,\mathrm{n}}$ depend also on

the injector chain of the collider. If $\epsilon_{\mathrm{n}} = \epsilon_{x,\mathrm{n}} = \epsilon_{y,\mathrm{n}}$ and $\beta^* = \beta^*_x = \beta^*_y$, then Eq.(1.2) can be written as

$$\mathcal{L} = \frac{S_{\mathrm{f}}}{4\pi} f_{\mathrm{rev}} n_{\mathrm{B}} N_{\mathrm{b}} \frac{N_{\mathrm{b}}}{\epsilon_{\mathrm{n}}} \frac{\beta_0 \gamma_0}{\beta^*}. \tag{1.5}$$

Thus the instantaneous luminosity is proportional to the current of one circulating beam $I_{\mathrm{b}} = q f_{\mathrm{rev}} n_{\mathrm{B}} N_{\mathrm{b}}$ and to the beam brightness [6]

$$B_{\mathrm{n}} \coloneqq \frac{N_{\mathrm{b}}}{\epsilon_{\mathrm{n}}}. \tag{1.6}$$

The instantaneous luminosity is also proportional to the total particle energy $E_{\mathrm{tot}}$ (usually in the collider $\beta_0 \approx 1$ and $E_{\mathrm{tot}} \propto \gamma_0$), and it is inversely proportional to $\beta^*$. Note that the definition of brightness in Eq.(1.6) is not unique (see for example Refs.[7, 8]).

The quantities brightness and luminosity are important figures of merit of the beam quality and usually they need to be maximized. As shown below, the LHC injector chain largely determines the beam brightness at the LHC collision point, unless significant transverse emittance blow-up or losses occur in the collider itself.

## 1.3 The HL-LHC and LIU Projects

The proton run of the LHC during 2010-2013 was very successful thanks to the discovery of the Higgs Boson in 2012 [2, 9]. The accelerators of the injector complex made a fundamental contribution to the performance of the LHC being able to deliver beams with $N_{\mathrm{b}} \approx 1.7 \cdot 10^{11}$ ppb (protons per bunch) with half the expected normalized transverse emittance [10]. As a consequence, the beam brightness was more than doubled and it was possible to almost compensate the significant transverse emittance blow-up experienced in the LHC, the reduced beam collision energy of 4 TeV relative to the design 7 TeV, and the halved number of bunches injected per fill. Overall a peak luminosity of $7.5 \cdot 10^{33}$ $\mathrm{cm}^{-2}\,\mathrm{s}^{-1}$ was reached, instead of the design value of $10^{34}\,\mathrm{cm}^{-2}\,\mathrm{s}^{-1}$. The on-going second run of the LHC (2015-2018) has also proven to be successful, since in 2017 a peak luminosity of $2 \times 10^{34}\,\mathrm{cm}^{-2}\,\mathrm{s}^{-1}$ was reached, doubling the design value [10].

In spite of being beyond nominal, the current performance of the LHC injector complex is insufficient to fulfill the requests of the High Luminosity LHC (HL-LHC) Project, which aims at accumulating about $300\,\mathrm{fb}^{-1}$/year of integrated luminosity with protons starting from Run 4 in 2025, relying on a leveled luminosity of $7.5 \times 10^{34}\,\mathrm{cm}^{-2}\,\mathrm{s}^{-1}$ [11]. To reach this challenging target, one of the most significant directives of the HL-LHC Project is to double the intensity of the beam injected into the LHC while multiplying by a factor of 2.4 its brightness. This request should be fulfilled by the end of Run 3 in 2024. The LHC Injector Upgrade (LIU) Project has the important task to perform all the needed upgrades in the LHC injector chain in order to fulfill the HL-LHC requests. As mentioned in the previous Section, the beam brightness has to be increased at the beginning of the LHC injector chain and then possibly preserved along the accelerator complex. Therefore, in order to attain the new required beam parameters at LHC injection, the LIU Project has planned serious upgrades also for the PSB, the first synchrotron in the LHC proton injector chain.

Another ambitious goal established by the HL-LHC Project is to double the number of lead ions at the LHC injection. In the baseline of the LIU Project the number of bunches extracted from the SPS should be doubled. A sophisticated RF manipulation called momentum slip-stacking is supposed to interleave two SPS batches in longitudinal phase space in order to halve the bunch spacing from 100 ns to 50 ns. Momentum slip-stacking has never been used in the SPS and it will need a significant upgrade of the Low Level RF system during Long Shutdown 2 (LS2, 2019-2021).

## 1.4 Motivations and Goals of the Thesis

As discussed in the previous Section, the LIU Project includes different challenging upgrades of the LHC injector chain completed in LS2. In particular, this thesis focuses on studies of longitudinal beam dynamics including collective effects for PSB proton beams and SPS ion beams. Beam dynamics simulations are of paramount importance to predict future machine performance with the new beam and machine parameters. Since a numerical code able to simulate complex beam dynamics in reasonable computing time is needed, the macro-particle code BLonD (Beam Longitudinal Dynamics) has been developed at CERN and the necessary algorithms needed for the studies have been implemented and optimized. In order to prove code reliability, numerous benchmarks between BLonD, other codes and analytical formulas have been performed.

There are three main goals of this thesis. The first one is to show the fundamental features of the BLonD code which helped in performing the required studies for the LIU Project. Relevant benchmarks are also presented for code validation and optimization. The second aim is to analyze the longitudinal beam stability of the PSB proton beams after upgrades (in 2021), taking into account in simulations collective effects and Low Level RF control systems. The third goal is the design and optimization of the momentum slip-stacking dynamics for SPS ion beams after LS2, in order to prove the feasibility of the method while providing the required beam quality at SPS extraction. Simulations of this complicated RF manipulation using an accurate SPS impedance model and realistic beam parameters are essential step in realization of this RF gymnastics.

## 1.5 Outline of the Thesis

Chapter 1 is an Introduction. Chapter 2 presents some fundamental notions of the theory of synchrotron motion in accelerators. The BLonD code is also introduced, and its main characteristics are described. Emphasis is placed on some important algorithms and concepts which have been crucial for the beam dynamics studies shown later in the thesis. Whenever possible, a link between theory and simulations has been discussed in presenting theoretical aspects of beam dynamics.

A review of the main approaches used in longitudinal beam dynamics codes to compute collective effects is presented in Chapter 3. Two of these methods, the ones used in the BLonD and MuSiC codes, adopt quite different techniques for induced voltage calculation and for this reason they are examined in detail through

extensive benchmarks between them and comparison with analytical formulas. The goal is to check the BLonD reliability for the simulations performed in this thesis, which in many cases include collective effects. The benchmarks presented here are also important since they provide a fundamental understanding of numerical issues encountered when collective effects are included in simulations. Related numerical pitfalls that need to be avoided are highlighted.

Chapter 4 starts with a detailed description of some of the main PSB machine and beam parameters, emphasizing the difference between the current situation and the after-upgrade scenario. The consequences of the LIU Project requests in terms of parameter values are explained. One Section is then dedicated to describe the conventions used in the PSB to measure the longitudinal bunch length and emittance. Studies using both measurements and simulations, needed for taking the decision to replace the current ferrite RF systems with Finemet® ones after upgrade, are shown. Then the derivation of the future PSB longitudinal space charge impedance, very important in non-ultrarelativistic energy machines, is presented. The full PSB longitudinal impedance model is also described, singling out the Finemet® cavity contribution with and without the effect of the beam loading compensation through Low Level RF cavity-based feedbacks. Then double RF operation in the PSB is analyzed in detail, giving emphasis to the effects of the multi-turn induced voltage on the RF phase calibration between the main and second RF systems. Finally simulation results for PSB nominal and high intensity beams are presented, beam stability issues are highlighted, and suggestions for possible cures are given.

Controlled longitudinal emittance blow-up in the PSB is currently needed to counteract transverse direct space charge effects at PS injection. After LS2 it will become even more important due to the higher required longitudinal emittances. While presently the blow-up is achieved using a high-harmonic RF phase modulation generated by a dedicated RF cavity, Chapter 5 introduces another method, never used in the PSB, based on the injection of band-limited RF phase noise into the main harmonic RF system. The effect of phase noise has very interesting features and its usage can complement the phase modulation technique. Then attention is given to the modeling and implementation in the BLonD code of the PSB beam-based feedbacks (phase and radial loops), which are and will be crucial to preserve beam stability in operation along the entire cycle. Since the phase noise will be counteracted by the phase loop, the interaction between them is analyzed. Then important measurements proving that the phase noise technique will be able to satisfy the LIU requirements are shown. Finally more realistic simulations for the after-upgrade beams are performed, using all the tools developed in Chapter 4, and including beam-based feedbacks and longitudinal emittance blow-up.

Chapter 6 introduces first the principle behind momentum slip-stacking, which is supposed to be used in the SPS after RF upgrade to interleave two ion batches in the longitudinal phase space halving the bunch distance. This complicated RF manipulation needs the design and optimization of numerous parameters, momentum and RF programs. Therefore Chapter 6 aims at finding the optimal sets of parameters for the three different optics available in the SPS. Beam dynamics simulations are performed including an accurate longitudinal impedance model and using realistic beam parameters. Simulation results are carefully analyzed to establish that the LIU requests can be fulfilled. The last part of Chapter 6 deals with beam stability

considerations and it provides suggestions to counteract possible limitations due to collective effects.

Chapter 7 provides a summary of the thesis, highlighting the main conclusions and the personal achievements.

Finally Appendix A contains some elements of transverse beam dynamics which are needed to understand several important concepts presented in this thesis.

# Chapter 2

# Fundamentals of Synchrotron Motion and the BLonD Code

## 2.1 Introduction

The BLonD (Beam Longitudinal Dynamics) code was started in 2014 in the RF group of the Beams Department at CERN [12]. During the past years this tool has been steadily developing and nowadays it allows, through macro-particle simulations, to perform almost all the tasks required for longitudinal beam dynamics studies in synchrotrons, such as acceleration of multi-bunch beams in multi-harmonic RF systems, including RF feedbacks, and beam manipulations, all with intensity effects. In addition great effort was and is still applied to speed up the computations through conversion of Python functions into C++ routines, using also parallelization and vectorization techniques [13, 14]. This is necessary for the computationally-demanding simulations BLonD has to deal with. The BLonD code has been used to simulate beams in all the CERN synchrotrons (the first was the SPS [15, 16]) and it has been adopted also at GSI (Germany) and Fermilab (USA). Figure 2.1 shows graphically how the particle tracking works in BLonD and illustrates some of the code features. All of them and many others will be presented either in this Chapter or later.

Some fundamental notions of longitudinal beam dynamics which will be used extensively throughout the thesis are also presented in this Chapter. Since often these concepts have been translated into algorithms, which then have been implemented into the BLonD code, this Chapter tries to link theory and algorithms whenever possible.

## 2.2 Definition of Synchrotron

A synchrotron is a specific type of circular particle accelerator which, through the use of electromagnetic fields, is able to accelerate and confine a charged particle beam keeping the same closed orbit. The electric field is responsible for the particles acceleration. The magnetic field, which bends the beam into its cyclic path, increases during acceleration, being synchronized to the rising energy of the particles. In this thesis the term acceleration indicates an increase in energy of the particle and not a

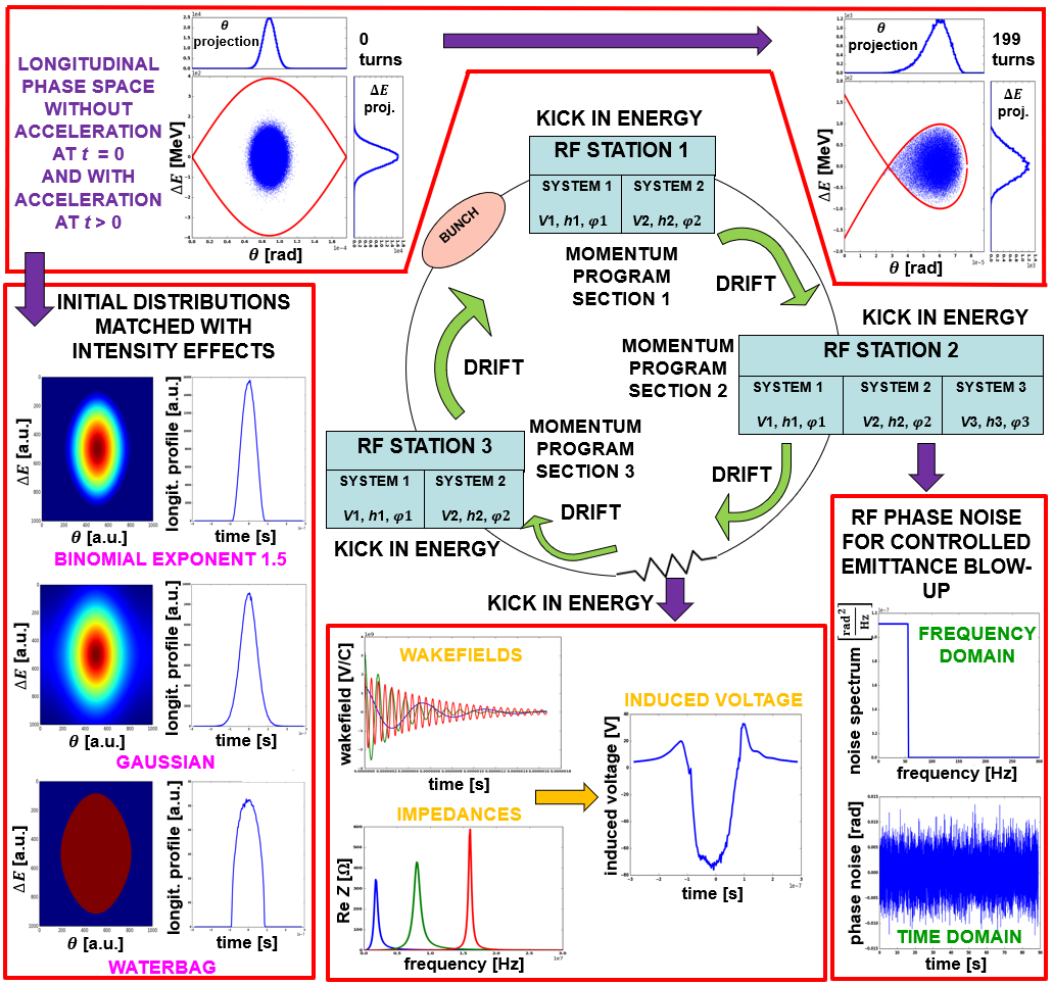


**Figure 2.1.** Scheme illustrating some features of the BLonD code. In the center, a schematic drawing of an example of synchrotron is shown. The several red boxes illustrate, starting from the top and moving clock-wise: beam acceleration, RF phase noise injection for longitudinal emittance blow-up, induced-voltage calculations and generation of stationary beam distributions taking into account intensity effects.

change of the direction of its velocity vector.

The force $\boldsymbol{F}$ acting on a particle with charge $q$ and velocity $\boldsymbol{v}$ in an electromagnetic field is called Lorentz force and is given by (see e.g. Ref.[17])

$$\boldsymbol{F} = q(\boldsymbol{\mathcal{E}} + \boldsymbol{v} \times \boldsymbol{B}). \tag{2.1}$$

The electric $\boldsymbol{\mathcal{E}}$ and magnetic $\boldsymbol{B}$ fields are provided respectively by radio-frequency (RF) cavities and dipole magnets placed along the ring. The energy gain per turn of the particle is given by

$$(\Delta E)_{\text{gain}} = \oint_{S_{\text{ct}}} \boldsymbol{F} \cdot \boldsymbol{ds} = q \oint_{S_{\text{ct}}} \boldsymbol{\mathcal{E}} \cdot \boldsymbol{ds} + q \int_0^{T_0} \boldsymbol{v} \times \boldsymbol{B} \cdot \boldsymbol{v} dt = q \int_{\text{RF gaps}} \boldsymbol{\mathcal{E}} \cdot \boldsymbol{ds}, \tag{2.2}$$

where the contour integrals are taken around the closed trajectory $S_{\text{ct}}$ and $T_0$ is the time needed to perform one revolution turn. Note that the magnetic field, which is

perpendicular to the particle orbit, does not contribute to the energy increase of the particle.

Let us suppose that the synchrotron is perfectly circular with the central orbit having radius $\rho_0$. In other words we suppose that the dipole magnets, responsible for the particle bending, are placed all around the ring. At a given energy, the centrifugal force acting on the circulating particle has to be exactly compensated by the bending magnetic field. Therefore the following relation must hold

$$F = \frac{mv^2}{\rho_0} = qvB, \tag{2.3}$$

where $m$ is the mass of the particle. Rearranging Eq.(2.3) one obtains the so-called magnetic rigidity formula [17]

$$B\rho_0 = \frac{p}{q}. \tag{2.4}$$

This last expression shows that the magnetic field has to be proportional to the particle momentum at each revolution turn in order to accelerate the particle while keeping it on a circular trajectory. In other words, the RF cavities, responsible for the increase of the particle momentum, have to be synchronized with the magnetic field.

In reality a synchrotron is never perfectly circular, since the dipoles do not cover the full ring to leave space, for example, to straight sections where the RF cavities can be placed. However, to be able to properly bend a particle in a closed trajectory, combining all the dipoles together a circle of dipole bending radius $\rho_0$ is obtained and therefore Eq.(2.4) is still valid. It is possible to define a mean radius of the machine $\overline{R}$, with $\overline{R} > \rho_0$, and the corresponding mean circumference $C_{\text{ring}} = 2\pi\overline{R}$. The average dipole field is defined as [18]

$$\overline{B} \coloneqq \frac{1}{C_{\text{ring}}} \oint_{S_{\text{ct}}} B ds = \frac{1}{C_{\text{ring}}} \left( \int\limits_{\text{straights}} B ds + \int\limits_{\text{dipoles}} B ds \right) = \frac{\rho_0 B}{\overline{R}}, \tag{2.5}$$

since the dipole field is zero in the straight sections and independent on $s$ along the dipoles. Using Eq.(2.4) we find indeed a generalization of the magnetic rigidity formula

$$\overline{B}\,\overline{R} = \frac{p}{q}. \tag{2.6}$$

From now on the mean radius of the machine will be denoted without the bar. Note that in our derivations above we neglected, as a first approximation, the presence of higher order (quadrupolar, sextupolar, etc.) magnetic fields and self-induced electromagnetic fields, since all of these contributions are generally small relative to the centrifugal and bending forces.

## 2.3 Energy Gain per Turn

Let us consider an RF cavity having length $l_{\text{gap}}$ in a synchrotron. We assume that a generic particle traverses the RF gap along its central axis, where generally the

electric field $\mathcal{E}$ is purely longitudinal. If we fix a certain point $s$ along the gap then the electric field at $s$ depends on time according to (see e.g. Ref.[17])

$$\mathcal{E}(t) = \hat{\mathcal{E}} \sin(\omega_{\mathrm{rf}}\, t + \phi_{\mathrm{rf}}), \tag{2.7}$$

where $\hat{\mathcal{E}}$ is the design amplitude of the electric field, while $\omega_{\mathrm{rf}}$ and $\phi_{\mathrm{rf}}$ are respectively the RF angular frequency and phase of $\mathcal{E}$. Starting from Eq.(2.2) and assuming only one RF gap we have

$$(\Delta E)_{\mathrm{gain}} = q \int_{-\frac{l_{\mathrm{gap}}}{2}}^{\frac{l_{\mathrm{gap}}}{2}} \mathcal{E}(s) ds = q\hat{\mathcal{E}} \int_{-\frac{l_{\mathrm{gap}}}{2}}^{\frac{l_{\mathrm{gap}}}{2}} \sin\left(\frac{\omega_{\mathrm{rf}}}{v} s + \phi_{\mathrm{rf}}\right) ds \tag{2.8}$$

In traveling wave structures, as those used in the SPS [19], the phase velocity of the RF wave can be adjusted to match the particle speed, in such a way that the particle sees the same phase $\hat{\phi}_{\mathrm{rf}}$ of the electric field all along its passage through the gaps. Equation (2.8) simply becomes

$$(\Delta E)_{\mathrm{gain}} = q\hat{\mathcal{E}} \int_{-\frac{l_{\mathrm{gap}}}{2}}^{\frac{l_{\mathrm{gap}}}{2}} \sin\hat{\phi}_{\mathrm{rf}}\, ds = qV_{\mathrm{rf}} \sin\hat{\phi}_{\mathrm{rf}}, \tag{2.9}$$

where $V_{\mathrm{rf}} = \hat{\mathcal{E}} l_{\mathrm{gap}}$ is the maximum voltage that can be obtained through the cavity.

In standing wave cavities, as those installed in the PSB [20], the RF wave is not propagating according to the particle speed. In this case the particle will see different RF phases along its passage through the gap. Assuming that the change in particle velocity along the gap is negligible and starting from Eq.(2.8), it follows that

$$(\Delta E)_{\mathrm{gain}} = q\hat{\mathcal{E}} \int_{-\frac{l_{\mathrm{gap}}}{2}}^{\frac{l_{\mathrm{gap}}}{2}} \cos\left(\frac{\omega_{\mathrm{rf}}}{v} s\right) \sin\phi_{\mathrm{rf}}\, ds = \frac{2q\hat{\mathcal{E}} v \sin\phi_{\mathrm{rf}}}{\omega_{\mathrm{rf}}} \sin\left(\frac{\omega_{\mathrm{rf}}\, l_{\mathrm{gap}}}{2v}\right), \tag{2.10}$$

where the sum trigonometric identity and the fact that the sinusoidal function is odd in the interval $[-l_{\mathrm{gap}}/2, l_{\mathrm{gap}}/2]$ have been used. Rearranging the factors the following expression is obtained

$$(\Delta E)_{\mathrm{gain}} = qV_{\mathrm{rf}}\, T_{\mathrm{a}} \sin\phi_{\mathrm{rf}}, \tag{2.11}$$

where

$$T_{\mathrm{a}} = \frac{\sin\left(\frac{\omega_{\mathrm{rf}}\, l_{\mathrm{gap}}}{2v}\right)}{\frac{\omega_{\mathrm{rf}}\, l_{\mathrm{gap}}}{2v}} \tag{2.12}$$

is called transit time factor. Notice that $T_{\mathrm{a}} < 1$ and that $T_{\mathrm{a}}$ converges to one when the argument of the sinusoidal function goes to zero. In addition $\omega_{\mathrm{rf}}\, l_{\mathrm{gap}}/(2v) \propto l_{\mathrm{gap}}/C_{\mathrm{ring}}$ (see next Section), therefore if $l_{\mathrm{gap}} \ll C_{\mathrm{ring}}$ then $T_{\mathrm{a}} \approx 1$ in Eq.(2.11). In this thesis $T_{\mathrm{a}} = 1$ is always assumed.

## 2.4 Longitudinal Equations of Motion

In this Section the longitudinal equations of motion for one particle circulating in a synchrotron will be derived. The derivation here follows the BLonD code documentation [21] and is in part similar to what is reported in Ref.[22].

The particle will receive first a kick in energy through all the RF systems (cavities) present in one RF station and then will drift along the ring through the dipole magnetic fields (see also Fig.2.1). In the case of multiple RF stations, the particle will go in one turn through the different stations taking the corresponding kicks in energy and drifting from one station to the following. In order to simplify the notation and according to what will be used later, the presence of just one RF station in the ring is assumed.

The design (synchronous) energy program $E_0^{(n)}$ is assumed to be given for each revolution turn (for every $n$); roughly said, this program defines the energy values the circulating beam on average should have turn after turn in order to be accelerated. From $E_0^{(n)}$ the momentum $p_0^{(n)}$ and the relativistic quantities $\beta_0^{(n)}$ and $\gamma_0^{(n)}$ can be derived. Defining $R_0$ as the average radius of the design orbit (usually the central orbit of the beam pipe), the angular frequency will be $\omega_{\mathrm{rev},0}^{(n)} = \beta_0^{(n)} c/R_0$ and the corresponding revolution period will be $T_0^{(n)} = 2\pi/\omega_{\mathrm{rev},0}^{(n)}$. The design momentum is assumed to be synchronized with the average magnetic field program $B_0^{(n)}$ according to the previously discussed formula

$$B_0^{(n)} R_0 = p_0^{(n)}/q. \tag{2.13}$$

Hence, a particle located on the design orbit and leaving the RF station with the synchronous energy will remain on the design orbit and will return to the RF station after exactly one revolution period $T_0$; we will call this particle "synchronous". Note that in the present thesis the subscript 0 refers to the synchronous particle or to the design programs associated with it. As was observed in the previous Section, it is also assumed that the length of the RF station is small relative to the ring circumference.

An external reference time $t_{\mathrm{ref}}^{(n)}$ can then be defined using the values $T_0^{(n)}$

$$t_{\mathrm{ref}}^{(n)} \coloneqq \sum_{i=1}^{n} T_0^{(i)}, \quad n = 0, 1, 2 \ldots \tag{2.14}$$

From that, the arrival time $t^{(n)}$ of an arbitrary particle to the RF station relative to the reference time at turn $n-1$ can also be defined

$$\Delta t^{(n)} \coloneqq t^{(n)} - t_{\mathrm{ref}}^{(n-1)}, \quad n = 1, 2, 3 \ldots \tag{2.15}$$

From Eqs.(2.14) and (2.15) it follows that

$$t^{(n)} \in \left[ t_{\mathrm{ref}}^{(n-1)}, t_{\mathrm{ref}}^{(n)} \right] \quad \text{or} \quad \Delta t^{(n)} \in \left[ 0, T_0^{(n)} \right] \tag{2.16}$$

The phase of the RF voltage of the $k^{\mathrm{th}}$ RF system at the arrival time $t^{(n)}$ of the particle is

$$\begin{gathered} \phi_{\mathrm{rf},k}(t^{(n)}) = \int_0^{t^{(n)}} \omega_{\mathrm{rf},k}(\tau) d\tau + \phi_{\mathrm{offset},k}^{(n)} = \\ \sum_{i=1}^{n-1} \omega_{\mathrm{rf},k}^{(i)} T_0^{(i)} + \left( t^{(n)} - t_{\mathrm{ref}}^{(n-1)} \right) \omega_{\mathrm{rf},k}^{(n)} + \phi_{\mathrm{offset},k}^{(n)} = \omega_{\mathrm{rf},k}^{(n)} \Delta t^{(n)} + \phi_{\mathrm{rf},k}^{(n)}. \end{gathered} \tag{2.17}$$

The quantity $\sum_{i=1}^{n-1} \omega_{\mathrm{rf},k}^{(i)} T_0^{(i)}$ is a multiple of $2\pi$ if and only if the condition $\omega_{\mathrm{rf},k}^{(i)} = h\omega_{\mathrm{rev},0}^{(i)}$ is satisfied for each $i$, where $h$ is the main harmonic number of the ring defining the amount of bunches one synchrotron can accelerate simultaneously. The term $\phi_{\mathrm{offset},k}^{(n)}$ can describe, for example, the effect of RF phase noise or constant phase offsets. Thus, according to Eq.(2.11) the total energy change in one turn of the particle is

$$E^{(n+1)} = E^{(n)} + q \sum_{k=1}^{n_{\mathrm{rf}}} V_{\mathrm{rf},k}^{(n)} \sin\left(\omega_{\mathrm{rf},k}^{(n)} \Delta t^{(n)} + \phi_{\mathrm{rf},k}^{(n)}\right), \tag{2.18}$$

where $n_{\mathrm{rf}}$ is the number of RF systems in the section. Defining $\Delta E^{(n)} := E^{(n)} - E_0^{(n)}$ we have

$$\Delta E^{(n+1)} = \Delta E^{(n)} + q \sum_{k=1}^{n_{\mathrm{rf}}} V_{\mathrm{rf},k}^{(n)} \sin\left(\omega_{\mathrm{rf},k}^{(n)} \Delta t^{(n)} + \phi_{\mathrm{rf},k}^{(n)}\right) - \left(E_0^{(n+1)} - E_0^{(n)}\right). \tag{2.19}$$

To derive the second equation of motion for a generic particle, we start with the expression

$$t^{(n+1)} = t^{(n)} + 2\pi/\omega_{\mathrm{rev}}^{(n+1)}, \tag{2.20}$$

where $\omega_{\mathrm{rev}}^{(n)}$ is the angular revolution frequency of the particle at $n^{\mathrm{th}}$ turn. Relative to the reference time, we obtain

$$\Delta t^{(n+1)} = \Delta t^{(n)} + \frac{2\pi}{\omega_{\mathrm{rev}}^{(n+1)}} - \frac{2\pi}{\omega_{\mathrm{rev},0}^{(n+1)}} = \Delta t^{(n)} + T_0^{(n+1)} \left( \frac{1}{1 + \frac{\omega_{\mathrm{rev}}^{(n+1)} - \omega_{\mathrm{rev},0}^{(n+1)}}{\omega_{\mathrm{rev},0}^{(n+1)}}} - 1 \right). \tag{2.21}$$

The frequency slippage of an off-momentum particle during one turn is defined with respect to the design synchronous particle [17],

$$\frac{\Delta\omega_{\mathrm{rev}}}{\omega_{\mathrm{rev},0}} = \frac{\omega_{\mathrm{rev}} - \omega_{\mathrm{rev},0}}{\omega_{\mathrm{rev},0}} = -\eta(\delta)\delta = -\left(\eta_0 + \eta_1\delta + \eta_2\delta^2 + \ldots\right)\delta, \tag{2.22}$$

where $\delta = \Delta p/p_0 = \Delta E/(\beta_0^2 E_0)$ is the relative off-momentum of the particle and $\eta_i$ are the slippage factors defined through the momentum compaction factors $\alpha_i$ (e.g. $\eta_0 = \alpha_0 - 1/\gamma_0^2$). The factors $\alpha_i$ are constant numbers for a given machine and depend on the optics. Using Eq.(2.22), we can rewrite Eq.(2.21) as

$$\Delta t^{(n+1)} = \Delta t^{(n)} + T_0^{(n+1)} \left( \frac{1}{1 - \eta(\delta)^{(n+1)}\delta^{(n+1)}} - 1 \right). \tag{2.23}$$

The energy where $\eta_0 = 0$ is called transition energy and the corresponding gamma is $\gamma_{\mathrm{tr}} = 1/\sqrt{\alpha_0}$. When $|\gamma_0 - \gamma_{\mathrm{tr}}| \gg 0$ then the linear approximation can be taken in Eq.(2.22) and, since usually $|\eta_0\delta| \ll 1$, we obtain

$$\Delta t^{(n+1)} \approx \Delta t^{(n)} + T_0^{(n+1)} \left( \frac{1}{1 - \eta_0^{(n+1)}\delta^{(n+1)}} - 1 \right) \approx \Delta t^{(n)} + T_0^{(n+1)} \eta_0^{(n+1)} \delta^{(n+1)}. \tag{2.24}$$

If $|\gamma_0 - \gamma_{\rm tr}| \approx 0$ then additional terms should be taken in Eq.(2.22), and Eq.(2.23) should be used.

Finally, the two discrete longitudinal equations of motion for the particle $i$ in the bunch can be written in the form

$$\Delta E_i^{(n+1)} = \Delta E_i^{(n)} + q \sum_{k=1}^{n_{\rm rf}} V_{{\rm rf},k}^{(n)} \sin\left(\omega_{{\rm rf},k}^{(n)} \Delta t_i^{(n)} + \phi_{{\rm rf},k}^{(n)}\right) - \left(E_0^{(n+1)} - E_0^{(n)}\right) + q V_{{\rm ind},i}^{(n)}, \tag{2.25}$$

$$\Delta t_i^{(n+1)} = \Delta t_i^{(n)} + \frac{T_0^{(n+1)} \eta_0^{(n+1)}}{\left(\beta_0^2\right)^{(n+1)} E_0^{(n+1)}} \Delta E_i^{(n+1)}, \tag{2.26}$$

where $V_{{\rm ind},i}^{(n)} \equiv V_{{\rm ind},i}^{(n)}(\{\Delta t_m^{(n)}\}_m)$ is the so-called induced voltage which acts on the particle $i$ and is induced by all the other particles in the beam due to collective effects (see next Chapter).

Equations (2.25) and (2.26) can be considered as a map $\mathcal{M}$ from a point $(\Delta t_i^{(n)}, \Delta E_i^{(n)})$ to another point $(\Delta t_i^{(n+1)}, \Delta E_i^{(n+1)})$ in the $(\Delta t, \Delta E)$ plane. Neglecting the collective effects term in the RHS of Eq.(2.25), the motion of the various particles in phase space becomes decoupled, and the fact that the Jacobian determinant of the map $\mathcal{M}$ is equal to one,

$$J(\mathcal{M}) = \begin{vmatrix} \frac{\partial(\Delta t_i^{(n+1)})}{\partial(\Delta t_i^{(n)})} & \frac{\partial(\Delta t_i^{(n+1)})}{\partial(\Delta E_i^{(n)})} \\ \frac{\partial(\Delta E_i^{(n+1)})}{\partial(\Delta t_i^{(n)})} & \frac{\partial(\Delta E_i^{(n+1)})}{\partial(\Delta E_i^{(n)})} \end{vmatrix} = 1, \tag{2.27}$$

implies that the phase space area is conserved under $\mathcal{M}$. This property is related to the fact that $\Delta t$ and $\Delta E$ are canonical (or conjugate) variables, that the dynamics is symplectic and that the Louville theorem holds true.

The two difference Eqs.(2.25) and (2.26) define the so-called synchrotron motion in the longitudinal phase space $(\Delta t, \Delta E)$. The coordinate $\Delta t$ of a particle changes followed by an impulse which modifies only the other coordinate $\Delta E$. Therefore the dynamics under study is impulsive where the drift is acceleration-free. A continuous system can be derived from Eqs.(2.25) and (2.26) to introduce the Hamiltonian of the synchrotron motion (see next Section), however the differential equations obtained are only continuous approximations to the impulsive system under study. Sometimes in literature the opposite reasoning is adopted, considering the difference equations as a discrete approximation of the continuous system. The differential equations corresponding to Eqs.(2.25) and (2.26) are

$$\dot{\Delta E_i} = \frac{q}{T_0} \sum_{k=1}^{n_{\rm rf}} V_{{\rm rf},k} \sin(\omega_{{\rm rf},k} \Delta t_i + \phi_{{\rm rf},k}) - \frac{\delta E_0}{T_0} - \frac{q}{T_0} V_{{\rm ind},i} = -\frac{\partial H}{\partial \Delta t_i}, \tag{2.28}$$

$$\dot{\Delta t_i} = \frac{\eta_0}{\beta_0^2 E_0} \Delta E_i = \frac{\partial H}{\partial \Delta E_i}, \tag{2.29}$$

where the dot operator represents the derivative with respect to time $t$, assuming that $dt = T_0$. The Hamiltonian of the system $H$ will be presented later. All the RF and machine parameters defined in Eqs.(2.25) and (2.26) for every revolution turn $n$ now depend on the continuous variable $t$.

## 2.5 Small-amplitude Synchrotron Motion

Neglecting collective effects and supposing that only one RF system is present, Eqs.(2.28) and (2.29) can be rewritten as

$$\dot{\Delta E} = \frac{q}{T_0} V_{\mathrm{rf}} (\sin\phi - \sin\phi_{\mathrm{s}}), \tag{2.30}$$

$$\dot{\phi} = \frac{\omega_{\mathrm{rf}} \eta_0}{\beta_0^2 E_0} \Delta E, \tag{2.31}$$

where $\phi = \omega_{\mathrm{rf}} \Delta t + \phi_{\mathrm{rf}}$. In particular the synchronous phase $\phi_s = \omega_{\mathrm{rf}} \Delta t_{\mathrm{s}} + \phi_{\mathrm{rf}}$ satisfies by definition the equation

$$\Delta E_0 = q V_{\mathrm{rf}} \sin(\phi_{\mathrm{s}}) \tag{2.32}$$

Expanding $\sin\phi = \sin(\phi_s + \Delta\phi)$ around $\phi_s$ and supposing a slow variation in time of $\phi_s$ relative to $\phi$ we obtain from Eqs.(2.30) and (2.31) the following differential equation for $\Delta\phi$

$$\ddot{\Delta\phi} + \omega_{\mathrm{s0}}^2 \Delta\phi = 0, \tag{2.33}$$

where $\omega_{\mathrm{s0}}$ is the so-called small-amplitude angular synchrotron frequency given by

$$\omega_{\mathrm{s0}} = \sqrt{\frac{\omega_{\mathrm{rf}} q V_{\mathrm{rf}} (-\eta_0 \cos\phi_{\mathrm{s}})}{T_0 \beta_0^2 E_0}} \tag{2.34}$$

after imposing the stability condition

$$\eta_0 \cos\phi_{\mathrm{s}} \leq 0. \tag{2.35}$$

Solving Eq.(2.33 ) we obtain

$$\phi(t) = \phi_{\mathrm{s}} + \hat{\phi} \cos(\omega_{\mathrm{s0}} t), \tag{2.36}$$

where $\hat{\phi}$ is the amplitude of the oscillations. Therefore particles close to the synchronous particle perform pendulum-like synchrotron oscillations around it. The stability condition implies that $\phi_s \in [-\pi/2, \pi/2]$ below transition energy ($\eta_0 < 0$) and $\phi_s \in [\pi/2, 3\pi/2]$ above transition energy ($\eta_0 > 0$). Acceleration of the particles is in particular obtained if $\phi_s \in [0, \pi/2]$ (below transition) and if $\phi_s \in [\pi/2, \pi]$ (above transition), while deceleration is obtained taking the corresponding other values for $\phi_s$.

## 2.6 Hamiltonian of the Synchrotron Motion

The Hamiltonian corresponding to Eqs.(2.28) and (2.29) is given by

$$\begin{aligned} H(\Delta t, \Delta E) &= \int \dot{\Delta t}\, d(\Delta E) - \int \dot{\Delta E}\, d(\Delta t) \\ &= \frac{\eta_0}{2\beta_0^2 E_0} \Delta E^2 + \frac{q}{T_0 \omega_{\mathrm{rf},k}} \sum_{k=1}^{n_{\mathrm{rf}}} V_{\mathrm{rf},k} \cos(\omega_{\mathrm{rf},k} \Delta t + \phi_{\mathrm{rf},k}) \\ &\quad + \frac{\delta E_0}{T_0} \Delta t + \frac{q}{T_0} \int V_{\mathrm{ind}}(\Delta t)\, d(\Delta t) + C_H, \end{aligned} \tag{2.37}$$

where $C_H$ is an arbitrary constant. The potential well $U_{\mathrm{tot}}$ is defined as the sum of the RF and induced potentials:

$$U_{\mathrm{tot}}(\Delta t) \coloneqq U_{\mathrm{rf}}(\Delta t) + U_{\mathrm{ind}}(\Delta t), \tag{2.38}$$

where

$$U_{\mathrm{rf}}(\Delta t) \coloneqq \frac{q}{T_0 \omega_{\mathrm{rf},k}} \sum_{k=1}^{n_{\mathrm{rf}}} V_{\mathrm{rf},k} \cos(\omega_{\mathrm{rf},k} \Delta t + \phi_{\mathrm{rf},k}) + \frac{\delta E_0}{T_0} \Delta t, \tag{2.39}$$

$$U_{\mathrm{ind}}(\Delta t) \coloneqq \frac{q}{T_0} \int V_{\mathrm{ind}}(\Delta t)\, d(\Delta t) \tag{2.40}$$

We fix the constant $C_H$ in such a way that the absolute minimum of $U_{\mathrm{tot}}$ is equal to zero.

Every stable particle trajectory in longitudinal phase space is associated to a maximum time amplitude of oscillations $\overline{\Delta t}$ and to a constant value of the Hamiltonian $H(\overline{\Delta t}, 0)$. The equation of the particle trajectory can be derived from Eq.(2.37) taking the real values of

$$\Delta E(\Delta t) = \pm \sqrt{\frac{2\beta_0^2 E_0}{|\eta_0|} [H(\overline{\Delta t}, 0) - U(\Delta t)]}. \tag{2.41}$$

The area $\epsilon_{\mathrm{l}}$ enclosed by the particle trajectory is named particle emittance and is given by

$$\epsilon_{\mathrm{l}}(\overline{\Delta t}) = \sqrt{\frac{2\beta_0^2 E_0}{|\eta_0|}} \oint [H(\overline{\Delta t}, 0) - U(\Delta t)]^{\frac{1}{2}} d(\Delta t). \tag{2.42}$$

Equations (2.41) and (2.42) can also be used to define the stable trajectory with maximum $\overline{\Delta t}$ (the separatrix $\Delta E^{\mathrm{sep}}$) and the portion of phase space enclosed by it (the bucket area $A_{\mathrm{b}}$).

Eliminating $\Delta E$ through Eqs.(2.29) and (2.41), inverting and then integrating in $dt$, we can obtain the expression for the so-called synchrotron period $T_{\mathrm{s}}(\overline{\Delta t})$, that is the time needed for a particle to perform a complete oscillation in phase space:

$$T_{\mathrm{s}}(\overline{\Delta t}) = \sqrt{\frac{\beta_0^2 E_0}{2|\eta_0|}} \oint [H(\overline{\Delta t}, 0) - U(\Delta t)]^{-\frac{1}{2}} d(\Delta t). \tag{2.43}$$

The synchrotron frequency $f_{\mathrm{s}}(\overline{\Delta t})$ is obtained inverting $T_{\mathrm{s}}(\overline{\Delta t})$. Another way to compute $T_{\mathrm{s}}$ is to set $\overline{U} = U(\overline{\Delta t}) = H(\overline{\Delta t}, 0)$ in Eq.(2.42) and calculate

$$\frac{d\epsilon_{\mathrm{l}}}{d\overline{U}} = T_{\mathrm{s}} \tag{2.44}$$

Equivalently, the synchrotron frequency $f_{\mathrm{s}}$ for all the amplitudes $\overline{\Delta t}$ is obtained computing the ratio of the derivatives of the potential well and the emittance with respect to $\overline{\Delta t}$.

## 2.7 Frenet-Serret Coordinate System and Longitudinal Coordinates

As it was mentioned before, the synchronous particle always follows the reference trajectory. A curvilinear right-handed coordinate system $(\hat{x}, \hat{s}, \hat{y})$ (called Frenet-Serret system) can be associated to a generic particle circulating along the synchrotron, where the $\hat{x}$ unit vector points radially outward, $\hat{s}$ is tangent to the design path and points in the direction of motion of the particle and $\hat{y}$ is perpendicular to the plane where the reference trajectory lies (see for example Fig.2.2). The coordinate $s$, which is the path length measured along the design orbit from the point $s = 0$, can be thought as independent variable. Therefore the so-called betatron or transverse coordinates $x$ and $y$ are functions of $s$. It follows that, for every $s$, $x(s) = 0$ and $y(s) = 0$ for the synchronous particle.

The Frenet-Serret system is generally used in transverse beam dynamics. However it cannot describe the relative longitudinal distance between two particles at a given time. To do that we have to set the time as independent variable and therefore each particle will be associated with a triple $(x(s(t)), s(t), y(s(t)))$.

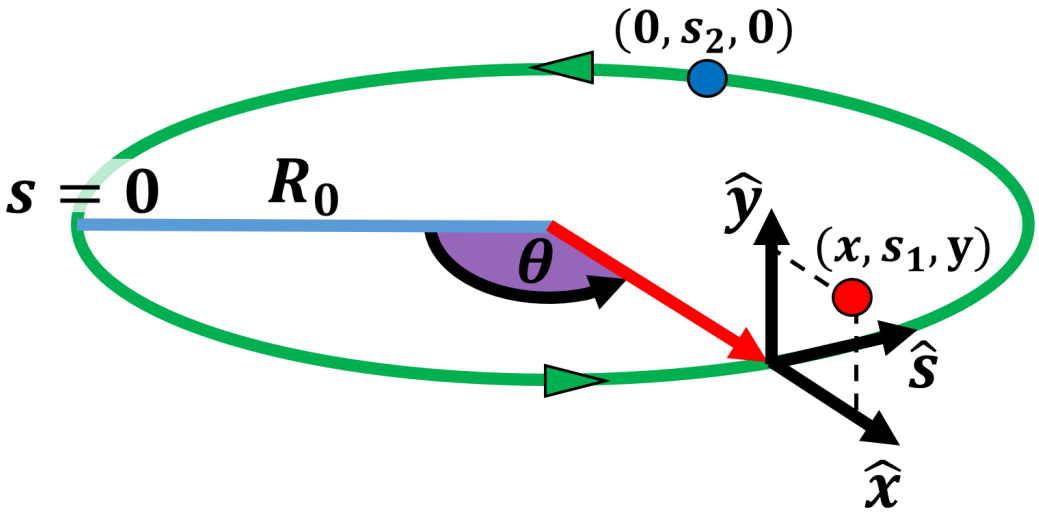


**Figure 2.2.** Curvilinear Frenet-Serret right-handed coordinate system $(\hat{x}, \hat{s}, \hat{y})$ following a generic particle (in red) along the synchrotron. The unit vector $\hat{x}$ points radially outward, $\hat{s}$ is tangent to the reference circumference (in green) of radius $R_0$ and points in the direction of motion of the particle and $\hat{y}$ is perpendicular to the plane of the design orbit. The coordinate $s$ is the path length measured along the design orbit from the $s = 0$ axis, while $\theta$ is the corresponding angular displacement. The synchronous particle (in blue) has always the betatron coordinates $x$ and $y$ equal to 0. For a given time $\bar{t}$, $s(\bar{t})$ equals $s_1$ and $s_2$ for the generic and synchronous particles respectively.

Defining the new longitudinal variable $\Delta s^{(n)} := 2\pi R_0 - (s^{(n-1)} \bmod 2\pi R_0)$, we can relate $\Delta s$ to the $\Delta t$ introduced in Eq.(2.15) through the following expression

$$\Delta s^{(n)} = \beta_0^{(n)} c \Delta t^{(n)}. \tag{2.45}$$

If we denote by $\theta$ the angular displacement from the $s = 0$ axis and we define

$\Delta\theta^{(n)} \coloneqq 2\pi - (\theta^{(n-1)} \bmod 2\pi)$ then

$$\Delta s^{(n)} = R_0 \Delta\theta^{(n)}. \tag{2.46}$$

Finally, starting from Eq.(2.17), we define $\Delta\phi_{\mathrm{rf}}^{(n)} \coloneqq \phi_{\mathrm{rf}}(t^{(n)}) \bmod 2\pi h$. If $\phi_{\mathrm{offset}} = 0$ and $\omega_{\mathrm{rf}} = h\omega_{\mathrm{rev},0}$ for each revolution turn then

$$\Delta\phi_{\mathrm{rf}}^{(n)} = \omega_{\mathrm{rf}}^{(n)} \Delta t^{(n)} = h\Delta\theta^{(n)}. \tag{2.47}$$

Analogously to the conjugate pair of longitudinal coordinates ($\Delta t$, $\Delta E$), the betatron $x$ and $y$ coordinates also have their corresponding canonical variables (the transverse momentums $p_x$ and $p_y$, see [17]), and several of the quantities introduced before for the longitudinal plane (like the Hamiltonian and emittance) can be defined also for the transverse planes. Usually the beam dynamics can be decoupled and studied independently in the longitudinal and transverse planes due to the fact that the synchrotron motion is much slower than the betatron one. This thesis focuses on the longitudinal plane, however Appendix A presents some principles of transverse beam dynamics useful to understand specific concepts introduced in this work (see for example Eq.(1.2)).

## 2.8 Longitudinal Bunch Profile

Let us consider a bunch of $N_{\mathrm{M}}$ particles in the longitudinal phase space $(\Delta t, \Delta E)$, where $\Delta t \in [0, T_{\mathrm{rf}}]$, being $T_{\mathrm{rf}} = T_0/h$ the RF period. It is possible to count how many particles $n_1$ are contained in the bin or slice ($\Delta t_1 < \Delta t < \Delta t_2$, $\Delta E$), where $\Delta t_2 = \Delta t_1 + \Delta$, being $\Delta$ the time step (Fig.2.3, left). Repeating the procedure for consecutive bins in phase space, and counting how many particles $n_i$ are contained in the bin ($\Delta t_i < \Delta t < \Delta t_{i+1}$, $\Delta E$), one obtains the so-called discrete longitudinal bunch profile $n$ or the continuous not-normalized line-density $\lambda$ when $\Delta$ converges to zero and the number of particles is large enough to be considered infinite (Fig.2.3, right). Supposing that the entire bunch is sliced, then

$$\sum_i n_i = N_M, \quad \int_{T_{\mathrm{rf}}} \lambda(t)dt = N_M. \tag{2.48}$$

Once the longitudinal bunch profile is obtained, numerous quantities of interest can be computed, as for example the bunch position $m_\lambda$ and length $\tau_l$. Unless otherwise specified, in the present thesis $m_\lambda$ is defined as the average position of the bunch profile, therefore

$$m_\lambda = \frac{\int_{T_{\mathrm{rf}}} \lambda(t) t\, dt}{\int_{T_{\mathrm{rf}}} \lambda(t)\, dt}. \tag{2.49}$$

For simplicity of notation, $m_\lambda$ will also denote the bunch-profile average position in phase coordinate, after having multiplied Eq.(2.49) by $\omega_{\mathrm{rf}}$.

The bunch length can be computed in numerous ways, and some of them will be mentioned in the following Chapters. Notice that the chosen convention determines a certain stable particle-trajectory with Hamiltonian $H_\tau$ and longitudinal emittance $\epsilon_{\mathrm{l}}$ (see Fig.2.3).

The evolutions of $m_\lambda$ and $\tau_l$ along the acceleration cycle allow to determine respectively the so-called dipole and quadrupole oscillations, which provide important indications whether or not the beam suffers any instability or quality degradation.

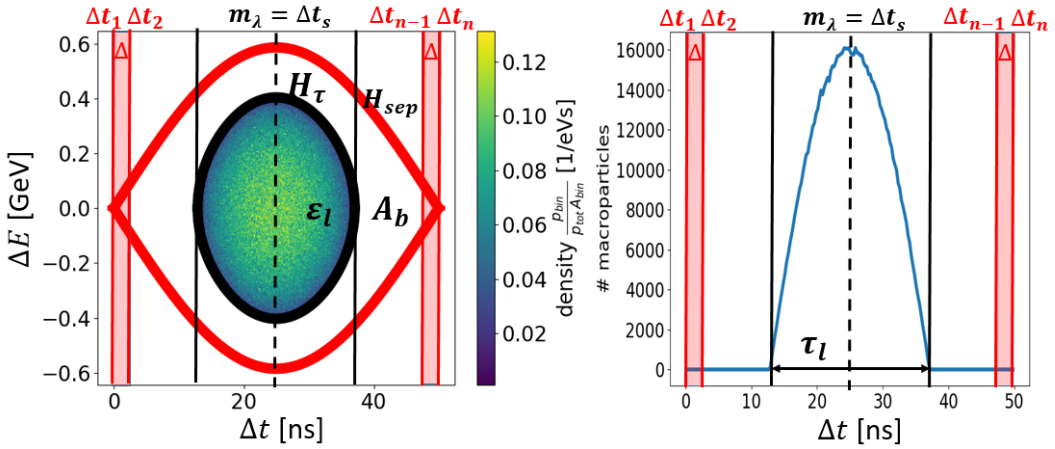


**Figure 2.3.** Example of bunch of particles contained inside an RF bucket in longitudinal phase space $(\Delta t, \Delta E)$ (left) and corresponding longitudinal bunch-profile $n$ (right). The bucket area $A_\mathrm{b}$ is delimited by the separatrix curve in red having Hamiltonian $H_\mathrm{sep}$. The profile is obtained slicing the bunch in phase space with a certain time step $\Delta$. In this example the synchronous time $\Delta t_\mathrm{s}$ and the bunch-profile average position $m_\lambda$ coincide. Moreover, in this case, the end-to-end bunch length $\tau_\mathrm{l}$ determines a stable particle-trajectory with Hamiltonian $H_\tau$ and emittance $\epsilon_\mathrm{l}$.

.

## 2.9 Bunch Shaping in a Double RF System

Double RF systems can be used to shape the bunch profile, for example making it longer or shorter once the longitudinal emittance $\epsilon_\mathrm{l}$ is given. This shaping can be useful for different reasons, such as when the profile cannot be larger than a certain value in order for the beam to be extracted without losses or when the maximum value of the line density has to be reduced in order to lower the transverse space charge tune spread (see Chapter 4). Another important purpose is to increase the synchrotron frequency spread along the bunch enhancing the so-called Landau damping mechanism which helps in stabilizing the beam (see Chapter 3).

The total RF voltage seen by the beam is

$$V_{\mathrm{rf},tot}(\Delta t) = V_{\mathrm{rf},1} \sin(\omega_{\mathrm{rf},1}\Delta t + \phi_{\mathrm{rf},1}) + rV_{\mathrm{rf},1} \sin(n\omega_{\mathrm{rf},1}\Delta t + \phi_{1,2}), \tag{2.50}$$

where $V_{\mathrm{rf},1}$ and $V_{\mathrm{rf},2} = rV_{\mathrm{rf},1}$ are respectively the voltage amplitudes of the main and second RF systems (usually $r \leq 1$ for bunch shaping), $\phi_{1,2}$ is the relative phase between them and $n > 1$ is the integer ratio between the frequencies of the two systems.

The phase $\phi_{1,2}$ determines the double RF operating mode. The name of the mode reflects the effect that the double RF system has on the bunch profile. For a stationary bucket below transition energy and for $n$ even, the bunch-shortening mode (BSM) is obtained choosing $\phi_{1,2} = 0$, while bunch-lengthening mode (BLM) is achieved selecting $\phi_{1,2} = \pi$, see for example Fig.2.4. Above transition energy, or when $n$ is odd, the opposite is true.

Fixing all the other machine and RF parameters, and assuming constant longitudinal emittance, usually the BSM mode gives higher synchrotron frequency spread

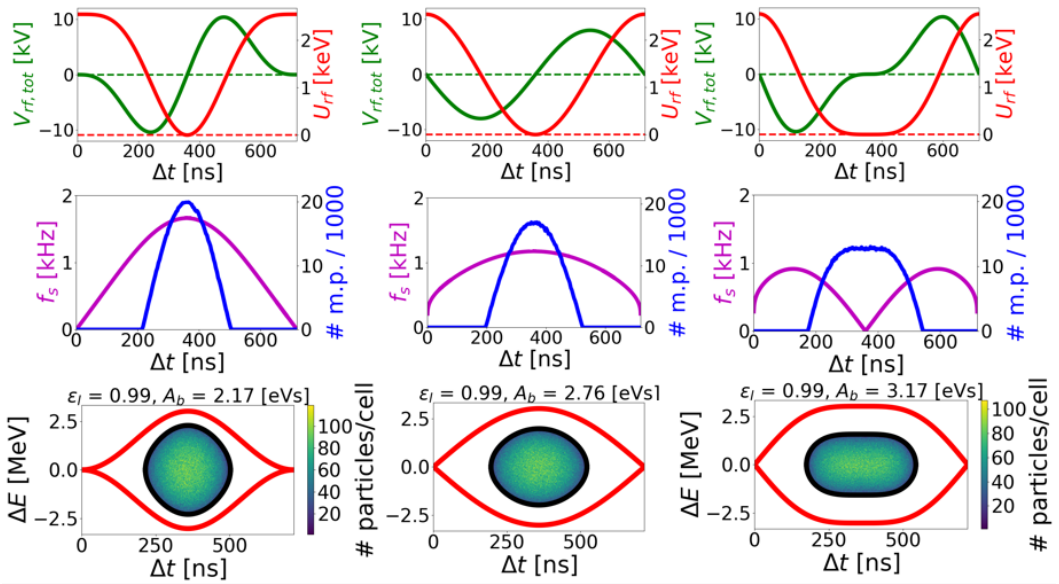


**Figure 2.4.** RF voltage $V_{\mathrm{rf},tot}$ (green), RF potential $U_{\mathrm{rf}}$ (red), synchrotron frequency distribution $f_s$ (magenta), bunch profile or number of macroparticles per slice (blue) and longitudinal phase space for the cases of double RF BSM (left), BLM (right) and single RF (middle). Here $r = 0.5$ and $n = 2$. The emittance $\epsilon_{\mathrm{l}} = 0.99$ eVs and the bucket area $A_{\mathrm{b}}$ are also indicated. Realistic examples using current PSB machine and RF parameters (e.g $h = 1$ and $V_{\mathrm{rf},1} = 8$ kV), however the buckets are supposed stationary ($p_0 = 1$ GeV/c).

along the bunch, however the peak line density also increases and the bucket area decreases, see for example Fig.2.4. On the contrary, the BLM mode is advantageous in all these respects, even though it requires a large accuracy for $\phi_{1,2}$ difficult to achieve in the presence of strong collective effects and it can reduce the longitudinal instability threshold for relatively long bunches [23].

## 2.10 Bunch Generation in the BLonD Code

Stationary particle distributions can be used for theoretical studies and for generation of bunches in macro-particle simulations [24]. In this Section we will explain how to generate a bunch in longitudinal phase space using a stationary distribution when the Hamiltonian of the synchrotron motion contains both the RF and induced potential. Sometimes such a generated bunch is said to be "matched" with intensity effects.

### 2.10.1 Stationary Distributions

Let's suppose the bunch we want to generate has $N_{\mathrm{tot}}$ particles enclosed in a domain $D$. A longitudinal distribution function $\psi = \psi(\Delta t, \Delta E, t)$ is a positive real function such that the number of particles $dN$ occupying the infinitesimal area $d(\Delta t)d(\Delta E)$ at time $t$ is

$$dN(t) = N_{\mathrm{tot}}\psi(\Delta t, \Delta E, t)d(\Delta t)d(\Delta E). \tag{2.51}$$

Integrating Eq.(2.51) over $D$ we obtain for every $t$

$$1 = \iint_D \psi(\Delta t, \Delta E, t) d(\Delta t) d(\Delta E). \tag{2.52}$$

Note that $\psi$ can also be interpreted as a probability density function, that is as the probability to find a particle in the area $d(\Delta t)d(\Delta E)$ in the vicinity of the point $(\Delta t, \Delta E)$. The distribution $\psi$ is said to be stationary when it does not depend explicitly on the time $t$, that is $\psi = \psi(\Delta t, \Delta E)$.

The time evolution of $\psi(\Delta t, \Delta E, t)$ can be computed as

$$\frac{d\psi}{dt} = \frac{\partial \psi}{\partial t} + \frac{\partial \psi}{\partial \Delta t}\dot{\Delta t} + \frac{\partial \psi}{\partial \Delta E}\dot{\Delta E}. \tag{2.53}$$

Using Eqs.(2.28) and (2.29) we obtain

$$\frac{d\psi}{dt} = \frac{\partial \psi}{\partial t} + [\psi, H]_{\{\Delta t, \Delta E\}}, \tag{2.54}$$

where the Poisson bracket of two generic functions $f$ and $g$ relative to a canonical pair of coordinates $q$ and $p$ is defined as

$$[f, g]_{\{q,p\}} = \frac{\partial f}{\partial q}\frac{\partial g}{\partial p} - \frac{\partial g}{\partial q}\frac{\partial f}{\partial p}. \tag{2.55}$$

From the continuity equation [25]

$$\frac{\partial \psi}{\partial t} + \frac{\partial}{\partial \Delta t}(\psi \dot{\Delta t}) + \frac{\partial}{\partial \Delta E}(\psi \dot{\Delta E}) = 0, \tag{2.56}$$

and using again Eqs.(2.28) and (2.29), we obtain the so-called Liouville equation

$$\frac{d\psi}{dt} = 0, \tag{2.57}$$

which, together with the hypothesis that $\psi$ is stationary, implies that the Poisson bracket in Eq.(2.54) vanishes

$$[\psi, H]_{\{\Delta t, \Delta E\}} = 0. \tag{2.58}$$

Notice that any distribution of the form $\psi = \psi(H)$ satisfies Eq.(2.58).

### 2.10.2 Algorithm for Bunch Generation

In the following we describe the algorithm used in BLonD to generate a bunch in longitudinal phase space according to a generic distribution function $\psi = \psi(H)$, see also Ref.[26]. We focus on the physical concepts behind the algorithm neglecting the technicalities necessary to efficiently write the code. We assume given the emittance $\epsilon_{l,\tau}$ of the bunch to be generated. It follows that $\psi$ has to depend on a parameter $H_\tau(\epsilon_{l,\tau})$, therefore $\psi = \psi_{H_\tau}(H)$.

First we suppose that the induced potential is identically equal to zero ($U_{\text{tot}} = U_{\text{rf}}$). The following steps have to be performed (we call the entire procedure R)

1. $U_{\mathrm{tot}}$ is computed integrating the energy equation of motion (2.28); then $U_{\mathrm{tot}}$ is restricted to the interval $[\Delta t_l, \Delta t_r]$ where the separatrix is defined (we call the restriction $\bar{U}_{\mathrm{tot}}$). In general $\Delta t_l$ and $\Delta t_r$ are found by analyzing the shape of $U_{\mathrm{tot}}$, including its local and absolute maxima and minima. In the simplest case of single RF without acceleration $\Delta t_{\mathrm{l}} = 0$, $\Delta t_r = T_{\mathrm{rf}}$.

2. Since $min(\bar{U}_{\mathrm{tot}}) = 0$ (see Section 2.6) we can find the maximum value of $\Delta E$ for the separatrix using Eq.(2.41)

$$max(\Delta E_{\mathrm{sep}}) = \sqrt{\frac{2\beta_0^2 E_0}{|\eta_0|} \max(\bar{U}_{\mathrm{tot}})} \tag{2.59}$$

3. The grid of points $G = [\Delta t_l, \Delta t_r] \times [-max(\Delta E_{\mathrm{sep}}), max(\Delta E_{\mathrm{sep}})]$ can be defined; by construction, $G$ contains the full bucket. The time and energy resolution steps of $G$ are named respectively $\Delta_1$ and $\Delta_2$.

4. The trajectories having the values in $[\Delta t_l, \Delta t_r]$ as amplitudes are computed using Eq.(2.41). Integrating the trajectories using Eq.(2.42) the corresponding emittances $\epsilon_{\mathrm{l}}$ are obtained. The values of the Hamiltonian are already available since $H = \bar{U}_{\mathrm{tot}}$. Therefore a function $H(\epsilon_{\mathrm{l}})$ is obtained.

5. The parameter $H_\tau$ is found interpolating $H(\epsilon_{\mathrm{l}})$ with $\epsilon_{l,\tau}$.

6. The values of the Hamiltonian at the points of grid $G$ are obtained as

$$H_G = \frac{|\eta_0|}{2\beta_0^2 E_0} \Delta E_G^2 + \bar{U}_{\mathrm{tot}}(\Delta t_G). \tag{2.60}$$

7. The distribution $\psi$ is evaluated on the grid points using $H_G$ and $H_\tau$, we call $\psi_G$ this restriction. If a grid point $Q$ lies on a trajectory having $H_Q > H_{\mathrm{sep}}$, then $\psi_G(Q)$ is set to zero in order to avoid generating particles outside of the RF bucket. This event can happen if and only if $\psi(H)$ decays after $H_{\mathrm{sep}}$.

8. From the discretization of $\psi$ on $G$, it follows that

$$\sum_{Q \in G} \psi_G(Q) \Delta_1 \Delta_2 = A, \tag{2.61}$$

   with $A$ in general different from one. Therefore a discrete probability function on $G$ can be obtained defining

$$\Psi_G(Q) \coloneqq \frac{\psi_G(Q)}{\sum_{Q \in G} \psi_G(Q)}, \tag{2.62}$$

   This procedure of renormalization can be applied also when $\psi(H)$ decays after $H_{\mathrm{sep}}$, since in this case Eq.(2.52) is violated after having imposed $\psi(H) = 0$ for $H > H_{\mathrm{sep}}$.

9. If the resolution steps $\Delta_1$ and $\Delta_2$ are small enough and if $\psi$ is a continuous function of $H$, then we can assume that $\psi$ provides a constant value for each point belonging to a given cell of the grid. Therefore, if $Q \in G$, then $\Psi_G(Q)$ is

the probability that a generic particle of the bunch to be generated belongs to the cell containing $Q$. To select a specific point of the cell, a value from the uniform distribution defined on the cell itself has to be extracted.

10. Following the previous point, particles are generated independently from each other using three random number generators, one associated with the probability function $\Psi_G$ to select the cell in $G$ and the other two related to two independent uniform distributions in order to determine the coordinates $\Delta t$ and $\Delta E$ inside the selected cell.

If the induced potential is different from zero, then $U_{\text{ind}}$ is added to $U_{\text{rf}}$ in R. However $U_{\text{ind}}$ depends on the profile of the bunch to be yet generated. This implies a circular reasoning. Notice that, if a stationary distribution including collective effects exists, then the profile used to compute $U_{\text{ind}}$ must correspond to the profile of the generated bunch for every application of R. One possible way to numerically resolve this circular reasoning is to apply the following iterative algorithm

1. A bunch matched only with the RF potential is generated following R.
2. The corresponding profile is used to compute $U_{\text{ind}}$ and another bunch is generated through R.
3. The previous step is repeated an arbitrary number of times.

At each step of this iterative algorithm we compute the error between two consecutive beam profiles. The error can be defined for example as the root mean square of the difference between the two profiles. When the error is relatively small, the algorithm is terminated and the solution to our problem is found. Sometimes the error does not converge to zero: this is generally due to the fact that the intensity effects are relatively high or that the error between the profile of the bunch generated at point 1. and the solution profile is too large. In this last case more convenient initial conditions have to be used starting from the solutions obtained applying the algorithm for lower beam intensities.

### 2.10.3 Examples of Stationary Distribution and Line Densities

One class of distributions commonly used for proton beams in theoretical studies and simulations is the so-called binomial amplitude [27]

$$\psi_{H_\tau,\mu}(H) = \begin{cases} \psi_0(H_\tau,\mu)\left(1-\frac{H}{H_\tau}\right)^\mu, & 0 \le \frac{H}{H_\tau} \le 1 \\ 0, & \frac{H}{H_\tau} \ge 1 \end{cases} \tag{2.63}$$

where $\psi_0$ is a normalization factor such that Eq.(2.52) is satisfied, $H_\tau$ is the value of the Hamiltonian along the trajectory enclosing all the particles and $\mu \ge 0$ is a free parameter.

For small amplitudes, in a stationary single RF bucket without collective effects and after a rescaling of the phase space coordinates, we have $H \propto \hat{r}^2$, where $\hat{r}$ is the amplitude of the synchrotron motion [24]. Substituting in Eq.(2.63) and integrating with respect to $\Delta E$ to obtain the corresponding line densities, we can easily explain

the names given to some binomial distribution and line densities: $\mu = 0$ provides a "water bag" density, while $\mu = 0.5$ and $\mu = 1$ give respectively a parabolic line and parabolic amplitude densities (see also Fig.2.5).

Another common distribution density, usually used for electron beams, is the so-called Gaussian [24] (the name is again explained substituting $H$ with $\hat{r}^2$)

$$\psi_{H_\tau}(H) = \psi_0(H_\tau) e^{-2\frac{H}{H_\tau}}, \quad H \geq 0 \tag{2.64}$$

which, contrary to the binomial one, never vanishes with $H$. Notice that $H_\tau$ corresponds to the value of the Hamiltonian enclosing around 95% ($4\sigma$) of the particles.

As discussed before, in order to avoid generating particles outside the bucket, the condition $\psi_{H_\tau}(H) = 0$ for $H > H_{\text{sep}}$ has to be established; this restriction, which always concerns the Gaussian distribution, never modifies the binomial distributions whenever $H_\tau < H_{\text{sep}}$. Notice also that, when generating a bunch with the method described previously, the normalization factors in Eqs.(2.63) and (2.64) can be neglected, since the probability function defined in Eq.(2.62) is invariant with respect to those factors. We can therefore equivalently consider the not-normalized distributions $\widetilde{\psi} = \psi/\psi_0$ for our studies.

Figure 2.5 shows some mentioned not-normalized distributions, together with the corresponding normalized bunch profiles obtained from the generated bunches through the method explained in Section 2.8. Fixed a certain emittance $\epsilon_{l,\tau}$ and therefore $H_\tau$, all the binomial profiles become zero at $\Delta t_1$ and $\Delta t_2$, which are identified through the intersections of the axis $\Delta E = 0$ with the particle-trajectory having $H_\tau$ as Hamiltonian. However the different values taken by $\mu$ change significantly the density of the particles contained in $H_\tau$, implying for example more noticeable tails of the bunch profile when $\mu$ increases. As expected, the bunch profile of the Gaussian distribution extends along the full bucket length.

## 2.11 Ring Periodicity

In this Section, to give a concrete example, we consider the discrete equations of motion (2.25) and (2.26) with only one RF system, $h = 1$, $\eta_0 < 0$, without collective effects, RF phase modulations or corrections. We will give at the end some considerations useful for generalization.

The simplified equations are

$$\Delta E_i^{(n+1)} = \Delta E_i^{(n)} + qV_{\text{rf}}^{(n)} \sin\left(\omega_{\text{rev},0}^{(n)} \Delta t_i^{(n)} - \pi\right) - \left(E_0^{(n+1)} - E_0^{(n)}\right), \tag{2.65}$$

$$\Delta t_i^{(n+1)} = \Delta t_i^{(n)} - \frac{T_0^{(n+1)} |\eta_0^{(n+1)}|}{\left(\beta_0^2\right)^{(n+1)} E_0^{(n+1)}} \Delta E_i^{(n+1)}. \tag{2.66}$$

Notice that $\phi_{\text{rf}} = -\pi$. Indeed the stability condition for synchrotron motion Eq.(2.35) implies $\phi_s = \omega_{\text{rev},0}\Delta t_{\text{s}} + \phi_{\text{rf}} \approx 0$, while Eq.(2.16) requires $\Delta t_s \approx T_0/2$. With the same reasoning it follows that $\phi_{\text{rf}} = 0$ above transition.

Without loss of generality, we can refer to Fig.2.6 to explain how to correct Eqs.(2.65) and (2.66) when the geometry of the ring has to be taken into account.

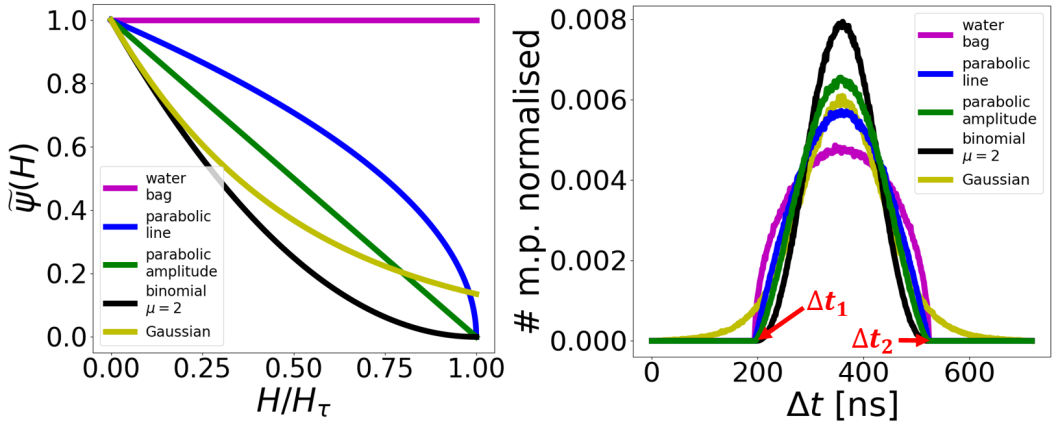


**Figure 2.5.** (Left) Different not-normalized stationary distributions $\widetilde{\psi} = \psi/\psi_0$: water bag (magenta), parabolic line (blue), parabolic amplitude (green), binomial with $\mu = 2$ (black) and Gaussian (yellow). (Right) Normalized bunch profiles obtained using the distributions shown on the Left Figure after the generation of the corresponding bunches in longitudinal phase space. The points $\Delta t_1$ and $\Delta t_2$ where the binomial distributions vanish are identified through $H_\tau$ (see the text). The machine and RF parameters chosen in this example are the same used for the single RF case shown in Fig.2.4 ($\epsilon_{l,\tau} = 0.99$ eVs).

We assume that two particles $P$ and $Q$ outside of the RF bucket are about to drift away from the phase space $(\Delta t, \Delta E)$ at first turn, before the first kick in energy is given through the sine wave in blue. We analyze the behaviors of the two particles independently:

- particle $P$. Since $\Delta E_P > 0$, this particle drifts to the left in phase space. At the beginning $\Delta t_P^{(1)} > 0$ and, after the first kick and drift through Eqs.(2.65) and (2.66), a $\Delta t_P^{(2)} < 0$ is obtained. This means that $P$ has to be kicked in energy and drifted one more time with the sine wave in blue before being "synchronized" with the other particles at second turn. In order to do that the reference time has to be changed, from $t_{ref}^{(1)}$ to $t_{ref}^{(0)}$, obtaining

$$\overline{\Delta t_P^{(1)}} = \Delta t_P^{(2)} + T_0^{(1)}. \tag{2.67}$$

  Then the equations of motion with the sine wave in blue are applied again only on this particle having $\overline{\Delta t_P^{(1)}}$ obtaining as a result a new $\Delta t_P^{(2)}$, this time in $[0, T_0^{(2)}]$, as desired. Then the particle will again drift to the left turn after turn and the procedure is repeated whenever $\Delta t_P < 0$.

- particle $Q$. Since $\Delta E_Q < 0$, this particle drifts to the right in phase space. At the beginning $\Delta t_Q^{(1)} < T_0^{(1)}$ and, after the first kick and drift with the sine wave in blue, a $\Delta t_Q^{(2)} > T_0^{(2)}$ is obtained. This means that the particle will not be kicked by the sine wave in green skipping the second turn and waiting for the other particles to be kicked and drifted in order to be synchronized with them at third turn. Therefore this time only a change of reference time from $t_{ref}^{(1)}$ to $t_{ref}^{(2)}$ is needed

$$\Delta t_Q^{(3)} = \Delta t_Q^{(2)} - T_0^{(2)}. \tag{2.68}$$

Then the particle will again drift to the right turn after turn and the procedure is repeated whenever $\Delta t_Q^{(n)} > T_0^{(n)}$.

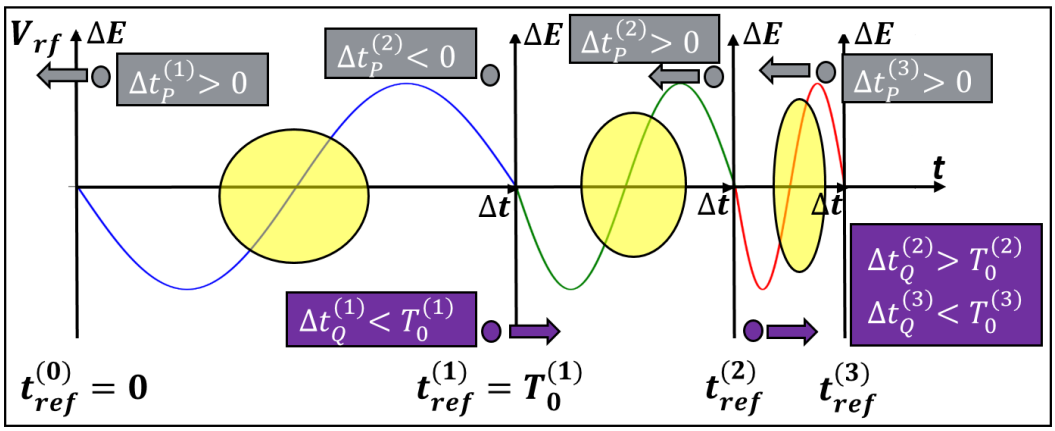


**Figure 2.6.** Scheme showing how the ring periodicity algorithm works for an accelerating bucket below transition energy with one RF system and $h = 1$. Three revolution turns are considered, with $T_0^{(1)} > T_0^{(2)} > T_0^{(3)}$. The different buckets are represented with yellow-colored ellipses (the bunches are not identified). The uncaptured particle $P$ (in gray) with $\Delta E_P^{(1)} > 0$ drifts to the left at first turn and $\Delta t_P^{(2)} < 0$ at second turn. A second kick from the sine wave in blue makes $\Delta t_P^{(2)} > 0$ and the particle is synchronized with the bunch at second turn. The uncaptured particle $Q$ (in purple) with $\Delta E_Q^{(1)} < 0$ moves to the right at first turn and $\Delta t_Q^{(2)} > T_0^{(2)}$ at second turn. This particle skips the second turn with the sine wave in green and the synchronization with the bunch occurs at third turn.

Figure 2.7 shows an example of an accelerating bucket below transition energy with single RF system and $h = 1$. Notice that if the ring periodicity algorithm is not applied, Eqs.(2.65) and (2.66) make all the particles crossing the line $\Delta t = T_0^{(n)}$ in phase space drift away to the right to plus infinity. This is in contradiction with the ring geometry the equations indirectly refer to, and could give undesirable results for example when the beam losses have to be computed accurately or when an un-bunched beam has to be captured inside an RF bucket.

The algorithm just described can be extended without any complications to the case above transition energy or in presence of multiple RF systems, since the procedure depends only on the conventions used to define the longitudinal coordinate $\Delta t$. Notice that there could be cases where parts of the bucket go beyond the line $\Delta t = T_0^{(n)}$ in phase space, for example when the phase loop changes the design RF frequency making the bucket shift relative to $[0, T_0^{(n)}]$, or when a second RF system with relatively high voltage is added in BLM during acceleration. In these cases the bunch will be split in phase space into two portions, which however behave as a whole.

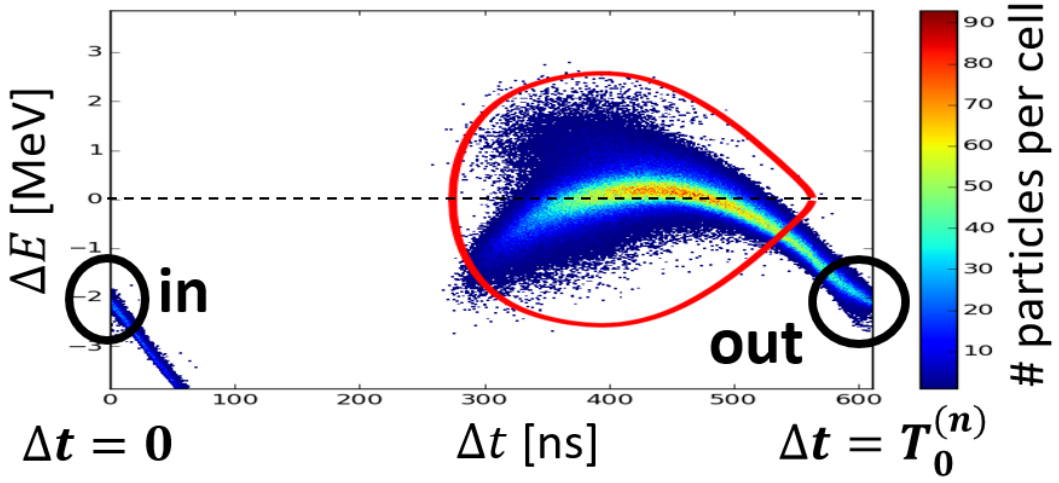


**Figure 2.7.** Example of accelerating bucket below transition energy with single RF system and $h = 1$. The particles flowing out from the right edge $\Delta t = T_0^{(n)}$ enter back from the left edge $\Delta t = 0$ thanks to the ring periodicity algorithm.

## 2.12 Differential Equations for Synchronous Parameters

The mean radius $R_0$ of a synchrotron is generally known. If only one of the other three parameters $B_0$, $p_0$, $f_{\mathrm{rev},0}$ is also known, then the remaining two can be derived using Eq.(2.13) and the relation $f_{\mathrm{rev},0} = \beta_0 c/(2\pi R_0)$. In this Section we will prove that the same holds if small deviations from the synchronous particle parameters are considered, namely only two parameters out of four are independent. The differential relations which we derive are very useful for several RF beam manipulations, as we will see later in this Section.

For the first relation, we start from $f_{\mathrm{rev},0} = \beta_0 c/(2\pi R_0)$. Therefore

$$\frac{\Delta f_{\mathrm{rev}}}{f_{\mathrm{rev},0}} = \frac{\Delta\beta}{\beta_0} - \frac{\Delta R}{R_0}. \tag{2.69}$$

Since $p = m_0\gamma v$ ($m_0$ is the rest mass of the particle) and $\Delta\gamma/\Delta v = v_0\gamma_0^3/c^2$ we obtain

$$\frac{\Delta p}{\Delta v} = \gamma_0 m_0 + \frac{m_0 v_0^2 \gamma_0^3}{c^2} = \gamma_0^3 m_0 \tag{2.70}$$

or, rearranging the terms,

$$\frac{\Delta\beta}{\beta_0} = \frac{1}{\gamma_0^2}\frac{\Delta p}{p_0}. \tag{2.71}$$

Combining Eqs.(2.69) and (2.71) we obtain the first desired relation

$$\frac{\Delta f_{\mathrm{rev}}}{f_{\mathrm{rev},0}} = \frac{1}{\gamma_0^2}\frac{\Delta p}{p_0} - \frac{\Delta R}{R_0}. \tag{2.72}$$

For the second relation, we start from the definition of the momentum compaction factor $\alpha_{\mathrm{c}}$ [17]

$$\alpha_{\mathrm{c}} = \frac{p_0}{R_0}\frac{\partial R}{\partial p} = \alpha_0 + 2\alpha_1\delta + 3\alpha_2\delta^2 + \dots. \tag{2.73}$$

Truncating the series at the constant term $\alpha_0$ we obtain

$$\left.\frac{\partial R}{\partial p}\right|_{p=p_0} = \frac{R_0}{p_0}\alpha_0, \tag{2.74}$$

and integrating

$$R = \frac{R_0}{p_0^{\alpha_0}} p^{\alpha_0}. \tag{2.75}$$

Rearranging the terms it follows that

$$p = p_0 \left(\frac{R}{R_0}\right)^{\frac{1}{\alpha_0}}. \tag{2.76}$$

Using the magnetic rigidity formula for the synchronous particle Eq.(2.13) we obtain

$$p = qB_0\rho_0 \left(\frac{R}{R_0}\right)^{\frac{1}{\alpha_0}}, \tag{2.77}$$

and, taking the logarithms and differentiating, the second desired relation is

$$\frac{\Delta p}{p_0} = \frac{\Delta B}{B_0} + \gamma_{\mathrm{tr}}^2 \frac{\Delta R}{R_0}. \tag{2.78}$$

From Eqs.(2.72) and (2.78) we can obtain the other two equations in the following group

$$\frac{\Delta p}{p_0} = \gamma_0^2 \frac{\Delta f_{\mathrm{rev}}}{f_{\mathrm{rev},0}} + \gamma_0^2 \frac{\Delta R}{R_0}, \tag{2.79}$$

$$\frac{\Delta p}{p_0} = \gamma_{\mathrm{tr}}^2 \frac{\Delta R}{R_0} + \frac{\Delta B}{B_0}, \tag{2.80}$$

$$\frac{\Delta B}{B_0} = \gamma_{\mathrm{tr}}^2 \frac{\Delta f_{\mathrm{rev}}}{f_{\mathrm{rev},0}} + \frac{\gamma_0^2 - \gamma_{\mathrm{tr}}^2}{\gamma_0^2} \frac{\Delta p}{p_0}, \tag{2.81}$$

$$\frac{\Delta B}{B_0} = \gamma_0^2 \frac{\Delta f_{\mathrm{rev}}}{f_{\mathrm{rev},0}} + (\gamma_0^2 - \gamma_{\mathrm{tr}}^2) \frac{\Delta R}{R_0}. \tag{2.82}$$

Since the condition of harmonicity between the RF and revolution frequencies must always hold, we can substitute $f_{\mathrm{rf}} = h f_{\mathrm{rev}}$ in the equations above. Notice also that these four relations are useful not only to study the changes of the synchronous particle parameters from turn to turn, but also to quantify the parameters of a generic particle close to the synchronous one at a given machine turn.

It is instructive to see what happens when one of the quantities $\Delta R$, $\Delta f_{\mathrm{rev}}$, $\Delta B$, $\Delta p$ is set to zero in the above four equations.

### 2.12.1 Case 1: $\Delta R = 0$

The previous equations reduce to

$$\frac{\Delta p}{p_0} = \frac{\Delta B}{B_0}, \quad \frac{\Delta p}{p_0} = \gamma_0^2 \frac{\Delta f_{\mathrm{rev}}}{f_{\mathrm{rev},0}}, \quad \frac{\Delta B}{B_0} = \gamma_0^2 \frac{\Delta f_{\mathrm{rf}}}{f_{\mathrm{rf},0}}. \tag{2.83}$$

We have $\Delta R = 0$ for example in the classical case when the beam is accelerated keeping it on the same design orbit. The first relation in Eq.(2.83) can be also derived differentiating directly Eq.(2.13), assuming no radial displacement for the synchronous particle from turn to turn. The second relation indicates that, when the beam is maintained on the same orbit while the energy increases, the beam revolution frequency also raises. The third relation shows how the operational magnetic field and RF frequency programs have to be related to each other to keep the beam on the nominal trajectory during acceleration.

### 2.12.2 Case 2: $\Delta f_{\mathbf{rev}} = 0$

In this case the equations reduce to

$$\frac{\Delta p}{p_0} = \gamma_0^2 \frac{\Delta R}{R_0}, \quad \frac{\Delta B}{B_0} = \frac{\gamma_0^2 - \gamma_{\mathrm{tr}}^2}{\gamma_0^2} \frac{\Delta p}{p_0}, \quad \frac{\Delta B}{B_0} = (\gamma_0^2 - \gamma_{\mathrm{tr}}^2) \frac{\Delta R}{R_0}. \tag{2.84}$$

One realistic example to explain these relations can be given considering the fixed-frequency injection currently operationally used at the CERN PSB. In this machine the injection is done with $\Delta f_{\mathrm{rf}} = 0$ for few milliseconds, while $\Delta B > 0$. Since the injection happens below transition energy, Eq.(2.84) implies $\Delta p < 0$ and $\Delta R < 0$, meaning that the beam will experience a deceleration while moving inwards the beam pipe.

### 2.12.3 Case 3: $\Delta p = 0$

In this case the equations reduce to

$$\frac{\Delta f_{\mathrm{rev}}}{f_{\mathrm{rev},0}} = -\frac{\Delta R}{R_0}, \quad \frac{\Delta B}{B_0} = -\gamma_{\mathrm{tr}}^2 \frac{\Delta R}{R_0}, \quad \frac{\Delta B}{B_0} = \gamma_{\mathrm{tr}}^2 \frac{\Delta f_{\mathrm{rev}}}{f_{\mathrm{rev},0}}. \tag{2.85}$$

The first relation can be used to understand why a beam debunches when all the RF systems are turned off at an energy plateau with constant design magnetic field. When the RF voltages are set to zero, the condition $\Delta p = 0$ holds for all the particles inside the bunch. All the particles having a radial displacement $\Delta R < 0$ relative to the design trajectory will have $\Delta f_{\mathrm{rev}} > 0$ and therefore will move to the left, turn after turn, in the $(\Delta t, \Delta E)$ phase space, which reference system is linked to the design trajectory. The opposite will happen if $\Delta R > 0$ and the beam will therefore debunch. Note that this mechanism can also be inferred directly from the equations of motion Eqs.(2.25) and (2.26) when $\Delta E_i^{(n+1)} = \Delta E_i^{(n)}$ for every particle $i$ and every revolution turn $n$, assuming the intensity effects negligible.

The second relation in Eq.(2.85) can be used for example at injection in a synchrotron to center a beam which has a radial displacement relative to the central trajectory. In this case $\Delta p = 0$ (the constant energy at injection is the one coming from the injector) and a measurement of the displacement $\Delta R$ at first turn allows to find the desired $\Delta B$ needed for trajectory alignment.

### 2.12.4 Case 4: $\Delta B = 0$

The equations reduce to

$$\frac{\Delta p}{p_0} = \gamma_{\mathrm{tr}}^2 \frac{\Delta R}{R_0}, \quad \frac{\Delta f_{\mathrm{rev}}}{f_{\mathrm{rev},0}} = -\eta_0 \frac{\Delta p}{p_0}, \quad \frac{\Delta f_{\mathrm{rev}}}{f_{\mathrm{rev},0}} = \frac{\gamma_{\mathrm{tr}}^2 - \gamma_0^2}{\gamma_0^2} \frac{\Delta R}{R_0}. \tag{2.86}$$

Focusing at a given revolution turn and supposing that the magnetic field is constant everywhere, we can notice that the second relation in Eq.(2.86) can also be obtained from the formula (Eq.(2.22)) of the frequency slippage of an off-momentum particle relative to the synchronous one, after having truncated the series at the constant term.

The third relation in Eq.(2.86) will be important in Chapter 5 when beam-based feedback models will be included in longitudinal beam dynamics simulations for the CERN PSB. We will see that, since the input of the radial feedback is the radial displacement of the beam relative to the design trajectory, a convenient way to compute $\Delta R$ is using the third formula in Eq.(2.86), after having calculated the correction $\Delta\omega_{\mathrm{rf}}$ given by all the feedbacks.

Finally the three relations in Eq.(2.86) will be fundamental when the slip-stacking dynamics for the CERN SPS will be studied in Chapter 6. There we will see that, at constant design magnetic field and energy, a circulating beam can be radially displaced inwards or outwards and accelerated or decelerated simply varying the design RF frequency program. To give an example above transition energy, an increase of RF frequency will make the beam decelerate and move inwards the beam pipe.

Considering again Eq.(2.17), a variation in the design RF frequency leads to a change in the RF phase according to the relation

$$\phi_{\mathrm{rf}}^{(n)} = \phi_{\mathrm{offset}}^{(n)} + \sum_{i=1}^{n-1} \omega_{\mathrm{rf}}^{(i)} T_0^{(i)} = \phi_{\mathrm{offset}}^{(n)} + \sum_{i=1}^{n-1} 2\pi h \frac{\Delta\omega_{\mathrm{rf}}^{(i)}}{\omega_{\mathrm{rf},0}^{(i)}}. \tag{2.87}$$

Indeed, the first term $\phi_{\mathrm{offset}}$ in the previous equation refers to phase modulations and constant offsets, such as the shift of $-\pi$ needed below transition energy (see Eq.(2.65)), while the second term accounts for variations of the RF frequency relative to the design one $\omega_{\mathrm{rf},0} = h\omega_{\mathrm{rev},0}$. When $\Delta\omega_{\mathrm{rf}} \neq 0$, for example during slip-stacking at constant magnetic field or during fixed-frequency injection with increasing magnetic field, this second term has to be explicitly included in the equations of motion Eqs.(2.25) and (2.26). If not included, wrong results are obtained, for example the sinusoidal RF voltage as a function of time will not be continuous from turn to turn. Note finally the shift in indexes between $\phi_{\mathrm{rf}}$ and $\Delta\omega_{\mathrm{rf}}$: if $n$ is the first index for which $\Delta\omega_{\mathrm{rf}} \neq 0$, then the RF phase will be corrected for the first time at turn $n+1$.

# Chapter 3

# Calculation of Collective Effects in Longitudinal Beam Dynamics Codes

## 3.1 Introduction

When studying the dynamics of high intensity beams, in addition to the external guiding fields, it is necessary to take into account, in a self-consistent way, the effects of the self-induced electromagnetic fields, which in time domain are described using the concept of wakefields, and in frequency domain that of coupling impedances [28]. This Chapter covers several fundamental issues and solutions which emerge from simulation codes dealing with longitudinal beam instabilities generated by self-induced electromagnetic fields in circular machines [29].

To simplify the beam dynamics study, it is generally convenient to distinguish between short range wakefields, which decay within the length of one bunch, and long range wakefields, which can last for many revolution turns or influence multiple bunches in one turn. The latter are generated by resonant impedance modes with high quality factors and produce, under some conditions, coupled bunch instabilities. A linear perturbation theory is generally used to analytically study beam instabilities. However, in order to analyze the behavior of the beam under the influence of wakefields also in the non-linear regime, and for more complex impedance models, use of particle simulations is necessary. In the simulation codes, which take into account collective effects related to impedance-induced fields, the equations of motion of a single charge in a bunch are quite simple (see e.g. Eqs.(2.25) and (2.26)). However, the inclusion of the effect of wakefield, which is also called beam induced voltage, and which couples the motion of different particles, requires care due to the possible introduction of numerical noise and non-physical phenomena.

The basic idea behind the numerical calculation of the beam-induced voltage in longitudinal beam dynamics codes has not changed since at least the 1980s [30]. The first official release in 1984 of the FermiLab code ESME [31] has been an important reference for many years to calculate the beam induced voltage and its effect on the beam dynamics. Over a period of more than thirty years, several longitudinal beam dynamics codes using short range wakefields [32, 33, 34], and both short and long

range wakefields [35, 36] in circular accelerators have been developed and have been proven to be reliable tools in the comprehension of the longitudinal collective effects. Other relatively recent longitudinal beam dynamics codes have been developed at Fermilab (United States) [37], J-PARC (Japan) [38] and CSNS (China) [39]. All these codes use the same numerical techniques or close variants for induced voltage calculations. Examples of particle codes which take into account also the transverse beam dynamics, while containing dedicated routines for induced voltage computations, can be found in Refs.[40, 41, 42, 43]. Certainly the code evolution cannot be compared with the exponential increase in computational power during the past forty years [44]. Nevertheless these days it is possible to simulate many bunches over a long period of time including beam controls.

The way how the electromagnetic fields acting on a charge and produced by all the others can be included in simulations is discussed in the following Section. The evaluation of the effects of short and long range wakefields generally requires different approaches which are reviewed in Sections 3.3 and 3.4 respectively. The study of this subject will continue in Section 3.7, where significant benchmarks between two very different tracking codes will be shown. Other methods of simulation of impedance-induced instabilities, different from tracking codes, are presented in Section 3.5. The conventions used in the following Sections refer to Chapter 1, where the equations of motion used in code BLonD are derived.

## 3.2 Common Approach in Wakefield Simulations

In order to write the longitudinal equations of motion of a single particle in a circular accelerator, it is generally assumed, for simplicity, that the energy exchange between a charge and the surrounding accelerator environment is localized in a single place of the machine. This assumption can be valid for example when the bunch length is comparable to the ring circumference (like in CERN PSB where $h = 1$) or when all the RF cavities are placed close to each other in the ring and the impedance-induced electromagnetic fields along the machine are quite uniform. However, in some cases, the assumption can be too rough. For example, the FCC accelerator [45] has a design circumference of about 100 km with $h = 130680$, and the RF cavities are designed to be positioned in different places along the ring. In such cases it is possible to divide the circumference in several sectors and consider multiple energy exchanges between the beam and the environment for each revolution turn. Strong space charge effects can also require the splitting of the ring circumference, since the local effect of this force varies over one turn because of different environment conditions along the ring, such as beam-pipe cross-section shapes and dimensions.

The common approach used in longitudinal simulation codes is to model each bunch as an ensemble of particles, every particle governed by Eqs.(2.25), (2.26) and to track these particles turn after turn. Since in a real bunch the number of charges $N_\mathrm{P}$ is usually in the range ($10^8$-$10^{12}$) and, sometimes, even more, it would be necessary to have a very high computing power, with the help of parallel clusters, to track all the particles. For this reason macro-particles, which gather together a given number of charges, are generally used. The maximum possible amount of simulated macro-particles depends on the available computing power. We will see in

Section 3.6 and 4.4 that the number of macro-particles $N_{\mathrm{M}}$ needed to accurately simulate a system taking into account collective effects is not easily defined. Varying $N_{\mathrm{M}}$ in a given simulation is often necessary to show small dependence of the results on the simulation parameters.

Without the presence of wakefield, Eqs.(2.25) and (2.26) can be easily numerically solved turn by turn, since the particles are independent from each other. The term which couples the equations of different particles, making the tracking more complicated, is the induced wakefield voltage $V_{\mathrm{ind}}(\Delta t)$. This is the voltage acting on a charge in a position $\Delta t$, and induced by all the other charges. This voltage depends on the normalized longitudinal bunch distribution $\lambda(\Delta t)$ according to the relation [46]

$$V_{\mathrm{ind}}(\Delta t) = Q_{\mathrm{tot}} \int_{T_0} d\Delta t' w_{\parallel}(\Delta t - \Delta t')\lambda(\Delta t'), \tag{3.1}$$

where $Q_{\mathrm{tot}}$ is the total charge of the beam, and $w_{\parallel}$ is the wake function of a point charge or Green function. In Eq.(3.1) we assume that the induced voltage decays in one revolution period $T_0$. In order to include also the multi-turn wakes, we have to add a sum over previous turns in the above convolution integral, as we will discuss in Section 3.3. The convolution integral in Eq.(3.1) is also called wake potential. It represents the energy gained or lost by a unity charge due to the entire beam. If a charge is traveling with a speed close to the speed of light, due to the causality property, the upper bound of the integral can be replaced by $\Delta t$ because $w_{\parallel}(\cdot) = 0$ for negative arguments.

In writing Eq.(3.1) we have described the behavior of the particle ensemble, representing a bunch, with a continuous distribution function, as this is often done in theoretical methods, even if the real structure of a bunch is discrete. In a simulation code we have the opposite approach, based on a number of macro-particles reduced with respect to the real number of charges in a bunch. In this case Eq.(3.1), or the expanded version with the long-range wakefields, can be transformed into

$$V_{\mathrm{ind}}(\Delta t) = \frac{Q_{\mathrm{tot}}}{N_{\mathrm{M}}} \sum_{j=1}^{N_{\mathrm{M}}} w_{\parallel}(\Delta t_i - \Delta t_j) \tag{3.2}$$

with $\Delta t_i$ being the longitudinal position of the $i^{\mathrm{th}}$ macro-particle and $N_{\mathrm{M}}$ the total number of macro-particles. If the bunch is traveling close to the speed of light, in the above summation we have to use $w_{\parallel}(0)/2$ instead of $w_{\parallel}(0)$ at $\Delta t_i = \Delta t_j$, due to the fundamental theorem of beam loading [47].

Equation (3.2) has to be evaluated at each turn and for each macro-particle. This means that, at each turn, the calculation of wakefields in simulations requires order of $N_M^2$ operations. For example, in order to track $(10^6 - 10^7)$ macro-particles, at each turn more than about $10^{12}$ operations are needed, and this task can be accomplished, at least for the moment, only on parallel computing clusters. In order to reduce the computing time in the evaluation of the wakefield effects, the bunch is usually divided into $N_{\mathrm{S}}$ slices, or bins, of width $\Delta$ and center at $\Delta t_{i\Delta}$, each $i^{\mathrm{th}}$ slice containing $n_i(\Delta)$ macro-particles. Supposing that slices act as point charges, the induced voltage at the center of each slice can be then evaluated by using the

relation

$$V_{\mathrm{ind}}(\Delta t_{i\Delta}) = \frac{Q_{\mathrm{tot}}}{N_{\mathrm{M}}} \sum_{j=1}^{N_S} n_j(\Delta) w_{\parallel}(\Delta t_{i\Delta} - \Delta t_{j\Delta}). \tag{3.3}$$

Exploiting the fact that the Fourier transform of a convolution sum is equal to the product of the Fourier transforms of the operands, the induced voltage in Eq.(3.3) can be also computed as

$$V_{\mathrm{ind}}(\Delta t_{i\Delta}) = \frac{Q_{\mathrm{tot}}}{N_M \Delta} \mathrm{IDFT}(Z_{\parallel} S), \tag{3.4}$$

where $Z_{\parallel} = \mathrm{DFT}(w_{\parallel})$ is the longitudinal impedance and $S = \mathrm{DFT}(n)$ is the bunch spectrum, with $n \equiv \{n_j\}_{j=1}^{N_S}$ the sliced bunch profile. In Eq.(3.4) DFT and IDFT stand for the discrete Fourier transform and its inverse. The slice size is linked to the maximum sampled frequency for $Z$ through the relation $f_{\max} = 1/(2\Delta)$. These two methods operating in time and frequency domain should in principle give the same results, but in several cases different number of slices and macro-particles have to be chosen to obtain the same accuracy (see Section 3.5).

Once the induced voltage is known at the positions $\Delta t_{i\Delta}$, a linear interpolation (or higher order one) permits to evaluate the wake potential acting on any macro-particle of the bunch. Since in general the number of slices needed to resolve accurately a bunch profile is between few hundreds and some thousands, this greatly reduces the number of operations.

The approach of using slices to compute the induced voltage has been widely used in simulations (e.g in BLonD and ESME), and over the years it has been demonstrated to give reliable results. However, particular care has to be taken when choosing the size and the number of the slices (and, of course, of macro-particles). As we will see later, a low number of slices reduces the computing time, but it could suppress some physical micro-structures in the bunch leading to instabilities. On the other side, slices can introduce numerical noise, additional to that of macro-particles, making necessary, in some cases, a parametric study of any possible dependence of the results on the number of slices and macro-particles. One intuitive approach (and also preliminary check) to determine the slice size is to consider the product of the bunch spectrum and the impedance, which appears in Eq.(3.4). This allows to identify a certain $f_{\max}$ above which the absolute value of this product can be considered negligible. The chosen frequency defines the slice size and finally the number of macro-particles has to be increased by steps until a convergence of results is reached.

## 3.3 Simulations with Short Range Wakefields

Simulations with short range wakefields can be performed according to the previous equations once the short range wake function $w_{\parallel}$ of a beam-coupling impedance is known.

The coupling impedance model of a machine is generally obtained as a sum of contributions from different elements. Each device is simulated using the help of dedicated electromagnetic computer codes, such as CST Particle Studio [48],

GdfidL [49], or ACE3P [50]. From the impedance, with the inverse discrete Fourier transform, the wakefield can be obtained.

One important problem that sometimes arises in simulations is the necessity to use a very big number of slices to properly reconstruct the correct induced voltage. In such a case the code becomes too cumbersome and other solutions have to be found. As an example, let us take the wakefield of a broad-band resonator, which sometimes is also used as a simplified impedance model of an accelerator. Here an intuitive approach will be used while in Subsection 3.5.1 this subject will be studied more in detail. The longitudinal wakefield for a resonator is given by [46]

$$w_{\parallel}(t) = \frac{2\pi f_{\mathrm{r}} R_{\mathrm{sh}}}{Q_{\mathrm{r}}} e^{-\Gamma t} \left[ \cos(\bar{\omega} t) - \frac{\Gamma}{\bar{\omega}} \sin(\bar{\omega} t) \right], \tag{3.5}$$

where $\Gamma = \pi f_{\mathrm{r}}/Q_{\mathrm{r}}$ and $\bar{\omega} = \sqrt{4\pi^2 f_{\mathrm{r}}^2 - \Gamma^2}$. The three resonator parameters $R_{\mathrm{sh}}$, $Q_{\mathrm{r}}$ and $f_{\mathrm{r}}$ are respectively the shunt impedance, the quality factor and the resonant frequency. The corresponding longitudinal impedance is

$$Z_{\parallel}(f) = \frac{R_{\mathrm{sh}}}{1 + i Q_{\mathrm{r}} \left( \frac{f_{\mathrm{r}}}{f} - \frac{f}{f_{\mathrm{r}}} \right)}. \tag{3.6}$$

Figure 3.1 shows the induced voltage for a broad-band resonator with unit quality factor, produced by a Gaussian bunch with rms bunch length $\sigma_t$ 2.4 times larger than the resonant wavelength (relativistic case). If we consider a longitudinal interval of $\pm 5\sigma_t$ for the bunch profile, in order to have about 20 slices per wavelength, about 480 slices for the Gaussian bunch are needed. Indeed, from Fig.3.1, we can see that, with 500 slices, Eq.(3.3) for the Gaussian bunch gives a slightly different result with respect to the theoretical wake potential, and only with 1000 slices the induced voltage is very close to the theoretical one. With such a large number of slices a very big number of macro-particles has to be used, because there is the need to have a reasonable number of particles in each slice for proper beam simulations. If the number is not sufficiently high the strong fluctuations of macro-particles from one slice to another could produce non-physical effects.

There is however the possibility to bypass this problem by using, in Eq.(3.3), instead of the Green function, the wake potential (induced voltage) of a very short Gaussian bunch [51]. Indeed, in the same figure, with the cyan dashed line, we have also represented the induced voltage as given directly by a simulation with only 100 slices, for which we have used in Eq.(3.3) in place of $w_{\parallel}$, the wake potential of a Gaussian bunch 10 times shorter than the simulated one. As can be seen from the figure, with 100 slices we obtain a result similar to that obtained with 1000 slices and the Green function. Also using the method in frequency domain, it is possible to obtain the correct induced voltage with only about 150 slices (see Subsection 3.5.1 for a similar example).

## 3.4 Simulations with Long Range Wakefields

For simulations involving long range wakefields, in addition to the slice size problem, the main issue is the necessity to know the wakefield as a function of time until it

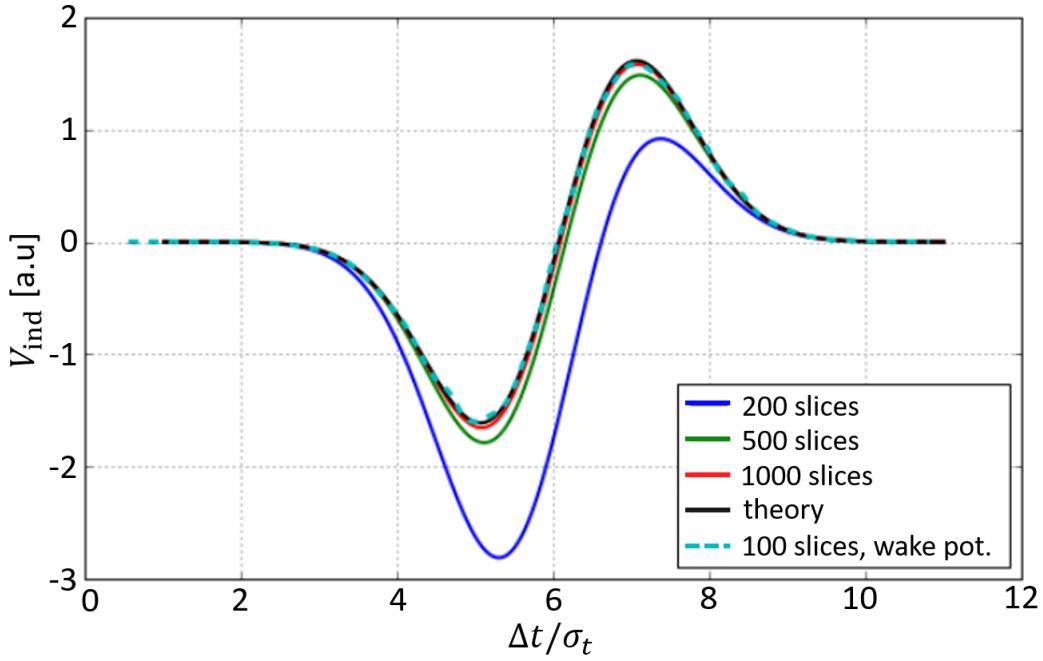


**Figure 3.1.** Beam induced voltage for a broad-band resonator produced by a Gaussian bunch with rms length a factor 2.4 larger than the resonant wavelength. The voltage has been obtained by using 200 slices (blue), 500 slices (green) and 1000 slices (red). The cyan dashed line represents the induced voltage obtained with only 100 slices by using, as Green function, the wake potential of a Gaussian bunch 10 times shorter. The black line, representing the theoretical induced voltage, is below the cyan line.

becomes negligible. The long range wakefields are usually generated by resonant modes with a high quality factor, so depending on its value and on the resonant frequency, the wake can influence many bunches for many turns. This requires the calculation of a very long interaction of the wakefield with the beam. Different simulation codes have different approaches to tackle this problem.

For example, in the BLonD code [52], the approach is to store into memory, at each turn, the sum of the present induced voltage extended to the future and the induced voltage derived from the past after appropriate time shift of one revolution period. A complication arises in presence of acceleration: the time frame, which length is the revolution period, shrinks turn after turn and, as a consequence, an interpolation is needed each turn when the present voltage is summed with the voltage from the past.

Another method, used in the tracking parallel code SPACE [43], expands the long range wakefields in Taylor series and stores the moments of the longitudinal distribution of all the bunches in previous turns. This method requires a slowly varying wakefield and, in addition, the number of terms for the Taylor expansion has to be wisely chosen together with the order of the derivative method to calculate the derivatives of the wake. However, the strength of the algorithm derives from the fact that the induced voltage acting on a certain bunch can be calculated in parallel via master-to-slave processor communications. This means that at each turn, after having applied the single particle equations of motion, the various moments

of the present longitudinal bunch profiles are calculated independently by different processors. These independent computations are then communicated to the master processor which can sum them with the other calculated moments from previous turns which have been stored into memory.

In some cases it is reasonable to suppose that the wake function does not change significantly in a certain longitudinal frame. This idea was explored in [41]. Whenever the wake amplitude does not change more than 0.1% in a certain longitudinal frame, all the slices contained in that window are replaced by a single slice characterized by a wake that is an average of the wake values of all the concerned slices. The frame length can be even of the order of the bunch length or the revolution period. Using this approximation, the convolution sum to calculate the long range wakefields can be significantly simplified.

An alternative approach, which has been developed and used in the simulation code MuSiC [36], exploits a matrix formalism to transport the wakefield of resonators, both broad-band and narrow-band, from one macro-particle to the following one, removing the need to resort to the convolution sum, avoiding problems related to bunch slices, and eliminating the necessity to store long range wakefields. The code allows to simulate simultaneously the effects of short and long range wakefields for both the single and multi-bunch beam dynamics and including intra-bunch motion. It also contains an algorithm for a frequency domain feedback system to damp coupled-bunch instabilities. The drawback of the MuSiC approach is that it requires a fit of the machine coupling impedance with a sum of resonators (as in Eq.(3.6)), which are used as input in place of the wakefield.

## 3.5 Vlasov Solvers and Other Methods

In addition to simulation codes, which track macro-particles turn after turn, a different approach can be used, and it consists in solving numerically the time domain Vlasov equation with the inclusion of wakefields. Using the same conventions adopted in Chapter 2, the Vlasov nonlinear integro-differential equation can be written as [53]

$$\frac{\partial \psi}{\partial t} + \frac{\partial \psi}{\partial \Delta t}\frac{\partial H}{\partial \Delta E} - \frac{\partial \psi}{\partial \Delta E}\frac{\partial H}{\partial \Delta t} = 0, \tag{3.7}$$

where $\psi$ is the phase space longitudinal distribution and $H$ is the Hamiltonian in Eq.(2.37) accounting for both the RF field and the collective forces generated by the wakefields.

As first approach, it would seem that Eq.(3.7) could be treated by the usual methods for partial differential equations, as the finite differences, to approximate the phase space longitudinal distribution function $\psi$ on nodes of a finite grid. However, such a technique fails completely with or without implicit time stepping, and not because of any effect of the nonlinear terms, but because it does not preserve the symplectic form of the equation [54]. Different and more appropriate methods must therefore be applied, as for example an integration of the equation using a discretization of the local Perron Frobenius operator [54]. In Ref.[55] instead, an algebraic technique of solution, that is suited for general evolution-type equations and that can also be applied to the Vlasov equation, extended to the non-linear

case, has been developed, and it is based on the evolution operator technique, widely exploited in the solution of quantum mechanical problems. Codes solving the Vlasov equation have been developed to study single bunch effects [56, 57] as alternative to multi-particle tracking codes, and they generally guarantee a very smooth evolution of the beam distribution function in time that allows to reduce, and in some cases to completely eliminate, the effect of numerical noise. Usually, the computing time for a code solving the Vlasov equation is comparable to that of the multi-particle tracking codes because the problem due to the slices previously discussed is avoided but, in any case, in order to calculate the collective force in the Hamiltonian term, the convolution integral of Eq.(3.1) has to be performed over a finite phase space grid.

## 3.6 Damping Mechanisms to Counteract Collective Effects

Damping mechanisms are essential in circular accelerators for beam stabilization, since wakefields, as well as other sources of noise present in a given machine, can perturb the beam motion. These mechanisms can be either active or passive.

An example of active damping is given by the RF phase loop related to the main accelerating RF cavity and implemented in the Low Level RF system of some accelerators (see Chapter 5 for an example concerning the PSB ring). The phase loop measures the bunch position relative to the RF bucket center and then corrects the RF frequency at consecutive revolution turns in order to align the RF bucket with the bunch. The main effect of the RF phase loop on the beam dynamics is the damping of the bunch-core (dipole) oscillations.

An example of passive or intrinsic damping mechanism is given by the so-called Landau damping [58]. In the longitudinal plane and for bunched beams, Landau damping can reduce, under certain conditions, the bunch dipole oscillations thanks to the spread in the synchrotron frequencies of the individual particles forming the bunch. However, when the bunch intensity is sufficiently high, the frequency spread is significantly reduced by the wakefields and loss of Landau damping (LLD) occurs.

An important threshold formula for LLD can be derived for an accelerator with constant $\mathrm{Im}Z/n$ ($n = f/f_{\mathrm{rev},0}$) and with a small real-part impedance treated as a perturbation. The formula is given by [59]

$$N_{\mathrm{b}} < \frac{F|\eta_0|E_0}{q^2\beta_0^2}\frac{\tau}{\mathrm{Im}Z/n}\left(\frac{\Delta E}{E_0}\right)^2\frac{\Delta\omega_{s,\mathrm{ind}}}{\omega_{\mathrm{s0,ind}}}, \tag{3.8}$$

where $F$ is a form factor depending on the bunch distribution, $\tau$ is the bunch length, $\Delta\omega_{s,\mathrm{ind}}/\omega_{\mathrm{s0,ind}}$ and $\Delta E/E_0$ are respectively the relative synchrotron frequency and energy spreads. Equation (3.8) will be used in Chapter 6 to evaluate LLD for ion beams in the SPS after CERN upgrade.

## 3.7 Benchmarks Between BLonD and MuSiC

As discussed in the previous Sections, different numerical approaches are available to compute the induced voltage. Here we will briefly review two of them and then two

significant benchmarks will be presented. From Eq.(3.2), fitting a general wake by resonators, a propagation matrix can be constructed to compute the induced voltage from particle to particle and this approach is used by the MuSiC code. On the other hand, since $N_{\mathrm{M}}$ can be large and the number of resonators obtained from the fit of the realistic impedance can be numerous, a slicing of the bunch profile is used in BLonD to compute the induced voltage either in time domain with a convolution between the wake and the line density (Eq.(3.3)), or in frequency domain performing an inverse Fourier-transform on the product of bunch spectrum and impedance (Eq.(3.4)). The length of one slice defines the maximum frequency $f_{\max}$ taken into account (Nyquist theorem) and the resolution in frequency domain $\Delta f$ is related to the length $t_{\max}$ of the induced voltage to be included in simulations ($t_{\max} = 1/\Delta f$). Finally, a linear interpolation is used to define the voltage for particles in-between slices.

The dedicated studies [60] have shown the consistency of the MuSiC and BLonD approaches for two different scenarios characterized respectively by a broad-band (short-range wakefield) and a narrow-band (long-range wakefield) resonators. These two cases are described below, where the chosen ring and RF parameters do not refer to any real ring in particular.

### 3.7.1 Short Range Wakefields

The induced voltage due to a broad-band resonator impedance with a resonant frequency $f_{\mathrm{r}}$ much higher than the bunch cut-off frequency $1/\tau_{\mathrm{l}}$ (with $\tau_{\mathrm{l}}$ the bunch length) can be difficult to simulate: physical contributions are lost if $f_{\max}$ is set too low and noise can be included if $f_{\max}$ is too high.

In the considered example, the resonant frequency $f_{\mathrm{r}}$=100 MHz, the quality factor $Q = 1$ and the shunt impedance $R_{\mathrm{sh}} = 10^7\Omega$. A proton bunch having a Gaussian line density with rms bunch length $\sigma_t = 3/f_{\mathrm{r}}$ is used:

$$\lambda(t) = \frac{1}{\sqrt{2\pi}\sigma_t} e^{-\frac{t^2}{2\sigma_t^2}}, \tag{3.9}$$

The RF system has harmonic number h=1, RF frequency $f_{\mathrm{rf}} = 1.9$ MHz and peak voltage $V_1 = 1$ MV, the design energy $E_0 = 13$ GeV, the circumference is $C_{\mathrm{ring}} = 157$ m and the slip factor is $\eta = 0.0549$. The bunch intensity, $N_{\mathrm{P}} = 10^{12}$, is chosen so that the initial induced voltage $V_{\mathrm{ind}}$ has a peak value of 0.8 MV (high intensity effect). The unmatched to the RF bucket initial distribution in phase space is used to see different beam dynamics (filamentation, losses and later equilibrium in phase space) during the same simulation.

Figure 3.2 shows the initial normalized bunch spectrum, the resonator impedance and their product using $N_{\mathrm{S}} = 5000$ slices of the bucket length (frequency axis is in log scale). It can be seen that 50 slices (first dashed vertical line) are enough to consider the main frequency components of the induced voltage (red curve), but the impedance peak at high frequency (blue curve) is not included. Increasing $N_S$ up to 1000, the resonator impedance is resolved. Figure 3.2 shows also that, for a given $N_S$, the number of macro-particles should be sufficient to avoid noise at high frequency.

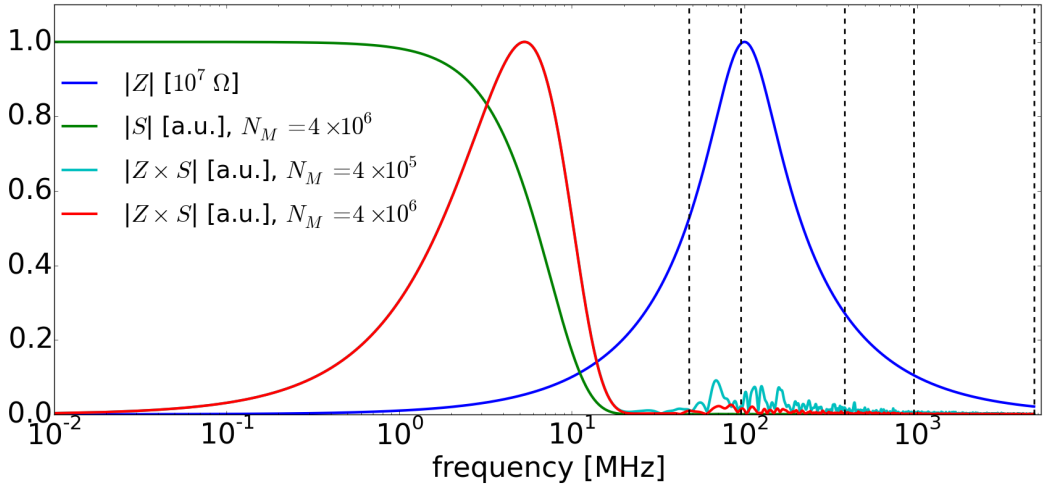


**Figure 3.2.** Normalized absolute value of the bunch-spectrum $S(f)$ (green) calculated from a Gaussian line density with $\sigma_t = 30$ ns, unnormalized impedance $|Z(f)|$ (blue) computed through Eq.(3.6) and their normalized product (red) for $N_\mathrm{S} = 5000$ and $N_\mathrm{M} = 4 \cdot 10^6$. The vertical dashed lines, from left to right, mark $f_\mathrm{max}$ corresponding to 50, 100, 400, 1000, 5000 slices. For $N_\mathrm{M} = 4 \cdot 10^5$ high frequency noise is observed (cyan). The main contribution of $|Z \cdot S|$ is covered using 50 slices.

The induced voltage generated by the bunch using $N_\mathrm{M} = 4 \cdot 10^6$ macro-particles using the MuSiC and BLonD approaches is shown in Fig.3.3. The MuSiC voltage, compared to the analytical formula, is characterized by high amplitude and high frequency components, since $N_\mathrm{M}$ is not high enough (increasing $N_\mathrm{M}$ the voltage converges to the analytical one). Using $N_\mathrm{S} = 1000$ in frequency domain calculations in BLonD, the voltage is close to the MuSiC one. This is reasonable since, once $N_\mathrm{M}$ is chosen, the system is defined, and high values of $N_S$ allow higher frequencies to be sampled. On the other hand a voltage with a significant vertical offset with respect to the MuSiC solution is obtained using $N_\mathrm{S} = 1000$ in time domain approach in BLonD. Finally, choosing $N_\mathrm{S} = 50$ gives an output close in amplitude to the analytical one, but without high frequency components. Since the frequency domain algorithm converges faster than the time domain one in this case, the first is used. The difference between the two BLonD algorithms is explained by the broad-band nature of the resonator. The wakefield contains many high frequency modulations and needs more accuracy whereas the broad-band impedance needs not a high resolution to be resolved.

Figure 3.4 shows the average bunch position as a function of the number of turns using the MuSiC and BLonD codes. The frequency domain approach is used in BLonD choosing different number of slices. Figure 3.4 shows the bunch dipole-oscillations only after that longitudinal emittance blow-up and losses due to collective effects have occurred. One can see that, increasing $N_\mathrm{S}$ in BLonD, the dipole oscillations converge to the MuSiC ones. Notice that using just 50 or 100 slices the beam dynamics change completely (green and red colors): the bunch is always stable and there are no instabilities or particle losses, due to the low resolution in frequency domain which does not allow the resonant impedance-peak to be properly

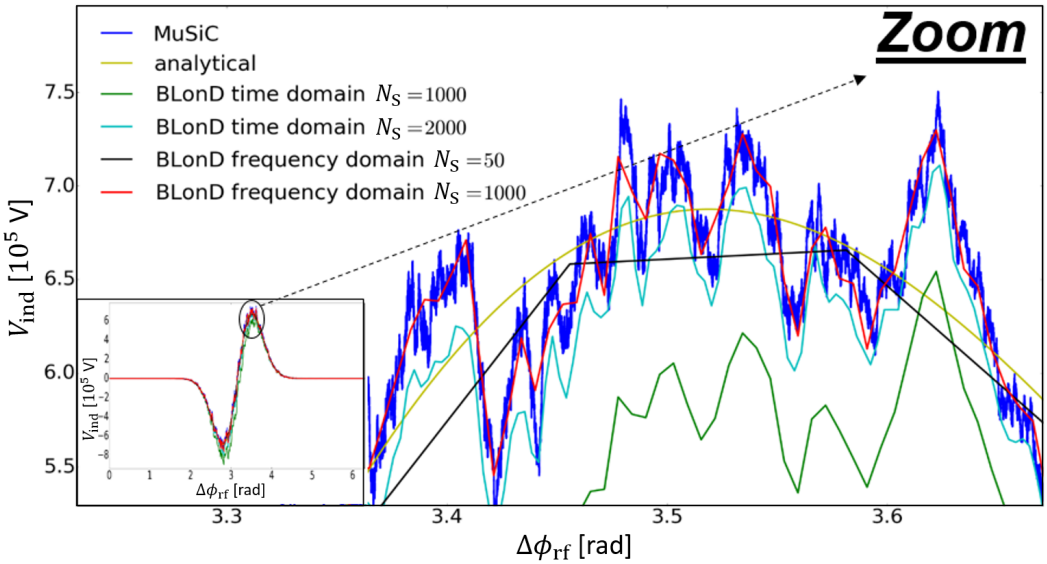


**Figure 3.3.** Zoom in induced voltage (left bottom corner) generated by the initial Gaussian bunch for $N_M = 4 \cdot 10^6$. Here $\Delta\phi_{rf} = \omega_{rev,0}\Delta t$. Different methods of induced-voltage calculation are shown.

resolved. The collective effects leading to instability and losses start to be visible choosing $N_S = 400$ (cyan line). Convergence between MuSiC and BLonD results is reached for $N_S = 1000$ (magenta line) and it is even better with $N_S = 5000$ (yellow color), when also the particle losses are in agreement. Figure 3.5 compares the bunch distributions in phase space obtained at turn number 23000 using the MuSiC code (right) and the BLonD code ($N_S = 50$ or $N_S = 5000$, respectively left and middle). One can see that choosing $N_S = 50$ does not lead to any instability or emittance blow-up, therefore wrong results are obtained. On the contrary, if the MuSiC code is used or if $N_S$ is properly increased in BLonD, the correct beam dynamics is recovered: the corresponding bunches blow up covering the full bucket area. Notice that, in this last case, remarkable agreement is obtained between the two codes.

Finally in BLonD, assuming $N_S = 1000$, $N_M$ was increased from 4 to 50 million in order to verify convergence of simulation results. No significant differences in beam losses and bunch dipole/quadrupole oscillations were observed. This convergence analysis shows that the strong instability observed both with the MuSiC and BLonD codes is real and not induced by numerical noise.

Concerning the computational cost, the broad-band resonator and the wake decaying in one turn allow the largest possible $\Delta f$ in BLonD to be chosen ($\Delta f = f_0/N_S$, where $f_0$ is the revolution frequency) or equivalently to consider only the revolution harmonics in the induced voltage computation. The result is that the BLonD algorithm is much faster than the MuSiC one (factor 27 for $N_M = 4 \cdot 10^6$ and $N_S = 5000$).

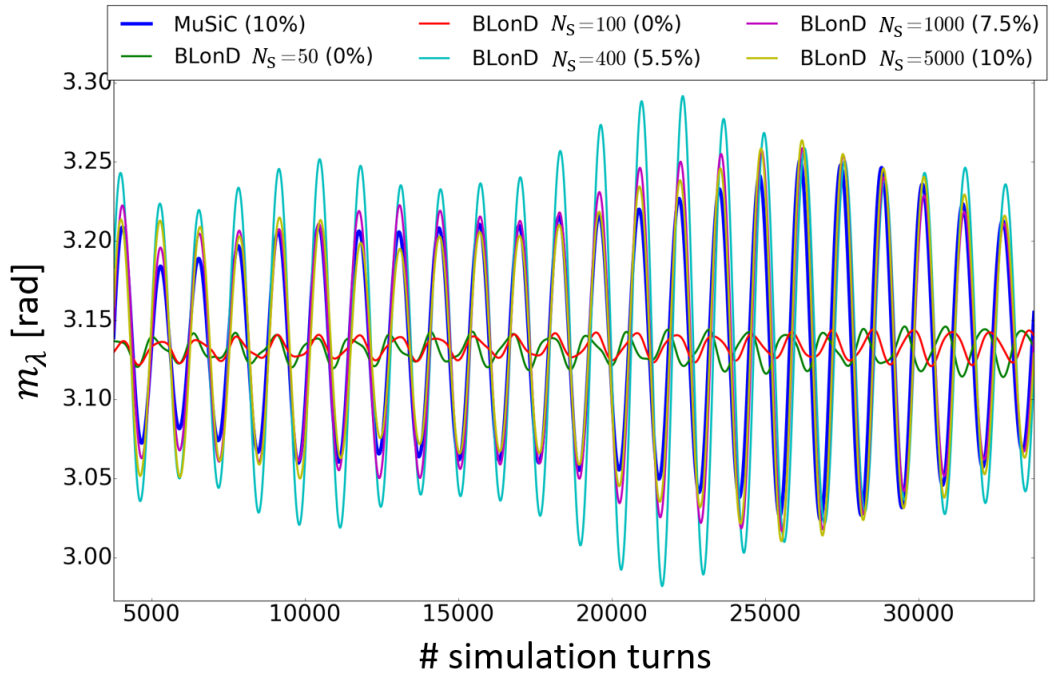


**Figure 3.4.** Bunch dipole-oscillations after turn number 4000 obtained using the MuSiC and BLonD codes. The number of macroparticles is $N_M = 4 \cdot 10^6$ for both codes. The BLonD simulations are performed in frequency domain using different values for the number of slices $N_S$. The percentage of particle losses is in parentheses.

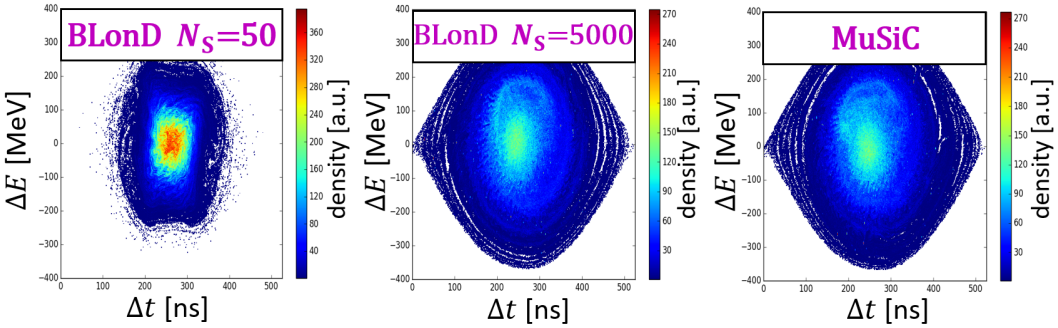


**Figure 3.5.** Bunch distributions in phase space at turn number 23000 (see also Fig.3.4) using the BLonD code with $N_S = 50$ (left), $N_S = 5000$ (middle) or the MuSiC code (right).

### 3.7.2 Long Range Wakefields and Robinson Instability

For a resonant impedance with quality factor $Q \gg 1$ and relatively low frequency $f_r$, the wakefield can couple multiple bunches or even the same bunch on multiple turns. If the resonant frequency $f_r$ is close to an integer multiple $p$ of the revolution frequency, then Robinson instability can be observed [61]. The growth rate of the instability can be obtained from the imaginary part of the synchrotron frequency shift computed with the linearized Vlasov's equation. Supposing a Gaussian line

density as in Eq.(3.9), the analytical expression for growth rate is [36]

$$\frac{1}{\tau_\mathrm{a}} = \frac{-\eta e^2 N_\mathrm{P}}{2E_0 T_0^2 \omega_\mathrm{s}} \sum_{m=\pm 1} m\,(p\omega_{\mathrm{rev},0} + m\omega_\mathrm{s})\,\mathrm{Re}Z(p\omega_{\mathrm{rev},0} + m\omega_\mathrm{s})\,G_m(x), \tag{3.10}$$

where $\omega_s$ is the angular synchrotron frequency, $e$ the proton charge and $G_m(x) = 2e^{-x^2} I_m(x^2)/x^2$ is the form factor with $x = (pf_0 + mf_\mathrm{s})\sigma_t$ and $I_m$ the modified Bessel function of the first kind.

In the case studied below $p = 2$, the resonator parameters are $f_\mathrm{r} = 2f_0 + f_\mathrm{s}$, $Q = 5000$ and $R_\mathrm{sh} = 40\,\mathrm{k}\Omega$. In addition, $N_\mathrm{P} = 4 \cdot 10^{12}$, $E_0 = 13$ GeV, $\eta = 0.0217$, $T_0 = 2.1$ µs, $f_\mathrm{s} = 264.1$ Hz. The RF system has $h = 7$, $f_\mathrm{rf} = 3.3$ MHz and $V_1 = 165$ kV, while $C_\mathrm{ring} = 628$ m. Then the instability growth time found from Eq.(3.10) is $\tau_\mathrm{a} = 59.3$ ms for $\sigma_t \leq 3.3$ ns and the results from MuSiC and BLonD should converge to $\tau_\mathrm{a}$ for short bunches (no Landau damping).

The initial bunch spectrum with $\sigma_t = 3.3$ ns decays above 200 MHz whereas the resonant impedance is negligible above 1 MHz, as Fig.3.6 shows. It is then not straightforward to choose $f_\mathrm{max}$ in BLonD simulation. In addition $\Delta f$ is another key parameter, since the wake decays over thousands of revolution periods and it is not evident how many turns to take into account. The time domain approach is used in BLonD to simulate this case since the narrow-band resonator requires a very small $\Delta f$ in frequency domain making simulations computationally heavy: Fig.3.6 shows that the impedance peak is not perfectly resolved even choosing $\Delta f = 70$ Hz, which corresponds to $t_\mathrm{max} \approx 7000\,T_0$. The MuSiC approach avoids all these difficulties since no slices are used and $N_\mathrm{M}$ is the only parameter to be studied.

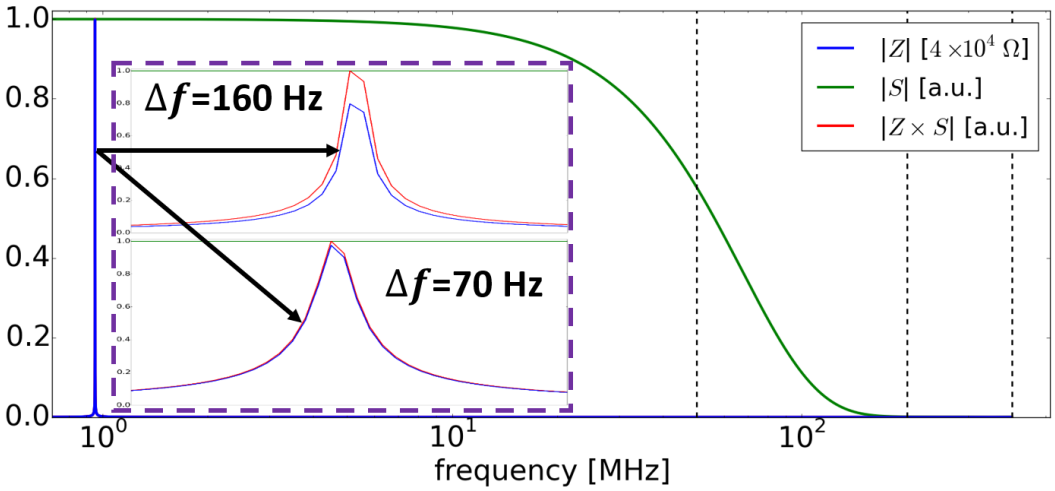


**Figure 3.6.** Normalized absolute value of the bunch-spectrum $S(f)$ (green) calculated from a Gaussian line density with $\sigma_t = 3.3$ ns, unnormalized impedance $|Z(f)|$ (blue) computed through Eq.(3.6) and their normalized product (red). The vertical dashed lines, from left to right, mark the values 50 MHz, 200 MHz and 400 MHz. The bunch-spectrum decays to zero before 200 MHz. Due to the narrowness of the resonator impedance, two zooms onto it are shown, where $\Delta f = 160$ Hz ($t_\mathrm{max} \approx 3000\,T_0$, top) and $\Delta f = 70$ Hz ($t_\mathrm{max} \approx 7000\,T_0$, bottom).

The instability growth time was examined in MuSiC as a function of $N_\mathrm{M}$ and compared with $\tau_a = 59.3$ ms from Eq.(3.10) (see Fig.3.7). When increasing $N_\mathrm{M}$,

convergence is observed (63.0 ms) but not to $\tau_a$. This can be explained by the non-linearities of the RF wave (Landau damping). Decreasing sufficiently the bunch length, non-linearities are suppressed and, as shown in Fig.3.7, the inverse growth rate converges to $\tau_a$. This proves the validity of the MuSiC algorithm and helps the number of macro-particles to be used for comparison with the BLonD approach to be chosen.

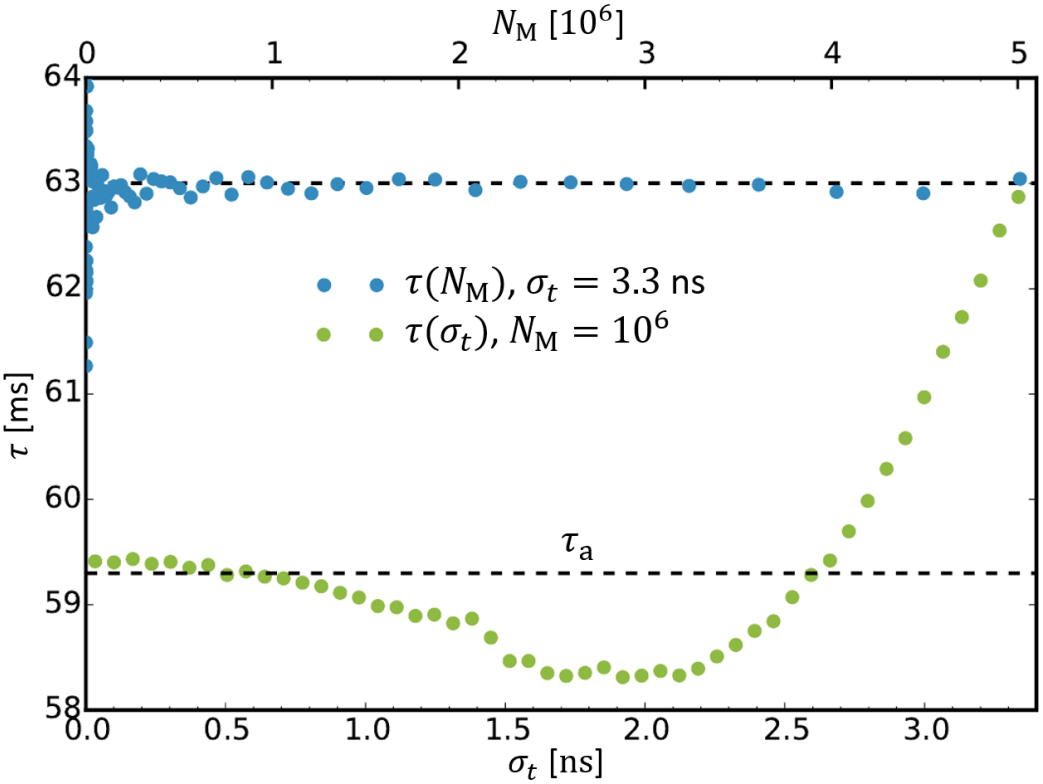


**Figure 3.7.** Instability growth time $\tau$ as a function of $N_M$ for $\sigma_t = 3.3$ ns (blue) and as a function of $\sigma_t$ for $N_M = 10^6$ (green) from MuSiC simulations. The dashed lines mark $\tau = \tau_a = 59.3$ ms and $\tau = 63$ ms, which are respectively the convergence values for the green dots for small $\sigma_t$ and for the blue dots for large $N_M$.

Using $\sigma_t = 3.3$ ns and $N_M = 10^6$ in BLonD, the dependence of the inverse growth rate on $\Delta f$ and $f_{max}$ was also studied and is shown in Fig.3.8. Fixing $f_{max} = 200$ MHz to cover the bunch spectrum in Fig.3.6, the inverse growth rate convergences to 63.0 ms for relatively small $\Delta f < 70$ Hz, as expected from the MuSiC simulations and also examining the zooms shown in Fig.3.6. A scan of $f_{max}$ for two given values of $\Delta f$ shows consistency of results and therefore agreement between BLonD and MuSiC simulations.

However the computational time $T$ in MuSiC ($T \approx N_M = 10^6$) is lower by factor 5, since the number of slices used in BLonD to resolve $f_{max} = 200$ MHz is multiplied by the number of memory turns in which the wake decays ($T \approx f_{max}/\Delta f = 200$ MHz/70 Hz $\approx 3 \cdot 10^6$). One way to speed up the calculations in BLonD would be to act only on not-empty buckets. In case of multi-bunch beams, MuSiC is expected to be less efficient than BLonD. The reason is that $T$ scales with

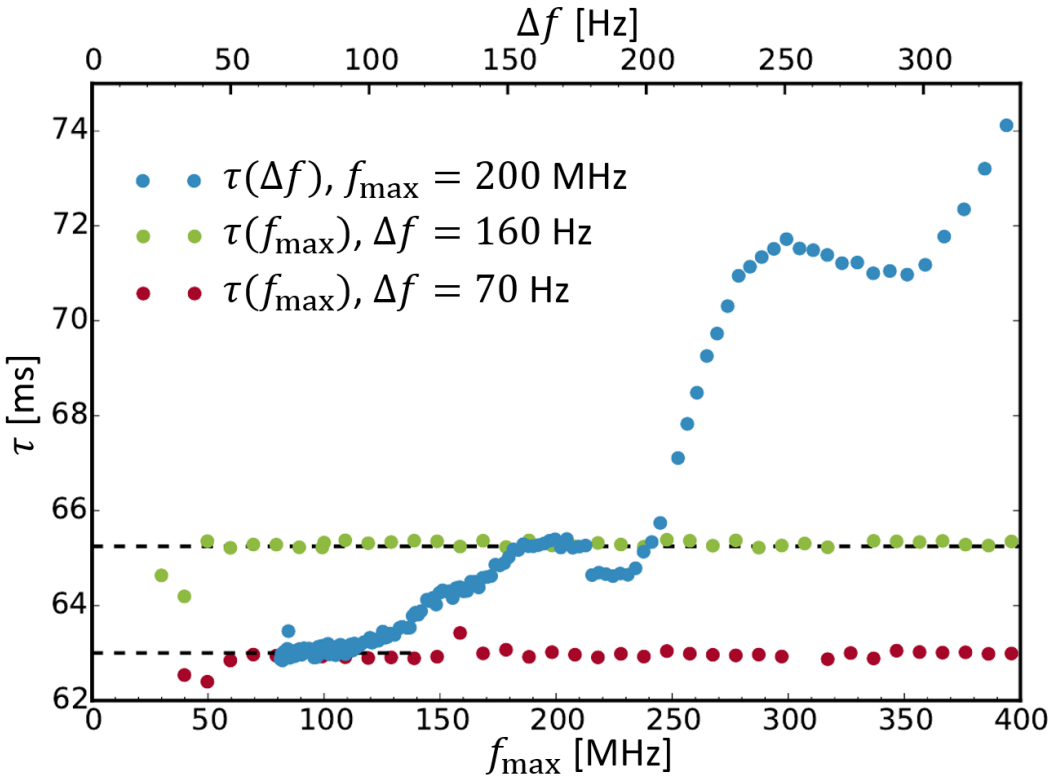


**Figure 3.8.** Instability growth time $\tau$ as a function of $\Delta f$ for $f_{\max} = 200$ MHz (blue) and versus $f_{\max}$ for $\Delta f = 160$ Hz (green) and $\Delta f = 70$ Hz (red) from BLonD simulations ($\sigma_t = 3.3$ ns, $N_{\mathrm{M}} = 10^6$). The dashed lines mark $\tau = 63$ ms and $\tau = 65.3$ ms, which are respectively the convergence values for the red and green dots for sufficiently high $f_{\max}$. All the results shown are obtained through simulations in time-domain with $t_{\max} = 1/\Delta f$ and $\Delta = 1/(2f_{\max})$.

$N_{\mathrm{M}}$ in the MuSiC code while in BLonD $T$ would scale mostly with the parameters $N_{\mathrm{S}}$ and $\Delta f$ which would not change from the case of single-bunch simulations if the entire ring is sliced.

## 3.8 Conclusions

The first part of this Chapter introduced the concepts of wakefield and impedance, before presenting the most common approaches used to calculate collective effects in longitudinal beam dynamics codes. Particular attention has been paid to differentiate time and frequency domain calculations, as well as computations of short and long-range wakefields. It also emerged that the choice of numerical parameters such as number of macro-particles and slices in simulations can be delicate.

Afterwards, two different approaches for longitudinal induced-voltage calculation have been compared, the ones used by the BLonD and MuSiC codes. Two benchmarks have been performed: in the first a relatively long bunch is perturbed by a short-range wakefield generated by a broad-band resonator, in the second a long-range wake field created by a narrow-band resonator couples the relatively short bunch-profile

on consecutive revolution turns.

Consistency of the MuSiC and BLonD approaches in induced voltage calculation was shown for the two different cases. In the benchmark with short-range wakefield, after having determined a proper number of macro-particles, the BLonD results obtained in frequency domain converged to the MuSiC result by increasing the number of slices, as expected. Particular care had to be taken in BLonD to avoid under-sampling the bunch profile as physical contributions could be lost and wrong results obtained. The absence of slices in MuSiC allowed all these parameter-space studies to be avoided, however the computational time was much higher than for BLonD, since the frequency resolution $\Delta f$ could be safely large in BLonD due to the broad-band nature of the resonator.

In the second benchmark, the analytical value of the Robinson instability growth-rate was used as a reference. First, results coming from the MuSiC code varying the bunch length showed that convergence of the instability growth-rate to the analytical value is obtained for relatively small bunch length, when Landau damping is negligible. The analysis also determined the minimum number of macro-particles able to give consistency to the MuSiC results. As for the BLonD code, computations were performed in time domain due to the narrowness of the resonator impedance and, after a careful choice of the number of slices and revolution turns to be taken into account for the multi-turn wake, good agreement with the MuSiC code and the analytical value for the growth-rate has been found. In this benchmark the BLonD code required more computational time than the one needed by the MuSiC code since, even neglecting the cumbersome frequency domain approach, too many points had to be taken in time domain to obtain reliable results.

# Chapter 4

# PSB: Collective Effects

## 4.1 Introduction

The PS Booster (PSB) at CERN is the first synchrotron in the proton injector chain of the Large Hadron Collider (LHC). It consists of four super-imposed rings (Fig.4.1), each of them able to accelerate one or two bunches of protons from 50 MeV to 1.4 GeV kinetic energy, see Table 4.1. In the following, unless otherwise specified, the expression "PSB" will refer generically to one of the four rings, which are practically identical.

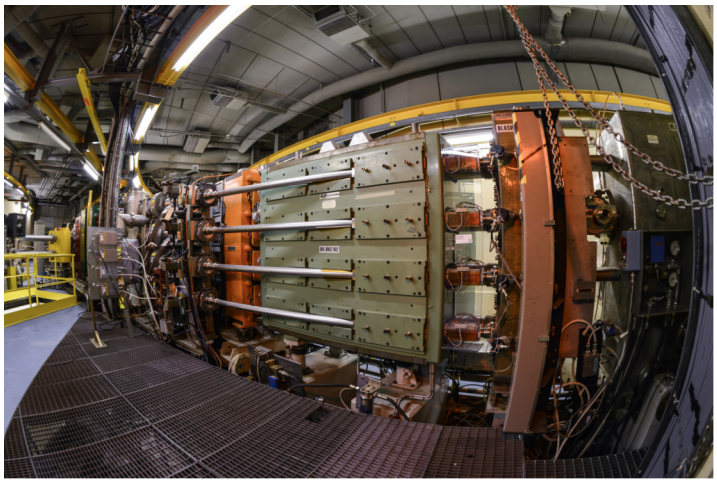

**Figure 4.1.** Photo of the CERN PSB. The beam pipes of the four super-imposed rings are clearly visible. *Courtesy of CERN.*

The injector of the PSB is the linear accelerator Linac2, while the next synchrotron in the chain is the Proton Synchrotron (PS). The cycle length of the PSB is 1.2 s, the acceleration starts at 275 ms (with a positive rate of change of the magnetic field) and ends at 800 ms, supposing the counting starts at zero. At 275 ms the beam is un-bunched, covering the full ring and the RF voltage is zero. It takes roughly 10 ms for the beam to be captured inside the longitudinal RF bucket determined by the accelerating RF voltage.

In the PSB jargon the cycle times are indicated with the letter "C", for example

275 ms is expressed as C275; we will use this notation also. The PSB is a relatively small accelerator with a radius of $R_0 = 25$ m and a bending radius of $\rho_0 = 8.2$ m. The transition gamma $\gamma_{\mathrm{tr}}$ is 4.08 and the zero order momentum compaction factor $\alpha_0 = 0.06$. The PSB operates below transition energy ($\gamma_0$ increases from 1.05 to 2.49 along the ramp) and therefore is not an ultra-relativistic machine ($\beta_0$ rises from 0.31 to 0.92).

**Table 4.1.** Some of the main CERN PS Booster machine and RF parameters for the current operation [2, 62]. The last four rows refer to current nominal LHC-type beam parameters.

| | |
|---|---|
| Particles accelerated | protons |
| Number of bunches | 1 or 2 bunches/ring (4 rings) |
| Injector, next synchrotron | Linac2, PS (Proton Synchrotron) |
| Cycle length, start-end accel. [ms] | 1200, 275-800 (C275-C800) |
| $R_0$, $C_{\mathrm{ring}}$, $\rho_0$ [m] | 25, 157.1, 8.2 |
| $\gamma_{\mathrm{tr}}$, $\alpha_0$ | 4.08, 0.06 |
| $E_{0,\mathrm{kin}}^{\mathrm{C275}}$ [MeV], $f_{0,\mathrm{rev}}^{\mathrm{C275}}$ [MHz], $\gamma_0^{\mathrm{C275}}$, $\beta_0^{\mathrm{C275}}$ | 50, 0.60, 1.05, 0.31 |
| $E_{0,\mathrm{kin}}^{\mathrm{C800}}$ [GeV], $f_{0,\mathrm{rev}}^{\mathrm{C800}}$ [MHz] , $\gamma_0^{\mathrm{C800}}$, $\beta_0^{\mathrm{C800}}$ | 1.4, 1.75, 2.49, 0.92 |
| RF systems | C02, C04, C16 (narrow-band, ferrite) |
| Revolution harmonics | C02 $h = 1$, C04 $h = 2$, C16 $h \in [5, 20]$ |
| Resonant frequencies [MHz] | C02 0.6-1.8, C04 1.2-3.9, C16 6-16 |
| Q factors of RF systems | C02 0.7-2.7, C04 1.7-7.6, C16 10-19 |
| Shunt impedance of RF [kΩ] | C02 0.25-0.4, C04 0.35-0.47, C16 2-1.5 |
| Maximum peak RF voltages [kV] | C02 ($\hat{V}_{\mathrm{rf},1}$): 8, C04: 8, C16: 6 |
| $f_{\mathrm{s0}}^{\mathrm{C275}}$-$f_{\mathrm{s0}}^{\mathrm{C800}}$ [kHz], $Q_{\mathrm{s0}}^{\mathrm{C275}}$-$Q_{\mathrm{s0}}^{\mathrm{C800}}$ ($\hat{V}_{\mathrm{rf},1}$) | 1.98-0.45, $3.28 \cdot 10^{-3}$ - $0.26 \cdot 10^{-3}$ |
| $\epsilon_{\mathrm{l}}^{\mathrm{C285}}$ [eVs], $\tau_{\mathrm{l}}^{\mathrm{C285}}$ [ns], $\delta_{\mathrm{rms}}^{\mathrm{C285}}$ | 1.0, 1100, $2.4 \cdot 10^{-3}$ |
| $\epsilon_{\mathrm{l}}^{\mathrm{C800}}$ [eVs], $\tau_{\mathrm{l}}^{\mathrm{C800}}$ [ns], $\delta_{\mathrm{rms}}^{\mathrm{C800}}$ | 1.3, 180, $0.9 \cdot 10^{-3}$ |
| $N_{\mathrm{b}}^{\mathrm{C285}}$ [ppb], $\epsilon_{\mathrm{x,y,n}}^{\mathrm{C285}}$ [µm], $\Delta Q_{x,y}^{\mathrm{C285,sc}}$ | $17.7 \cdot 10^{11}$, 2.14, (0.51, 0.59) |
| $N_{\mathrm{b}}^{\mathrm{PS\ inj}}$ [ppb], $\epsilon_{\mathrm{x,y,n}}^{\mathrm{PS\ inj}}$ [µm], $\Delta Q_{x,y}^{\mathrm{PS\ inj,sc}}$ | $16.5 \cdot 10^{11}$, 2.25, (0.25, 0.30) |

Each of the PSB rings has three tunable narrow-band ferrite RF systems called C02, C04 and C16, see Table 4.1. The main RF system C02 (Fig.4.2, top), used to accelerate the beam ($h = 1$), has a maximum peak RF voltage $\hat{V}_{\mathrm{rf},1}$ of 8 kV and its resonant frequency $f_{\mathrm{r}}$ is in the range 0.6 MHz − 1.8 MHz. Correspondingly to this frequency range, the quality factor $Q_r$ varies from 0.7 to 2.7 while the shunt impedance $R_{\mathrm{sh}}$ increases from 0.25 kΩ to 0.4 kΩ. The C04 system ($h = 2$) is used for bunch shaping, generally in the bunch lengthening mode, to reduce the longitudinal

peak line density in the PSB and therefore to minimize the transverse direct space charge tune spread (see the definition later); the C04 maximum peak RF voltage is $\hat{V}_{\mathrm{rf},2} = 8$ kV and the resonator parameters are shown in Table 4.1. Finally the C16 cavity has harmonic number $h$ in the interval [5,20] and a peak RF voltage of $\hat{V}_{\mathrm{rf},3} = 6$ kV (see Table 4.1 for the resonator parameters). This RF system is used to blow up the bunch longitudinal emittance in a controlled way using RF phase modulation, since large longitudinal emittances are needed at the PS flat bottom to reduce the longitudinal peak line density and transverse space charge effects.

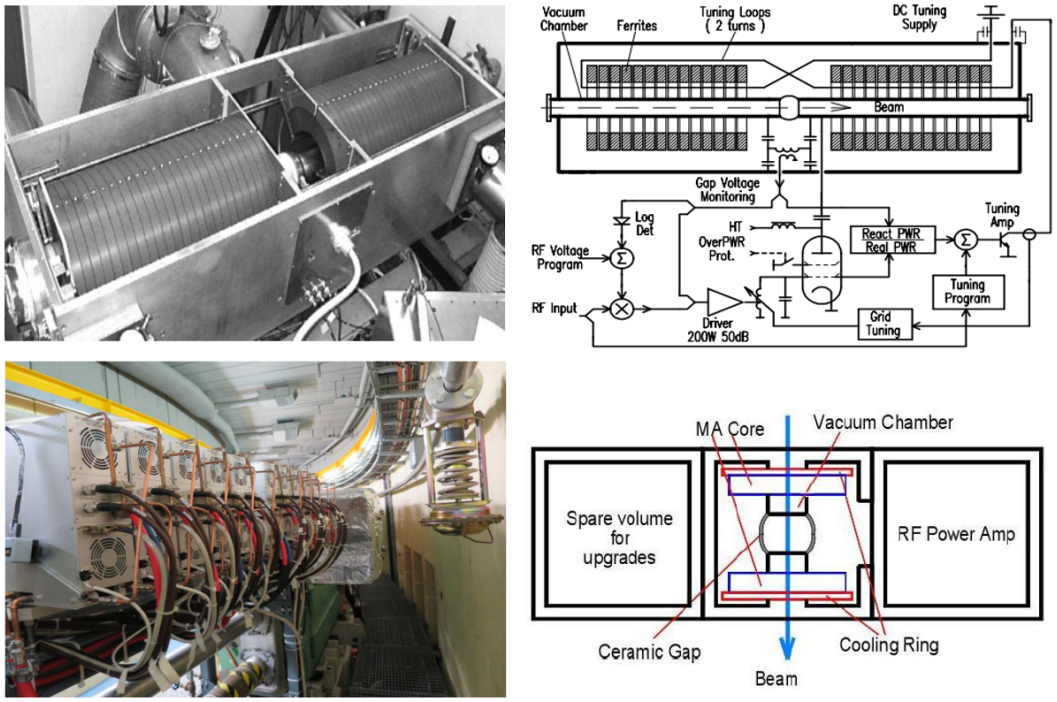


**Figure 4.2.** Top: photo of the current PSB C02 ferrite RF cavity (left) and corresponding system layout (right) [20]. Bottom: photo of the Finemet® prototype ten-cell RF system installed in PSB Ring 4 (left, *courtesy of M. Haase, CERN*) and layout of one basic accelerator cell (right, *courtesy of M. Paoluzzi, CERN* [63]).

Assuming acceleration in single RF system with $V_{\mathrm{rf},1} = 8$ kV (without considering collective effects) the zero amplitude synchrotron frequency $f_{\mathrm{s0}}$ decreases along the ramp from 1.98 kHz to 0.45 kHz, while the synchrotron tune $Q_{\mathrm{s0}}$ diminishes from $3.28 \cdot 10^{-3}$ to $0.26 \cdot 10^{-3}$.

The PSB accelerates many types of proton beams, each of them having different parameters and purposes (see next Chapter). One of them is the so-called high-brightness LHC25ns (or nominal) beam which at the end of the accelerator chain provides protons to the four LHC experiments for particle physics studies. The LHC25ns beam intensity at C285 (after RF capture) is $N_{\mathrm{b}} = 17.7 \cdot 10^{11}$ ppb and arrives at $N_{\mathrm{b}} = 16.5 \cdot 10^{11}$ ppb at PSB extraction energy (5% of losses, which is the maximum allowed value). The longitudinal emittance at C285 is 1 eVs; it becomes 1.3 eVs after controlled longitudinal emittance blow-up in the PSB. The bunch length $\tau_{\mathrm{l}}$ measured in time significantly decreases during acceleration, varying from

1100 ns to 180 ns along the ramp (while $\delta_{\mathrm{rms}} = \Delta p_{\mathrm{rms}}/p_0$ changes from $2.4 \cdot 10^{-3}$ to $0.9 \cdot 10^{-3}$).

The reference convention to measure the longitudinal bunch length in the PSB, and therefore the longitudinal emittance, according to what explained in Chapter 2, is called "Foot Tangent Method" [64]. This procedure, together with other relevant ones, will be described in the following Section. When not directly specified, the reference conventions will be used in the present Chapter and in Chapter 5.

Transverse direct space charge at PSB and PS injections is one of the main limitations for beam brightness [65], since the large generated tune spread crosses crucial resonance lines in the tune diagram. The following expression gives the maximum betatron tune shift due to transverse direct space charge effects (details are given in the Appendix A)

$$\Delta Q_X^{\mathrm{sc}} = -\frac{r_{\mathrm{p}}\hat{\lambda}}{2\pi\beta_0^2\gamma_0^3}\oint \frac{\beta_X(z)}{\sigma_X(z)[\sigma_x(s)+\sigma_y(z)]}dz \approx -\frac{r_{\mathrm{p}}\hat{\lambda}C_{\mathrm{ring}}}{4\pi\beta_0\gamma_0^2\epsilon_n} \propto \frac{B_{\mathrm{n}}C_{\mathrm{ring}}}{\beta_0\gamma_0^2\tau_s}, \qquad (4.1)$$

where $X = x$ or $X = y$, $r_{\mathrm{p}}$ is the classical particle radius, $\epsilon_{\mathrm{n}} = \epsilon_{x,\mathrm{n}} = \epsilon_{y,\mathrm{n}}$ the transverse normalized emittance, $B_{\mathrm{n}}$ the brightness and $\hat{\lambda}$ the maximum value of the longitudinal line density, which is expressed in number of charges per meter and has bunch length $\tau_s = \beta_0 c\tau_l$.

Currently the nominal beam experiences a blow-up of 5% in its normalized emittance, starting from a value of 2.14 µm at PSB injection and arriving at 2.25 µm at the end of the PS flat-bottom. The horizontal and vertical maximum tune shifts vary respectively from 0.51 to 0.25 and from 0.59 to 0.31, see Table 4.1.

It is important to mention that currently the limitation in beam brightness along the LHC injector chain does not come from the PSB (Fig.4.3, left). Indeed, the SPS beam loading and longitudinal instabilities limit the maximum bunch intensity achievable at SPS extraction, while the transverse space charge at PS flat-bottom determines the largest possible transverse emittance, since the resonance line $8Q_y = 50$ limits the maximum vertical tune shift to 0.31 [66, 67].

Notice that the curve representing the PSB brightness is a straight line, suggesting that, even if $\Delta Q_x^{\mathrm{sc}} \neq \Delta Q_y^{\mathrm{sc}}$ at PSB injection, the relation of proportionality between the tune shift and the brightness in Eq.(4.1) could be used setting $\epsilon_{\mathrm{n}} = (\epsilon_{x,\mathrm{n}} + \epsilon_{y,\mathrm{n}})/2$ [68]. The same does not applies for the PS case, where the beam energy spread and the ring horizontal dispersion are not negligible in the evaluation of the horizontal beam size at flat-bottom. Therefore the correct expression in Eq.(4.1) must be used to compute the maximum tune shifts and, as a result, the corresponding curve in the limitation diagram is not a straight line.

### 4.1.1 After-upgrade Scenario

As was outlined in the introductory Chapter, the intensity and brightness for nominal LHC beams is supposed to increase respectively by a factor of 2 and 2.4 to fulfill the requests of the HL-LHC Project.

These new beam parameters will be reached directly in the PSB. Indeed, to fully compensate the double intensity in Eq.(4.1), leaving the current tune spread unvaried, the kinetic energy at PSB injection after LS2 will be increased from 50 MeV to 160 MeV, since $(\beta_0\gamma_0^2)_{160\ \mathrm{MeV}}/(\beta_0\gamma_0^2)_{50\ \mathrm{MeV}} = 2$. Because of the increased injection

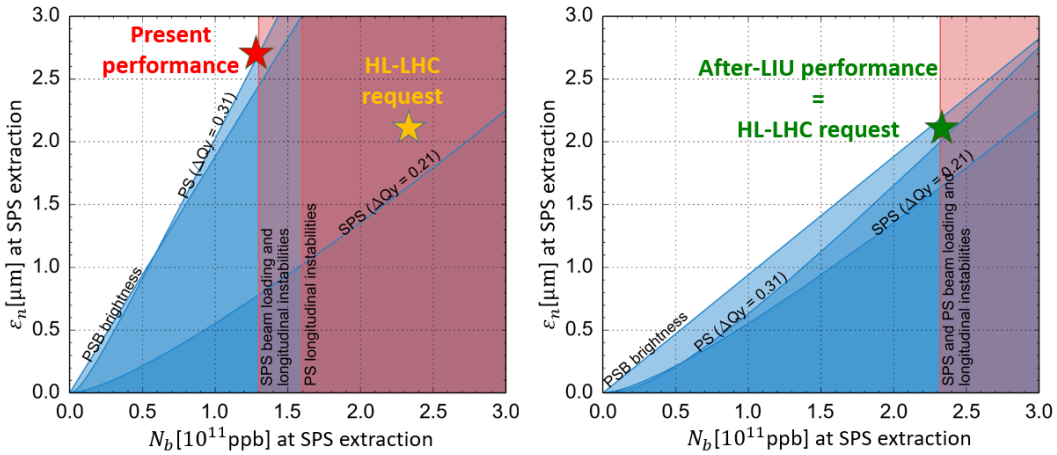


**Figure 4.3.** Left: proton limitation diagram for current situation showing which normalized transverse emittances $\epsilon_\mathrm{n}$ and bunch intensities $N_\mathrm{b}$ are allowed at SPS extraction (450 GeV/c). The red star indicates that the optimal brightness currently possible has been achieved. Transverse emittance limitations are due to the transverse direct space charge at PS flat-bottom (the maximum vertical tune shift cannot exceed 0.31), while intensity limitations are given by the SPS beam loading and longitudinal instabilities. The HL-LHC requests ($\epsilon_\mathrm{n} = 2.1$ µm, $N_\mathrm{b} = 2.3 \cdot 10^{11}$ ppb) are marked by the yellow star. Right: predicted proton limitation diagram for the after-LIU scenario, where the green star indicates that the expected values of bunch transverse emittance and intensity at SPS extraction coincide with the ones requested by the HL-LHC Project. *Courtesy of G. Rumolo, CERN, 2018* [66].

energy, a scaling calculation shows that the longitudinal emittance at the future PSB injection has to be 1.4 eVs instead of the current 1 eVs; in this way the bunch length $\tau_s$ in Eq.(4.1) will be preserved changing from 50 MeV to 160 MeV, leaving again the current tune spread unvaried. Finally, to have the additional increase in brightness after doubling the intensity, the normalized transverse emittance has to be decreased from 2.14 µm to 1.72 µm, causing an increase in tune spread relative to the current situation. Estimations using the correct expression in Eq.(4.1) predict that the new maximum tune shifts will be $\Delta Q_x^{\mathrm{sc}} = 0.58$ and $\Delta Q_y^{\mathrm{sc}} = 0.69$. These two values can be reached moving the PSB working point above the half-integer line $2Q_y = 9$ after having adequately compensated the corresponding resonance using a dedicated set of quadrupoles and sextupoles [69, 70].

To enable all these changes at PSB injection, Linac2 will be replaced by the new Linac4, which will provide $H^-$ hydrogen ions to the PSB at 160 MeV kinetic energy. The new injection scheme, according to the LIU baseline, will consist of a multi-turn injection of chopped trains of Linac4 micro-bunches at 352.2 MHz with given bunch length and energy spread [71]. This will allow injecting the micro-bunches directly inside the RF bucket, avoiding some of the current losses due to the RF capture of an un-bunched beam. The new, so-called $H^-$ charge-exchange injection system, based on a stripping foil will substitute the scheme currently used with Linac2, which relies on one septum magnet which deflects the injected beam. This change will allow first to tailor the required transverse emittance in the PSB using transverse phase

space painting realized with the new KSW kicker magnets [72]. In addition it will reduce almost to zero the large amount of losses (50% of the injected beam) currently experienced, which are due to multiple unwanted interactions of the circulating beam with the septum magnet during the multi-turn injection process of Linac2 micro-bunches at 202.56 MHz.

As Fig.4.3 shows, all these upgrades at PSB injection would be useless if the transverse direct space charge would not be reduced at PS flat-bottom. Indeed, to cope with the current limitation and the future doubling of the bunch intensity at PS injection, another important upgrade will concern the PSB extraction energy, which will be raised from 1.4 GeV to 2 GeV for LHC-type beams, see again Eq.(4.1). In order to achieve that, the main power supply will have to be changed and small kickers and septa will be modified. Since the cycle length will remain 1.2 s, the acceleration rate for nominal beams will increase after LS2. Several studies have been done to propose a realistic momentum program for the after-upgrade scenario [73]. Figure 4.4 compares the suggested future cycle with the one currently used. Notice that the future acceleration rate will be considerably higher, mostly in the second half of the cycle. Figure 4.4 shows also the proposed cycle for future high-intensity fixed-target beams, which are supposed to be extracted at 1.4 GeV kinetic energy.

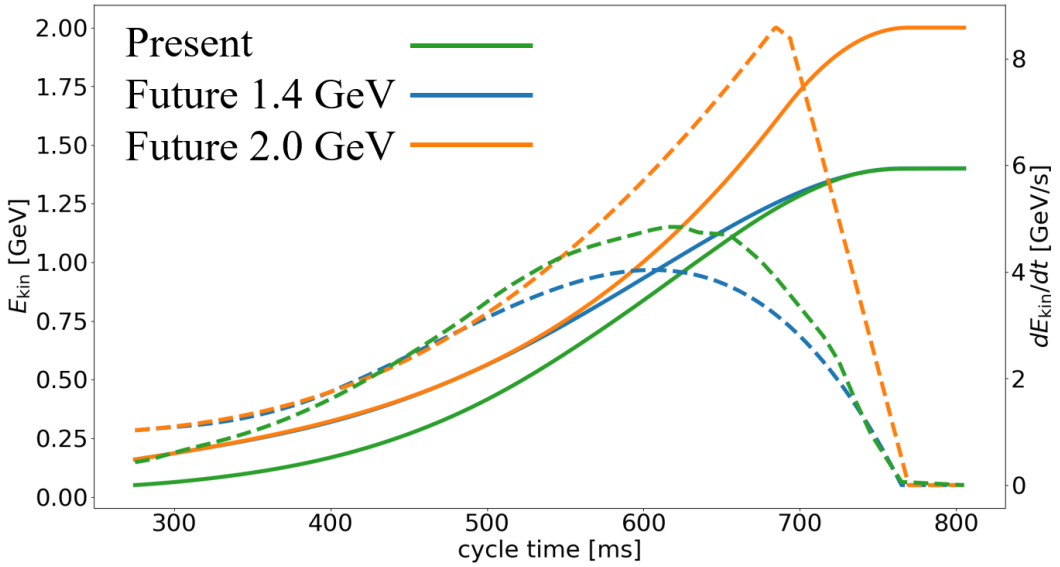


**Figure 4.4.** Current PSB kinetic energy program (green) compared to the proposed ones after LIU upgrade (blue and orange for extraction at 1.4 GeV and 2 GeV kinetic energy respectively). Their derivatives are also showed (dashed lines).

.

The next important upgrade for the after-LS2 scenario consists in blowing up the longitudinal emittance in the PSB in a controlled way from 1.4 eVs to 3 eVs, instead of the current increase from 1 eVs to 1.3 eVs. This will allow to reduce the peak line density even further at the PS injection, according to Eq.(4.1).

Notice that the PS brightness curve in Fig.4.3 is not a straight line, therefore the approximated formula for the tune shift in Eq.(4.1) cannot be used, instead the full calculation has to be done. It has been estimated that, after LIU upgrade,

the vertical maximum tune shift, responsible for the limitation, will remain equal to 0.31 [66, 2]. Assuming that all the planned upgrades for the PSB, PS and SPS will be successful, it will be possible to reach at LHC injection an intensity of $N_b = 2.3 \cdot 10^{11}$ ppb with a transverse normalized emittance of 2.1 µm (Fig.4.3, right). Therefore the HL-LHC requests will be entirely fulfilled.

The next significant upgrade concerns the PSB RF system. The current three tunable narrow-band ferrite RF cavities C02, C04 and C16 will be replaced by wide-band Finemet®-based units (see Section 4.3 to understand the motivations behind this change and Section 4.5 for an accurate description of the Finemet® impedance model). The new RF system will consist of 144 identical cells (see Fig.4.2), providing a total of 24 kV RF voltage per ring if the resonant frequency is below 5 MHz, otherwise the available RF voltage will linearly decay to 4 kV at 18 MHz [63]. The Finemet® gaps will cover all the frequencies from few hundreds kHz to above 20 MHz and will allow multi-harmonic operation, namely it will be possible to freely allocate on each gap a different RF voltage at the desired revolution harmonic, providing significant operational flexibility. In addition the new system will be modular, since every gap might be short-circuited in case of an amplifier break without influencing the other gaps.

Table 4.2 complements Table 4.1 and summarizes all the future parameters which will change with respect to the present situation. Since most of the PSB longitudinal beam dynamics studies presented later are focused on the HL-LHC scenario, the beam parameters reported in Table 4.2 concern the nominal HL-LHC beams in the PSB. Notice that, for this type of beam, the total losses and the normalized transverse emittance blow-up in the PSB are expected to be of 5% (maximum allowed LIU budget).

### 4.1.2 Outline of This Chapter

It has been explained that after-LS2 more demanding and challenging beam parameters will be required in the PSB to fulfill the HL-LHC directives. In addition the current PSB impedance model will not be valid anymore due, for example, to the introduction of the new Finemet® cavities. Therefore it is vital to perform accurate studies of the PSB longitudinal beam dynamics using a trustworthy simulation code as BLonD in order to predict possible future instability issues [74, 75]. An accurate longitudinal impedance model is needed which takes also into account reduction of the Finemet® beam loading voltage. Moreover it is of paramount importance to derive an accurate estimation of the longitudinal space charge effect along the future PSB cycle.

This Chapter is structured as follows. Section 4.2 summarizes the conventions currently used in PSB operation to measure longitudinal bunch length and emittance. Section 4.3 describes analysis, including comparison between some beam measurements and particle simulations, which helped in the decision to replace the current ferrite RF system with a new Finemet® one after LIU upgrade. Section 4.4 explains the followed procedure to obtain a reliable estimate of the longitudinal space charge at PSB injection energy, then used to compute the space charge values for the entire cycle by scaling. In Section 4.5 the full PSB longitudinal impedance model is presented in detail. Section 4.6 explains how a second RF harmonic system is used

**Table 4.2.** Some of the main CERN PS Booster machine and RF parameters for the after upgrade scenario [2, 63]. Current parameters which will not change after upgrade are not reported here (see Table 4.1). The last four rows refer to nominal LHC25ns beam parameters in the HL-LHC era.

| | |
|---|---|
| Injector | Linac4 |
| $E_{0,\mathrm{kin}}^{\mathrm{C275}}$ [MeV], $f_{0,\mathrm{rev}}^{\mathrm{C275}}$ [MHz], $\gamma_0^{\mathrm{C275}}$, $\beta_0^{\mathrm{C275}}$ | 160, 0.99, 1.17, 0.52 |
| $E_{0,\mathrm{kin}}^{\mathrm{C800}}$ [GeV], $f_{0,\mathrm{rev}}^{\mathrm{C800}}$ [MHz] , $\gamma_0^{\mathrm{C800}}$, $\beta_0^{\mathrm{C800}}$ | 2, 1.81, 3.13, 0.95 |
| RF systems | Finemet® (broad-band, modular) |
| Revolution harmonics | 1-20 (multi-harmonic operation) |
| Resonant frequencies [MHz] | 1-20 |
| Cavities configuration | 36 identical gaps per ring |
| Total RF voltage [kV] | 24 kV per ring if $hf_{0,\mathrm{rev}}$ <5 MHz |
| $f_{\mathrm{s0}}^{\mathrm{C275}}$-$f_{\mathrm{s0}}^{\mathrm{C800}}$ [kHz], $Q_{\mathrm{s0}}^{\mathrm{C275}}$-$Q_{\mathrm{s0}}^{\mathrm{C800}}$ ($\hat{V}_{\mathrm{rf},1}$= 8 kV) | 1.67-0.26, $1.69 \cdot 10^{-3}$ - $0.14 \cdot 10^{-3}$ |
| $\epsilon_{\mathrm{l}}^{\mathrm{C285}}$ [eVs], $\tau_{\mathrm{l}}^{\mathrm{C285}}$ [ns], $\delta_{\mathrm{rms}}^{\mathrm{C285}}$ | 1.4, 650, $1.8 \cdot 10^{-3}$ |
| $\epsilon_{\mathrm{l}}^{\mathrm{C800}}$ [eVs], $\tau_{\mathrm{l}}^{\mathrm{C800}}$ [ns], $\delta_{\mathrm{rms}}^{\mathrm{C800}}$ | 3, 205, $1.5 \cdot 10^{-3}$ |
| $N_{\mathrm{b}}^{\mathrm{C285}}$ [ppb], $\epsilon_{x,y,\mathrm{n}}^{\mathrm{C285}}$ [µm], $\Delta Q_{x,y}^{\mathrm{C285,sc}}$ | $34.2 \cdot 10^{11}$, 1.72, (0.58, 0.69) |
| $N_{\mathrm{b}}^{\mathrm{PS\ inj}}$ [ppb], $\epsilon_{x,y,\mathrm{n}}^{\mathrm{PS\ inj}}$ [µm], $\Delta Q_{x,y}^{\mathrm{PS\ inj,sc}}$ | $32.5 \cdot 10^{11}$, 1.80, (0.18, 0.30) |

in the PSB, together with the problem of RF phase calibration in the presence of collective effects. Finally Section 4.7 shows the simulation results for future nominal LHC25ns and high-intensity beams, providing for the second ones suggestions to reduce the observed instability.

## 4.2 Methods for Bunch Length Calculation in the PSB

In PSB operation, the beam current (or longitudinal profile) is measured using a tomoscope. Records of consecutive beam profiles allows to reconstruct in post-processing the bunch in longitudinal phase space using the principle of tomography [64], see Fig.4.5. The tomogram gives as output a density function $\psi_{i,j}$ such that, if $G = \Delta t \times \Delta E$ is a $m \times n$ grid on the longitudinal phase space with time and energy resolutions $d(\Delta t)$ and $d(\Delta E)$ then

$$\sum_{i=1}^{m}\sum_{j=1}^{n} \psi_{i,j} d(\Delta t) d(\Delta E) = A\,\mathrm{eVs} \tag{4.2}$$

Note that the stable phase is equal to zero in the tomogram conventions, contrary to what assumed when the equations of motion were derived in Chapter 2 below transition energy. Therefore $\Delta t \in [-T_0/2, T_0/2]$.

Three different ways of computing the longitudinal emittance are available in operation. The first one is the so-called statistical RMS Emittance, or $1\sigma$ emittance,

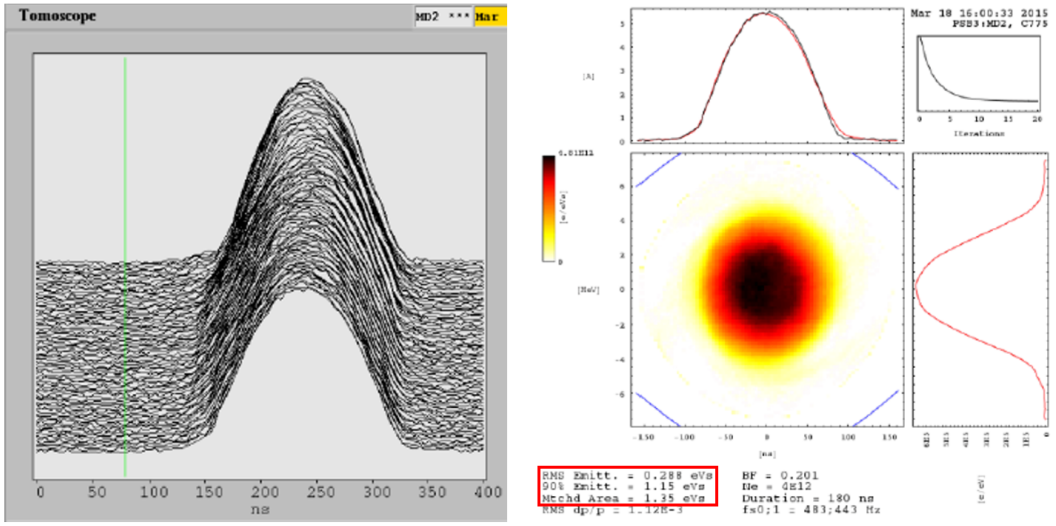


**Figure 4.5.** (Left) Example of PSB measurements of consecutive beam profiles obtained through the tomoscope. (Right) Consequent reconstruction of the bunch distribution in longitudinal phase space using the tomography principle (density of particles expressed through the color bar, the separatrix is in blue). The two profiles shown are the projections in time and energy of the distribution. The decaying curve on the top-right corner gives an indication of the error of the reconstructed bunch versus the number of iterations of the tomogram algorithm. The red square highlights the three methods used in operation to evaluate the bunch longitudinal emittance (see text for details).

given by the following formula [76]:

$$\epsilon_{l,rms} = \pi\sqrt{(\overline{\Delta t^2} - \overline{\Delta t}^2)(\overline{\Delta E^2} - \overline{\Delta E}^2) - (\overline{\Delta t \Delta E} - \overline{\Delta t}\ \overline{\Delta E})^2} \tag{4.3}$$

where

$$\overline{\Delta t^p \Delta E^q} = \frac{\sum_{i=1}^{m}\sum_{j=1}^{n}\psi_{i,j}\Delta t_i^p \Delta E_j^q d(\Delta t)d(\Delta E)}{A\,\text{eVs}} \quad p,q = 0,1,2. \tag{4.4}$$

Notice that the possible bunch displacement in phase space relative to the stable fixed point $\Delta t = 0$, $\Delta E = 0$ is taken into account in Eq.(4.3).

The second definition is called 90% Emittance, which gives the area of the longitudinal phase space $S$ containing 90% of the total number of particles, that is

$$\epsilon_{l,90\%} = d(\Delta t)d(\Delta E)X, \tag{4.5}$$

where $X$ is the number of squares $d(\Delta t) \times d(\Delta E)$ contained in $S$. The value of $X$ is determined sorting the values $\psi_{i,j}$ in decreasing order obtaining a sequence $\widetilde{\psi_k}$ and then

$$\sum_{k=1}^{X}\widetilde{\psi_k}d(\Delta t)d(\Delta E) \leq 0.9A\,\text{eVs} \quad \text{and} \quad \sum_{k=1}^{X+1}\widetilde{\psi_k}d(\Delta t)d(\Delta E) > 0.9A\,\text{eVs}. \tag{4.6}$$

Finally the third definition of longitudinal emittance is called Matched Area since it corresponds to the area enclosed by a stable particle-trajectory with a given

Hamiltonian in longitudinal phase space. This definition has been and currently still is the most important since it is the reference convention used in beam-parameter PSB reports. As it was discussed in Chapter 2, the particle-trajectory needed to define the bunch emittance depends on the convention used to characterize the length of the bunch profile. In the particular case of the Matched Area, the profile length in the PSB tomogram is determined using the so-called Foot Tangent Method (Fig.4.6) after having smoothed the possibly noisy bunch profile with a Savitzky-Golay filter of order 4 [77]. Savitzky-Golay filters, when properly used in presence of over-sampled signals corrupted by high-frequency noise, are preferred to other low-pass filters, since they tend to preserve the bunch profile length and height.

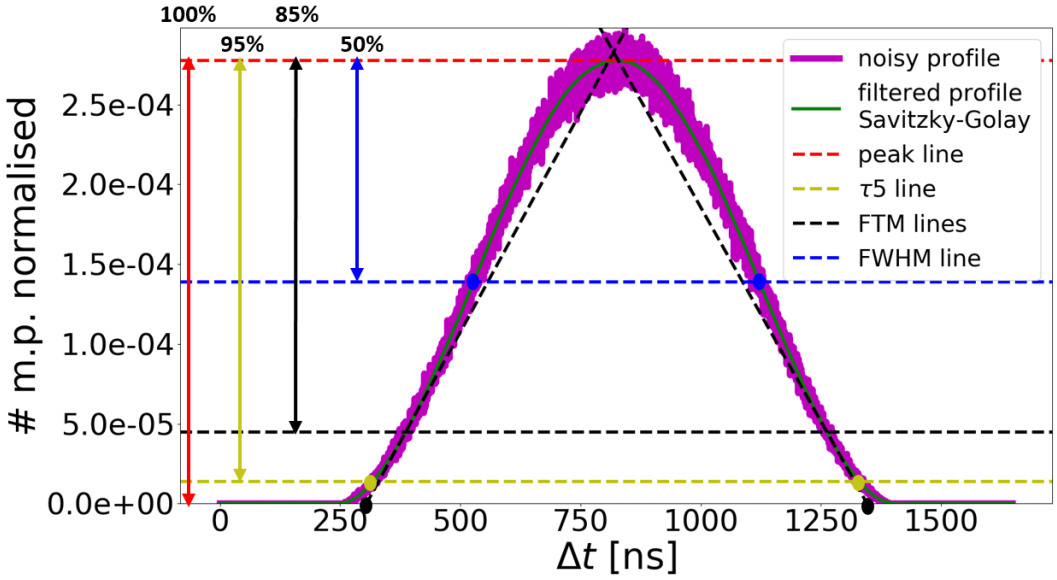


**Figure 4.6.** Example of bunch profile before and after the use of the Savitzky-Golay filter of order 4, similarly to what is done in the post-processing of the PSB tomogram algorithm. Three methods of bunch length computation are shown. FTM (Foot Tangent Method, used in the tomogram): the intersection points between the profile and the horizontal line at 15% of its peak are first considered, then the two tangent lines to the profile at these points are made intersect with the profile base. The resulting points (in black) determine the FTM bunch length. FWHM (Full Width Half Maximum) and $\tau 5$: the intersection points between the profile and the horizontal lines at 50% and 5% of its peak determine the corresponding bunch lengths (in blue and yellow respectively).

For our PSB studies, we will often refer to the Matched Area (denoted simply with $\epsilon_l$). Whenever needed we will also compute the bunch length (and therefore the emittance) using other conventions, namely the Full Width Half Maximum and the "$\tau 5$" ones, see Fig.4.6.

## 4.3 Finemet® RF System: Comparison Between Measurements and Simulations

A ten cell Finemet® prototype cavity was installed in 2014 in one of the four PSB rings for studies of RF upgrade project [78] and several beam measurements were

performed [79]. The goals of beam measurements were multiple: on one hand to understand which cavity system (current ferrite or new Finemet®) behaves better in the present situation from a longitudinal beam dynamics perspective, on the other hand to test the BLonD code so that it can be used to predict the beam parameters after upgrade.

The Finemet® cavities during measurements could be operated in three different configurations (see Section 4.5): the gaps could be short circuited (negligible impedance where the bunch spectrum sits), or set in open loop state (full impedance without any reduction) or programmed in closed loop configuration, where RF feedbacks decrease the beam-loading voltage in such a way that the full impedance has notches centered at the beam revolution harmonics 1, 2, 3 and 5. In addition it was possible in measurements to switch on and off the beam-based feedbacks (phase and radial loops) which allow a stable acceleration along the cycle (see Chapter 5).

Figure 4.7 shows important measurements indicating that the Finemet® gaps are preferable to the ferrite system from a longitudinal beam dynamics perspective. Peak-to-peak oscillation amplitudes of the bunch average position $m_{\mathrm{FWHM}}$ and length $\tau_{\mathrm{FWHM}}$, computed through the full-width-half-maximum, are plotted for ferrite and Finemet® systems between C500 and C700. Acceleration is done in a single RF system ($h = 1$) with the maximum available RF voltage: 8 kV for the C02 cavity and 7.2 kV for the Finemet® system (each of the ten gaps can provide approximately 720 V). The chosen bunch intensity for this measurements was $N_{\mathrm{b}} = 4.5 \cdot 10^{12}$ ppb. Phase and radial loops were active and the Finemet® system was operated in closed loop configuration. Figure 4.7 shows that the dipole and quadrupole oscillations of a beam accelerated through the ferrite system are larger respectively by a factor of 4 and 3 compared to the ones obtained with the Finemet® system, averaging on the cycle time interval C500-C700. In addition, looking at the error bars, it can be seen that Finemet® measurements benefit in general of more reproducibility and consistency.

Having ascertained in operation that the Finemet® gaps are preferable to the ferrite system, several comparisons between BLonD simulations and measurements of a bunch accelerated in a single RF system (using the C02 cavity with $V_{\mathrm{rf},1} = 8$ kV) were performed. Longitudinal space charge and the full PSB impedance model were included in simulations, counting also the contribution coming from the ten Finemet® gaps which were powered just to provide an additional source of impedance without delivering RF voltage to the beam. Phase and radial loops were turned off in measurements and therefore not included in simulations. As remarked before, the goal was to prove code reliability and predict the effects of the different RF systems on the after-upgrade longitudinal beam dynamics.

The first comparison concerned the evolution along the PSB cycle of the full-width-half-maximum bunch length of a beam with intensity $N_{\mathrm{b}} = 5 \cdot 10^{12}$ ppb. The ten Finemet® gaps were short circuited. As mentioned before, the current injection process with Linac2 cannot be satisfactorily simulated in the longitudinal plane, due to the impossibility to take into account the considerable losses due to the septum magnet. Therefore the comparison started at 350 ms, after beam recapture in the RF bucket. The measured profile at 350 ms (Fig.4.8, left) was fitted by a binomial

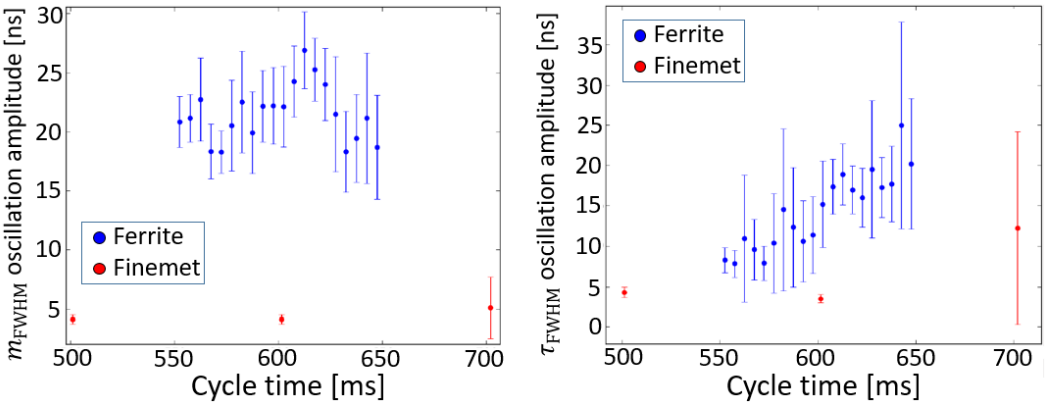


**Figure 4.7.** Measurements of the dipole (left) and quadrupole (right) peak-to-peak oscillation amplitudes for beams accelerated in a single RF system ($h = 1$) with the C02 ferrite cavity (blue, $V_{\mathrm{rf},1} = 8$ kV) or with ten Finemet® gaps (red, $V_{\mathrm{rf},1} = 7.2$ kV). The bunch intensity is $N_{\mathrm{b}} = 4.5 \cdot 10^{12}$ ppb, phase and radial loops are on. The effect of dedicated Finemet® beam-loading feedbacks consists in reducing the full Finemet® impedance through notches centered at the beam revolution harmonics 1, 2, 3 and 5 (see Section 4.5). The error bars on the measured values are determined by one standard deviation for each side. *Courtesy of S. Albright, CERN, 2015.*

line-density

$$\lambda(t) = \begin{cases} \lambda_0(\tau_{\mathrm{ee}}, \mu)\left(1 - 4\frac{t^2}{\tau_{\mathrm{ee}}^2}\right)^{\mu}, & |t| \leq \tau_{\mathrm{ee}}/2 \\ 0, & |t| > \tau_{\mathrm{ee}}/2 \end{cases}, \tag{4.7}$$

where $\lambda_0(\tau_{\mathrm{ee}}, \mu)$ is the normalization factor. The end-to-end bunch length was $\tau_{\mathrm{ee}} = 679.3$ ns and $\mu = 1.05$ (curve very close to a parabola). Different from the bunch-generation method described in Chapter 2, an algorithm in the BLonD code [80] allowed, using the Abel transform [81]

$$\psi(H(\Delta t, 0)) = -\frac{1}{\pi}\sqrt{\frac{|\eta_0|}{2\beta_0^2 E_0}}\int_{\Delta t}^{\infty}\frac{d\lambda(t)}{dt}\frac{dt}{\sqrt{U(t) - H(\Delta t, 0)}}, \tag{4.8}$$

to retrieve in simulations the stationary bunch distribution $\psi$ which had line density $\lambda$ and which was matched inside the RF bucket with collective effects. Notice that it was decided to match the distribution with an RF voltage of 9 kV, instead of the 8 kV used in measurements. The reason for this discrepancy in RF voltage for bunch generation was to create at the start of simulations, when $V_{\mathrm{rf},1} = 8$ kV, a mismatch leading to the same quadrupole oscillations as observed in measurements. An analogous approach, with an horizontal shift in time applied to the generated bunch distribution, was used to obtain the same dipole oscillations at 350 ms as seen in measurements.

Figure 4.8 (right) shows the full-width-half-maximum bunch length as a function of the cycle time from BLonD simulations and measurements. Each of the four sets of measured points in the figure contains values from two different PSB cycles (blue). In fact it is impossible to obtain data belonging to the same cycle for the entire ramp with sufficient resolution in time. In addition there are significant variations in intensity and bunch length from cycle to cycle. One can see significantly larger

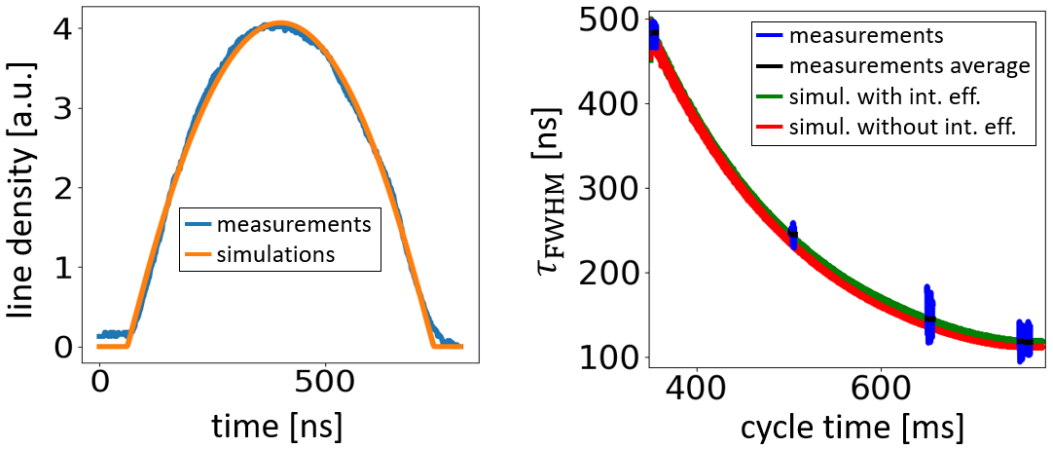


**Figure 4.8.** Left: comparison between measured (blue) and simulated (orange) longitudinal bunch profile at 350 ms PSB cycle-time. The simulated bunch profile is obtained fitting the measured one by a binomial line-density with end-to-end bunch length equal to 679.3 ns and $\mu = 1.05$. Right: full-width-half-maximum bunch length as a function of the cycle time in measurements and BLonD simulations for $N_b = 5 \cdot 10^{12}$ ppb, from 350 ms to 775 ms cycle-times. Acceleration is done in a single RF system (C02 cavity, $h = 1$) with constant RF voltage equal to 8 kV. Phase and radial loops are not active. Simulations are performed without (red) and with (green) collective effects (full PSB impedance model with space charge and the additional contribution of ten short-circuited Finemet® RF gaps). Each of the four shown sets of measurements (blue) refers to two different PSB cycles. Averages of $\tau_{FWHM}$ for the distinct groups of measurements are also shown (black). Simulations start at 350 ms with the bunch profile shown on the left figure. *Measurements courtesy of S. Albright, CERN, 2015.*

quadrupole oscillations in measurements than in simulations. This can be due for example to sources of noise present in the magnetic and RF frequency programs used in operation, in contrast to the smooth design ones adopted in simulations. However, if averages of $\tau_{FWHM}$ for the various groups of measurements are considered (black), good agreement is found between simulations including collective effects (green) and measurements, while underestimated bunch lengths are obtained neglecting intensity effects (red). Notice that the difference in $\tau_{FWHM}$ between simulations with and without collective effects is mostly due to the longitudinal space charge which increases the bunch length below transition energy.

Having gained trust in the ability of the BLonD code to reproduce measured beam parameters along the PSB cycle, the second comparison between simulations and measurements concerned the behavior of the extracted bunch length as a function of the extracted intensity. The bunch was again accelerated using only the C02 cavity with $V_{rf,1} = 8$ kV, and the ten Finemet® RF gaps were at first short circuited and then set in open loop mode. Figure 4.9 shows the results of the comparison and a reasonable agreement between measurements and simulations can be seen. This study also indicated that the Finemet® cavities, considered only as source of impedance without accelerating the beam, do not alter the considered longitudinal beam parameters for bunch intensities between $N_b = 50 \cdot 10^{10}$ ppb and $N_b = 500 \cdot 10^{10}$ ppb.

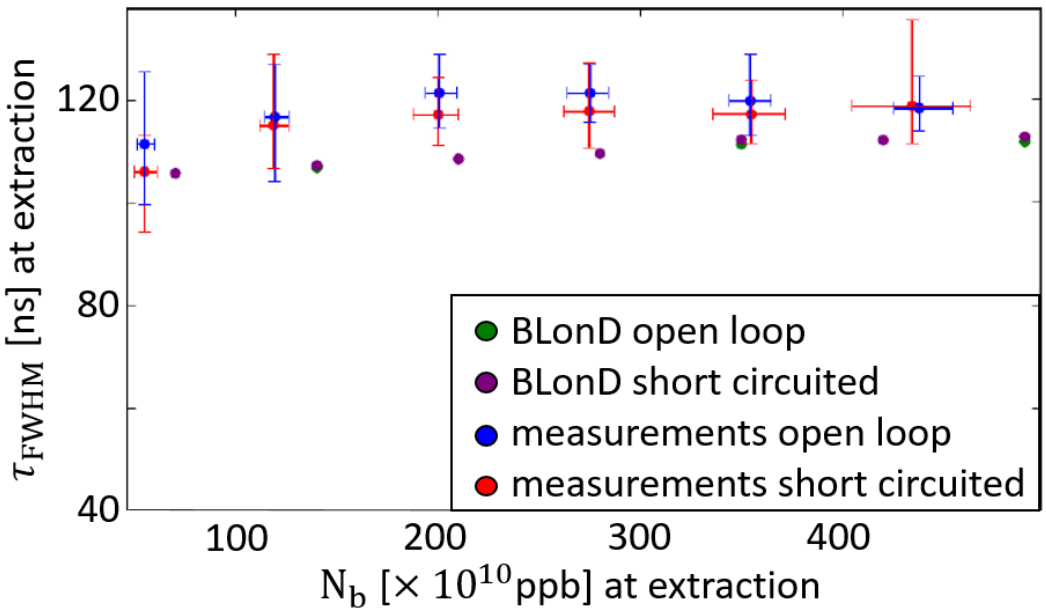


**Figure 4.9.** Comparison between measurements and BLonD simulations of the full-width-half-maximum bunch length at PSB extraction as a function of the extracted intensity. Acceleration is done in a single RF system (C02 cavity, $h = 1$) with constant RF voltage equal to 8 kV all along the cycle. Beam-based feedbacks (phase and radial loops) are off. Ten Finemet® RF gaps, short circuited or in open loop configuration, contribute to the total impedance seen by the beam. *Measurements courtesy of S. Albright, CERN, 2015.*

Finally simulations for after-upgrade beams in a single RF system were performed with the BLonD code to compare the effects of the ferrite and Finemet® RF systems on the future longitudinal beam dynamics. In the first simulated case (Fig.4.10, left), the bunch intensity and the $h = 1$ RF voltage were set to $N_b = 9 \cdot 10^{12}$ ppb and $V_{rf,1} = 8$ kV respectively, while the kinetic energy at extraction was 2 GeV (see Fig.4.4 for the adopted momentum program). In the second simulated case (Fig.4.10, right), the bunch intensity and the RF voltage were set to $N_b = 1.5 \cdot 10^{13}$ ppb and $V_{rf,1} = 15$ kV respectively, with a kinetic energy at flat top equal to 1.4 GeV (see again Fig.4.4). In both cases phase and radial loops were not included.

These two chosen bunch intensities, with the corresponding different acceleration cycles, were selected based on expected extreme values for future high-intensity beams. As mentioned in the introduction of this Chapter, the 36 Finemet® gaps planned to be installed after-upgrade in each of the four PSB rings will provide a maximum RF voltage of 24 kV. Therefore the value of $V_{rf,1} = 15$ kV used as an example in the second simulated case is feasible for the Finemet® system and, to allow comparison, was assumed to be deliverable also by the C02 ferrite cavity, which current maximum RF voltage is only 8 kV. The 36 Finemet® gaps were supposed to be in an optimistic closed loop configuration, meaning that the feedbacks reduce the full Finemet® impedance at all frequencies by the maximum possible factor of 63.

All simulations shown in Fig.4.10 started at C275 with the same rectangular distribution in longitudinal phase space formed by micro-bunches coming from Linac4. The distribution was uniform in time and water-bag in energy, with a total

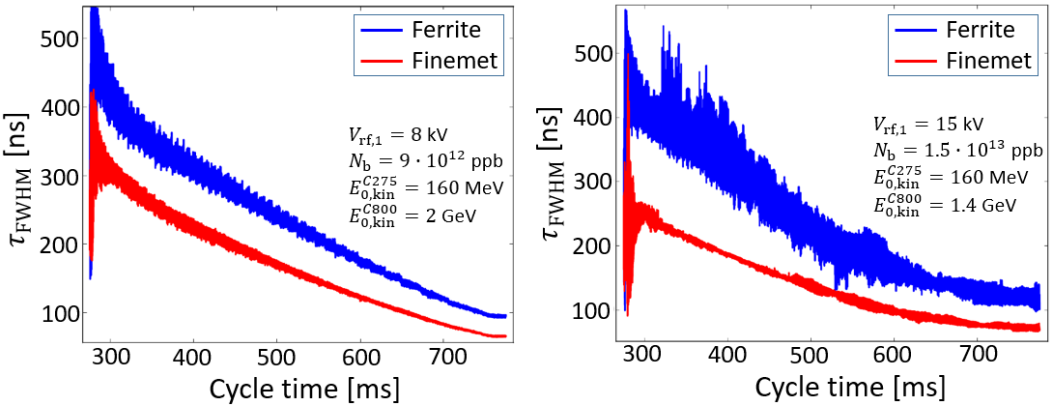


**Figure 4.10.** Simulations comparing the effects of the ferrite and Finemet® RF systems on the full-width-half-maximum bunch length along the future PSB cycles (Fig.4.4) for high-intensity beams. The bunches are accelerated in a single RF system ($h = 1$) with phase and radial loops off. All simulations start at C275 with the same micro-bunches coming from Linac4 and forming, in an accelerating bucket at 160 MeV, a rectangle which parameters correspond to the optimal case of unmodulated injection studied in [82]. The RF cavity impedance is given by the C02 resonator-like contribution for acceleration with the ferrite system (blue curve), while the impedance of 36 Finemet® gaps in an optimistic closed loop configuration (reduction of the full impedance at all frequencies by the maximum possible factor of 63) is considered for acceleration with the Finemet® system (red curve).

injected bunch length equal to 474 ns and an rms energy spread of 336 keV. These last two values were chosen to match the optimal case studied in [82] for a future unmodulated multi-turn injection of Linac4 micro-bunches into a PSB double RF bucket with $V_{rf,1} = 8$ kV ($h = 1$), $V_{rf,2} = 6$ kV ($h = 2$) and relative RF phase set in the bunch lengthening mode (see also Section 4.6). The optimal parameters found in [82] derived from a compromise between minimization of the peak line density for transverse space charge effect reduction and minimization of the needed number of turns in the multi-turn injection to reduce the amount of foil hits and blow-up due to the scattering at the screen in the new $H^-$ charge-exchange injection system.

Figure 4.10 shows that the bunch length oscillations along the future PSB cycles are significantly smaller if the acceleration is performed with the Finemet® system. In addition the ferrite cavity leads to an uncontrolled increase in bunch length during the interval C275-C300, when the initial rectangular distribution filaments in an accelerating bucket.

The results shown in this Section strongly contributed to the important decision to replace, after upgrade, all the present ferrite systems with Finemet® ones [63, 78].

## 4.4 Longitudinal Space Charge After LIU Upgrade

### 4.4.1 Space Charge Calculation Along the Ramp

The longitudinal space charge effect is very significant in low energy machines and an accurate estimation of its contribution to collective effects is very important. The

PSB, which can be considered a low energy machine with its current relativistic beta at injection equal to 0.31, operates below transition energy and therefore the longitudinal space charge has a defocusing effect [82, 83].

The longitudinal space charge $Z_{\mathrm{sc}}$ can be modeled by a purely imaginary impedance [84]. In the following, we assume that $|Z_{\mathrm{sc}}|/n$ does not depend on $f$, or that $|Z_{\mathrm{sc}}|$ is directly proportional to $f$ at a given energy [85]. Most of the times this approximation is reasonable and we will see later that the same can also be assumed in the PSB case.

The results derived in this Section will show that $|Z_{\mathrm{sc}}|/n \approx 600\ \Omega$ at the future PSB injection kinetic energy of 160 MeV. For the sake of comparison and to show the magnitude of this space charge value, $|Z_{\mathrm{sc}}|/n \approx 1\ \Omega$ at CERN SPS injection ($E_{\mathrm{kin}} = 25$ GeV), where longitudinal space charge plays an important role being even comparable to other impedance sources [80].

The longitudinal space charge induced voltage can be calculated starting from its expression involving the inverse Fourier transform $F^{-1}$

$$V_{\mathrm{sc}}(t) = eF^{-1}(Z_{\mathrm{sc}}S) = \frac{e}{2\pi}\int_{-\infty}^{+\infty} d\omega\, Z_{\mathrm{sc}}(\omega)\, S(\omega)\, e^{i\omega t} \tag{4.9}$$

Using the assumptions given before we can compute

$$\begin{aligned} V_{\mathrm{sc}}(t) &= \frac{e}{2\pi}\int_{-\infty}^{+\infty} d\omega\, i\frac{|Z_{\mathrm{sc}}|}{n} n\, S\, e^{i\omega t} = \frac{e}{2\pi}\frac{|Z_{\mathrm{sc}}|}{n}\frac{1}{\omega_{\mathrm{rev},0}}\int_{-\infty}^{+\infty} d\omega\, i\,\omega\, S\, e^{i\omega t} \\ &= \frac{e}{2\pi\omega_{\mathrm{rev},0}}\frac{|Z_{\mathrm{sc}}|}{n}\int_{-\infty}^{+\infty} d\omega S\frac{d}{dt}\, e^{i\omega t} = \frac{e}{2\pi\omega_{\mathrm{rev},0}}\frac{|Z_{\mathrm{sc}}|}{n}\frac{d}{dt}\int_{-\infty}^{+\infty} d\omega S\, e^{i\omega t}. \end{aligned} \tag{4.10}$$

Finally, noting that the integral term in the last expression of Eq.(4.10) is equal to $2\pi\lambda$, we obtain

$$V_{\mathrm{sc}}(t) = \frac{e}{\omega_{\mathrm{rev},0}}\frac{|Z_{\mathrm{sc}}|}{n}\frac{d}{dt}\lambda(t). \tag{4.11}$$

Equation (4.11) shows that the calculation of the space-charge induced-voltage is reduced to the computation of $|Z_{\mathrm{sc}}|/n$ for each beam energy through the acceleration cycle.

As observed above, the future bunch distribution at cycle-time C275 ($E_{\mathrm{kin}} =$ 160 MeV), being a rectangle in phase space, will start filamenting in an accelerating bucket. At cycle-time C285 ($E_{\mathrm{kin}} = 170$ MeV, $\beta_0 = 0.53$, $\gamma_0 = 1.18$) the bunch is expected to be matched with the RF bucket. Therefore in this Subsection we will focus on the calculation of $|Z_{\mathrm{sc}}|/n$ at C285, when the bunch will be at equilibrium, before using a rescaling formula to estimate the space charge values for all the energies along the future cycle, from 160 MeV to 2 GeV.

The following formula is often used to obtain a first approximation for $|Z_{\mathrm{sc}}|/n$ [86]

$$\frac{|Z_{\mathrm{sc}}|}{n} = \frac{Z_0 g}{2\beta_0\gamma_0^2} = \frac{Z_0}{2\beta_0\gamma_0^2}\left(1 + 2\ln\frac{b}{a}\right), \tag{4.12}$$

where $Z_0 \approx 377\,\Omega$ is the free-space impedance, $g$ is the so-called geometrical or form factor, $b$ and $a$ the radii of the chamber and beam longitudinal cross sections respectively. In fact Eq.(4.12) is exact only for chambers and beams having a longitudinal circular cross section and for beams with an uniform transverse distribution.

An additional hypothesis is that the field is calculated on axis, where the field is maximum. Therefore the impedance value obtained with Eq.(4.12) refers to the worst case scenario.

In order to obtain a first approximation for $|Z_{\mathrm{sc}}|/n$ at 170 MeV using Eq.(4.12), the values of $b$ and $a$ have to be found. Focusing first on $b$, it is important to note that the PSB can be divided into 211 sections, where each part differs from the two adjacent ones in cross section shape, dimension, or both. Figure 4.11 shows how the horizontal $b_x$ and vertical $b_y$ half-heights of the cross sections change as a function of the position $s$ in the PSB, see also Fig.4.13. Averaging along the ring, we obtain $\langle b_x \rangle = 66.6$ mm and $\langle b_y \rangle = 51.1$ mm. Therefore we can set $b = (\langle b_x \rangle + \langle b_y \rangle)/2 = 58.8$ mm.

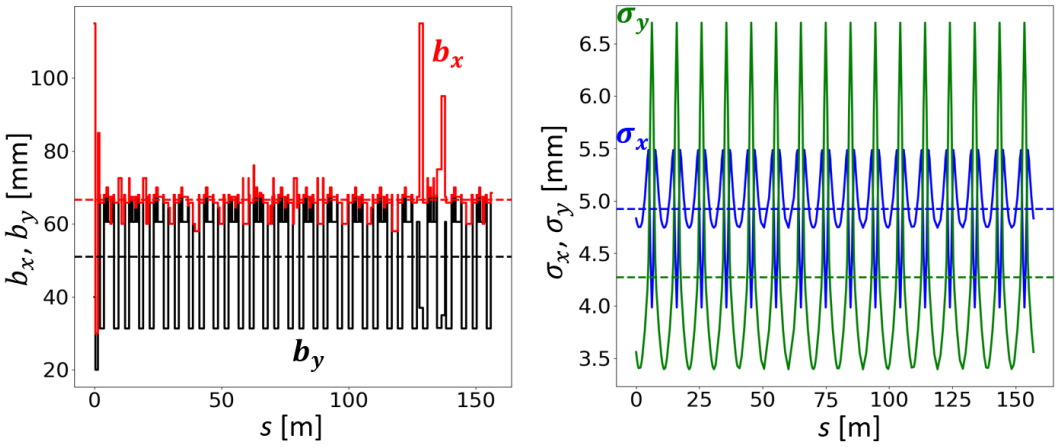


**Figure 4.11.** Left: horizontal (red) and vertical (black) half-heights of the different beam-pipe cross sections along the PSB ring. Right: rms sizes along the PSB ring of the horizontal and vertical Gaussian distributions (blue and green respectively) if $E_{\mathrm{kin}} = 170$ MeV, $\epsilon_{x,y} = 1.72$ µm and $\delta_{\mathrm{rms}} = 1.8 \cdot 10^{-3}$. The dashed horizontal lines mark the averages of the corresponding curves.

In order to find $a$, we first have to notice that the horizontal and vertical transverse distributions for nominal LHC beams after upgrade will not be uniform but will resemble a Gaussian, as it is currently the case. In addition the horizontal and vertical rms bunch sizes $\sigma_x$ and $\sigma_y$ will vary along the ring. Therefore, in rough approximation, we can suppose that the beam radius $a$ of a bi-Gaussian transverse distribution can be interpreted as twice the average of the averages of the horizontal and vertical rms bunch sizes along the ring, that is $a = \langle \sigma_x \rangle + \langle \sigma_y \rangle$.

To calculate $\sigma_x$ and $\sigma_y$ we can use the formulas derived in Appendix A

$$\sigma_x(s) = \sqrt{\beta_x(s)\epsilon_x + D_x^2(s)\delta_{\mathrm{rms}}^2}, \quad \sigma_y(s) = \sqrt{\beta_y(s)\epsilon_y}, \tag{4.13}$$

where $\epsilon_{x,y}$ are the geometrical emittances, $\beta_{x,y}$ are the transverse beta functions and $D_x$ is the horizontal dispersion function ($D_y$ is negligible in the PSB).

Table 4.2 has been used to estimate $\delta_{\mathrm{rms}}$ and $\epsilon_{x,y}$ at 170 MeV, therefore $\delta_{\mathrm{rms}} = 1.8 \cdot 10^{-3}$ and $\epsilon_{x,y} = \epsilon_{x,y,\mathrm{n}}/(\beta_0\gamma_0) = 2.74$ µm. Using the PSB betatron and dispersion functions shown in Fig.4.12, $\sigma_x$ and $\sigma_y$ can be computed for every position $s$ along

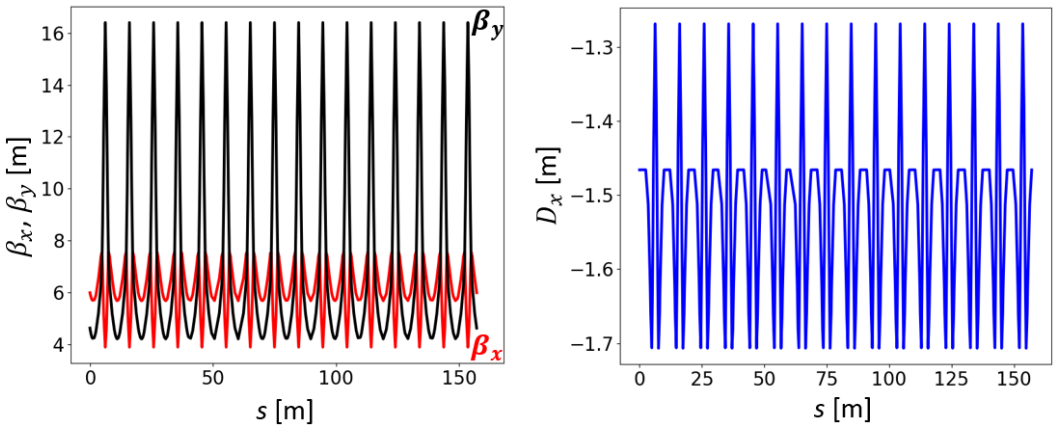


**Figure 4.12.** Horizontal and vertical PSB beta functions (left) and horizontal dispersion function (right) as a function of the position $s$ along the ring. *Courtesy of G. Rumolo, CERN, 2015.*

the ring, see Fig.4.11. The averages are $\langle\sigma_x\rangle = 4.93$ mm and $\langle\sigma_y\rangle = 4.27$ mm, therefore $a = 9.2$ mm.

Substituting $a$ and $b$ in Eq.(4.12), the following approximation for $|Z_{\mathrm{sc}}|/n$ at 170 MeV was obtained

$$\frac{|Z_{\mathrm{sc}}|}{n} = 1195.6\,\Omega. \tag{4.14}$$

As observed above, this impedance value refers to the worst case scenario of a field calculated on axis.

It has been suggested in Ref.[86] that it is more realistic to consider the average potential instead of the on-axis potential. Equation (4.12) then becomes

$$\frac{|Z_{\mathrm{sc}}|}{n} = \frac{Z_0}{2\beta_0\gamma_0^2}\left(0.5 + 2\ln\frac{b}{a}\right). \tag{4.15}$$

This expression, with the same values of $a$ and $b$ as used before, gives a second approximation for $|Z_{\mathrm{sc}}|/n$ at 170 MeV

$$\frac{|Z_{\mathrm{sc}}|}{n} = 1068.7\,\Omega. \tag{4.16}$$

In reality, as outlined previously, neither the beam nor the pipe cross sections are round and of constant dimensions along the ring. Therefore we expect that the two just found impedance values can only indicate the order of magnitude of $|Z_{\mathrm{sc}}|/n$ at 170 MeV. This is surely not sufficient for our studies, due to the strong contribution of the longitudinal space charge to the full impedance model (see Section 4.5). In addition an accurate value for $|Z_{\mathrm{sc}}|/n$ is needed since, from the relation

$$V_{\mathrm{sc}} \propto N_{\mathrm{b}}\frac{|Z_{\mathrm{sc}}|}{n}\frac{d}{dt}\frac{\lambda(t)}{N_{\mathrm{b}}}, \tag{4.17}$$

it follows that the threshold beam intensity $N_{\mathrm{b}}$ and the space charge impedance $|Z_{\mathrm{sc}}|/n$ are inversely proportional to each other, given a normalized longitudinal line

density and a threshold value of the space-charge induced-voltage. Consequently, errors in properly estimating $|Z_{\mathrm{sc}}|/n$ lead to uncertainties on the threshold beam intensity.

Therefore a tool able to accurately calculate the longitudinal space charge field in the PSB becomes necessary. A precise value of $|Z_{\mathrm{sc}}|/n$, used as an input in BLonD simulations, would allow to avoid unrealistic predictions for the after-LIU scenario.

### The LSC Code

At SLAC Laboratory it was developed a code called LSC (Longitudinal Space Charge) [84] able to solve the wave equation

$$\nabla^2 \boldsymbol{\mathcal{E}} - \frac{1}{c^2}\frac{\partial \boldsymbol{\mathcal{E}}}{\partial t} = \frac{\nabla \rho}{\epsilon_0} + \mu_0 \frac{\partial \boldsymbol{J}}{\partial t} \tag{4.18}$$

for the longitudinal component $\mathcal{E}_z$ of the space charge electric field. Here $\rho$ and $\boldsymbol{J}$ are the charge and current densities respectively, while $\epsilon_0$ and $\mu_0$ are the permittivity and permeability of free space.

In order to compute the space charge field in each of the 211 different PSB sections, the LSC code takes as input for each section: one pair of values for the rms transverse beam sizes $\sigma_x$ and $\sigma_y$ (we chose to average the values in Fig.4.11 (right) along the section), the aperture shape and size, the horizontal and vertical particle distribution types (Gaussian), and the beam energy (170 MeV). The LSC code then gives as output the length-normalized space-charge impedance $|Z_{\mathrm{sc}}|/L$, calculated either as an average over one rms transverse bunch width or on axis ($L$ stands for the length of the section). In the computations, the LSC code considers both the direct and indirect longitudinal space charge, meaning that the repulsive Coulomb forces between particles and the interactions between the beam and the pipe are taken into account.

The LSC code solves Eq.(4.18) using a Finite Element Method. Therefore it requires meshed models of the various cross sections as an input. There are four different aperture shapes in the PSB, see Fig.4.13: round for drift tubes (117), "rectangular" for dipoles (47), "diamond" for quadrupoles (44) and "oblong" for septum magnets at injection and extraction (3). The "rectangular" and "oblong" shapes are slightly different: the boundary of the "rectangular" shape is formed entirely by arcs of circumference (three different values for the radius are used) while the boundary of the "oblong" shape is composed of straight lines and arcs of circumference (only one radius is used), see again Fig.4.13. However, because of the similarity, every "rectangular" shape with a certain horizontal and vertical half-heights $b_x$ and $b_y$ has been converted to an "oblong" shape with the same half-sizes.

After having extrapolated the different cross-section boundaries from the drawings in Fig.4.13, the desired meshes for the LSC code were computed, see Fig.4.14. Notice that these grids are not banally uniform, as often happens when Finite Element Methods are used to solve partial differential equations.

Figure 4.15 shows two expected normalized bunch spectra at 170 MeV together with the output of the LSC code, each line refers to one of the 211 sections in which the PSB has been decomposed. When Eq.(4.11) was derived, it was supposed that

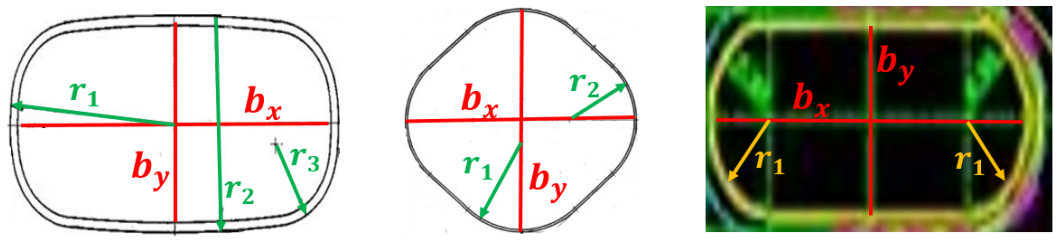


**Figure 4.13.** Drawings of the different types of chamber cross section in the PSB ring: "rectangular" (left) for dipoles, "diamond" (center) for quadrupoles and "oblong" (right) for septum magnets. The quantities $b_x$ and $b_y$ represent the horizontal and vertical half-heights of the cross-section. The radii of the different arcs of circumference are denoted by a numbered $r$. The drift tube cross-section is simply round with radius $r_1 = b_x = b_y$ and therefore not shown. *Courtesy of C. Zannini, M. Hourican and F. Chapuis, CERN, 2015.*

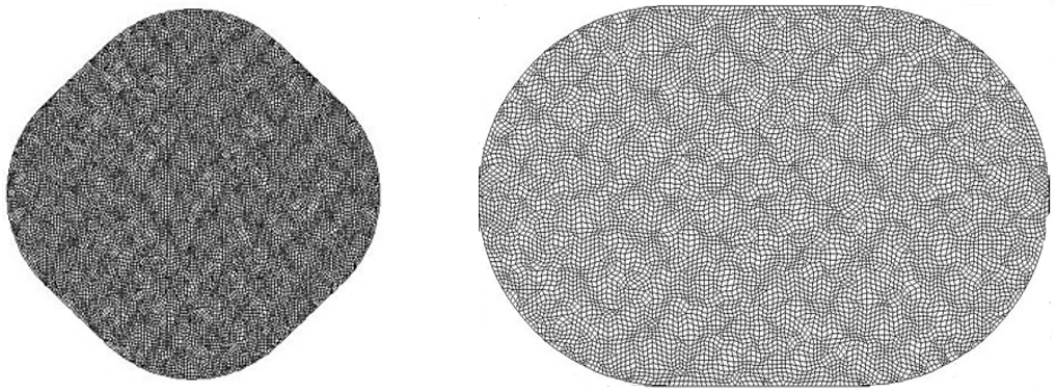

**Figure 4.14.** Dedicated meshes for the "diamond" (left) and "oblong" (right) PSB apertures to be used as inputs for the LSC code. *Courtesy of L. Wang, SLAC, 2015.*

$|Z_{\mathrm{sc}}|/n$ does not depend on the frequency. Figure 4.15 proves that this assumption is reasonable for the PSB case, at least at 170 MeV, since the beam spectra decay to zero before $|Z_{\mathrm{sc}}|/n$ starts dropping at roughly 100 MHz. For each of the 211 sections, the average of the correspondent $|Z_{\mathrm{sc}}|/(Ln)$ over the positive frequencies smaller than 30 MHz is taken (see Fig.4.15). Including the information about the section lengths, Fig.4.16 shows the variation of the length-normalized $|Z_{\mathrm{sc}}|/n$ along the ring.

In order to obtain one single value for the longitudinal space charge impedance at 170 MeV over one revolution turn, a weighted average has to be computed

$$\frac{|Z_{\mathrm{sc}}|}{n} = \sum_{i=1}^{211} L_i \left(\frac{|Z_{\mathrm{sc}}|}{Ln}\right)_i . \tag{4.19}$$

This expression gives the following value

$$\frac{|Z_{\mathrm{sc}}|}{n} = 608.3\,\Omega, \tag{4.20}$$

which refers to a space charge force averaged over one rms transverse beam width. Using the LSC code to evaluate the space charge force on beam axis and applying again Eq.(4.19), the value 637.6 Ω is obtained. Notice how these last two space charge estimations significantly differ from the ones obtained in Eqs.(4.14) and (4.16).

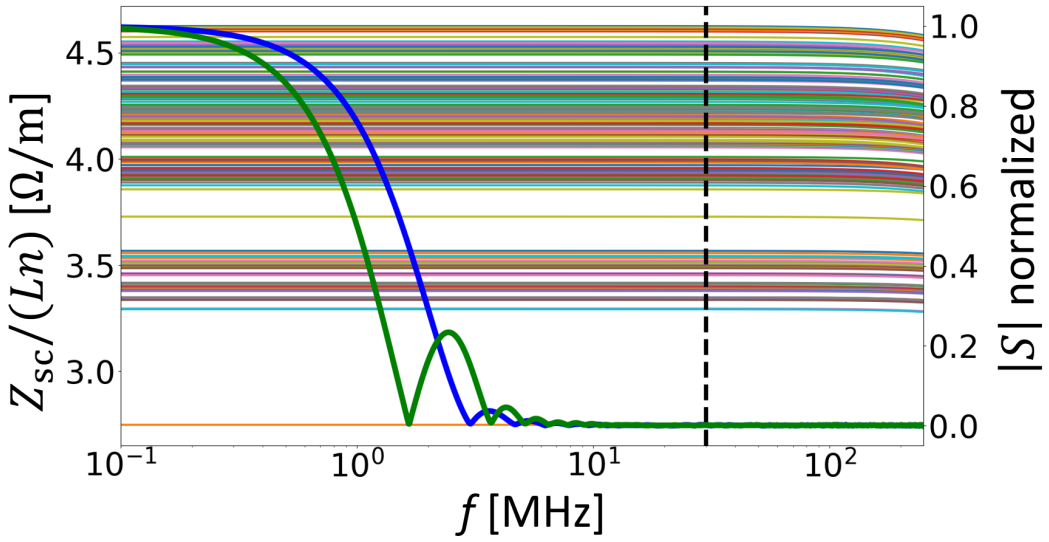


**Figure 4.15.** The length-normalized longitudinal space charge impedance $Z_{sc}/n$ as a function of frequency for the 211 different PSB sections at 170 MeV (output of the LSC code). Two different beam spectra of a bunch having a parabolic distribution density with emittance $\epsilon_l = 1.4$ eVs at 170 MeV are also shown: one refers to a bunch matched inside a single RF bucket ($V_{rf,1} = 16$ kV, blue line), the other corresponds to a bunch at equilibrium inside a double RF bucket ($V_{rf,1} = 8$ kV, $V_{rf,2} = 8$ kV, relative phase in bunch lengthening mode, green line). The dashed vertical line marks $f = 30$ MHz.

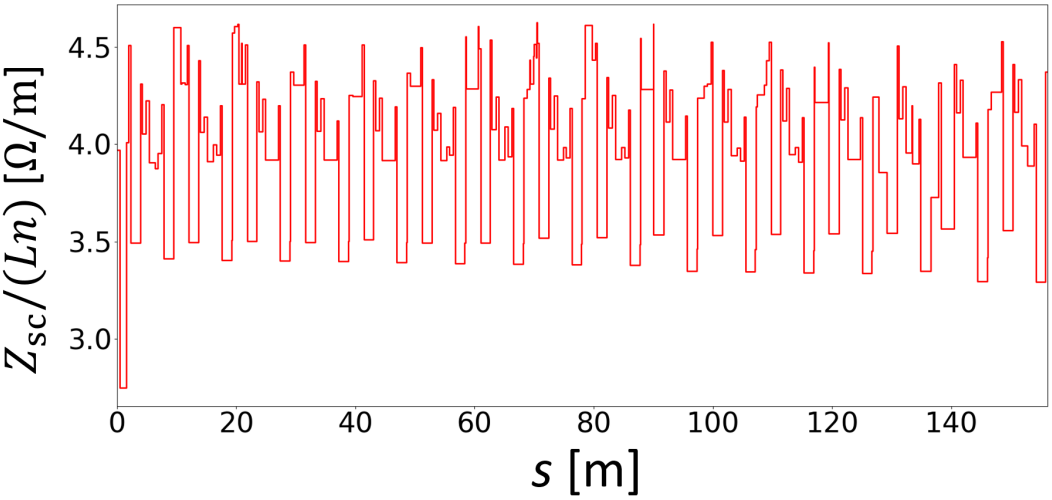


**Figure 4.16.** Variation of the length-normalized $|Z_{sc}|/n$ as a function of the position along the PSB ring.

Finally, Eq.(4.15) and the value in Eq.(4.20) have been used to have a rough

estimation of the space charge impedance at different energies of the future PSB cycle. The following relation for the average beam radius $a$ derives from Eq.(4.13)

$$a(E_{\mathrm{kin}}) \propto \sqrt{\frac{\epsilon_{x,y,\mathrm{n}}(170\,\mathrm{MeV})C_{\mathrm{bu}}(E_{\mathrm{kin}})}{\beta_0(E_{\mathrm{kin}})\gamma_0(E_{\mathrm{kin}})}}. \tag{4.21}$$

where $C_{\mathrm{bu}}$ is a factor depending on the kinetic energy which takes into account the expected 5% blow-up of the transverse normalized emittance along the PSB cycle. Considering the values in Table 4.2, we can assume that $C_{\mathrm{bu}} = 1$ for $E_{\mathrm{kin}} \in [160\,\mathrm{MeV}, 170\,\mathrm{MeV}]$, $C_{\mathrm{bu}} = 1.80/1.72$ for $E_{\mathrm{kin}} = 2$ GeV and that a linear interpolation can be done for all the kinetic energies between 170 MeV and 2 GeV. From Eq.(4.21) it follows that

$$a(E_{\mathrm{kin}}) = a(170\,\mathrm{MeV})\sqrt{C_{\mathrm{bu}}(E_{\mathrm{kin}})\frac{\beta_0(170\,\mathrm{MeV})\gamma_0(170\,\mathrm{MeV})}{\beta_0(E_{\mathrm{kin}})\gamma_0(E_{\mathrm{kin}})}}. \tag{4.22}$$

Computing the expression $\log(b/a)$ at 170 MeV using Eqs.(4.15) and (4.20), and developing $\log(b/a)$ at a generic energy using Eq.(4.22), the following formula is obtained

$$\begin{aligned}\frac{|Z_{\mathrm{sc}}|}{n}(E_{\mathrm{kin}}) = &\frac{\beta_0(170\,\mathrm{MeV})\gamma_0^2(170\,\mathrm{MeV})}{\beta_0(E_{\mathrm{kin}})\gamma_0^2(E_{\mathrm{kin}})}\frac{|Z_{\mathrm{sc}}|}{n}(170\,\mathrm{MeV}) \\ &+ \frac{Z_0}{2\beta_0(E_{\mathrm{kin}})\gamma_0^2(E_{\mathrm{kin}})}\log\left(\frac{\beta_0(E_{\mathrm{kin}})\gamma_0(E_{\mathrm{kin}})}{C_{\mathrm{bu}}(E_{\mathrm{kin}})\beta_0(170\,\mathrm{MeV})\gamma_0(170\,\mathrm{MeV})}\right)\end{aligned} \tag{4.23}$$

Equation (4.23) has been used to compute the longitudinal space charge impedance along the future PSB cycle with extraction at 2 GeV, see Fig.4.17. Note an impedance reduction of almost factor 8 between the injection and extraction energies. These values for $|Z_{\mathrm{sc}}|/n$ have been used in the BLonD code to evaluate the PSB longitudinal space charge induced voltage through Eq.(4.11).

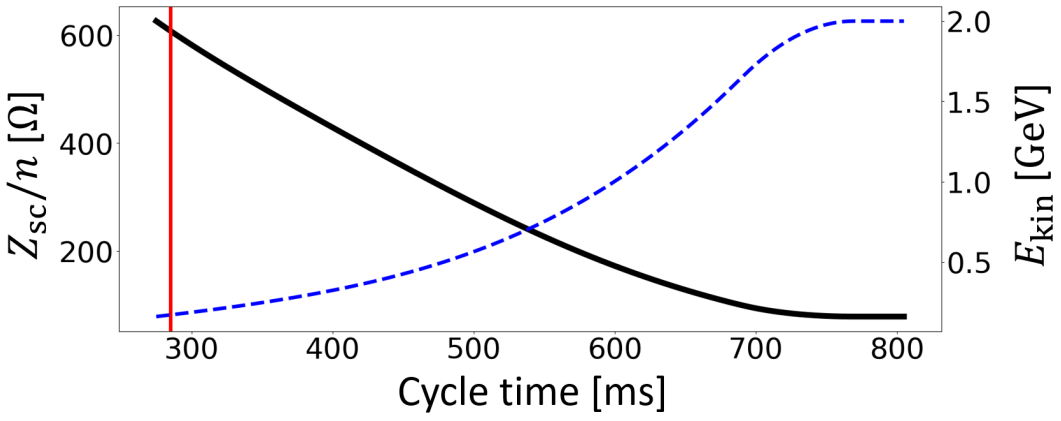


**Figure 4.17.** Estimation of the PSB longitudinal space charge impedance $|Z_{\mathrm{sc}}|/n$ (black) after CERN upgrade in the cycle-time interval 275 ms–805 ms (160 MeV–2 GeV cycle, blue). The red line marks the cycle-time 285 ms, when $|Z_{\mathrm{sc}}|/n = 608.3\,\Omega$ (value computed using the LSC code). At PSB flat top $|Z_{\mathrm{sc}}|/n = 79.2\,\Omega$.

### 4.4.2 Benchmarks with the PyORBIT Code at the Future Injection Energy

Several longitudinal space charge studies using the PyORBIT code [87] have been performed at CERN to optimize the future injection of Linac4 micro-bunches into the PSB [88, 82]. In order to validate the results coming from simulations, many benchmarks have been performed with the BLonD code.

PyORBIT is a so-called Particle-in-Cell (PIC) code [89] which, in addition to perform longitudinal and transverse tracking of particles considering the machine optics, is able to numerically compute the space charge effects in three dimensions. At each revolution turn, the PSB beam was sliced with two-dimensional grids perpendicular to the longitudinal axis, the transverse space charge forces were computed for each of them, and the beam transverse coordinates were updated. After these operations, before the starting of the next revolution turn, the longitudinal space charge induced voltage was computed in frequency domain using Eq.(4.9) and the energy coordinates of the particles were updated accordingly.

On the other hand, there are in BLonD possibilities to compute the longitudinal space-charge induced voltage either in frequency or time domain using respectively Eqs.(4.9) and (4.11). As we will see later, the second approach is generally used to reduce numerical noise. Therefore, in the following three benchmarks, the time domain computation has been chosen in the BLonD code.

#### Benchmark 1: PSB Injection Without Space Charge

Six rectangular particle distributions having different longitudinal emittances, uniform in time and water-bag in energy, were tracked for 10000 turns with acceleration, double RF system in bunch-lengthening mode ($V_{\mathrm{rf},1} = 8$ kV, $V_{\mathrm{rf},2} = 8$ kV) but without considering longitudinal space charge effects. Defining the bunching factor $B_{\mathrm{f}}$ as the ratio of the average and the peak line density

$$B_{\mathrm{f}} = \frac{\langle \lambda \rangle}{\hat{\lambda}}, \tag{4.24}$$

Fig.4.18 shows the evolution of $B_{\mathrm{f}}$ in the PyORBIT and BLonD codes. Since the transverse dynamics are not supposed to influence the longitudinal one, the expected agreement between the two codes was found.

#### Benchmark 2: PSB Parabolic Bunch at 160 MeV With Space Charge

The small-amplitude synchrotron frequency $f_{\mathrm{s0,ind}}$ of a parabolic bunch matched in a single RF bucket including space charge voltage below transition energy is given by [85]

$$f_{\mathrm{s0,ind}} = f_{\mathrm{s0}} \sqrt{1 - \frac{3qN_{\mathrm{b}}f_{\mathrm{rev},0}}{\pi^2 h V_{\mathrm{rf}}} \left( \frac{C_{\mathrm{ring}}}{\beta_0 c \tau_{\mathrm{l,eq}}} \right)^3 \left| \frac{Z}{n} \right|_{\mathrm{sc}}} \tag{4.25}$$

where $f_{\mathrm{s0}}$ is the synchrotron frequency without space charge effect and $\tau_{\mathrm{l,eq}}$ is the end-to-end bunch length of the parabolic bunch at equilibrium.

A parabolic bunch having $\tau_{l,0} = 148$ ns at 160 MeV in a single RF system with $V_{\mathrm{rf}} = 8$ kV was used as initial condition in the benchmark simulations. The

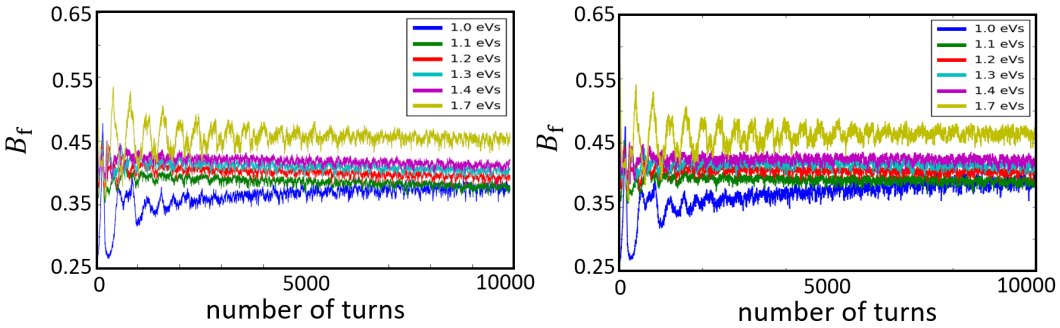


**Figure 4.18.** First benchmark between the PyORBIT (left) and BLonD (right) codes: evolution of the bunching factor $B_\mathrm{f}$ along the first 10000 turns at future PSB injection. Acceleration in a double RF system in bunch-lengthening mode ($V_{\mathrm{rf},1} = 8$ kV, $V_{\mathrm{rf},2} = 8$ kV). No space charge effects included. *PyORBIT simulations courtesy of V. Forte, CERN, 2015.*

longitudinal space charge impedance was assumed to be $|Z_\mathrm{sc}/n| = 796\,\Omega$. Notice that this impedance value has been computed using Eq.(4.12), with $a = 11$ mm (assuming $\sigma_{x,y} = 5.5$ mm) and $b = 30$ mm (roughly the lowest half-height of all the apertures). As previously discussed, these assumptions are not realistic, however they provided a quick estimation for code benchmarking purposes. The parabolic bunch was chosen to be in equilibrium only with the RF voltage, since the matching of the distribution with intensity effects could be dependent on the specific code. The particles were tracked for 10000 turns and afterwards the synchrotron frequency distribution was numerically calculated.

Figure 4.19 shows comparison of the synchrotron frequency distributions calculated by PyORBIT and BLonD for different bunch intensities. Since the parabolic bunch was not matched with intensity effects, emittance blow-up occurred for relatively high intensities and therefore the analytical value provided by Eq.(4.25), which assumes a parabolic bunch in equilibrium, was not valid anymore. However good agreement in results between the two codes was found for all the examined cases.

### Benchmark 3: Realistic PSB Distribution with Space Charge at 160 MeV

As a final benchmark, a realistic particle distribution in the PSB at 160 MeV, composed by micro-bunches coming from the future Linac4, has been tracked for 10000 turns considering acceleration and space charge effects. The uniform distribution in time was 474 ns long with $\delta_\mathrm{rms} = 1.36 \cdot 10^{-3}$ and the bunch intensity was $N_\mathrm{b} = 3{\cdot}10^{12}$ ppb. Double RF operation in bunch-lengthening mode ($V_{\mathrm{rf},1} = 8$ kV, $V_{\mathrm{rf},2} = 8$ kV) has been chosen, while $|Z/n|_\mathrm{sc} = 796\,\Omega$.

Figure 4.20 shows the normalized peak line density evolution from PyORBIT and BLonD simulations, with and without inclusion of space charge effect. For both codes the defocusing effect coming from space charge is visible (bunch lengthening) and good agreement was found.

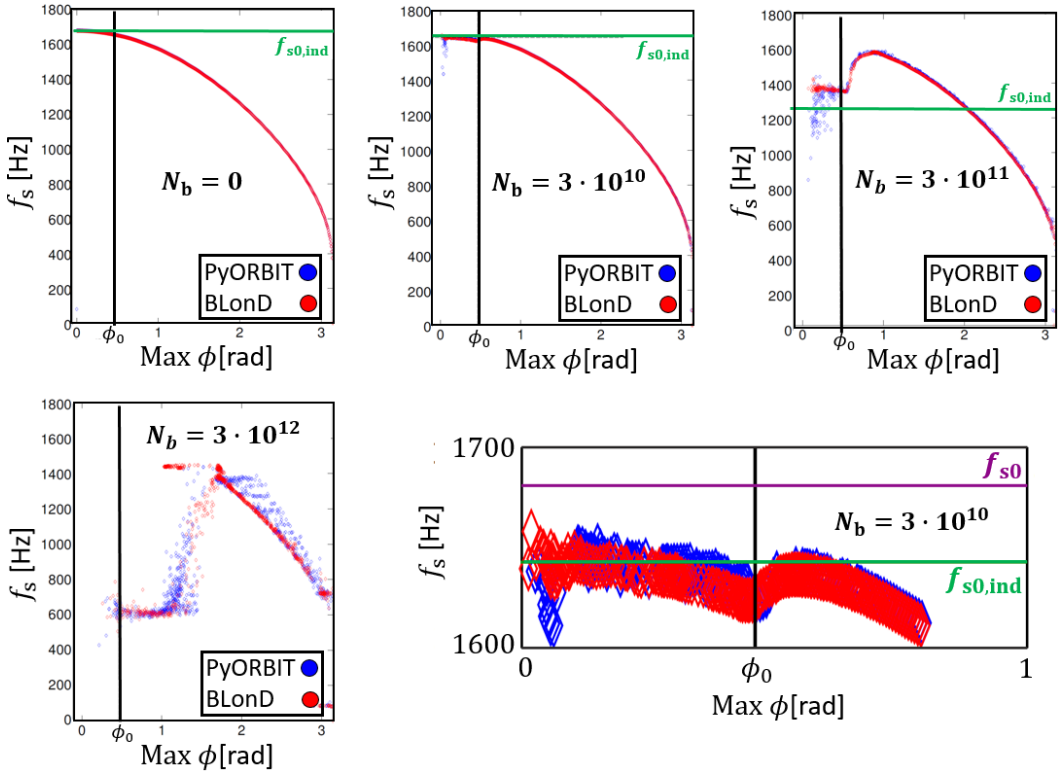


**Figure 4.19.** Second benchmark between the PyORBIT (blue) and BLonD (red) codes: synchrotron frequency distribution as a function of particle amplitude for different bunch intensities at 160 MeV. The distributions are computed after particle-tracking of 10000 turns, space charge effects are included. Initial conditions: parabolic bunch with end-to-end length $\phi_0$ matched with the RF voltage but not with space charge effects. The green horizontal line marks the small-amplitude synchrotron frequency with space charge effects, see Eq.4.25. The bottom-right plot is a zoom on the figure for $N_b = 3 \cdot 10^{10}$, the magenta line indicates the small-amplitude synchrotron frequency without space charge effects. *PyORBIT simulations courtesy of V. Forte, CERN, 2015.*

### 4.4.3 Space-charge Induced-voltage Computations in Time and Frequency Domain

As mentioned before, the longitudinal space charge induced voltage can be computed either in frequency or time domain using Eqs.(4.9) and (4.11) respectively. These two mathematically equivalent methods can provide different results when numerical simulations are involved. Moreover, in the just described three benchmarks no importance has been given to the numerical method used to compute the derivative of the line density in the BLonD code. The first-order difference scheme [90] has been used in all the three cases.

In this Subsection we consider again the simulation parameters utilized in the third benchmark and compare four methods to compute $V_{sc}$, three in time and one in frequency domain. In time domain, the derivative of the line density is computed through the first-order difference scheme, then with the second-order gradient algorithm [90], and finally using the Savitzky-Golay derivative smoothing filter of fourth order. The choice of this filter for derivative computation is motivated

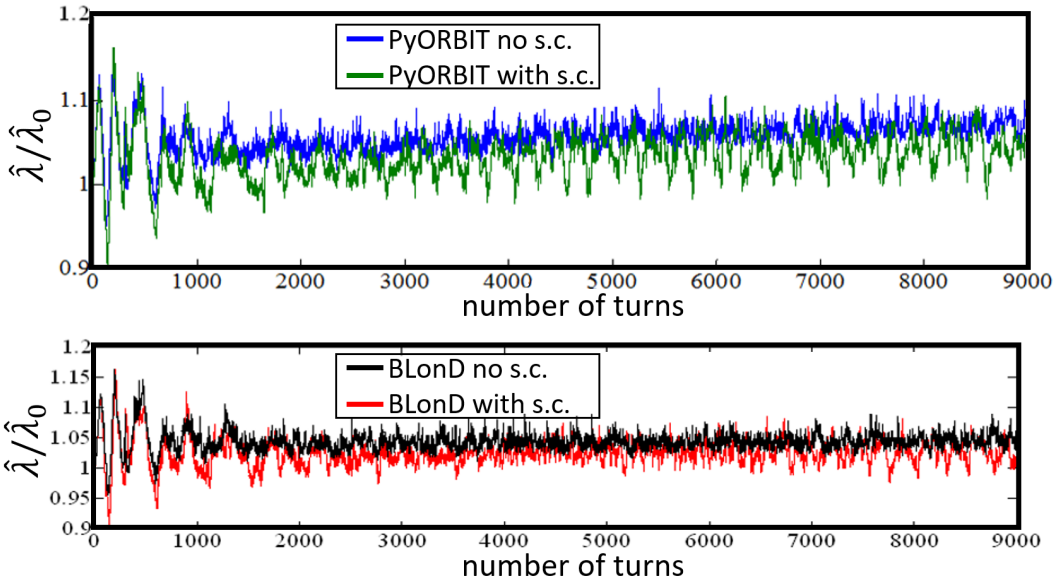


**Figure 4.20.** Third benchmark between the PyORBIT (top) and BLonD (bottom) codes: peak line density normalized to the initial one as a function of the number of revolution turns in the PSB, with and without consideration of space charge effects. Initial conditions: rectangular distribution at 160 MeV, acceleration in a double RF system in bunch lengthening mode ($V_{\mathrm{rf},1} = 8$ kV, $V_{\mathrm{rf},2} = 8$ kV). *PyORBIT simulations courtesy of V. Forte, CERN, 2015.*

by the fact that this method has been used for years in the PSB operation to smooth measured longitudinal bunch profiles and their derivatives in order to reconstruct the phase space distribution through tomography taking into account space charge effects (see Section 4.2).

The comparison of the several approaches to compute $V_{\mathrm{sc}}$ is performed for two reasons. The first is to prove consistency of the four methods and reliability of the results obtained in the third benchmark, which describes a case close to the expected PSB scenario after LIU upgrade. The second is to estimate the sensitivity of the different methods to numerical noise introduced in the bunch profile increasing the number of slices while keeping the amount of macro-particles unvaried. Indeed, after having obtained an accurate estimation for $|Z_{\mathrm{sc}}/n|$, the next goal is to identify a sufficiently reliable numerical method to compute the longitudinal space charge induced voltage.

Figure 4.21 shows the comparison results, taking as parameters of interest the percentage of lost particles, the bunching factor and the longitudinal emittance as a function of the number of revolution turns. If 300 slices are used, the four chosen methods for induced voltage computation provide roughly the same outputs if $N_{\mathrm{M}} = 5 \cdot 10^5$ (colors black, red, blue and green in Fig.4.21, left): there are no losses in all the cases, the bunching-factor curves converge on average towards the same value and the emittance curves are almost superimposed. This proves consistency of the four methods when $N_{\mathrm{S}} = 300$ and $N_{\mathrm{M}} = 5 \cdot 10^5$ (numerical parameters used in the third benchmark). Increasing the number of macro-particles to $N_{\mathrm{M}} = 5 \cdot 10^6$, no visible difference appears (colors magenta and yellow in Fig.4.21, left). This suggests

that the results obtained using $N_S = 300$ and $N_M = 5 \cdot 10^5$ are also reliable. Notice that the fourth order Savitzky-Golay filter is applied choosing the lowest value of 5 for the number of window points. The aim is to avoid unnecessary smoothing which could suppress important physical information while at the same time exploiting the smoothing to counteract possible sources of noise.

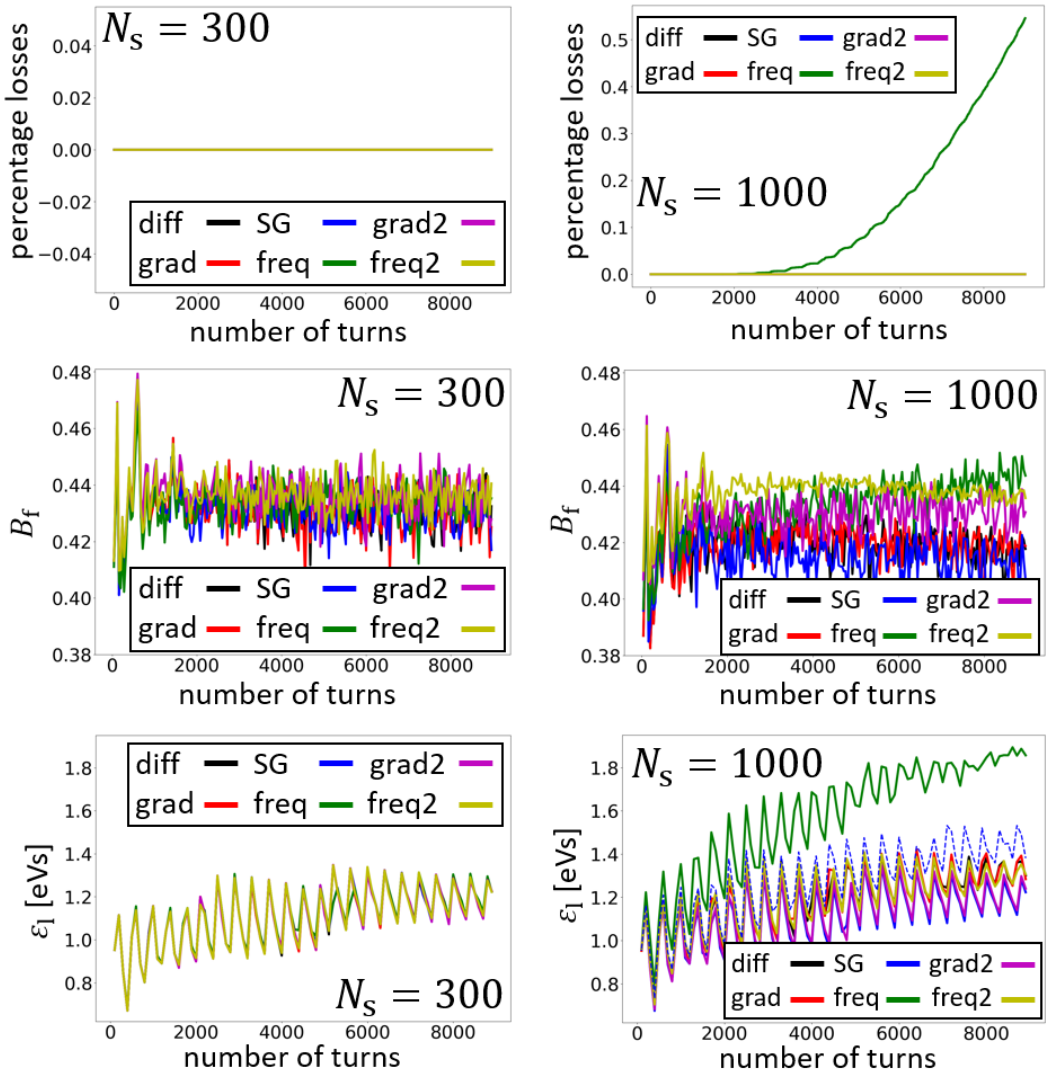


**Figure 4.21.** Percentage of losses (top), bunching factor (middle) and longitudinal emittance (bottom) as a function of the number of revolution turns using the same simulation parameters chosen in the third benchmark between the PyORBIT and BLonD codes, see Fig.4.20. The number of slices per bucket is 300 (left) or 1000 (right). Results obtained using four methods for space charge induced voltage calculation: first-order difference scheme (black), second-order gradient method (red), Savitzky-Golay derivative smoothing filter of fourth order with 5 or 17 window points (blue, see the text for details) and frequency domain approach (green). The magenta and yellow curves refer respectively to the gradient and frequency methods when the number of macro-particles is $N_M = 5 \cdot 10^6$, all the other curves assume $N_M = 5 \cdot 10^5$.

Increasing the number of slices from $N_S = 300$ to $N_S = 1000$ while keeping

$N_M = 5 \cdot 10^5$ fixed (colors black, red, blue and green in Fig.4.21, right), numerical noise is introduced. Adopting the results obtained using $N_S = 300$ as a reference, the frequency domain approach gives the worst result: losses of 0.5 %, increasing of bunching factor and significant emittance blow-up at the end of the simulation. This could be explained by the fact that with 1000 slices the numerical noise is amplified in frequency domain by the multiplication of a linear increase of space charge impedance with frequency. The best result comes from the use of the fourth order Savitzky-Golay filter, after having rescaled the number of window points from 5 to 17 in order to preserve the length of the window on which the filter acts ($N_S$ increases by slightly more than a factor of 3): zero losses are obtained and the correct emittance curve is reproduced, even if there is a visible decrease in bunching factor. Finally the difference and gradient schemes provide zero losses and relatively low emittance blow-up, while the decrease in bunching factor is comparable to the one obtained with the Savitzky-Golay filter. Notice that the proper choice of the number of window points for the filter is important: varying it for example from 17 to 5, the noise introduced by choosing $N_S = 1000$ is not smoothed anymore and a considerable emittance blow-up occurs (see the dashed line in the bottom-right plot of Fig.4.21).

Increasing the number of macro-particles by a factor of 10 when $N_S = 1000$ (colors magenta and yellow in Fig.4.21, right), the frequency and gradient methods provide results respectively close and in total accordance with what found previously using $N_S = 300$, see Fig.4.21. The difference and Savitzky-Golay approaches recover the correct solution as well. This suggests the rescaling

$$N_S \propto \sqrt{N_M} \tag{4.26}$$

for the selection of the histogram parameters in order to preserve the correctness of the obtained results. Notice that several studies on how to choose $N_S$ and $N_M$ when dealing with longitudinal space charge induced voltage computations have been done in the past [91, 92, 93]. Instead of Eq.(4.26), these studies recommend the rescaling

$$N_S \propto \sqrt[3]{N_M}, \tag{4.27}$$

for both time and frequency domain calculations, in order to preserve the rms error of the induced voltage gained per turn by a particle in a generic bin.

To summarize, the comparison in Fig.4.21 shows that the frequency domain approach is the most sensitive to noise, therefore its use cannot be suggested. The Savitzky-Golay filter provides the best result, however the success of this method strongly depends on the proper choice of the number of window points. In order to avoid any risk in under or over-smoothing the bunch profile in the complex and varied realistic beam dynamics simulations performed in this thesis, the Savitzky-Golay approach has been neglected as well. Finally the gradient and difference schemes show a similar sensitivity to noise when $N_S = 1000$ and the correct result is recovered after a proper increase of the number of macro-particles. Taking into account the order of these two methods, the gradient scheme has been generally preferred in this thesis for longitudinal space charge induced voltage computations.

Note that the use of filters to smooth the bunch profiles in simulations has not been considered in the present work: a dedicated study is needed since filters, if

not properly used, can suppress physical information, fail to counteract numerical noise or even enhance it (see the Savitzky-Golay example just discussed). As an alternative, control of numerical noise and consequent validation of simulation results have been achieved in this thesis through numerical convergence studies: keeping fixed the amount of bins (usually determined by physics reasonings), the number of macro-particles has been increased by steps until agreement in results was found.

## 4.5 Longitudinal Impedance Model After the PSB Upgrade

### 4.5.1 PSB Impedance Model

#### Finemet® Cavities

As described in the introduction of this Chapter, after LIU upgrade the PSB beam will be accelerated by Finemet® loaded cavities with broad-band impedance. In each of the four PSB rings there will be 36 Finemet® gaps able to provide a total RF voltage of 24 kV.

The Finemet® system can be operated in one of the following four configurations:

- Short-circuited: the cavities are installed in the ring but are short-circuited by gap relays. This mode of operation is usually adopted when the cavities are temporarily unused. The beam still sees some residual impedance, mostly at high frequencies.
- Open-loop: the RF gaps act without cavity feedback reducing their impedances.
- Closed-loop (power amplifier feedback): the RF gaps act with a fast RF feedback loop for beam loading compensation. This feedback is implemented in the power amplifier and is able to reduce the open-loop gap impedance by 10 amplitude-ratio dB [63].
- Closed-loop (power amplifier and Low Level RF feedbacks): in addition to the just mentioned fast RF feedback, the Finemet® gaps benefit from a wake-voltage cancellation feedback implemented in the Low Level RF electronics and able to lower the impedance at some given number of harmonics of revolution frequency by an average factor of 36 dB [94].

Figure 4.22 shows the longitudinal impedances related to the first three listed configurations for 36 Finemet® gaps. These impedances, which do not depend on the beam energy, have been both measured and numerically calculated [62]. Notice that the impedance for short-circuited gaps is significant only at relatively high frequencies compared to the beam revolution frequency after upgrade, which will range from 1 MHz to 1.8 MHz. Notice also that, in this same frequency range, the gap impedance for the closed-loop configuration with power-amplifier feedback is flat with negligible imaginary part.

Concerning the fourth listed configuration of the Finemet® RF system, impedance reduction at frequencies $hf_{\mathrm{rev},0}$ ($h = 1, \ldots, 8$) has been included in BLonD simulations taking into account the measured gain of the transfer function of the LLRF

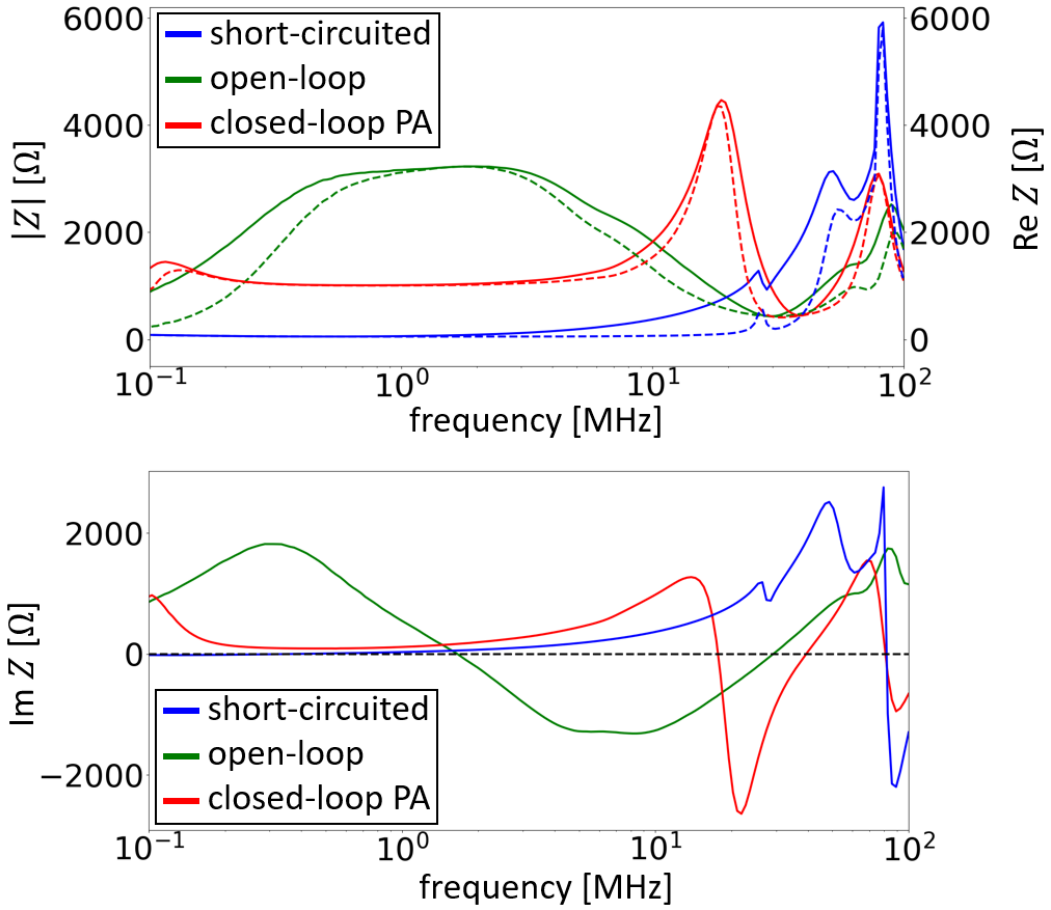


**Figure 4.22.** Impedance of 36 Finemet® RF gaps versus frequency: absolute value and real part (top, continuous and dashed lines respectively), imaginary part (bottom). Three different configurations for the cavities are shown: short-circuited (blue), open-loop (no feedback for impedance reduction, green) and closed-loop with power-amplifier fast RF feedback (open-loop impedance reduced by 10 dB at 1 MHz, red). The shown impedances do not depend on the beam energy. *Courtesy of M. Paoluzzi, CERN, 2015.*

wake-voltage cancellation feedback, as Fig.4.23 shows. Resonator impedances with parameters

$$f_{\mathrm{r}} = h f_{\mathrm{rev},0}, \quad R_{\mathrm{sh}} \approx \mathrm{Re}Z|_{f=f_{\mathrm{r}}}, \quad Q_r = f_{\mathrm{r}}/B_{\mathrm{w}}, \tag{4.28}$$

where $B_{\mathrm{w}}$ is the resonator bandwidth at -3 dB [95], have been subtracted from the impedance $Z$ in closed-loop configuration where only the power-amplifier feedback is active. The expression for the resonant frequency in Eq.(4.28) is due to the fact that the resonator has to be centered where the maximum impedance reduction occurs. Since the Finemet® impedance is in good approximation resistive, the value of $Z$ in $f_{\mathrm{r}}$ can be reduced to the desired value imposing $R_{\mathrm{sh}} \approx \mathrm{Re}Z|_{f=f_{\mathrm{r}}}$. Finally every subtracted resonator, independently of its resonant frequency, should have a bandwidth of 16 kHz at -3 dB, as measurements indicate. Therefore the quality factor should be set as specified in Eq.(4.28), where $B_{\mathrm{w}} = 16$ kHz.

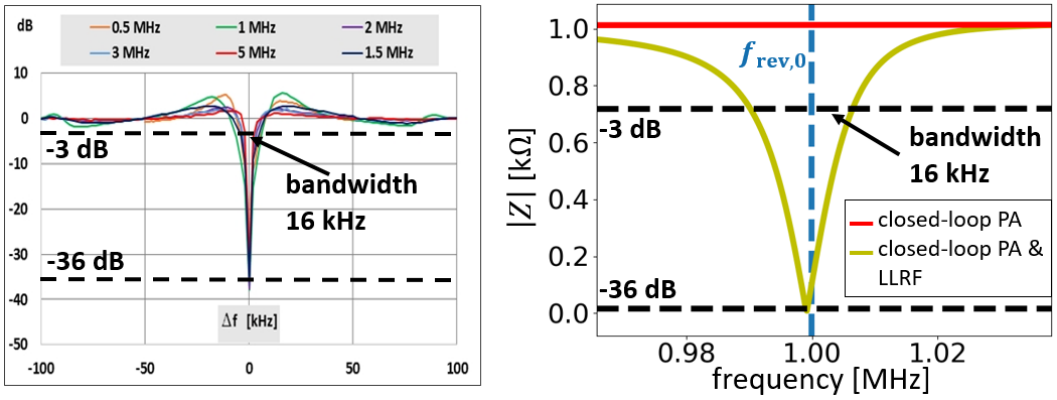


**Figure 4.23.** Left: measured gain of the transfer function of the Low Level RF feedback for Finemet®-wake reduction at different revolution frequencies. The average bandwidth at -3 dB is 16 kHz, the average gain is -36 dB. *Courtesy of M. Paoluzzi, CERN, 2015.* Right: example of Finemet® impedance reduction in simulations taking into account the measured gain of the transfer function shown on the left figure. Starting from the impedance $Z$ where only the power-amplifier feedback is active (red), the reduced impedance (yellow) is obtained subtracting a resonator with parameters $f_{\rm r} = f_{\rm rev,0} =$ 1000 kHz, $R_{\rm sh} = {\rm Re}Z|_{f=f_{\rm r}} = 1$ kΩ and $Q_r = f_{\rm rev,0}/B_{\rm w} = 62.5$, where $B_{\rm w} = 16$ kHz is the resonator bandwidth at -3 dB.

### Other impedances

In addition to the impedance of the Finemet® cavities, the other sources of impedance that have been taken into account in simulations are [96, 97]

- one extraction kicker
- extraction kicker cables
- KSW magnets to perform transverse painting at injection [72]
- resistive wall
- beam-pipe step-transitions

The impedances coming from the extraction kicker and resistive wall depend on the beam energy while the impedances of the cables and KSW magnets do not. The real and imaginary parts of these four impedances are shown in Fig.4.24. Notice that the model of the extraction kicker has been recently improved [98], however it has been proved in simulations that the updated impedance does not influence the longitudinal beam dynamics [99].

The last impedance in the previous list is purely imaginary, broad band and has a defocusing effect on the bunch [96], as the space charge impedance discussed above. Its value is

$$\frac{|Z_{\rm st}|}{f} = 34.67 \frac{\Omega}{\rm GHz}. \tag{4.29}$$

Figure 4.25 shows that this impedance is negligible in comparison with the space charge one.

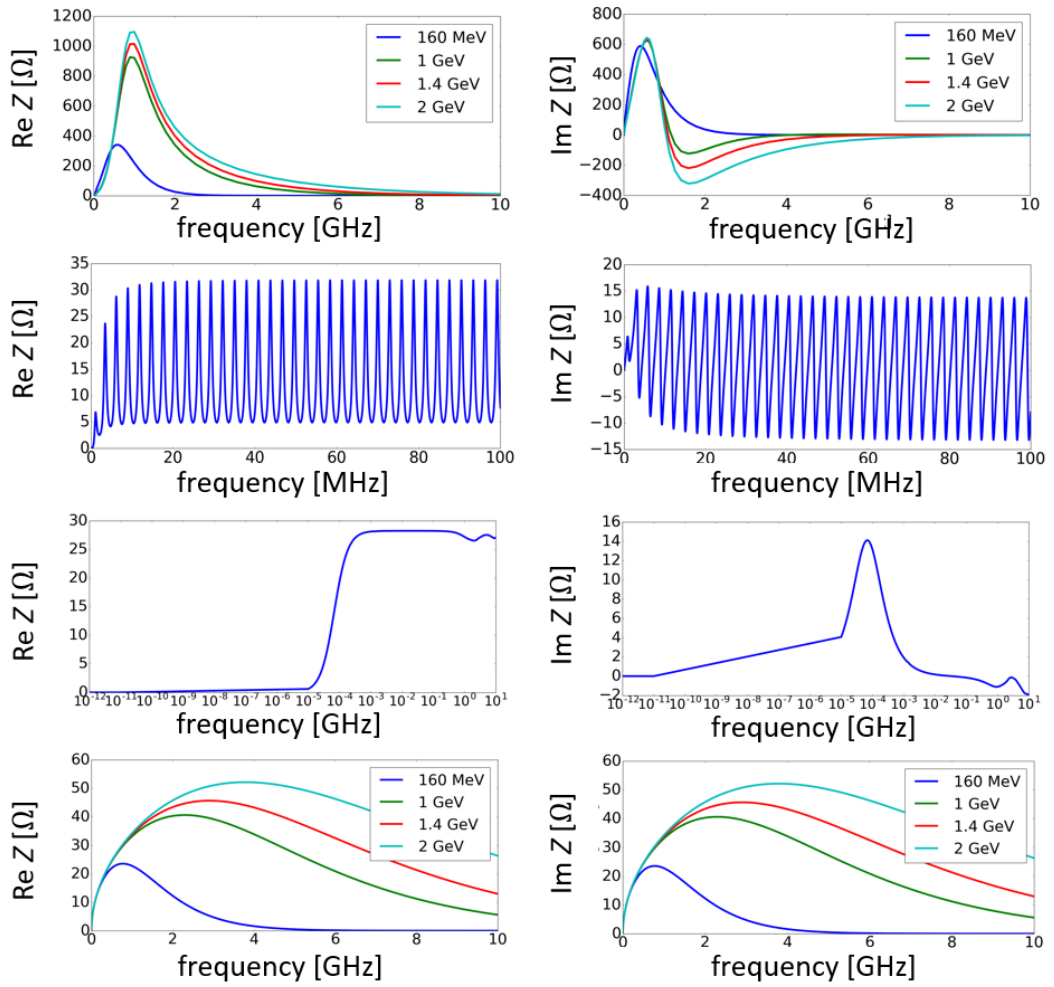


**Figure 4.24.** From top to bottom, real-part (left) and imaginary-part (right) impedance coming from the PSB extraction kicker, its cables, magnets to perform transverse painting at 160 MeV and resistive wall. Only the contributions from the extraction kicker and resistive wall depend on the beam energy. *Courtesy of C. Zannini, CERN, 2015.*

Figure 4.26 (left) compares the absolute value of the different impedance contributions at 160 MeV and 2 GeV kinetic energy. One can see that the Finemet® closed-loop impedance reduction is important since the lowered impedance is comparable to the other contributions at the affected harmonics of the revolution frequency. Figure 4.26 (right) shows the absolute value of the sum of the several impedances. Notice that the Finemet® contribution largely dominates all the other components.

Finally Fig.4.27 shows a bunch profile (left) for nominal LHC beam after-upgrade at 160 MeV, together with its spectrum (right). The longitudinal emittance is $\epsilon_l = 1.4$ eVs and $V_{\mathrm{rf},1} = 8$ kV, $V_{\mathrm{rf},2} = 8$ kV with relative phase in bunch lengthening mode (see later).

As expected, the induced voltage generated by space charge (red) follows the derivative of the line density, see Eq.(4.11).

The induced voltage generated by the sum of all the other impedances, considering

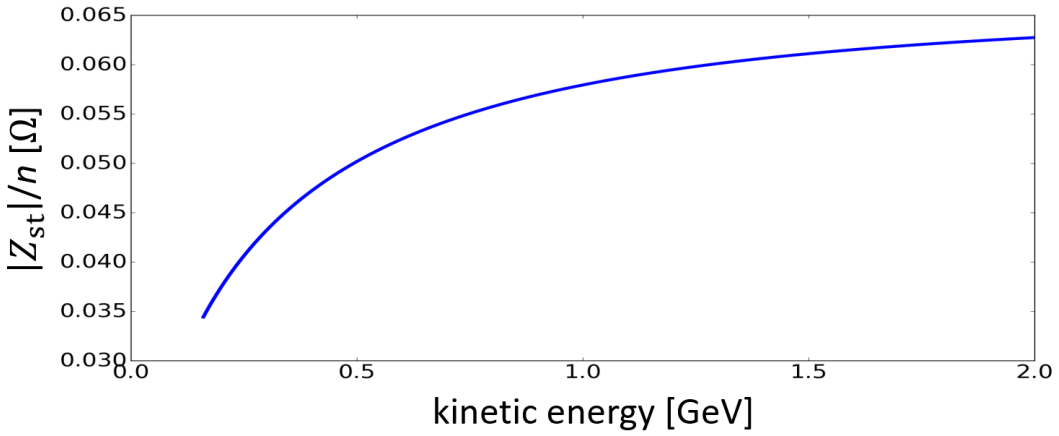


**Figure 4.25.** Variation of the beam-pipe step-transition impedance $|Z_{st}|/n$ as a function of kinetic energy from 160 MeV to 2 GeV in the PSB.

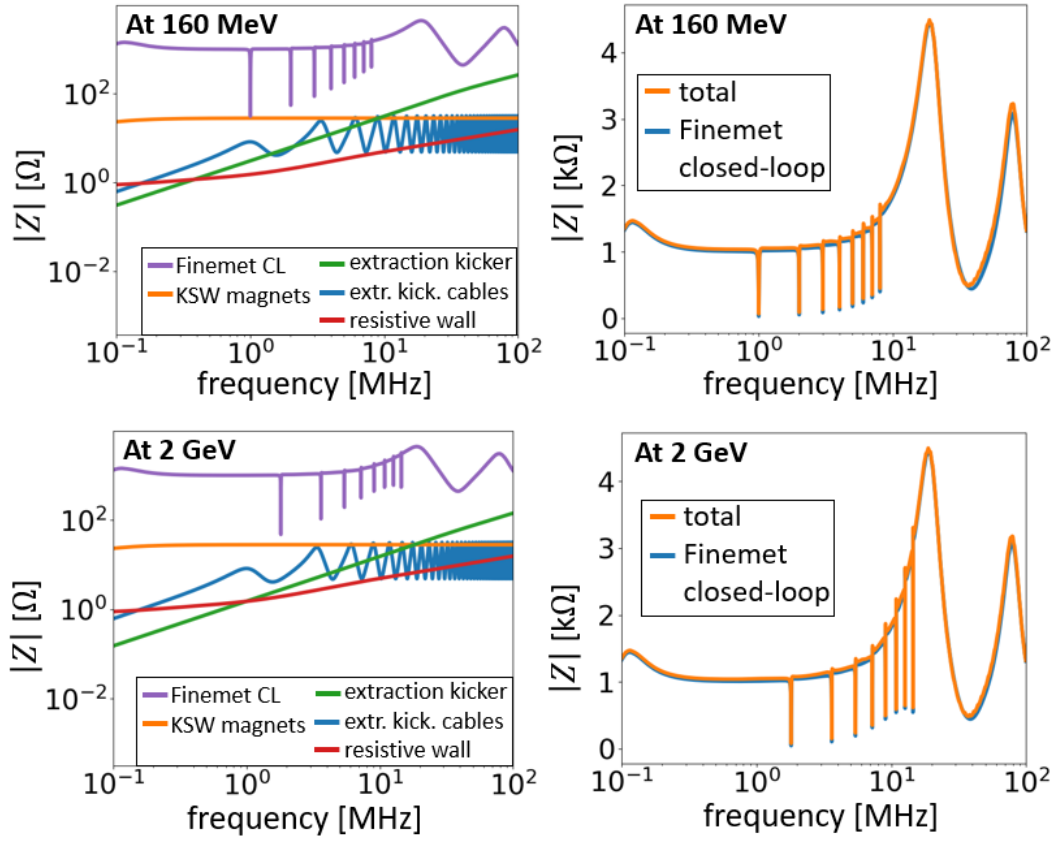


**Figure 4.26.** Absolute value of impedance for different sources (left) and absolute value of the sum of all the five contributions (right) at 160 MeV (top) and 2 GeV (bottom) in the PSB. The different impedance sources are: Finemet® RF cavities with closed-loop configuration (purple), KSW kicker magnets (orange), extraction kicker (green) and its cables (blue), resistive wall (red).

36 Finemet® gaps without LLRF impedance reduction, provides a voltage (magenta) which follows the shape of the line density. This can be explained considering that the Finemet® impedance without LLRF feedback is broad-band and resistive where the beam spectrum is located. Therefore

$$V_{\mathrm{ind}}(t) = \frac{e}{2\pi}\int_{-\infty}^{+\infty} d\omega\, Z(\omega)\, S(\omega)\, e^{i\omega t} \approx \frac{e\,\mathrm{Re}Z}{2\pi}\int_{-\infty}^{+\infty} d\omega\; S(\omega)\, e^{i\omega t} = e\,\mathrm{Re}Z\,\lambda(t). \tag{4.30}$$

However this resistive voltage does not decay in one revolution turn, helped by the fact that the PSB has $h = 1$ with bunches almost covering the full ring. Summing turn-by-turn the contributions coming from the previous revolution turns (see next Subsection), the accumulated induced voltage reaches an equilibrium if the bunch is stable. The magenta line in Fig.(4.27) represents the resistive voltage at equilibrium for a bunch matched inside the RF bucket with intensity effects.

Finally notice that, if space charge is neglected, the Low Level RF feedback for wake-voltage cancellation reduces drastically the induced voltage generated by the sum of all the impedances (black line). The reduction is so significant that, at low PSB energies, the total induced voltage (green line) coincides effectively with the space charge one.

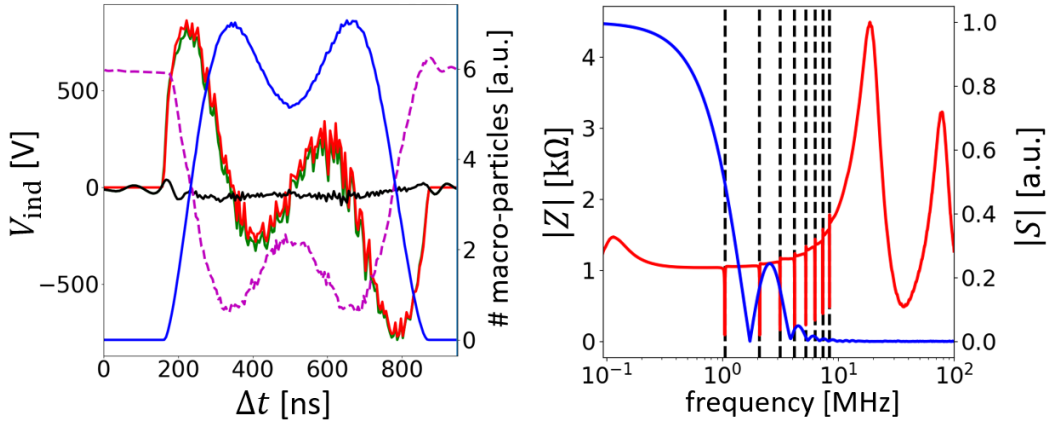


**Figure 4.27.** Left: bunch profile (blue) with $\epsilon_{\mathrm{l}} = 1.4$ eVs and $N_{\mathrm{b}} = 3.42 \cdot 10^{12}$ ppb at 160 MeV in a double RF system ($V_{\mathrm{rf},1} = 8$ kV, $V_{\mathrm{rf},2} = 8$ kV in bunch-lengthening mode). The time axis covers one revolution turn. The total induced voltage (green) generated by the bunch is the sum of the space charge contribution (red) and all the other impedance sources (black) described in Fig.(4.26) (left). If no Low Level RF feedback for wake-voltage cancellation is included, the black curve changes in the magenta-dashed line. The bunch is at equilibrium inside the RF bucket. Right: absolute value of the sum of all the considered impedances without space charge (red) and absolute value of the beam spectrum corresponding to the line density on the left image. The eight dashed vertical lines mark $hf_{\mathrm{rev},0}$, $h = 1, \ldots, 8$.

### 4.5.2 Multi-turn Wake

As was mentioned already in Chapter 3, in BLonD the multi-turn induced voltage is computed summing, at each revolution turn, the contribution coming from the past to the current one. In the presence of acceleration, an interpolation is needed

when these two contributions are summed together, independently on which time step $\Delta$ is chosen at each turn. This interpolation, together with the potentially high number of revolution periods to be considered in memory in order to see the induced voltage decay to zero and become negligible, can lead to relatively large computational costs.

The space-charge induced-voltage, calculated using Eq.(4.11), is not multi-turn. The one derived from other impedance sources can be calculated numerically in frequency domain through Eq.(3.4), where the discrete Fourier transform and its inverse suppose that the signal is periodic in time, with $f_{\max} = 1/(2\Delta)$ the maximum frequency that one is interested in and $\Delta$ the sample time interval.

In the case without acceleration and with stationary line density, one can consider the bunch profile as being periodic on the ring if there is no necessity to accurately resolve narrow-band parts of the impedance model. The period would be $T_0$ and consequently only the points corresponding to $f_{\mathrm{rev},0}$ and its multiples would be considered for calculation of induced voltage when the spectrum is multiplied by the impedance in Eq.(3.4).

In the PSB it is fundamental to consider an extended period for the bunch because the revolution period approximately halves from injection to extraction, the line density varies considerably along the ramp due to RF manipulations and high resolution in frequency domain is needed for example to accurately resolve the notches coming from the Finemet®-cavity LLRF feedback. This leads to the required resolution of the impedance curve in frequency domain.

Taking as an example the impedance model in Fig.(4.27) (right), assuming a period $T_0$ in PSB simulations implies that only the minima of the notches at frequencies $hf_{\mathrm{rev},0}$ are considered, obtaining a reduction of the impedance without feedback by -36 dB at all frequencies. This optimistic assumption is not realistic, since the particle synchrotron motion implies that the frequencies $hf_{\mathrm{rev},0} + pf_{\mathrm{s}0}$ have also to be taken into account in calculations (being $p$ an integer). Therefore the structure of the notches, for example their bandwidths of 16 kHz at -3 dB, is important and therefore it has to be properly resolved in frequency domain.

Let us examine again the case shown in Fig.(4.27) (left), where this time only the Finemet® induced voltage with wake-cancellation feedback is considered. As before, we assume for simplicity of explanation that the bunch is matched with intensity effects to the RF bucket and that the multi-turn induced voltage is at equilibrium. However the principle here described can also apply to general cases in simulations. Figure 4.28 (left) shows that the bunch generates a multi-turn induced voltage lasting at least 100 revolution turns. Figure 4.28 (right) shows that the multi-turn voltage in $T_0^{(1)}$ generated by the bunch profile in $T_0^{(0)}$ is such to almost compensate the current induced voltage (magenta) which assumes a sufficiently large period $T_0$ in the Fourier calculation or, equivalently, that the beam passes only once throughout the cavities. Therefore, the effective induced voltage seen by the beam at a given turn is the sum of these two contributions (see the green curve in $T_0^{(0)}$). As expected, the current induced-voltage assuming infinite period (magenta) is resistive where the bunch profile is located, since the Finemet® impedance without LLRF feedback is resistive and the effect of the notches can be seen only after the induced voltage reaches an equilibrium.

The PSB simulations performed for the after-LIU studies presented in this thesis assume a fixed multi-turn-wake period of $t_{\max} = 700\,T_0$, where $T_0$ is the revolution period at 160 MeV. This corresponds to a frequency-resolution of $\Delta f = 1.43$ kHz, which is sufficient to resolve the notches with bandwidth of 16 kHz at -3 dB shown in Fig.4.27 (right). Notice that, due to the fixed $\Delta f$, the depths of the notches in a given simulation can change together with $f_{\mathrm{rev},0}$, and therefore they can be different from the desired average value of -63 dB determined in measurements. However this variability is not more significant than the one found in measurements, where the gain bandwidth at -3 dB and depth at -36 dB change with $f_{\mathrm{rev},0}$ (Fig.4.23, left).

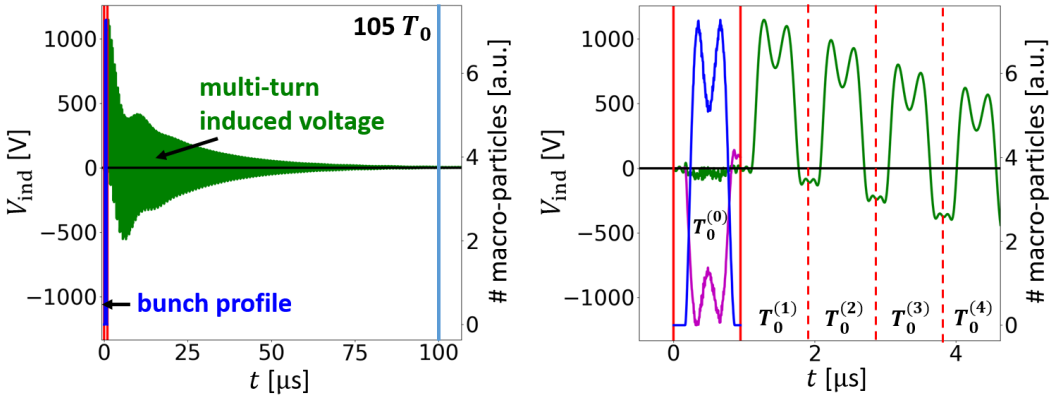


**Figure 4.28.** Left: multi-turn induced voltage (green) generated in simulation by the bunch profile in Fig.(4.27 (left) taking into account only the Finemet® contribution with wake-cancellation feedback. The bunch is matched with collective inside the RF bucket effects and the induced voltage, decaying after roughly 105 revolution periods, is at equilibrium. Right: zoom onto the bunch profile shown on the left. The red vertical lines mark the different revolution periods. The magenta curve indicates the current resistive induced voltage seen by the beam in one given revolution turn assuming that the beam passes only once through the cavities (sufficiently large period $T_0$ in the Fourier calculation).

## 4.6 Double RF Operation with Intensity Effects

In the current PSB operation with nominal-LHC and high-intensity beams, the voltage of the second RF system ($h = 2$) is currently added to the accelerating voltage in bunch lengthening mode for most of the acceleration cycle (usually $V_{\mathrm{rf},1} = 8$ kV and $V_{\mathrm{rf},2} = rV_{\mathrm{rf},1}$, $r \in [0.5, 1]$). Bunch lengthening mode is used to reduce the longitudinal peak line density and consequently the transverse space charge tune spread. Figure 4.27 (left) shows an example of bunch profile obtained in simulation where the two RF systems are in bunch lengthening mode, with a relative phase calibrated in such a way that the two peaks of the bunch profile have the same height.

It is expected that there will be double RF operation in bunch lengthening mode also after upgrade [88]. Therefore it is essential to determine the desired relative phase $\phi_{1,2}$ between the two RF systems for given $V_{\mathrm{rf},1}$ and $V_{\mathrm{rf},2}$. We will see that $\phi_{1,2}$ depends also on the synchronous phase shift caused by acceleration and the

resistive part of the induced voltage.

Considering Eq.(2.50), the total voltage seen by the PSB beam is

$$V_{\mathrm{tot}}(\Delta t) = V_{\mathrm{rf},1}\sin(\omega_{\mathrm{rf},1}\Delta t + \pi) + rV_{\mathrm{rf},1}\sin(2\omega_{\mathrm{rf},1}\Delta t + \phi_{1,2}) - V_{\mathrm{rf},1}\sin(\phi_{\mathrm{s}}) - V_{\mathrm{ind}}(\Delta t), \tag{4.31}$$

where $\Delta t \in [0, T_0]$.

Without acceleration and intensity effects $\phi_{1,2} = -\pi$ is the solution, independently of the value of $r \in [0.5, 1]$. The problem of determining $\phi_{1,2}$ becomes difficult when acceleration and collective effects are present. For this reason an algorithm to numerically determine $\phi_{1,2}$ has been developed in the BLonD code.

The idea of the algorithm is to integrate the total voltage $V_{\mathrm{tot}}$ to obtain the total potential $U_{\mathrm{tot}}$ and then determine $\phi_{1,2}$ through an iterative procedure in such a way that $U_{\mathrm{tot}}$ has two minima with the same depth, see Fig.4.29 (right). This procedure has to be done turn by turn while tracking since the impact of intensity effects are not foreseen at the beginning of a simulation: the phase computed at a given turn is used as initial condition to determine the phase at the consecutive turn. If the minima of $U_{\mathrm{tot}}$ have the same depth, then the two peaks in the bunch profile have the same height (Fig.4.29, right). On the contrary, choosing a wrong phase is equivalent to have a potential well with two not-aligned minima, see Fig.4.29 (left and middle), where $\phi_{1,2}$ is determined neglecting acceleration and collective effects ($\phi_{1,2} = -\pi$ rad, left) or just intensity effects (middle).

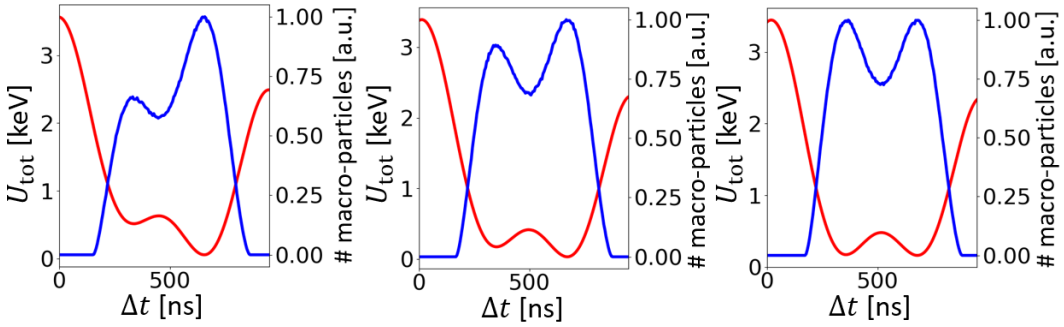


**Figure 4.29.** Bunch profile (blue) with $\epsilon_{\mathrm{l}} = 1.4$ eVs and $N_{\mathrm{b}} = 3.42 \cdot 10^{12}$ ppb at 160 MeV matched in a double RF bucket with intensity effects. The voltages are $V_{\mathrm{rf},1} = 8$ kV and $V_{\mathrm{rf},2} = 8$ kV, while the relative phase between the two RF systems is $\phi_{1,2} = -\pi$ rad (left), $\phi_{1,2} = -3.46$ rad (middle) and $\phi_{1,2} = -3.59$ rad (right). The corresponding total potentials are in red. Space charge and all the impedance sources shown in Fig.(4.26) (left) are included in simulations, however the Finemet® impedance is considered without the action of the LLRF feedback.

Figure 4.30 (left) shows examples of numerically calculated $\phi_{1,2}$ for BLM operation after LIU upgrade in the cycle-time interval C300–C350. One can see that, neglecting collective effects but including acceleration (green), $\phi_{1,2}$ is significantly different from the solution $\phi_{1,2} = -\pi$ valid for the case without acceleration. Adding collective effects and in particular the impedance of 36 Finemet® gaps without LLRF impedance reduction, $\phi_{1,2}$ reaches its minimum values (blue). Taking into account the Finemet® LLRF feedback, the obtained $\phi_{1,2}$ (red) lies in between the other two curves, closer to the green one.

The qualitative behavior of these three curves can be explained examining Fig.4.30 (right), where the average position of the bunch profile is shown as a function of the cycle time. One can notice that higher values for the synchronous phase shift, due only to acceleration (green) or also to collective effects (red and blue), correspond to lower values for $\phi_{1,2}$. Indeed, for a given $\phi_{1,2}$, larger synchronous phase shifts make the right peak in the bunch rise relative to the left one, therefore lower values for $\phi_{1,2}$ are needed in order to realign the two peaks, see Fig.4.29. Finally, as mentioned above, the LLRF wake-cancellation feedback drastically reduces the Finemet® impedance which is in good approximation resistive and dominates the PSB impedance model: this explains why the red curves are relatively close to the green ones in Fig.4.30.

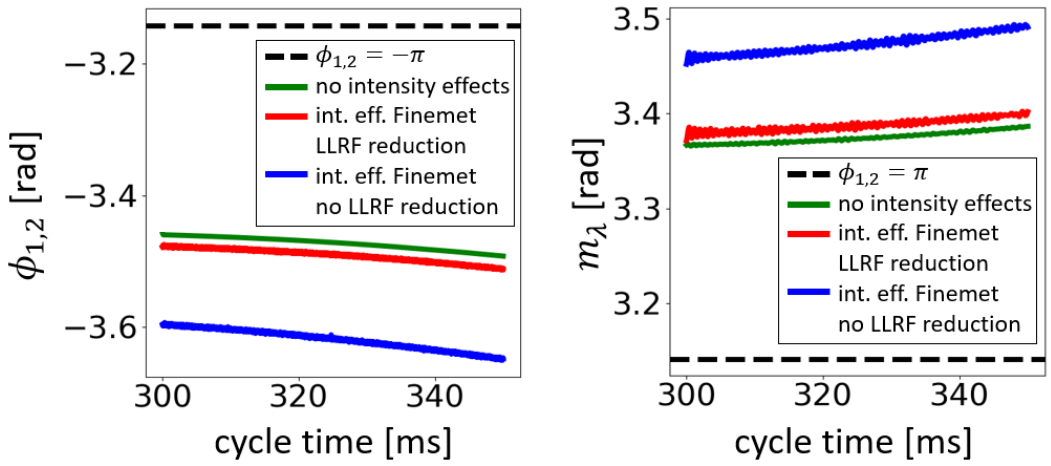


**Figure 4.30.** Left: calculated relative phase between the $h = 1$ and $h = 2$ PSB RF systems for bunch-lengthening mode as a function of the cycle time between C300 ($E_{\mathrm{kin}} = 187$ MeV) and C350 ($E_{\mathrm{kin}} = 247$ MeV). The voltages are constant and equal to $V_{\mathrm{rf},1} = 8$ kV and $V_{\mathrm{rf},2} = 8$ kV, the bunch emittance is $\epsilon_{\mathrm{l}} = 1.4$ eVs. Neglecting collective effects, the green line is obtained. Including space charge and the full PSB impedance model with $N_{\mathrm{b}} = 3.42 \cdot 10^{12}$ ppb, the red and blue curves are obtained, which assume respectively 36 Finemet® gaps with and without impedance reduction by the LLRF feedback. Right: average position of the bunch profile as a function of the cycle time considering the same parameters and configurations described for the left image.

In operation, the programmed relative phase $\phi_{1,2}$ does not correspond to the phase of the two RF systems. This discrepancy, due mostly to cable delays and the different positions of the RF cavities along the ring, is also sensitive to hardware and LLRF settings, beam intensity and which of the four PSB rings is used. A manual calibration of $\phi_{1,2}$ is therefore needed: the phase has to be empirically determined using beam measurements at different times of the acceleration cycle and then a linear interpolation is performed for intermediate intervals. Being unknown the relationship between the programmed and actual relative phase, it is currently not possible to compare simulation results similar to those shown in Fig.4.30 (left) with measurements.

## 4.7 Simulation Results for the After-upgrade Scenario

All the studies presented here assume the full PSB impedance model discussed in the previous Sections. Closed-loop operation of the Finemet® gaps with impedance reduction through the LLRF feedback is considered in simulations. Unless otherwise specified, the first eight harmonics of the revolution frequency are affected by the feedback, being this the baseline for the after-upgrade scenario [100].

Two types of beam were examined, both with kinetic energy of 2 GeV at PSB extraction. The first, which has already been described above, is the nominal-LHC beam with $N_\mathrm{b} = 3.42 \cdot 10^{12}$ ppb and $\epsilon_\mathrm{l} = 1.4$ eVs at injection energy. The second is the expected high-intensity beam with $N_\mathrm{b} = 1.6 \cdot 10^{13}$ ppb for the ISOLDE (On-Line Isotope Mass Separator) fixed-target experiment [101, 102, 103]. As a first test, the longitudinal emittance for this high-intensity beam was set to 1.0 eVs (current operational value), but recent optimization studies assume $\epsilon_\mathrm{l} = 1.5$ eVs after LIU upgrade [104].

The designed RF voltage programs used in simulations are shown in Fig.4.31 (Cycle I). The first part of the ramp (from C275 to C350) is performed with a double RF system in bunch lengthening mode to reduce the transverse space charge tune spread, using $V_{\mathrm{rf},1} = 10$ kV and $V_{\mathrm{rf},2} = 10$ kV. With $V_{\mathrm{rf},1} = V_{\mathrm{rf},2}$ the line density has two peaks of similar height, see for example Fig.4.27.

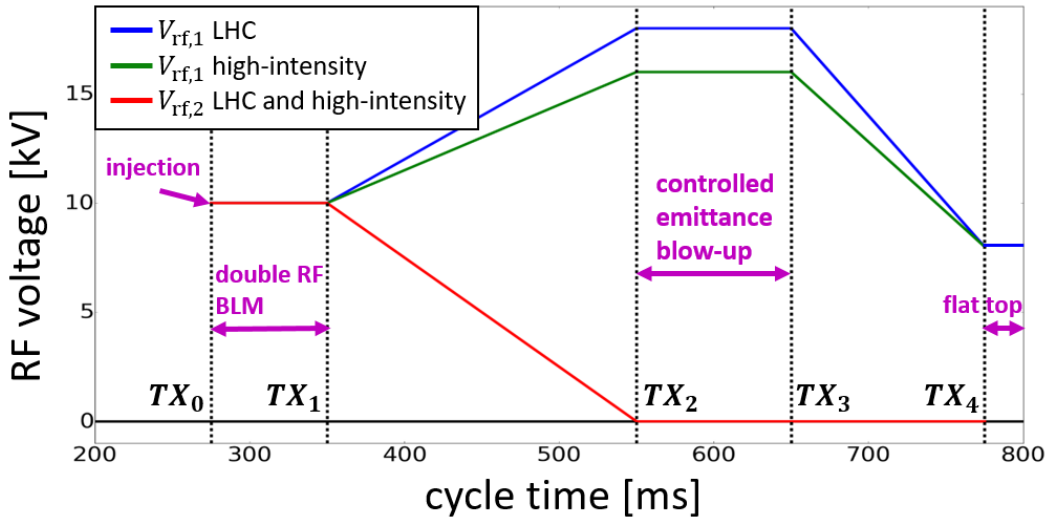


**Figure 4.31.** Example of designed voltage programs (cycle I) for the $h = 1$ and $h = 2$ PSB RF systems for nominal-LHC ($N_\mathrm{b} = 3.42 \cdot 10^{12}$ ppb) and high-intensity ($N_\mathrm{b} = 1.6 \cdot 10^{13}$ ppb) beams after LIU upgrade. Double RF operation in bunch lengthening mode is performed between the injection time $TX_0 = 275$ ms and $TX_1 = 350$ ms with $V_{\mathrm{rf},1} = 10$ kV and $V_{\mathrm{rf},2} = 10$ kV. Controlled longitudinal emittance blow-up in a single RF system is performed between $TX_2 = 550$ ms and $TX_3 = 650$ ms with RF voltage equal to 18 kV and 16 kV for nominal and high-intensity beams respectively. At flat top, which starts at $TX_4 = 775$ ms, the voltage is $V_{\mathrm{rf},1} = 8$ kV.

In the interval C350–C550 $V_{\mathrm{rf},2}$ is dropped to zero, while $V_{\mathrm{rf},1}$ is increased to 18 kV and 16 kV for LHC and high-intensity beams respectively. This difference is due to the fact that the Finemet® amplifiers have to provide a part of their available

current to reduce beam loading (impedance reduction mentioned above), which is larger for bunches with higher current [73].

During C550–C650 it is planned to increase the initial emittance to 2.6 eVs for high-intensity and 3 eVs for LHC beams in a single RF system. Band-limited RF noise injected in the phase loop of the $h = 1$ RF system has been used for blow-up (see next Chapter).

Finally $V_{\mathrm{rf},1}$ is dropped to 8 kV (current peak accelerating voltage) in the interval C650–C775 and then is kept constant at flat-top until C800 to have the desired bunch length $\tau_l < 205$ ns at extraction for both beams. This limitation is defined by the rise-time of the PSB recombination-kicker located in the beam transfer-line connecting the PSB and the PS [105].

Simulations started at cycle time C290, assuming a bunch matched with intensity effects inside the RF bucket, and ended at C800. Beam-based feedbacks (phase and radial loops, see next Chapter) acted from $TX_2$ until flat top.

### 4.7.1 LHC-nominal Beams

No instability was found for LHC-nominal beams and it was possible to smoothly blow up the emittance to the requested 3 eVs in the interval C550–C650 using all the voltage manipulations described earlier. The bunch length at extraction was $\tau_{\mathrm{l}} = 200$ ns and there were only few losses (<0.01%) when the RF voltage was decreased from 18 kV to 8 kV.

Figure 4.32 (left) shows the average bunch position along the cycle, together with the synchronous phase in a single RF system with voltage $V_{\mathrm{rf},1}$ neglecting collective effects. Notice that the phase loop is able to damp, in a relatively short time after $TX_3$, the significant dipole oscillations coming from the RF phase noise injection before $TX_3$. On the contrary and as expected from its function, the phase loop is not able to damp after $TX_3$ the quadrupole oscillations, which persist up to flat top.

### 4.7.2 High-intensity Beams

It was impossible to smoothly accelerate the high-intensity beam along the acceleration cycle while performing controlled longitudinal emittance blow-up. This was due to instabilities occurring at 480 ms, 640 ms and 700 ms, which led to significant dipole and quadrupole oscillations in addition to bunch-length growth, as shown in Fig.4.33, where the planned RF phase noise injection in $[TX_2, TX_3]$ is not applied. As expected, the synchronous phase shift due to the resistive part of the impedance is larger here relative to the one visible in Fig.(4.32), due to the higher intensity simulated. Notice also the dipole oscillations at C290 which are damped before $TX_1$: due to the high intensity it was even difficult to match the bunch with collective effects inside the RF bucket.

The reason for these instabilities can be found examining the bunch distribution in the longitudinal phase space, as shown for example in Fig.4.34, which refers to the cycle-time C483, soon after the start of the first instability. One can see that a modulation with a frequency of 21 MHz perturbs the bunch. Observe also that the Finemet® impedance has a significant peak at 19 MHz with a large bandwidth of 7.5 MHz at -3 dB if the LLRF feedback is neglected (Fig.4.26, right). This is a

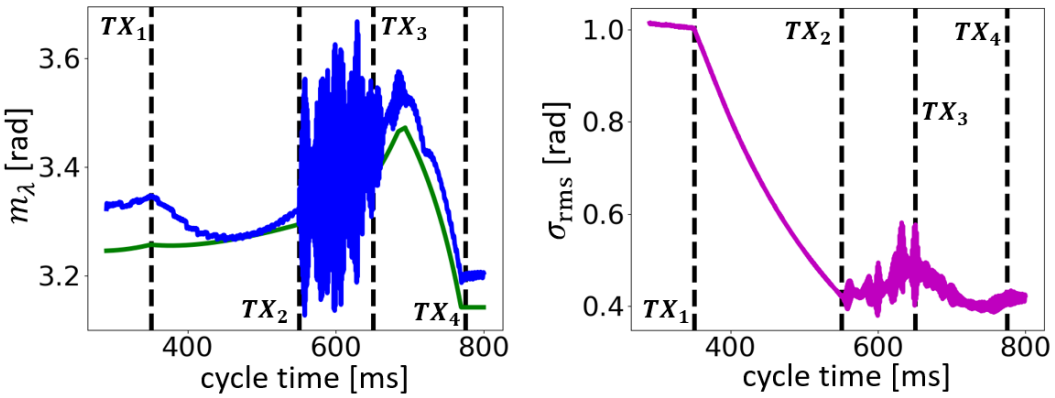


**Figure 4.32.** Left: average bunch position (blue) as a function of the cycle time for nominal-LHC beams with $N_\mathrm{b} = 3.42 \cdot 10^{12}$ ppb and $\epsilon_\mathrm{l} = 1.4$ eVs at C290, when the bunch is matched inside the RF bucket with intensity effects. The used RF programs are shown in Fig.4.31. The green curve represents the synchronous phase in a single RF system with voltage $V_{\mathrm{rf},1}$ neglecting collective effects. RF phase noise for controlled emittance blow-up is applied between $TX_2$ and $TX_3$. Phase and radial loops act from $TX_2$ onward. Right: 1-rms bunch length as a function of the cycle time with the same conditions described for the left image.

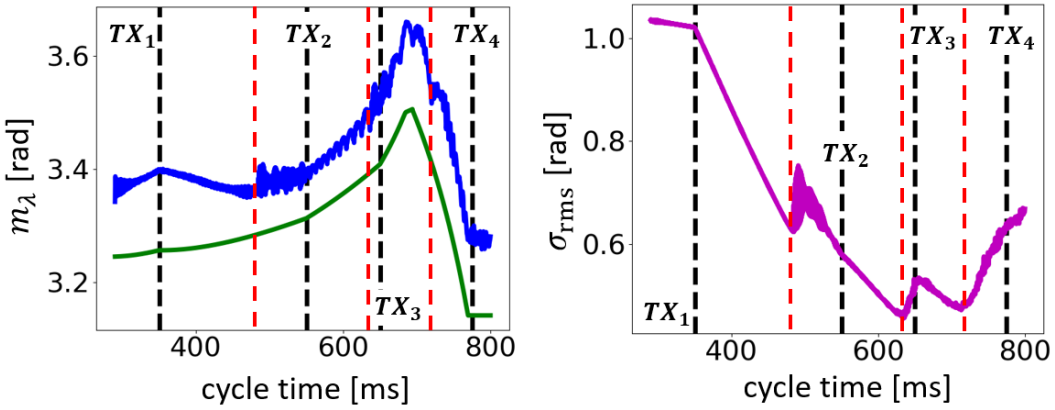


**Figure 4.33.** Left: average bunch position (blue) as a function of the cycle time for high-intensity beams with $N_\mathrm{b} = 1.6 \cdot 10^{13}$ ppb and $\epsilon_\mathrm{l} = 1.0$ eVs at C290, when the bunch is matched inside the RF bucket with intensity effects. The used RF programs are shown in Fig.4.31. The green curve represents the synchronous phase in a single RF system with voltage $V_{\mathrm{rf},1}$ neglecting collective effects. The three red vertical lines mark the cycle times when the instabilities start, namely C480, C640 and C700. RF phase noise for controlled emittance blow-up is not applied. Phase and radial loops are not included. Right: 1-rms bunch length as a function of the cycle time with the same conditions described for the left image.

clear indication that the high-frequency induced voltage generated by the Finemet® cavities leads to micro-wave instability [106] as the bunch becomes shorter during the acceleration cycle, or equivalently as the bunch spectrum becomes longer interacting more with the 19 MHz peak in the impedance model.

Figure 4.33 (right) confirms what just observed. Whenever the bunch length

becomes too small, the instability is triggered and leads to fast bunch-length growth, which in turn makes the beam stable again. Later in the acceleration cycle, higher beam energies and possibly some RF manipulations reduce again the bunch-length to such a degree that the next instability starts and the same pattern repeats.

Notice that the LLRF feedback assumed in simulations is not supposed to suppress this instability since, even considering the maximum revolution frequency along the cycle of 2 MHz and supposing that the 16 kHz bandwidth at -3 dB of the notches is sufficient to properly reduce the Finemet® impedance, eight harmonics of the revolution frequency can cover only up to 16 MHz.

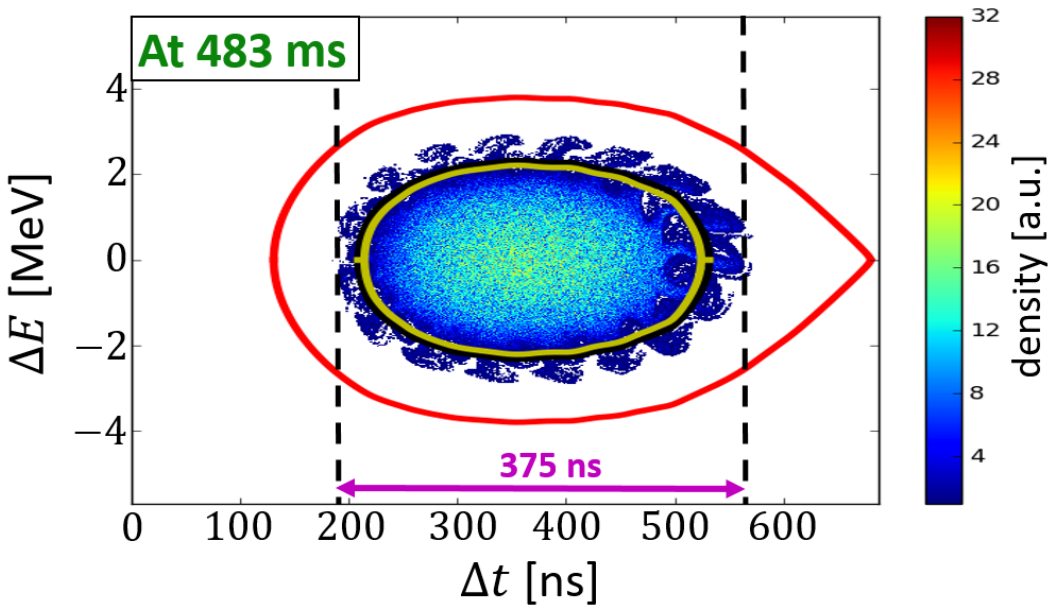


**Figure 4.34.** High-frequency modulation in the bunch distribution at cycle time C483 ($f_{\mathrm{rev},0}$ = 1.46 MHz), after the start of the first instability shown in Fig.4.33. The separatrix is in red, the yellow and black curves correspond respectively to the stable particle-trajectories determined by the Foot Tangent Method and $\tau 5$ conventions for bunch-length calculation. The color bar indicates the particle density. Since 8 oscillations occur in 375 ns, the modulation frequency is 21 MHz.

Since it should be possible to increase the number of revolution harmonics at which the Finemet® impedance is reduced, that number was raised in simulations from 8 to 16 in order to cover the impedance peak at 19 MHz from cycle-time C480, when $f_{\mathrm{rev},0}$ = 1.46 MHz, onward. In this way, the start of the first instability remained the same and the only positive effect was the delay of the second instability until 700 ms (compare the green and red curves in Fig.4.35). This so mediocre improvement is due to the insufficient bandwidth of the notches compared to the one of the impedance peak located at 19 MHz: increasing for example the notch bandwidth at -3 dB from 16 kHz to 160 kHz, and again considering the first 16 revolution harmonics in the impedance reduction, no instabilities were observed until C730. However, since the notch bandwidth of 16 kHz is not expected to change after LIU upgrade, no parametric studies were performed in this respect.

Similar studies were done neglecting all the RF manipulations present in Cycle I

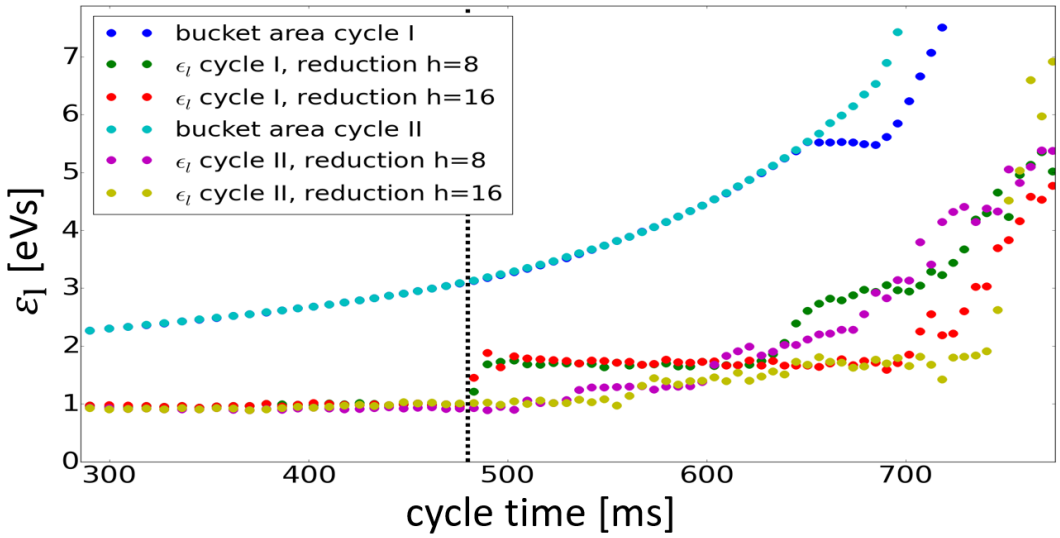


**Figure 4.35.** Longitudinal emittance $\epsilon_l$ as a function of the cycle time for simulated high-intensity future beams with $N_\mathrm{b} = 1.6 \cdot 10^{13}$ ppb and $\epsilon_\mathrm{l} = 1.0$ eVs at 290 ms, when the bunch is matched with intensity effects inside the RF bucket. The extraction energy is 2 GeV. No controlled longitudinal blow-up is applied, the emittance growths are due to instabilities. The RF voltage programs for Cycle I are shown in Fig.4.31, while Cycle II assumes acceleration in a single RF system from C290 to flat top with constant $V_{\mathrm{rf},1} = 16$ kV. Finemet® impedance reduction by the LLRF feedback at the first 8 or 16 harmonics of the revolution frequency is considered. Instability for Cycle I configuration starts at 480 ms (vertical line). The bucket areas for the two cycles along the ramp are also shown.

and accelerating the beam in a single RF system with constant $V_{\mathrm{rf},1} = 16$ kV (Cycle II, magenta and yellow curves in Fig.4.35). These additional simulations were performed in order to verify that the RF manipulations do not contribute to the observed instabilities and to determine simpler RF settings able to reproduce the instabilities without including unnecessary complications.

Using Cycle II, the instability started at 505 ms and 560 ms considering 8 and 16 revolution harmonics respectively. This indicates that the RF voltage manipulations performed in Cycle I make the first instability start earlier. However, the final emittance at 800 ms is smaller for beams accelerated in Cycle I since, similarly to what observed above, an instability which starts earlier in the cycle increases the bunch length and emittance providing relatively more stability and margin for bunch shrinking later in the ramp.

Finally notice that negligible losses (<0.001%) have been found in the simulations presented in this Subsection. This can be explained examining Fig.4.35: although the micro-wave instability leads to considerable uncontrolled emittance blow-up, the bucket areas for both Cycles I and II are large enough to contain the bunch along the ramp.

### 4.7.3 Requirements for the LLRF Wake-cancellation Feedback after LIU-upgrade

The instability found above for high-intensity beams with initial emittance of 1.0 eVs is quite critical and can heavily influence the future beam quality for PSB fixed-target experiments like ISOLDE. In addition, increasing from 8 to 16 the number of harmonics of the revolution frequency which are affected by the LLRF wake-cancellation feedback did not lead to significant improvements.

For this reason dedicated studies have been performed to determine in simulations how many revolution harmonics the LLRF feedback should be acting on to suppress the observed micro-wave instability, varying $\epsilon_\mathrm{l}$ from 1.0 eVs to 1.4 eVs and $N_\mathrm{b}$ from $1 \cdot 10^{13}$ ppb to $1.6 \cdot 10^{13}$ at cycle-time C290. Acceleration in a single RF system with constant $V_{\mathrm{rf},1} = 16$ kV has been assumed, with no controlled longitudinal emittance blow-up and inactive phase and radial loops. The notch bandwidth is assumed to be 16 kHz at -3 dB.

As one can see from the left image in Fig.4.36, supposing a LLRF feedback acting on the first eight revolution harmonics, the beam becomes always unstable along the ramp. As expected, fixed a certain bunch intensity, the instability starts later with larger emittances (or bunch lengths), since for those cases the beam spectrum components at 19 MHz have lower amplitudes at a given cycle-time. Moreover and reasonably, for a given longitudinal emittance, the instability starts earlier increasing the bunch intensity.

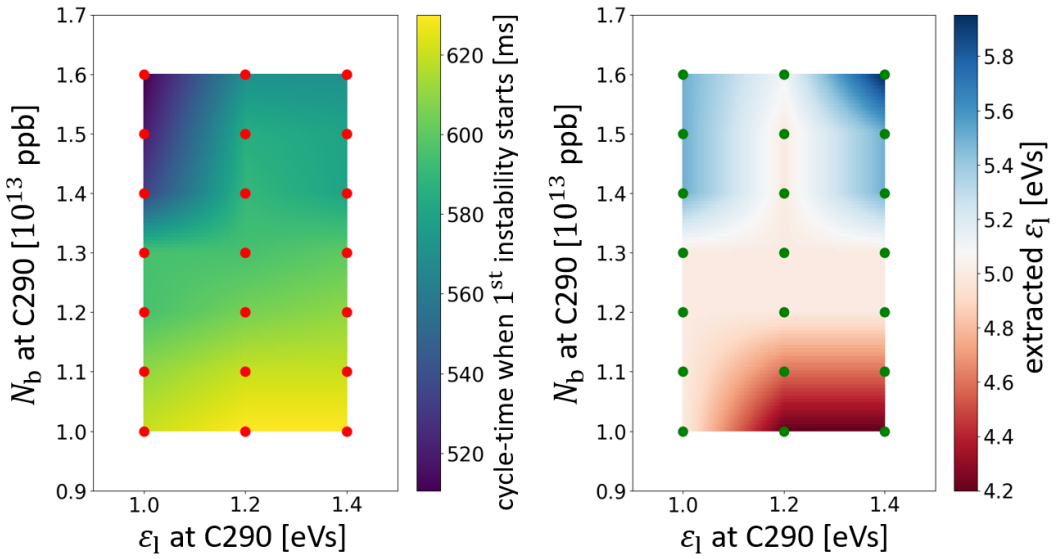


**Figure 4.36.** Instability diagrams for after-LIU high-intensity beams supposing that the LLRF feedback reduces the Finemet® impedance at the first 8 harmonics of the revolution frequency with a notch bandwidth of 16 kHz at -3 dB. Acceleration in a single RF system with constant $V_{\mathrm{rf},1} = 16$ kV is assumed, with no controlled longitudinal emittance blow-up and no action of the phase and radial loops. The color bars indicate when the first instability starts along the cycle (left) and the extracted emittance (right) as a function of the bunch intensity and emittance at C290. The simulation results are marked by red dots, an interpolation is performed for intermediate points. All the combinations shown lead to instability and emittance blow-up.

A similar reasoning can be applied for the right image in Fig.4.36, where the extracted emittance after uncontrolled blow-up is larger for initial higher intensities and lower emittances. However, one can notice that, when the bunch intensity is large enough ($N_b \geq 1.2 \cdot 10^{13}$ ppb), the extracted emittance for initial 1 eVs and 1.4 eVs bunches is roughly the same. As observed in the previous Subsection, this can be due to the fact that 1.0 eVs bunches start to be unstable earlier in the ramp than 1.4 eVs bunches (see Fig.4.36, left) and earlier but smaller increases in bunch-length lead to relatively more stable beams later in the cycle.

Increasing the number of revolution harmonics for Finemet®-impedance reduction from 8 to 16, the instability diagrams change significantly, as shown in Fig.4.37. Examining in particular the case with initial emittance of 1.4 eVs (close to the expected value for ISOLDE beams after upgrade), one can see that the bunch is always stable up to $N_b = 1.4 \cdot 10^{13}$ ppb, while for higher intensities the emittance blow-up is minimum ($\epsilon_l = 1.6$ eVs at extraction for $N_b = 1.6 \cdot 10^{13}$ ppb).

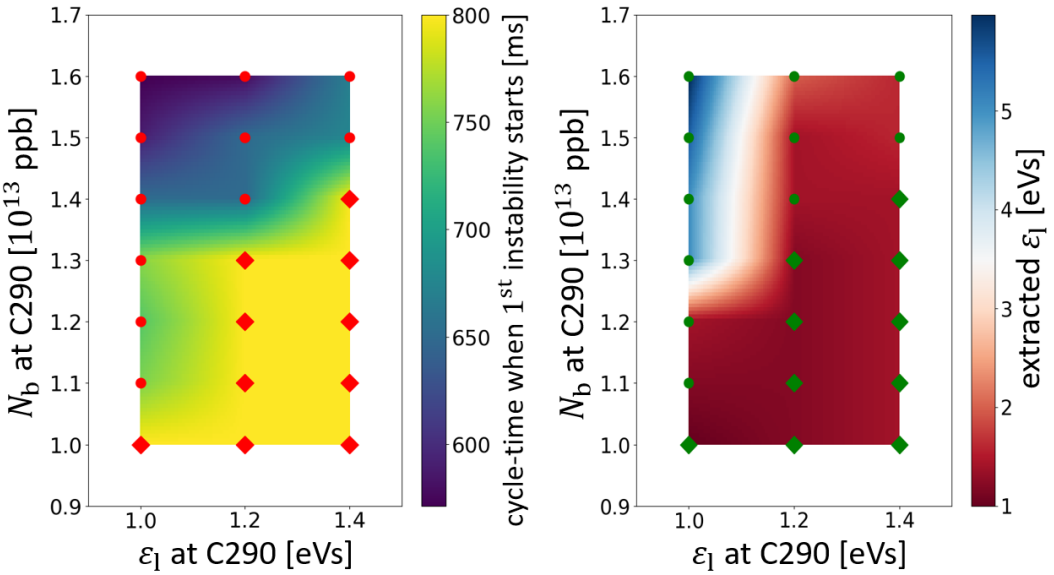


**Figure 4.37.** Instability diagrams for after-upgrade high-intensity beams supposing that the LLRF feedback reduces the Finemet® impedance at the first 16 harmonics of the revolution frequency. All the other parameters and conditions are equal to the ones described in Fig.4.36. The red marks represent simulation results and an interpolation is performed for intermediate points. A dot-mark indicates that the corresponding combination of bunch intensity and emittance at C290 leads to instability and emittance growth, a diamond-mark represents a combination which does not lead to any instability. For visual reasons the start time of the instability is set to C800 (end of the cycle) when the bunch is stable throughout the ramp.

These studies suggest that, in order to accelerate the planned highest-intensity beam after LIU upgrade, Finemet® impedance reduction at the first sixteen harmonics of the revolution frequency should be considered as a requirement for the LLRF wake-cancellation feedback. If this specification cannot be fulfilled and a lower number of revolution harmonics will be considered, further optimizations of the RF settings along the cycle become necessary: for example, the use of a double RF

system in bunch-lengthening mode for both acceleration and controlled longitudinal emittance blow-up (performed as soon as possible in the cycle) would allow probably to keep the bunch length far from the micro-wave instability threshold.

## 4.8 Conclusions

Several critical upgrades will concern the CERN PSB after 2021, following the challenging directives of the LIU Project which aim is to provide beams to the LHC with a brightness increased by more than a factor of 2 relative to the present situation. Many of the changes which the PSB will experience concern the longitudinal beam dynamics. Therefore dedicated studies and realistic simulations are needed to foresee possible beam-instability issues in the after-upgrade scenario.

This Chapter showed how these studies were carried out. The macro-particle simulations were performed with the CERN BLonD code.

Beam measurements and beam dynamics simulations significantly contributed to the important decision to completely replace the currently-used ferrite RF systems with Finemet® ones after LIU upgrade.

Numerous benchmarks against the PyORBIT code and comparisons with analytical formulas have been done in order to give the BLonD code reliability when dealing with space charge computations. In this respect, additional numerical studies have been carried out to determine a trustworthy method to calculate the space charge induced voltage, very important contribution to the total induced voltage in the not-ultra-relativistic PSB machine.

For the first time, full-cycle simulations of the future PSB longitudinal beam dynamics were performed using a realistic impedance model, a careful estimation of the longitudinal space charge, Low Level RF feedbacks and controlled longitudinal emittance blow-up. Moreover, it was emphasized the importance to properly take into account multi-turn wakefields in simulations and to have an algorithm able to determine the relative phase between two RF systems in a double RF operation in bunch-lengthening mode in presence of collective effects.

Two types of beam were analyzed for the after-upgrade scenario, the nominal-LHC high-brightness beam and the ISOLDE high-intensity one. For the first, no instability was found and it was possible to smoothly accelerate the bunch along the cycle with negligible losses and performing the required controlled longitudinal emittance blow-up in the presence of phase and radial beam-based feedbacks. On the contrary, micro-wave instability due to the Finemet® impedance was found for the high-intensity beam. This instability, which led to severe uncontrolled emittance blow-up, was observable with different RF voltage programs. It was suggested to increase from 8 to 16 the number of harmonics of the revolution frequency which are affected by the LLRF wake-cancellation feedback.

# Chapter 5

# PSB: Beam-based Feedbacks and RF Phase Noise for Controlled Longitudinal Emittance Blow-up

## 5.1 Introduction

As was described in the previous Chapter, controlled longitudinal emittance blow-up in the PSB is needed to decrease the peak line density of the bunches injected into the PS and therefore reduce the transverse space charge tune spread.

Controlled emittance blow-up (from 1 eVs to 1.4 eVs) for nominal-LHC beams in the CERN PSB is currently achieved using sinusoidal phase modulation of a dedicated high-harmonic RF system, the so-called C16 RF cavity [107, 108]. In 2021, after the LIU upgrade, beams with 3 eVs emittance should be extracted to the PS. Beam measurements and simulation studies have shown that the future required emittance blow-up can be achieved using an optimized phase modulation of the C16 RF system [108].

In this Chapter another method of blow-up in the PSB is presented [109], that is the injection of band-limited phase noise in the main RF system ($h = 1$). Bunch shaping and blow-up using band-limited noise have already been studied in several papers (see for example [110]). This technique, never tried in the PSB, has been successfully implemented at CERN in the SPS and LHC [111, 112], where there are no dedicated RF systems for blow-up and the acceleration cycles are longer.

There are three main reasons to propose an alternative to the current method of blow-up. As mentioned in the previous Chapter, the RF phases between the different PSB RF systems are not accurately known in operation. Since the theory of high-harmonic phase modulation requires the knowledge of these RF phases, in general longer times are needed in operation to properly set the parameters for an effective blow-up with this technique. On the contrary, band-limited phase noise requires only the knowledge of the synchrotron frequency distributions along the acceleration cycle, which usually can be determined with good accuracy in simulations having at disposal a reliable estimation of the synchrotron phase shift caused by longitudinal

space charge effects. The second reason is that the present method for blow-up implies the use of a dedicated RF system that can be removed with noise injection in the main RF system. Finally, the proposed technique, in addition to blow up the beam, is able to reduce even more the peak line density of the beam decreasing further the impact of longitudinal and transverse space charge effects.

One possible disadvantage of using band-limited phase noise concerns the time needed for blow-up, which in general is higher when phase noise is applied relative to phase modulation. Another complication could arise from the interaction of the LLRF phase loop with the injected RF noise, since both act on the RF phase. In addition, phase noise cannot be injected turn by turn through the phase loop but only at a limited sampling rate, therefore the designed noise spectrum has a limitation on its maximum (Nyquist) frequency. However, as the present Chapter will show, all these possible disadvantages will not be a limitation for the PSB, both in the current and after-upgrade scenarios.

## 5.2 The Band-limited RF Phase Noise

The effect of band-limited phase noise on particles lies in-between the diffusion generated by white phase noise acting on all synchrotron frequencies and the resonant excitation created by sinusoidal phase modulation at frequencies close to zero-amplitude synchrotron frequency.

Specifically, only the particles with a synchrotron frequency inside a certain band are affected by RF phase noise (see Fig.5.1).The band upper limit $f_{\mathrm{up}}$ is above the bunch zero-amplitude synchrotron frequency $f_{\mathrm{s0,ind}}$ to affect fully the bunch core and its lower limit $f_{\mathrm{down}}$ is related to the target bunch length (or emittance) to be reached. Figure 5.1 shows also that space charge, defocusing in the PSB (below transition), lowers the zero-intensity synchrotron frequency $f_{\mathrm{s0}}$ and the noise band should follow this shift.

Band-limited RF phase noise was obtained "coloring" white phase noise in frequency domain with the desired probability density and Fourier-transforming the result to time domain, similarly to the implementation in the LHC [113]. The detailed procedure is shown below.

Let us assume that the RF phase noise is applied at revolution turns $1, \ldots, N_{\mathrm{turns}}$ and that $T_0$ is constant. The first step is to generate white noise $w_n$ in time domain using

$$w_n = \cos(2\pi u_n)\sqrt{-2\ln v_n} \quad n = 1, \ldots, N_{\mathrm{turns}} \tag{5.1}$$

where $u_n$ and $v_n$ are uniform independent random variables in the interval $[0, 1]$. Then the discrete Fourier transform is applied to $w_n$

$$W_l = \sum_{n=1}^{N_{\mathrm{turns}}} w_n e^{-2\pi i \frac{ln}{N_{\mathrm{turns}}}}, \quad l = -\frac{f_{\mathrm{rev,0}}}{2}, \ldots, 0, \ldots, \frac{f_{\mathrm{rev,0}}}{2}, \tag{5.2}$$

where, to give a concrete example, it is assumed that $N_{\mathrm{turns}}$ is an odd number. Notice that the maximum frequency is $f_{\mathrm{max}} = f_{\mathrm{rev,0}}/2$, the frequency step is $\Delta f = f_{\mathrm{rev,0}}/N_{\mathrm{turns}}$ and the array $W_l$ has $N_{\mathrm{turns}}$ values. Afterwards the desired band-limited

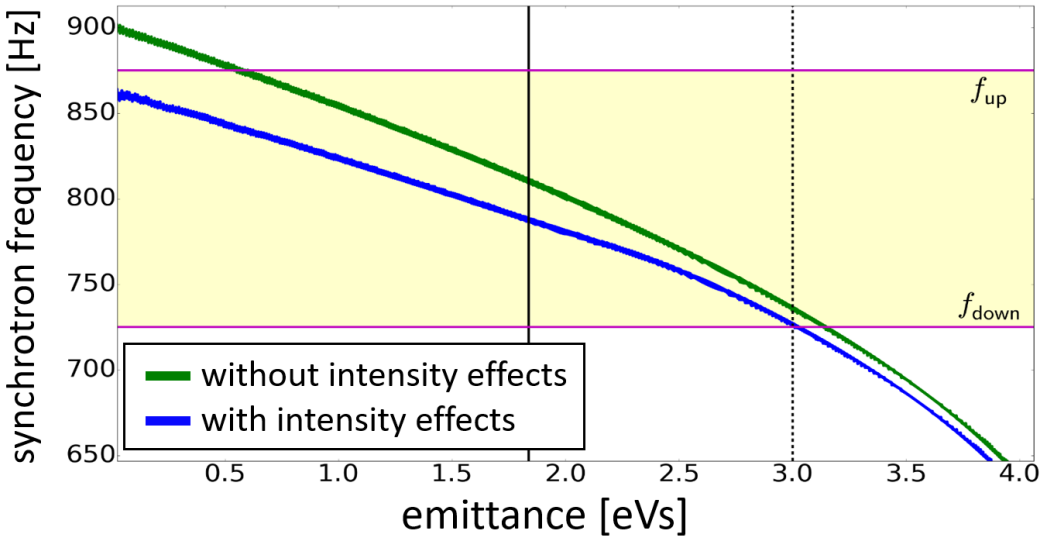


**Figure 5.1.** Synchrotron frequency distribution as a function of emittance in a single RF system ($V_{\mathrm{rf},1} = 16$ kV) calculated without (green) and with (blue) collective effects for after-upgrade LHC beams ($N_{\mathrm{b}} = 3.42 \cdot 10^{12}$ ppb) in the PSB at $E_{\mathrm{kin}} = 1$ GeV (cycle-time C600). The bunch emittance is 1.8 eVs (continuous black line). RF phase noise in the band defined by $f_{\mathrm{down}} = 725$ Hz and $f_{\mathrm{up}} = 875$ Hz (magenta lines) has to be applied if the target emittance is 3 eVs (dashed black line)

.

noise probability density is constructed

$$s_l = \sqrt{S^{\mathrm{d}}_{\mathrm{noise},l} f_{\mathrm{rev},0}}, \quad l = -\frac{f_{\mathrm{rev},0}}{2}, \ldots, 0, \ldots, \frac{f_{\mathrm{rev},0}}{2}, \tag{5.3}$$

where $S^{\mathrm{d}}_{\mathrm{noise}}$ [rad$^2$/Hz] is a real function called double-sided noise-power spectral density. Then the white noise in frequency domain is multiplied by $s_l$ obtaining

$$\Phi_l = s_l W_l, \quad l = -\frac{f_{\mathrm{rev},0}}{2}, \ldots, 0, \ldots, \frac{f_{\mathrm{rev},0}}{2}. \tag{5.4}$$

Finally, performing an inverse discrete Fourier transform on $\Phi_l$, the phase noise in time domain is obtained

$$\phi^{(n)}_{\mathrm{noise}} = \frac{1}{N_{\mathrm{turns}}} \sum_{l=-f_{\mathrm{rev},0}/2}^{f_{\mathrm{rev},0}/2} \Phi_l e^{2\pi i \frac{ln}{N_{\mathrm{turns}}}}, \quad n = 1, \ldots, N_{\mathrm{turns}}. \tag{5.5}$$

The double-sided noise-power spectral density $S^{\mathrm{d}}_{\mathrm{noise}}$ determines the rms phase noise as [114]

$$\phi^{\mathrm{rms}}_{\mathrm{noise}} = \sqrt{f_{\mathrm{rev},0} \langle S^{\mathrm{d}}_{\mathrm{noise}} \rangle}, \tag{5.6}$$

where

$$\langle S^{\mathrm{d}}_{\mathrm{noise}} \rangle = \frac{\sum_{l=-f_{\mathrm{rev},0}/2}^{f_{\mathrm{rev},0}/2} S^{\mathrm{d}}_{\mathrm{noise},l}}{N_{\mathrm{turns}}}. \tag{5.7}$$

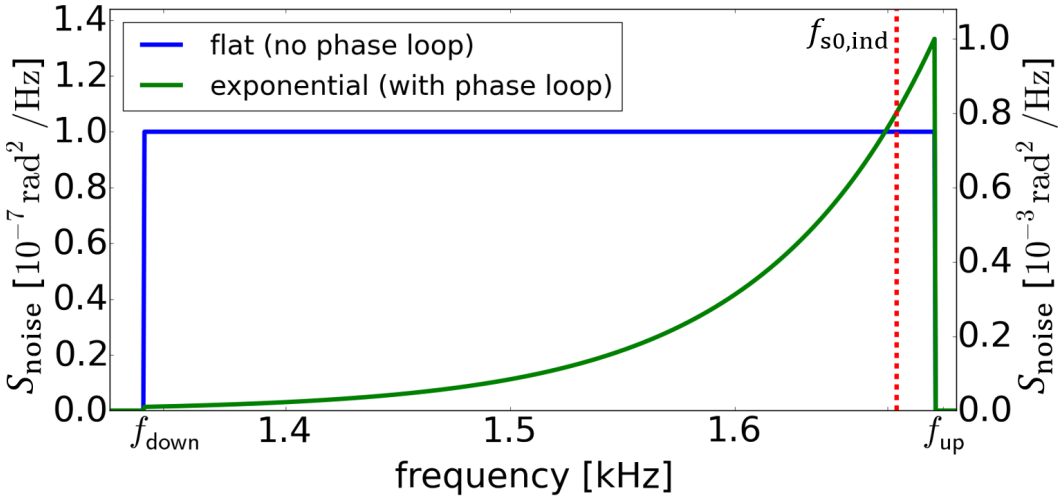


**Figure 5.2.** Examples of flat (left axis) and exponential (right axis) one-sided power-noise spectral density as a function of frequency. These functions were used respectively in simulations without and with phase loop to generate RF phase noise at $E_{kin} = 425$ MeV (cycle time 450 ms).

Notice that, equivalently, in simulations one-sided spectral densities $S_{noise} = 2S^{d}_{noise}$ have been used, which are defined only for positive frequencies and assume that real discrete Fourier transforms are performed (see for example Fig.5.2).

Starting from Eq.(4.31), the expression for the total RF voltage in the PSB at revolution turn $n$ when phase noise is injected directly into the main-harmonic cavity is

$$V_{tot}(\Delta t) = V_{rf,1}\sin(\omega_{rf,1}\Delta t + \pi + \phi^{(n)}_{noise}) + rV_{rf,1}\sin(2\omega_{rf,1}\Delta t + \phi_{1,2}) - V_{rf,1}\sin(\phi_s) - V_{ind}(\Delta t). \quad (5.8)$$

However, as the next Section will explain, the baseline for the after-upgrade scenario is the injection of the RF phase noise through the phase-loop. In this case $\phi_{noise}$ is not directly added to the RF phase as in Eq.(5.8) but, applying the phase-loop filter, it is converted to RF frequency noise which is added to $\omega_{rf,1}$.

## 5.3 Effects of Phase and Radial Loops

The operational scenario for controlled emittance blow-up during the future acceleration cycle is that the noise will be introduced into the beam phase loop (similarly to what is done in the SPS and LHC [112, 115]), rather than being injected directly into the main harmonic cavity. In this scenario the two following potential issues should be taken into account. First, the noise will be counteracted by phase loop. Additionally, the noise signal can be sampled only every 10 µs, which corresponds to the interval between two consecutive phase loop triggers in present LLRF system [116]. However we expect that this second limitation should not affect the phase noise performance, since the sampling frequency of 100 kHz should be well above the range of synchrotron frequencies concerned during blow-up (for example $f_{s0}$ is

below 1.7 kHz after C450 assuming acceleration in a single RF system with constant $V_{\mathrm{rf},1} = 16$ kV).

The main application of the phase loop is to damp the rigid-bunch dipole oscillations. This is usually done measuring at turn $n$ the difference $\Delta\phi$ between the phases of the beam and RF cavity signals and changing accordingly the RF frequency $\omega_{\mathrm{rf}}$ by $\Delta\omega_{\mathrm{pl}}$ at turn $n+1$. This passage from RF phase to frequency is performed since phase measurements could contain unwanted high-frequency components that are filtered when phase loop is applied (see next Subsection).

This RF frequency shift due to phase-loop operation leads to a change of the bunch orbit-radius $R$ from the design machine radius $R_0$, see Eq.(2.86). The aim of the radial loop is to maintain the orbit at the design one in the long run, reducing $|\Delta R| = |R - R_0|$. This is done giving a second contribution $\Delta\omega_{\mathrm{rl}}$ to $\omega_{\mathrm{rf}}$. Thus, for each turn, $\Delta\omega_{\mathrm{rf}} = \Delta\omega_{\mathrm{pl}} + \Delta\omega_{\mathrm{rl}}$, where the two contributions have usually opposite signs and $|\omega_{\mathrm{pl}}| > |\omega_{\mathrm{rl}}|$.

If the phase noise is introduced in the phase loop, then its contribution is summed to $\Delta\phi$. The usually flat band-limited noise spectrum $\Phi_l$ will then have a notch close to $f_{\mathrm{s0,ind}}$ that can slow down the diffusion of the core. A compensation for this effect can be adopted changing the shape of the noise spectral density, as it is done in the SPS [113], where a triangular $S_{\mathrm{noise}}$ centered in $f_{\mathrm{s0,ind}}$ is adopted. Similarly, an exponentially growing $S_{\mathrm{noise}}$ in the band $[f_{\mathrm{down}},\, f_{\mathrm{up}}]$ has been generally chosen in the present Chapter to generate RF phase noise for PSB applications (see for example Fig.5.2).

### 5.3.1 Modeling Phase and Radial Loops in BLonD

In order to obtain correct results for the effect of phase noise, it was necessary to model the phase and radial loops in BLonD, starting from the PSB RF synoptics.

In the PSB LLRF, $\Delta\phi$ is obtained through the measured In-Phase $I$ and Quadrature $Q$ components [117] of the $h = 1$ RF-cavity and beam signals [116]. The details are shown below.

The beam $B_{\mathrm{s}}$ and cavity $C_{\mathrm{s}}$ signals are first properly delayed and rotated to take into account respectively their nonidentical path group-delays and the distinct positions of the longitudinal pick-up and the main-harmonic cavity in the ring [116]. Then the signals are filtered to obtain only the Fourier component with frequency $\omega_{\mathrm{rf},1}$. That way the obtained sinusoidal functions can be decomposed into their correspondent $I$ and $Q$ components

$$\begin{aligned} B_{\mathrm{s}}(t) &= I_{\mathrm{B}} \cos(\omega_{\mathrm{rf},1} t) + Q_{\mathrm{B}} \sin(\omega_{\mathrm{rf},1} t) \\ C_{\mathrm{s}}(t) &= I_{\mathrm{C}} \cos(\omega_{\mathrm{rf},1} t) + Q_{\mathrm{C}} \sin(\omega_{\mathrm{rf},1} t). \end{aligned} \tag{5.9}$$

In the so-called phasor diagram $(I, Q)$, the signals can be expressed as vectors $B_{\mathrm{s}} = (I_{\mathrm{B}}, Q_{\mathrm{B}})$ and $C_{\mathrm{s}} = (I_{\mathrm{C}}, Q_{\mathrm{C}})$. Approximating $\Delta\phi$ with its sine and using the relation linking the cross-product of two vectors with the phase difference between them, the following expression provides $\Delta\phi$ in the PSB LLRF

$$\Delta\phi \approx \sin(\Delta\phi) = \frac{B_{\mathrm{s}} \times C_{\mathrm{s}}}{|B_{\mathrm{s}}||C_{\mathrm{s}}|} = \frac{I_{\mathrm{B}} Q_{\mathrm{C}} - I_{\mathrm{C}} Q_{\mathrm{B}}}{\sqrt{(I_{\mathrm{B}}^2 + Q_{\mathrm{B}}^2)(I_{\mathrm{C}}^2 + Q_{\mathrm{C}}^2)}} \tag{5.10}$$

The approximation in Eq.(5.10) is done assuming that $\Delta\phi$ is relatively small, and the purpose is avoiding using the inverse sinusoidal function which can be time-expensive in operation.

Similarly to what implemented in the LLRF, in simulations only the Fourier component with $\omega_{\mathrm{rf},1}$ is extracted from the bunch profile $\lambda$ through convolution [21], therefore

$$\int_0^{t_{\mathrm{rf}}} \cos(\omega_{\mathrm{rf},1}(t-\tau)-\phi_{\mathrm{rf}})\lambda(\tau)d\tau = \int_0^{t_{\mathrm{rf}}} \cos(\omega_{\mathrm{rf},1}\tau+\phi_{\mathrm{rf}})\lambda(\tau)d\tau \cos(\omega_{\mathrm{rf},1}t) + \int_0^{t_{\mathrm{rf}}} \sin(\omega_{\mathrm{rf},1}\tau+\phi_{\mathrm{rf}})\lambda(\tau)d\tau \sin(\omega_{\mathrm{rf},1}t). \quad (5.11)$$

The desired $\Delta\phi$ is then obtained as

$$\Delta\phi = \arctan\left(\frac{\int_0^{t_{\mathrm{rf}}} \sin(\omega_{\mathrm{rf},1}\tau+\phi_{\mathrm{rf}})\lambda(\tau)d\tau}{\int_0^{t_{\mathrm{rf}}} \cos(\omega_{\mathrm{rf},1}\tau+\phi_{\mathrm{rf}})\lambda(\tau)d\tau}\right). \quad (5.12)$$

Both in operation and simulations, the RF phase noise is added to $\Delta\phi$, which then becomes the actual input for the phase loop.

The phase loop in the PSB is characterized by a CIC (Cascaded Integrator-Comb) filter [116] able to remove undesired high frequency components from the $\Delta\phi$ samples. Applying the inverse Z-transform [118] onto the phase-loop transfer function

$$H_{\mathrm{tr}}(z) = g_{\mathrm{pl}}\frac{B_0^{\mathrm{pl}} + B_1^{\mathrm{pl}} z^{-1}}{1 - A_1^{\mathrm{pl}} z^{-1}}, \quad (5.13)$$

where $z$ is a complex number, the equation for the RF frequency correction at turn $n+1$ can be obtained as

$$\Delta f_{\mathrm{pl}}^{(n+1)} = A_1^{\mathrm{pl}}\Delta f_{\mathrm{pl}}^{(n)} + g_{\mathrm{pl}}\left(B_0^{\mathrm{pl}}\Delta\phi^{(n)} + B_1^{\mathrm{pl}}\Delta\phi^{(n-1)}\right). \quad (5.14)$$

Here the constants $A_1^{\mathrm{pl}} \approx 0.998$, $B_0^{\mathrm{pl}} \approx 0.999$ and $B_1^{\mathrm{pl}} = -0.999$ are determined by phase-loop stability reasons. The local gain $g_{\mathrm{pl}}$ is a positive parameter which value has to be adjusted case by case.

When the phase loop correction is applied at turn $n+1$, the bunch undergoes a radial displacement according to the relation

$$\frac{\Delta R^{(n+1)}}{R_0} = \frac{\Delta f_{\mathrm{rf}}^{(n+1)}}{f_{\mathrm{rf},0}^{(n+1)}}\frac{\gamma_{0,(n+1)}^2}{\gamma_{\mathrm{tr}}^2 - \gamma_{0,(n+1)}^2}, \quad (5.15)$$

Notice that in the LLRF the radial displacement is measured in millimeters using the transverse pickups, while Eq.(5.15) is used in simulations since no transverse dynamics is included in BLonD.

The radial displacement in Eq.(5.15) is the input for the radial loop at turn $n+1$. The displacement is filtered with a PI (Proportional-Integrator) corrector which contributes to the phase-loop stability [116]. The radial-loop correction to the RF frequency at turn $n+2$ can then be expressed as

$$\Delta f_{\mathrm{rl}}^{(n+2)} = k_{\mathrm{p}}\Delta R^{(n+1)} + k_{\mathrm{i}}\sum_{i=1}^{n+1}\Delta R^{(i)}, \quad (5.16)$$

where $k_\mathrm{p}$ and $k_\mathrm{i}$ are the proportional and integral gains. Adding the gain $K_\mathrm{r}$ we obtain

$$\Delta f_\mathrm{rl}^{(n+2)} = \Delta f_\mathrm{rl}^{(n+1)} + K_\mathrm{r}\left\{k_\mathrm{p}\left[\Delta R^{(n+1)} - \Delta R^{(n)}\right] + k_\mathrm{i}\Delta R^{(n+1)}\right\}. \tag{5.17}$$

Therefore, rearranging the terms and adding another filter coefficient $A_1^\mathrm{rl}$, the radial-loop correction at turn $n+2$ can then be expressed as

$$\Delta f_\mathrm{rl}^{(n+2)} = A_1^\mathrm{rl}\Delta f_\mathrm{rl}^{(n+1)} + g_\mathrm{rl}\left[B_0^\mathrm{rl}\Delta R^{(n+1)} + B_1^\mathrm{rl}\Delta R^{(n)}\right]. \tag{5.18}$$

Here the constants $A_1^\mathrm{rl} \approx 0.999$, $B_0^\mathrm{rl} \approx 3.000$ and $B_1^\mathrm{rl} = 0$ are determined by loop stability reasons. The local gain $g_\mathrm{rl}$, similarly to $g_\mathrm{pl}$, is a positive number and has to be decided depending on the particular machine and beam settings.

Finally, combining together the phase and radial loop corrections turn by turn, the RF frequency at turn $n+2$ will be

$$f_\mathrm{rf}^{(n+2)} = f_\mathrm{rf,0}^{(n+2)} + \Delta f_\mathrm{rf}^{(n+2)} = f_\mathrm{rf,0}^{(n+2)} - G_\mathrm{pl}\Delta f_\mathrm{pl}^{(n+2)} - G_\mathrm{rl}\Delta f_\mathrm{rl}^{(n+2)}, \tag{5.19}$$

where the global gains $G_\mathrm{pl}$ and $G_\mathrm{rl}$ are positive constants.

As observed before, the phase and radial loops cannot act every turn, but only every 10 µs. In order to simplify the notation, in this Subsection it has been assumed that the revolution turns $n+1$ and $n+2$ occur respectively at loop trigger-times $t_0 + 10\,\mu\mathrm{s}$ and $t_0 + 20\,\mu\mathrm{s}$, where $t_0$ is a generic trigger-time corresponding to turn $n$. In addition, the RF frequency corrections between two consecutive trigger times $t_0$ and $t_1$ are the same as the ones applied at $t_0$. Finally, the value for $\Delta\phi$ used at trigger time $t_1$ is calculated as the average of the values for $\Delta\phi$ determined between $t_0$ and $t_1$.

## 5.4 RF Phase Noise in Simulations for Future LHC-type Beams

The effect of band-limited phase noise on emittance blow-up during future acceleration ramp for nominal LHC beams was simulated using the BLonD code. The aim was to increase the emittance from 1.4 eVs (at injection energy of 160 MeV) to 3 eVs (at extraction energy of 2 GeV).

The full PSB impedance model was included in simulations. The Finemet® resistive impedance was reduced by the LLRF wake-cancellation feedback acting on the first eight harmonics of the revolution frequency.

First, simulations in a single RF system with constant RF voltage were performed, and afterwards a more realistic cycle has been used (Cycle II described in Section 4.7).

### 5.4.1 Single RF with Constant Voltage

#### Phase and Radial Loops not Included

The simulations were carried out using either $V_\mathrm{rf,1} = 8$ kV or $V_\mathrm{rf,1} = 16$ kV. The initial distribution at C275 was a rectangle whose parameters correspond to the

optimal case of unmodulated injection studied in [82]. At C290 (after filamentation) the emittance was roughly 1.1 eVs and 1.3 eVs using respectively $V_{\mathrm{rf},1} = 8$ kV and $V_{\mathrm{rf},1} = 16$ kV. Figure 5.3 shows that, using $V_{\mathrm{rf},1} = 8$ kV, there is no margin in the available bucket area to perform a smooth blow-up without losses. On the contrary, using $V_{\mathrm{rf},1} = 16$ kV and injecting RF phase noise directly into the main harmonic cavity between C450 and C600, it was possible to increase the emittance up to values between 2.8 eVs and 3 eVs at C775 with negligible losses (<0.01%), see Fig.5.3. Phase and radial loops were not included in simulations.

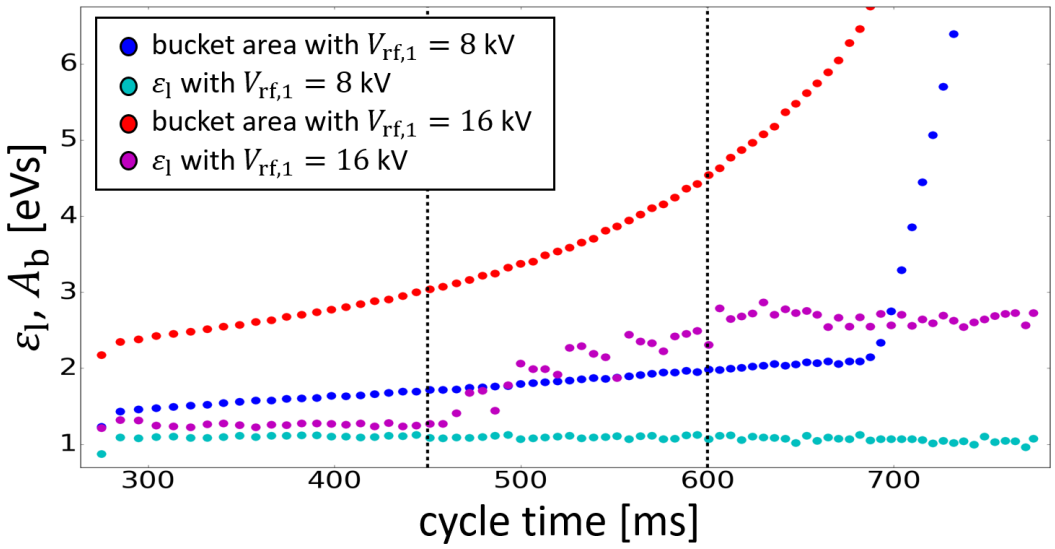


**Figure 5.3.** Simulated longitudinal emittance $\epsilon_{\mathrm{l}}$ and bucket area $A_{\mathrm{b}}$ as a function of the cycle time (C275–C775) for after-upgrade nominal-LHC beams ($N_{\mathrm{b}} = 3.42 \cdot 10^{12}$ ppb) in the PSB. Simulations are done in a single RF system including collective effects but not phase and radial loops. No controlled emittance blow-up is applied when $V_{\mathrm{rf},1} = 8$ kV. On the contrary, when $V_{\mathrm{rf},1} = 16$ kV, RF phase noise is injected directly into the $h = 1$ cavity between 450 ms and 600 ms (vertical lines): as a result, the emittance increases in a controlled way from 1.3 eVs to 2.8 eVs.

The noise was generated at regular intervals to follow the changes of the synchrotron and revolution frequencies during the blow-up time-interval C450–C600: $f_{\mathrm{s0}}$ decreases from 1.7 kHz to 0.9 kHz while $f_{\mathrm{rev},0}$ increases from 1.4 MHz to 1.65 MHz. In general, since $f_{\mathrm{rev},0}$ and $f_{\mathrm{s0}}$ vary significantly along the PSB cycle, ideally the noise should be often regenerated to follow these changes. However, if the regeneration is performed too often, then the resolution in frequency domain becomes unacceptably low, since $S_{\mathrm{noise}}$ will cover a band different from the desired one. A good compromise was found regenerating the RF phase noise program every 10000 turns ($\approx 7$ ms).

The spectral density $S_{\mathrm{noise}}$ was chosen to be flat in the band $[0.8\ f_{\mathrm{s0}},\ f_{\mathrm{s0}}]$. Indeed, for the examined intensity (nominal-LHC beams, $N_{\mathrm{b}} = 3.42 \cdot 10^{12}$ ppb), choosing $f_{\mathrm{up}} = f_{\mathrm{s0}}$ allows to affect fully the bunch core, since $f_{\mathrm{s0}} \approx 1.05 f_{\mathrm{s0,ind}}$ during C450–C600 due to space-charge synchrotron frequency shift. The value $f_{\mathrm{down}} = 0.8 f_{\mathrm{s0}}$ was chosen examining the synchrotron frequency distribution with intensity effects in the interval C450–C600 aiming at an emittance increase from 1.3 eVs to 3 eVs (see the principle in Fig.5.1). Finally, the amplitude of $S_{\mathrm{noise}}$ at 450 ms, rescaled

with $f_{\mathrm{rev},0}$ during the blow-up time-interval to have the same noise strength $\phi_{\mathrm{noise}}^{\mathrm{rms}}$, was gradually increased to a value leading to the required emittance at 600 ms (the optimum value was $S_{\mathrm{noise}} = 10^{-7}\mathrm{rad}^2/\mathrm{Hz}$ at 450 ms, see Fig.5.2).

### Phase and Radial Loops Included

Including phase and radial loops in simulations and injecting the noise into the phase loop, it was possible to rise the emittance from 1.4 eVs to 3 eVs. In order to counteract the phase loop action, the amplitude of $S_{\mathrm{noise}}$ in $f_{\mathrm{s0,ind}}$ had to be increased by four orders of magnitude with respect to the value used for the case without loops discussed above (Fig.5.2 shows the adopted exponential spectral-density at C450). The emittance evolution was similar to the one shown in Fig.5.3. The phase and radial loop gains were chosen in such a way that $\Delta\omega_{\mathrm{pl}}$ and $\Delta\omega_{\mathrm{rl}}$ had a stable evolution during the blow-up time-interval before converging to zero afterwards, implying that dipole oscillations are correctly damped after C600 (see Fig.5.4).

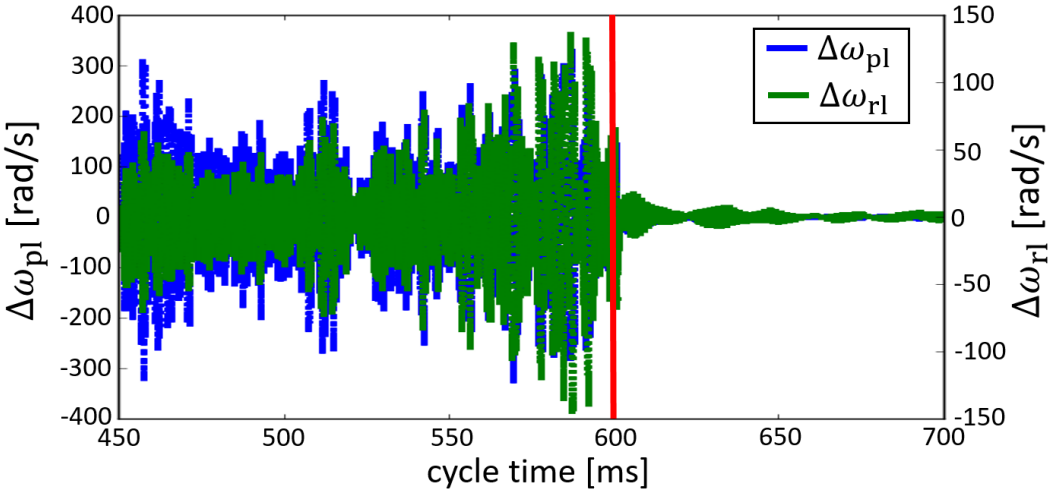


**Figure 5.4.** Phase-loop frequency correction $\Delta\omega_{\mathrm{pl}}$ (blue, left axis) and radial-loop frequency correction $\Delta\omega_{\mathrm{rl}}$ (green, right axis) as a function of the cycle time. Phase noise is injected into the phase loop only between 450 ms and 600 ms (red line). Phase and radial loops are always active. The figure refers to a simulation in a single RF system with $V_{\mathrm{rf},1} = 16$ kV including collective effects for after-upgrade LHC-nominal beams, where the RF phase noise increases the bunch emittance in a controlled way from 1.4 eVs to 3 eVs.

As discussed above, the injection of RF phase noise into the phase loop suggests the use of non-flat noise spectral densities. Therefore, an exponential $S_{\mathrm{noise}}$ was adopted. Figure 5.5 shows the bunching factor (blue) from C450 to C700. For comparison, the same simulation was repeated using flat noise spectral densities with and without inclusion of phase and radial loops (the amplitudes for $S_{\mathrm{noise}}$ were selected in order to obtain 3 eVs at flat top). Figure 5.5 shows the bunching factor evolutions also for these two additional configurations. Due to stronger bunch-core diffusion, an exponential $S_{\mathrm{noise}}$ gives a higher bunching factor at C700 than the one obtained using a flat spectral density, implying larger reductions in longitudinal space charge effect and transverse space charge tune spread. Similarly, if $S_{\mathrm{noise}}$ is

flat, the configuration where phase and radial loops are neglected leads to a larger $B_f$ at C700, since there is no counteracting effect coming from the loops which would slow down the bunch-core diffusion.

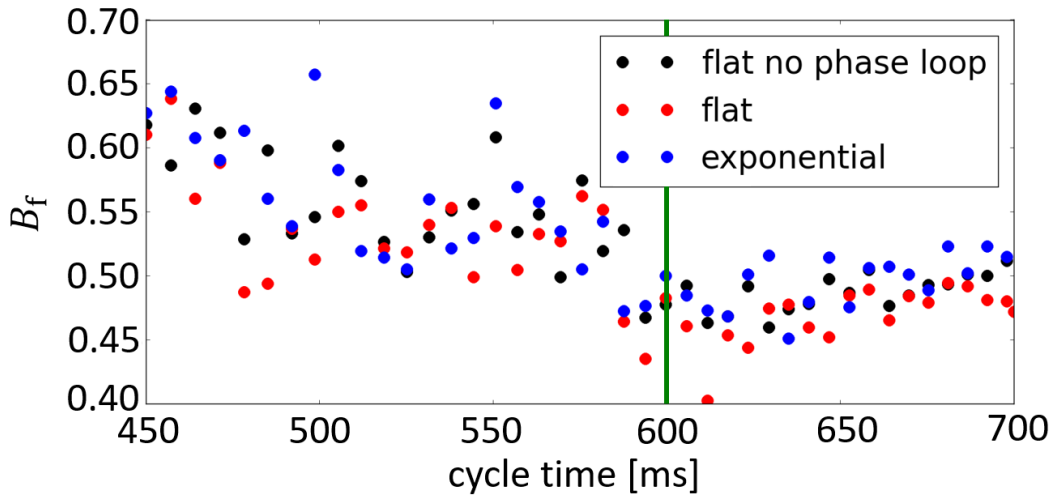


**Figure 5.5.** Bunching factor (blue) as a function of the cycle time using in simulation the same parameters and conditions described in the caption of Fig.5.4. Changing the shape of the noise spectral density from exponential to flat the red dots are obtained. Neglecting the phase and radial loops while using a flat spectral density, the black dots are obtained. Phase noise injection ends at 600 ms (green line). The emittance at 700 ms is $\epsilon_l = 3$ eVs for the three shown configurations.

### 5.4.2 A Possible Realistic Cycle

Using the more realistic voltage programs described in Fig.(4.31), and as already mentioned in Subsection 4.7.1, it was possible to increase the emittance of LHC-type beams from 1.4 eVs to the requested 3 eVs injecting RF phase noise through the phase loop in the time interval C550–C650 without observing any instability. Figure 5.6 shows the bunch distribution in the longitudinal phase space at C616 ($\epsilon_l = 1.9$ eVs) and C757 ($\epsilon_l = 3.0$ eVs), respectively during and after phase noise injection.

As was done for the simulations in a single RF system presented above (see for example Fig.5.4), phase and radial loops were applied also after C650 in order to quickly damp the residual dipole oscillations coming from the RF phase noise injection, see Fig.5.7.

The simulation results obtained in this Section for the nominal-LHC beams in the after-upgrade scenario suggest that RF phase noise could be successfully injected into the phase loop of the $h = 1$ RF system if a proper choice of the numerous concerned parameters is done. As expected, these promising results also show as a by-product that the limited phase-loop sampling-rate of 10 µs should not be an issue.

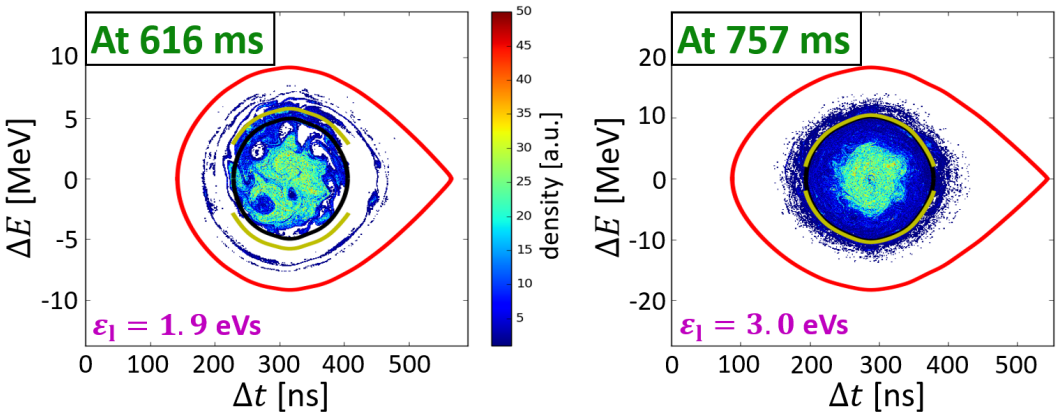


**Figure 5.6.** Bunch distribution at cycle time C616 (left) and C757 (right), respectively during and after RF phase noise injection, for nominal-LHC beams in the after-upgrade scenario using the voltage programs in Fig.(4.31). Phase noise is injected through the phase loop during C550–C650. Collective effects are included. The yellow and black curves correspond respectively to the particle trajectories determined by the Foot Tangent Method and $\tau 5$ conventions for bunch-length calculation. The emittances are $\epsilon_l = 1.9$ eVs (left) and $\epsilon_l = 3.0$ eVs (right).

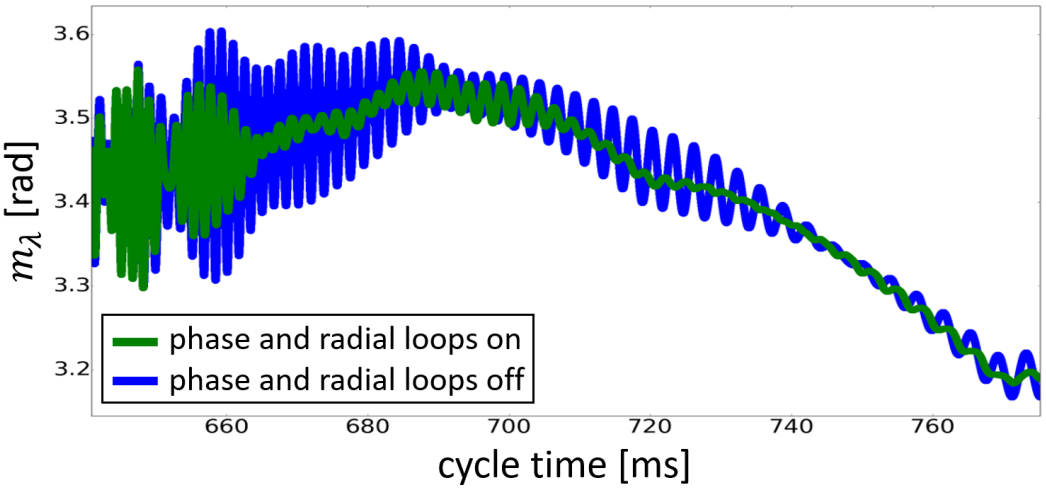


**Figure 5.7.** Average bunch position as a function of the cycle time, from 650 ms (end of RF phase noise injection) to 775 ms (flat top). Phase and radial loops are either on (green) or off (blue). The parameters and conditions of these simulations are described in the caption of Fig.(5.6).

## 5.5 Beam Measurements in Current Situation

After the new method was shown to work in simulations, numerous measurements have been performed in 2017 to verify if RF phase noise injection into the phase loop at $h = 1$ could substitute (or even complement) the high-harmonic phase modulation for different machine and beam parameters. In this Section we report the results of those measurements. For all the cases the noise was injected through the phase loop and not directly into the cavity. Notice that with the direct injection of the noise

into the $h = 1$ RF system, the phase and radial loop gains can be set to zero to avoid counteracting the phase noise. However all the measurements showed that the phase loop is essential in the PSB to damp dipole oscillations caused for example by noise in the magnetic and RF frequency programs. For this reason direct phase noise injection into the main harmonic RF system would not provide any advantage.

### 5.5.1 LHC25ns Beams

The LHC25ns beam is the present operational and also expected future beam for proton physics in the LHC [119]. The generation of LHC-batches with a 25 ns bunch-spacing is done in the PS using a multiple splitting technique [120]. The intensity per bunch is $N_\mathrm{b} \approx 1.65 \cdot 10^{12}$ ppb at PSB extraction, the emittances at injection and extraction are respectively 1.0 eVs and 1.3 eVs. Controlled longitudinal emittance blow-up is achieved using the high-frequency modulation generated by the C16 cavity, phase and radial loops are active all along the acceleration cycle. The ramp is done in a double RF system with $V_{\mathrm{rf},1} = 8$ kV and $V_{\mathrm{rf},2} = 6$ kV with relative phase in bunch lengthening mode until cycle-time C700, then the $h = 2$ RF voltage is dropped to zero so that the bunch length at extraction (180 ns) is compatible with the specifics required by the PS [121].

The application of phase-noise blow-up to the LHC25ns beam was the first to be examined due to its importance for present and future operation. All the currently operational beam parameters were kept, except that the C16 RF system was disabled. Two emittance values at extraction were targeted, 1.40 eVs (close to the present one) and 2.75 eVs (close to the value of 3 eVs required after upgrade).

Figures 5.8 and 5.9 show that it was possible to reach the targeted emittances at PSB flat-top (cycle-time C798) with correct choice of parameters for phase noise, radial and phase loops. Notice that, given a certain emittance and as a general beam quality criterion used in the PSB operation, bunches which have a bi-dimensional phase-space distribution closer to a uniform one are more desired, due to the fact that their bunching factor and rms bunch-length are larger, leading to reduced longitudinal and transverse space charge effects. As an example, the distributions shown in Figs.5.8 and 5.9 are quite satisfactory.

#### Generation of RF Phase Noise for LHC25ns Beams

The phase noise was generated numerically as described in the Sections above, before being used into the LLRF system during measurements, adjusting slightly the rms amplitude $\phi_\mathrm{noise}^\mathrm{rms}$ for each of the four rings. Taking as an example the emittance blow-up up to 1.40 eVs (the case of 2.75 eVs is conceptually the same), the phase noise program in the time interval C500–C600 was regenerated every 10 ms to follow the revolution and synchrotron frequency changes along the acceleration cycle.

Figure 5.10 shows the calculated synchrotron frequency distribution at C500 and C600 with the corresponding frequency bands used both in simulations and measurements. Since in this particular case the desired blow-up was small (from 1 eVs to 1.4 eVs) $f_\mathrm{down}$ was just 90% of the synchrotron frequency of the two lobe centers.

The value for $f_\mathrm{up}$ was chosen to match $f_\mathrm{s0}$ of the left-lobe synchronous phase

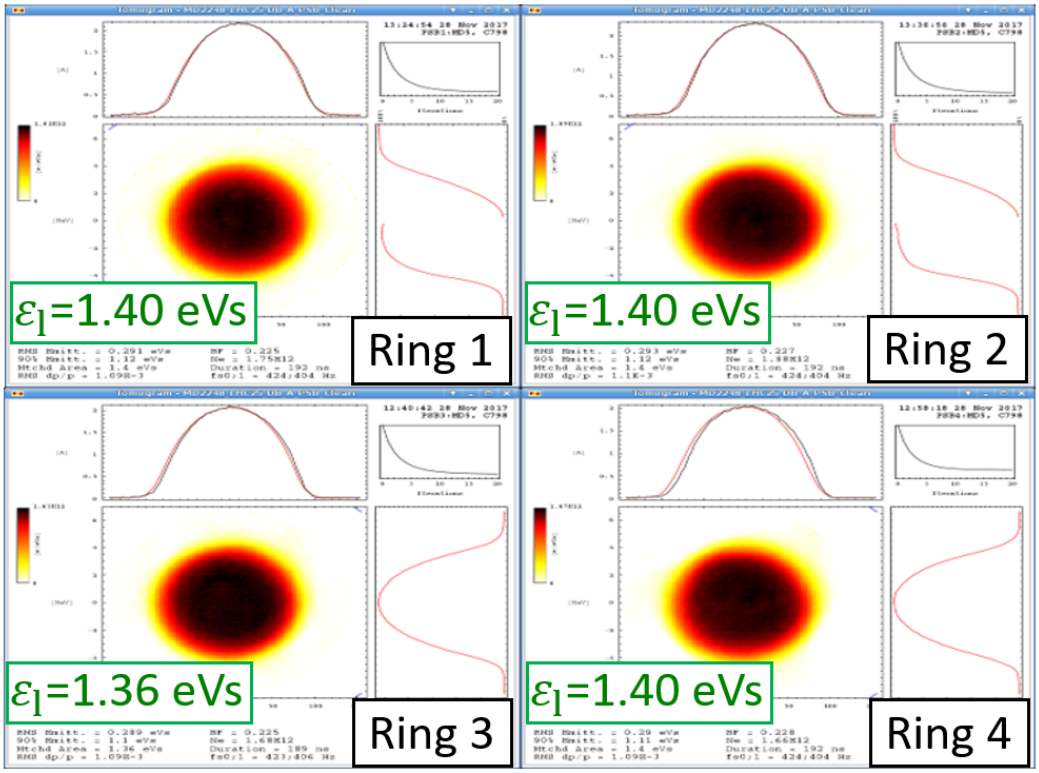


**Figure 5.8.** Reproduced phase space of measured LHC25ns bunches ($N_b \approx 1.65 \cdot 10^{12}$ ppb) using tomography at extraction energy ($E_{kin} = 1.4$ GeV) for the four PSB rings. Controlled longitudinal emittance blow-up is obtained through injection of RF phase noise into the phase loop of the C02 cavity. Phase noise is injected in the time interval 500 ms–600 ms, with the C04 RF system used in bunch lengthening mode ($V_{rf,1} = 8$ kV, $V_{rf,2} = 6$ kV). As needed, the emittances are $\epsilon_l \approx 1.4$ eVs.

(higher than the right one because of acceleration). In this way the noise bands covered completely the two bunch cores with some safety margin to account for possible imprecise estimations of the synchrotron frequency shift due to longitudinal space charge effects.

Notice that the two discontinuities of the emittance curve (blue) in Fig.5.10 are due to the inner separatrix confining the two internal lobes in phase space, see for example Fig.5.11): the emittance increases by a factor of two in correspondence of these two discontinuities since the trajectory just outside the inner separatrix includes both lobes.

It was possible to reproduce in simulations what was obtained in measurements. More specifically, performing a simulation including collective effects, using the same noise program as employed in measurements and adding phase and radial loops with the same gains used in operation ($G_{pl} = 0.2$, $G_{rl} = 3$, $g_{pl} = 3000\ s^{-1}\,rad^{-1}$, $g_{rl} = 2.2\ s^{-1}\,m^{-1}$), it was possible to obtain an emittance of 1.4 eVs at extraction energy. This result, in addition to prove the success of RF phase noise blow-up, confirms that simulation results are reliable.

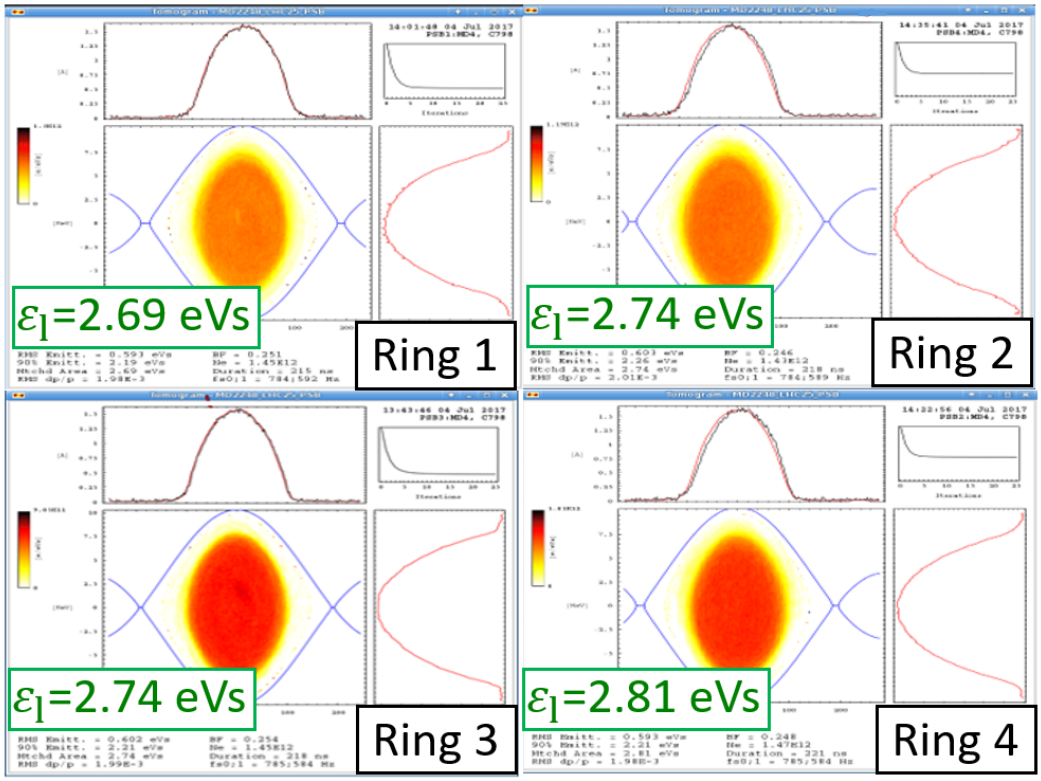


**Figure 5.9.** Phase space of measured LHC25ns bunches at PSB flat top, see parameters and conditions in the caption of Fig.5.8. As needed, the emittances are $\epsilon_l \approx 2.75$ eVs.

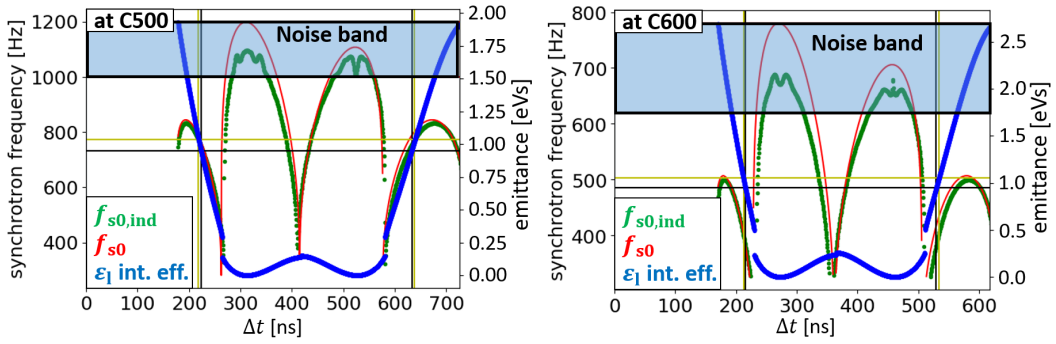


**Figure 5.10.** Synchrotron frequency distribution in simulation with and without intensity effects (green and red respectively) as a function of the particle position $\Delta t \in [0, T_0]$ at cycle-times C500 (left) and C600 (right). The emittance $\epsilon_l$ (blue) as a function of $\Delta t$ is also shown, taking into account collective effects. The vertical black and yellow lines mark the bunch lengths of a 1 eVs bunch using two different conventions (the horizontal lines mark the corresponding emittance values). Figure 5.11 shows the corresponding distributions in phase space.

### 5.5.2 ISOLDE Beams

The ISOLDE beam, already introduced in Section 4.7, usually consists of relatively high intensity. Currently $N_b \approx 8{\cdot}10^{12}$ ppb and $\epsilon_l = 1.8$ eVs at extraction energy [119].

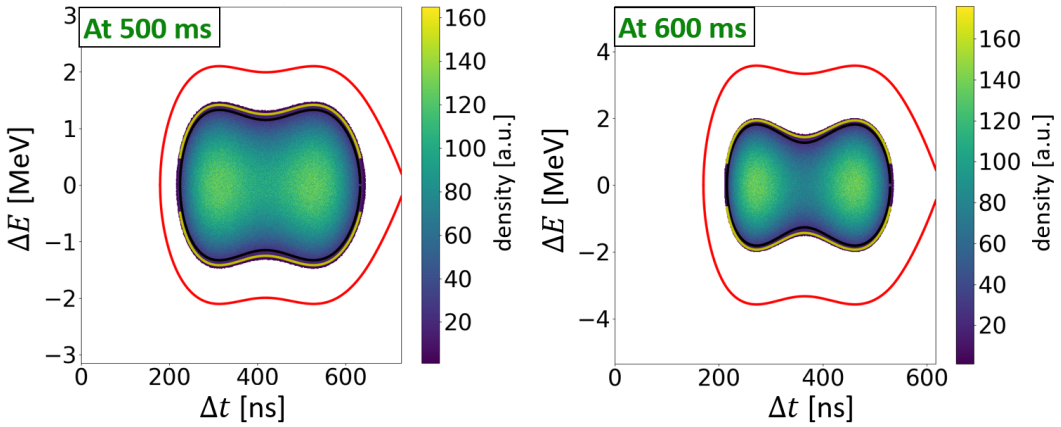


**Figure 5.11.** Simulated bunch distributions at C500 (left) and C600 (right) matched inside the RF bucket with intensity effects ($\epsilon_l = 1.0$ eVs). These bunches correspond to the ones mentioned in the caption of Fig.5.10.

The beam quality at extraction is not as important as for the LHC25ns beams.

The acceleration cycle until time C700 is done in a double RF system with $V_{rf,1} = 8$ kV and $V_{rf,2} = 8$ kV with relative phase set in bunch lengthening mode in order to maximize the longitudinal acceptance. After time C700, the C04 RF voltage is slowly ramped down to 2 kV. Phase and radial loops are active all along the acceleration cycle.

The same noise program as used for the LHC25ns beams was applied for this beam adjusting only the noise rms amplitude in order to reach $\epsilon_l = 1.8$ eVs at extraction energy. Note that, due to the higher bunch intensity, the synchrotron frequencies at the centers of the two lobes in phase space are approximately 100 Hz lower than the ones relative to the LHC25ns case, and therefore the adopted noise program was not optimal. However, knowing that the blow-up settings of the C16 RF system for ISOLDE beams are very different from the ones for LHC25ns beams and as a consequence not-negligible time is usually needed for setting up, the goal of the measurements was to prove that the same RF phase noise program can be used for two quite different beams obtaining results comparable to the ones had with the C16 cavity.

Indeed, Fig.5.12 shows that at extraction energy the beam qualities using the C16 RF system and the RF phase noise are comparable.

### 5.5.3 SFTPRO–MTE Beams

The SFTPRO–MTE beam is directed to the SPS for fixed-target physics experiments [119, 122]. The acronym MTE stands for Multi-Turn Extraction, which is a resonant extraction mechanism used in the PS when dealing with this particular type of beam [123].

The SFTPRO–MTE beam, which has $N_b \approx 5 \cdot 10^{12}$ ppb and $\epsilon_l \approx 1.0$ eVs at injection energy, needs $\epsilon_l \approx 2.6$ eVs at cycle time C700. A bunch splitting after C700 produces at extraction energy two bunches having each $N_b \approx 2.5 \cdot 10^{12}$ ppb and $\epsilon_l \approx 1.3$ eVs. The acceleration cycle is performed in a double RF system until time

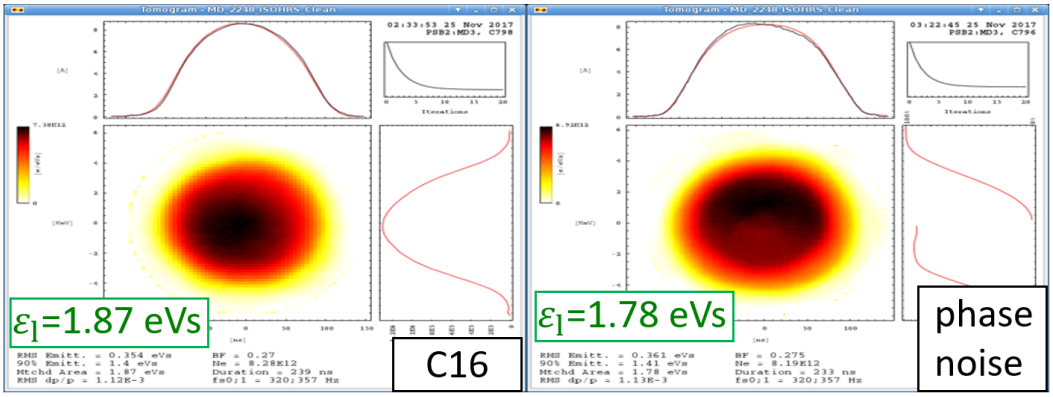


**Figure 5.12.** Reproduced phase space of measured ISOLDE bunches ($N_b \approx 8 \cdot 10^{12}$ ppb) using tomography at extraction energy ($E_{kin} = 1.4$ GeV). Controlled longitudinal emittance blow-up is obtained either using the C16 cavity (left) or injecting RF phase noise into the phase loop of the C02 cavity (right). Phase noise is injected in the time interval 500 ms–600 ms, with the C04 RF system used in bunch lengthening mode ($V_{rf,1} = 8$ kV, $V_{rf,2} = 8$ kV). As needed, the emittances are $\epsilon_l \approx 1.8$ eVs.

C700 using $V_{rf,1} = 8$ kV and $V_{rf,2} = 8$ kV with relative phase set in bunch-lengthening mode. From 700 ms to 800 ms, RF manipulations are performed to split the bunch. The C16 RF system acts for 200 ms in the interval 500 ms–700 ms in order to increase the emittance from 1 eVs to 2.6 eVs. Phase and radial loops are active all along the acceleration cycle.

Injecting RF phase noise during only 110 ms (from 550 ms to 660 ms) after a proper analysis of the synchrotron frequency distributions along the cycle as it was done for the LHC25ns beams, it was possible to obtain at extraction energy bunches of much better quality as compared to the ones had with the C16 cavity, see Fig.5.13.

### 5.5.4 BCMS Beams

The BCMS (Batch Compression, Merging and Splitting) has been the main operational beam for most of the year 2018 and will possibly be the next production beam for proton physics in the LHC after LIU upgrade, replacing the present LHC25ns beam [124, 119].

The BCMS beam ($N_b \approx 0.85 \cdot 10^{12}$ ppb) is currently accelerated in a single RF system with $V_{rf,1} = 8$ kV. No controlled emittance blow-up is required ($\epsilon_l \approx 0.9$ eVs along the ramp), however the C16 cavity is still active to affect only the bunch core reducing the line density amplitude and increasing the rms emittance. Phase and radial loops are active all along the acceleration cycle.

Knowing by experience from the previously examined types of beam the effectiveness of injecting RF phase noise in a double RF system with relative phase in bunch-lengthening mode, the C04 RF system with $V_{rf,2} = 6$ kV was added in measurements during the time interval 500 ms–600 ms. The noise was applied just for 20 ms, contrary to the 50 ms required by using the C16 cavity.

Figure 5.14 shows that the phase noise method can provide a bunch with better

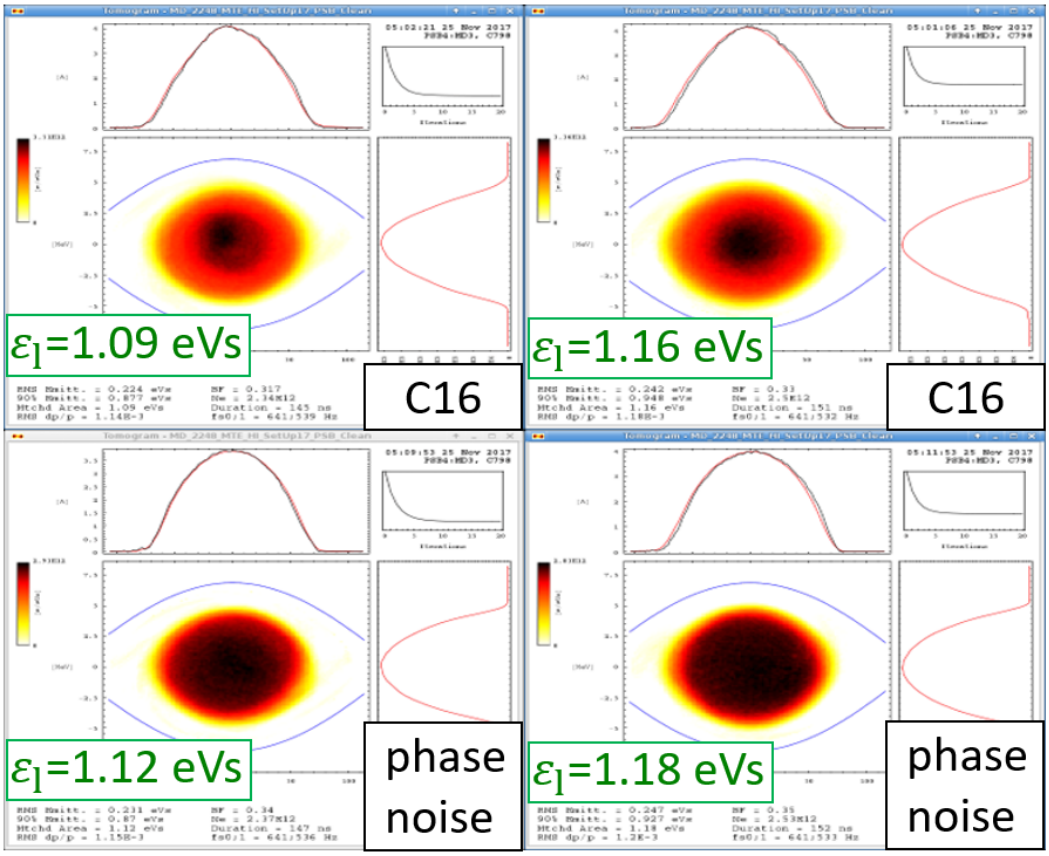


**Figure 5.13.** Phase space of measured SFTPRO–MTE bunches ($N_b \approx 5 \cdot 10^{12}$ ppb, $\epsilon_l \approx 2.6$ eVs before time C700) reproduced using tomography at extraction energy ($E_{kin} = 1.4$ GeV). RF manipulations between time C700 and flat top split the bunch into two bunches (left and right) having each $N_b \approx 2.5 \cdot 10^{12}$ ppb and $\epsilon_l \approx 1.3$ eVs. Controlled longitudinal emittance blow-up is obtained either using the C16 cavity for 200 ms (top) or injecting RF phase noise into the phase loop of the C02 cavity for 110 ms (bottom). Phase noise is injected with the C04 RF system used in bunch lengthening mode ($V_{rf,1} = 8$ kV, $V_{rf,2} = 8$ kV).

quality with respect to the result obtained using the C16 cavity: even if $\epsilon_l = 0.85$ eVs and $\epsilon_l = 0.843$ eVs using the C16 RF system and phase noise respectively, the rms emittance is higher injecting phase noise.

### 5.5.5 LHCINDIV Beams

The most difficult beam to prove that phase noise injection can replace the C16 high-harmonic modulation was the LHCINDIV type. This beam, due to its wide range in relatively-low bunch intensity and emittance values, is required in the commissioning filling patterns for the LHC and is also used for beam-physics studies in the PS and SPS [125, 119].

The RF cavities which are used during the acceleration cycle are the C02 and C16. The C16 RF system is used not for controlled emittance blow-up but for longitudinal shaving, which regulates the bunch intensity from $N_b \approx 2 \cdot 10^{10}$ ppb to

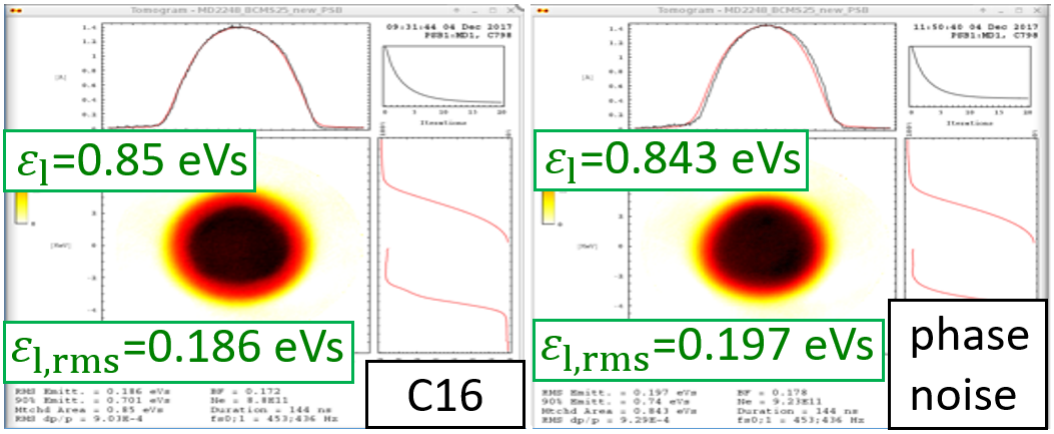


**Figure 5.14.** Reproduced phase space of measured BCMS bunches using tomography at extraction energy ($E_{kin}$ = 1.4 GeV). The intensity and emittance at flat top are respectively $N_b \approx 0.85 \cdot 10^{12}$ ppb and $\epsilon_l \approx 0.9$ eVs. No controlled longitudinal emittance blow-up is performed along the ramp, only rms-emittance increase is needed either using the C16 cavity (left) or injecting RF phase noise into the phase loop of the C02 cavity (right). Phase noise is injected adding the C04 RF system in bunch lengthening mode ($V_{rf,1} = 8$ kV, $V_{rf,2} = 6$ kV).

$N_b \approx 12 \cdot 10^{10}$ ppb. More precisely, in the interval 300 ms–400 ms, the $h = 1$ RF voltage is such that the zero-amplitude synchrotron frequency is constant during acceleration. This allows a proper action of the high-frequency modulation generated by the C16 cavity during this same time interval: since the bucket is full, increasing properly the voltage of the C16 cavity allows to push particles close to the separatrix outside of the bucket.

After the end of the longitudinal shaving at 400 ms when the needed intensity is reached, the C02 RF voltage is dropped during the next 20 ms to decrease the bucket area and obtain the desired emittance which will be preserved up to extraction energy (usually $\epsilon_l \approx 0.3$ eVs). Finally the voltage of the main RF system is increased up to 8 KV and then is kept constant until flat top, see Fig.5.15 (left). Phase loop is active all along the acceleration cycle, radial loop is unemployed.

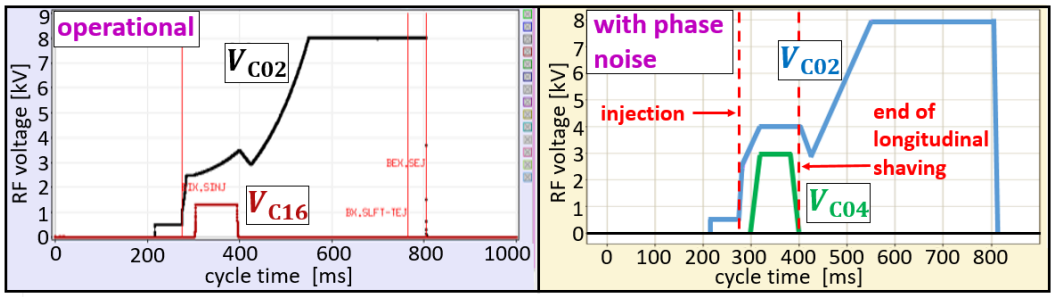


**Figure 5.15.** Operational (left) and proposed (right) RF voltage programs for LHCINDIV beams. For the proposed ones, the C16 cavity is disabled and RF phase noise is injected into the phase loop of the C02 cavity adding the C04 RF system in bunch-lengthening mode. Both the C16 RF system and phase noise are used for longitudinal shaving and not for controlled emittance blow-up.

Following the same reasoning adopted for all the previous examined beams, the C16 RF system was disabled in favor of the phase noise which was injected into the phase loop of the C02 cavity while keeping the C04 RF system in bunch-lengthening mode. Voltages $V_{\mathrm{rf},1}$ and $V_{\mathrm{rf},2}$ were set respectively to 4 kV and 3 kV to keep the same voltage ratio as for $V_{\mathrm{rf},1} = 8$ kV and $V_{\mathrm{rf},2} = 6$ kV which proved to be effective during blow-up for the other beams, see Fig.5.15 (right).

Figure 5.16 shows examples of LHCINDIV beams at extraction energy, where $\epsilon_{\mathrm{l}} \approx 0.3$ eVs and $N_{\mathrm{b}} \approx 1.0 \cdot 10^{11}$ ppb, using either the C16 cavity or the phase noise for longitudinal shaving: it can be seen that the beam qualities are similar.

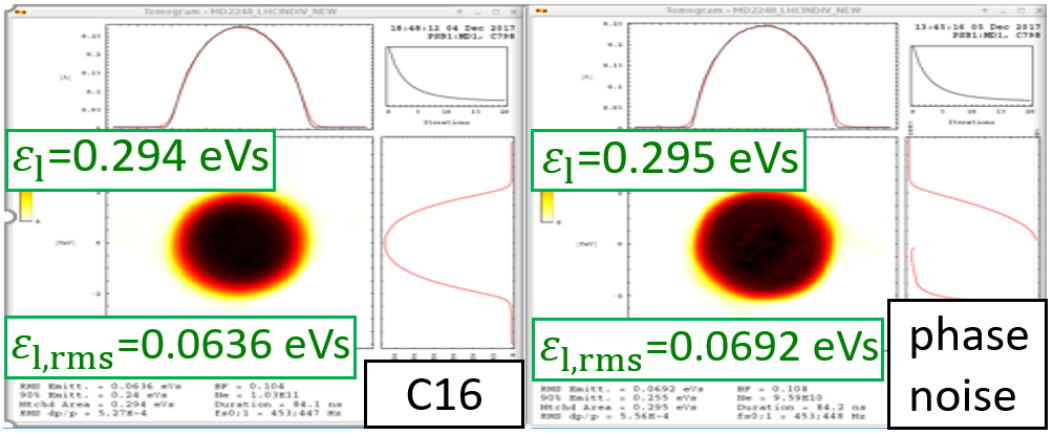


**Figure 5.16.** Reproduced phase space of measured LHCINDIV bunches using tomography at extraction energy ($E_{\mathrm{kin}} = 1.4$ GeV). The bunch intensity and emittance at flat top are respectively $N_{\mathrm{b}} \approx 1.0 \cdot 10^{11}$ ppb and $\epsilon_{\mathrm{l}} \approx 0.3$ eVs. These last two values are respectively obtained through longitudinal shaving in 300 ms–400 ms and decrease of the $h = 1$ RF voltage in 400 ms–420 ms. The longitudinal shaving is obtained either using the C16 cavity (left) or injecting RF phase noise into the phase loop of the C02 cavity (right). Phase noise is injected adding the C04 RF system in bunch-lengthening mode ($V_{\mathrm{rf},1} = 4$ kV, $V_{\mathrm{rf},2} = 3$ kV). No controlled longitudinal emittance blow-up is performed along the ramp.

Finally, after having obtained an emittance $\epsilon_{\mathrm{l}} = 0.3$ eVs through a proper decrease of the $h = 1$ RF voltage in 400 ms–420 ms, it was possible to extract different bunch intensities, or equivalently to obtain during shaving distinct amounts of particle losses, through a proper variation of the noise rms-amplitude in 320 ms–330 ms. Afterwards, the phase noise was kept active with constant rms-amplitude in 330 ms–380 ms only to diffuse the particles in the bunch-core and increasing, as a result, the rms emittance. Figure 5.17 shows the outcome of this phase-noise program design: the beam quality at extraction energy is remarkable, independently of the needed intensity.

## 5.6 Conclusions

Controlled longitudinal emittance blow-up for nominal-LHC beams in the PSB will be necessary after LIU-upgrade for proper reduction of transverse space charge effects at PS injection. This Chapter focused on an alternative to the present operational

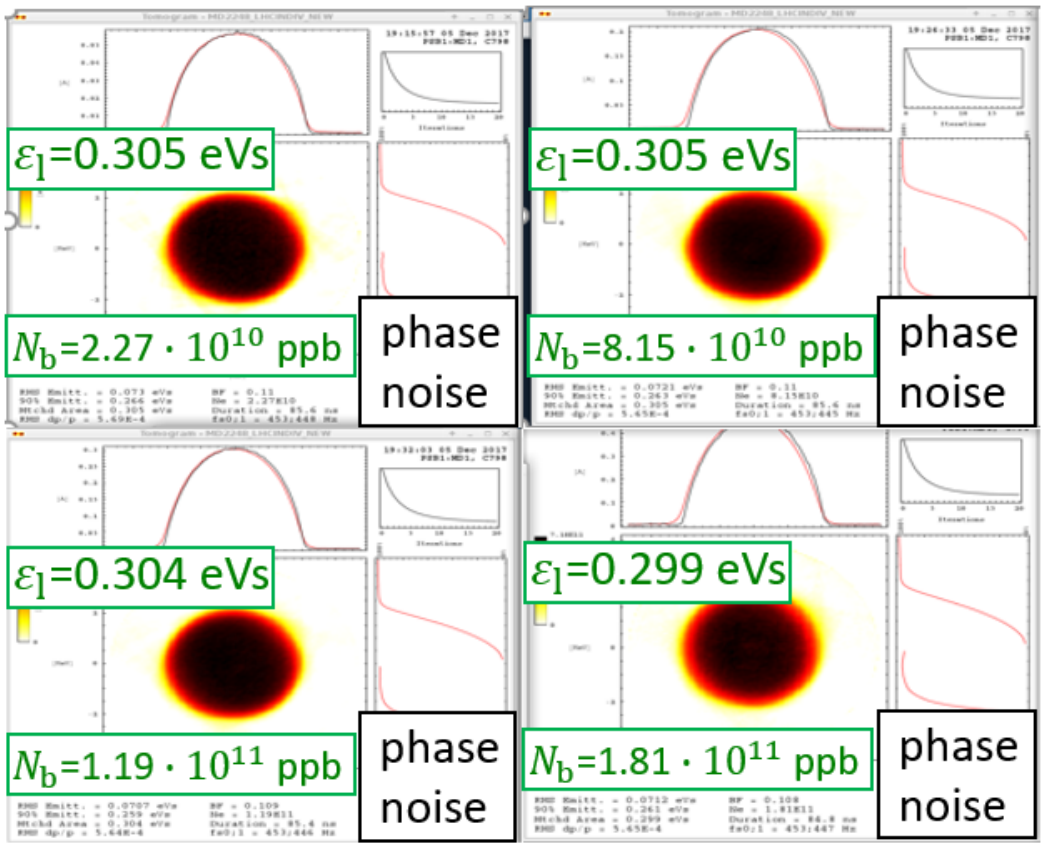


**Figure 5.17.** Reproduced phase space of measured LHCINDIV bunches using tomography at extraction energy ($E_{\text{kin}} = 1.4$ GeV). The emittance $\epsilon_l \approx 0.3$ eVs is determined by a proper decrease of the $h = 1$ RF voltage in 400 ms–420 ms. The different shown intensities are obtained performing longitudinal shaving through injection of RF phase noise into the $h = 1$ phase-loop in 320 ms–380 ms. Phase noise is injected adding the C04 RF system in bunch lengthening mode ($V_{\text{rf},1} = 4$ kV, $V_{\text{rf},2} = 3$ kV).

method of RF high-frequency modulation for emittance blow-up: the injection of band-limited RF phase noise into the main harmonic RF system.

After having presented the main advantages of this suggested method which was never tried in the PSB, the principle behind phase noise has been explained, together with the procedure for its numerical generation. Since it is expected that phase noise will be injected into the phase loop of the main harmonic RF system, an accurate model of the PSB Low Level RF phase and radial loops has been created and then implemented into the BLonD code. Benefiting also of what presented in the previous Chapter, it was possible to perform realistic simulations of the PSB longitudinal beam dynamics from injection to extraction energies including collective effects, RF manipulations and LLRF feedbacks.

The simulation results for future nominal-LHC beams showed that bunch excitation with phase noise can provide the required significant controlled longitudinal emittance blow-up in a fast-cycling machine with strong space charge like the PSB. For an optimized set of parameters it was possible to increase the bunch emittance

from 1.4 eVs to 3 eVs applying the RF phase noise only for 100 ms and using a possible realistic acceleration cycle. Since phase noise was applied without performing at the meantime any bunch shaping using the $h = 2$ RF system, phase-loop slowed down the diffusion process for particles located in the bunch-core and having synchrotron frequencies close to the zero-amplitude one. Therefore it was emphasized the importance of using non-flat noise spectral densities to compensate for this undesired effect which increases the peak line density and therefore space charge effects.

Finally numerous measurements of present operational PSB beams have been performed in order to test RF phase noise in the current scenario and predict its reliability for the future. The main result concerns the nominal-LHC beams: it has been possible to increase their longitudinal emittance from 1 eVs to 3 eVs in just 100 ms, suggesting that a similar result could be attained in the future. Moreover, four additional types of PSB beam, with very different features from each other, have been examined in order to prove that phase noise will be able to completely replace, or at least complement, the currently-used RF high-frequency modulation. It was found that RF phase noise, when applied during acceleration in a double RF system with relative phase set in bunch-lengthening mode, is able to successfully cover all the scenarios presently available in operation.

# Chapter 6

# SPS Ions: Slip-stacking

## 6.1 Introduction

The HL-LHC Project at CERN aims at doubling the peak luminosity of the Pb-ion beam after upgrade (2019-2021) [3]. To fulfill this requirement, the baseline of the LIU Project includes the decrease of the bunch spacing in the SPS from 100 ns to 50 ns through momentum slip-stacking (MSS) [3]. This technique, already used in operation in Fermilab [126], allows two batches with slightly different momenta to slip relative to each other before being stacked one on top of the other. An RF voltage high enough to recapture the stacked bunches allows to double the bunch intensity at the end of the process. A variant of MSS is considered in the SPS: the two batches are not stacked on top of each other, but interleaved (see Fig.6.1). This provides the desired bunch spacing reduction while the bunch intensity remains unchanged.

Momentum slip-stacking in the SPS is potentially feasible thanks to the planned upgrade of the 200 MHz traveling-wave cavities (TWC) [19]. These will be divided into two groups and the RF frequency of each group will be tuned to one batch. Since independent LLRF controls for the two groups will be available only in 2021, macro-particle simulations in the longitudinal plane are the only means to verify the MSS feasibility (alternative scenarios for bunch spacing decrease are being also considered [127]).

Preliminary simulations performed in 2014 showed promising results [128], however collective effects were not included and bunch parameter variations along the batches were not taken into account. In the present work a more elaborated study is presented. Beam measurements have provided realistic beam parameters which were used as initial conditions in simulations. Collective effects were included, using the latest longitudinal impedance model. Momentum and RF programs were designed to be used during and after MSS. Effort was spent to develop algorithms able to speed up the settings of the large number of parameters involved during MSS optimization. The CERN macro-particle simulation code BLonD [12] has been used for the studies.

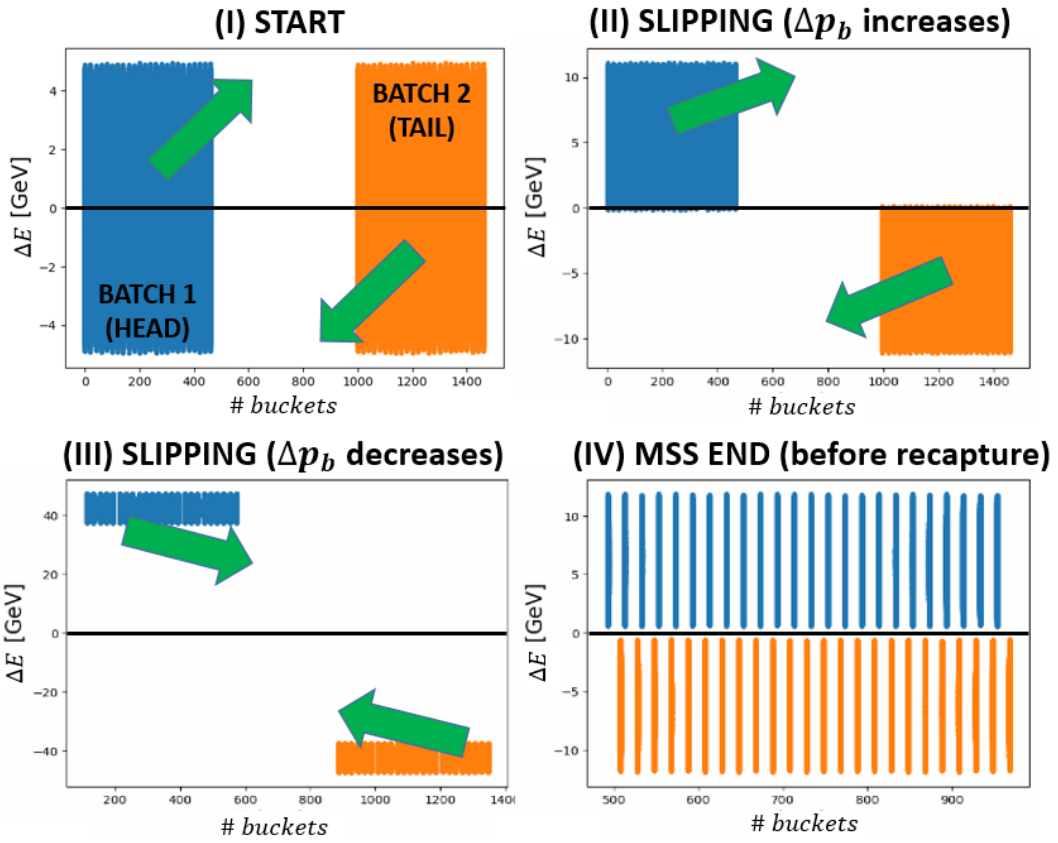


**Figure 6.1.** Example of planned MSS procedure in the SPS. The two batches, starting from Phase I, move in longitudinal phase space relative to each other. The black line marks $\Delta E = E - E_0 = 0$, where $E_0$ is the design energy. In Phase II the distance in momentum $\Delta p_b$ between the batches increases, while the opposite happens in Phase III. Recapture is done in Phase IV. The reference frame is synchronized with the design revolution period $T_0$.

## 6.2 Slip-stacking Principle

Momentum slip-stacking is usually performed at constant magnetic field $B_0$. The design momentum $p_0$ is then defined by the magnetic-rigidity formula introduced in Chapter 2

$$B_0 R_0 = p_0/q. \tag{6.1}$$

Keeping the magnetic field constant and using linear approximation, the following relations hold (see Chapter 2)

$$\frac{\Delta\omega_{\mathrm{rf}}}{\omega_{\mathrm{rf},0}} = -\eta_0 \frac{\Delta p}{p_0} = -\eta_0 \gamma_{\mathrm{tr}}^2 \frac{\Delta R}{R_0}. \tag{6.2}$$

The design $\omega_{\mathrm{rf},0} = h f_{\mathrm{rf},0}$ (with $h$ the harmonic number) can be derived from $p_0$, as well as the design $\gamma_0$. All the variables in Eq.(6.2) represent changes with respect to the corresponding design quantities. In a reference frame synchronized with the design revolution period $T_0$ (see the definition for $\Delta t$ in Chapter 2) a variation $\Delta\omega_{\mathrm{rf}}$

implies a change in the RF phase according to

$$\Delta\phi_{\mathrm{rf}} = \frac{2\pi h \Delta\omega_{\mathrm{rf}}}{\omega_{\mathrm{rf},0}}, \tag{6.3}$$

see Eq.(2.87).

Taking as an example the case in Fig.6.1 ($\eta_0 > 0$), the head batch will gain momentum when the RF frequency of the corresponding RF system is decreased. According to Eqs.(6.2) and (6.3) the batch will be displaced radially outwards while slipping to the right in phase. An analogous but opposite reasoning applies to the second batch.

The group of RF cavities which is not synchronized with the batch perturbs its motion. The severity of the perturbation is linked to the distance between batches in time and momentum. Indeed, the RF perturbation affects the batches only when their time-distance is smaller than the cavity filling time, which is approximately 1 µs (200 buckets) due to the relatively low quality-factor of the fundamental mode of the 200 MHz TWCs. For larger time-distances the different RF cavities can be safely switched on and off according to bunch passage time in order to completely avoid the RF perturbation (see Subsection 6.3.3).

The distance between batches in momentum also affects the severity of the RF perturbation, which in this case can be described by the slip-stacking parameter [129]

$$\alpha \doteq \frac{\Delta f_{\mathrm{rf,b}}}{f_{\mathrm{s0}}} = 2\frac{\Delta E_{\mathrm{b}}}{H_{\mathrm{b}}}, \tag{6.4}$$

where $\Delta f_{\mathrm{rf,b}}$ and $\Delta E_{\mathrm{b}}$ are respectively the differences in RF frequency and total energy between the two batches, $f_{\mathrm{s0}}$ is the zero amplitude synchrotron frequency of the unperturbed bucket and $H_{\mathrm{b}}$ is half of the bucket height. When $\alpha = 4$, the separatrices of the buckets associated with the two independent RF systems are tangent to each other. This value has been proven to be a lower limit for dynamic stability of the system [129]. If $\alpha \gg 4$, the perturbation averages within a synchrotron period and its effect is less damaging. However a large $\alpha$ at the end of MSS implies a higher RF voltage needed for recapture which leads to a larger emittance blow-up after filamentation. Phase IV in Fig.6.1 shows a beam configuration with $\alpha = 4$.

## 6.3 Momentum Slip-stacking in the SPS

As mentioned in Chapter 1, the LHC $Pb^{82+}$ ion beams in the SPS are currently accelerated from 17 $Z_a$GeV/c ($\gamma = 7$) to 450 $Z_a$GeV/c ($\gamma = 191$). Three different optics, called Q20, Q22 and Q26, are available in the SPS, depending on the working point adopted. In all cases, the beam energy crosses the transition energy during the first part of the ramp ($\gamma_{\mathrm{tr}}^{Q20} = 18$, $\gamma_{\mathrm{tr}}^{Q22} = 20$, $\gamma_{\mathrm{tr}}^{Q26} = 23$ [130]). The Q20 optics is currently used in operation. The accelerating RF system is the 200 MHz TWC ($h = 4620$). For proton beams, a forth harmonic RF system (800 MHz) is used in addition to the main one to enhance Landau damping [131, 23, 132]. However, this system is not used presently in operation with ion beams.

### 6.3.1 MSS Energy and SPS Momentum Program

The first choice to be made is the energy at which slip-stacking should be performed. At injection energy, poor lifetime due to the presence of relatively strong space charge, Intra-Beam Scattering (IBS) and RF noise prevent us from applying MSS there. On the other hand at flat top all particles lost during the RF manipulations would be transferred to the LHC. For these reasons an intermediate energy plateau has been chosen (300 $Z_a$GeV/c) which is quite far from the transition energy and provides a higher stability threshold as compared to the top energy.

Beam measurements in 2015 of one batch of 24 bunches accelerated in the SPS show that the beam is stable at 300 $Z_a$GeV/c [80], see Fig.6.2 which describes bunch length and position of the most unstable bunch in the batch. The bunch length $\tau_{\mathrm{FWHM,G}}$, which determines the longitudinal emittance $\epsilon_{\mathrm{FWHM,G}}$, is calculated using the full-width-half-maximum bunch length rescaled to $4\sigma_t$ of a Gaussian profile (convention used in the SPS). However, as we will see, the bunch profiles obtained after MSS are not Gaussian but they have two peaks with heights that can be different from each other while strongly varying from turn to turn. For this reason the bunch length and emittance in the present paper will be determined by the portion of the line density containing 95% of the particles.

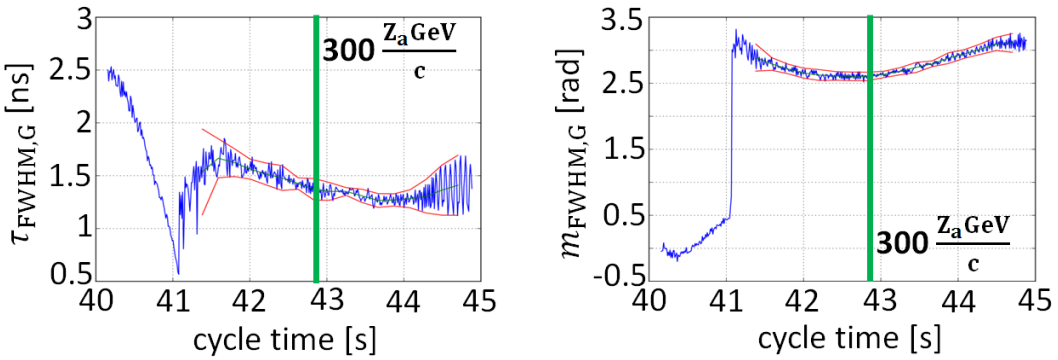


**Figure 6.2.** Beam measurements, along the operational SPS ion cycle (Q20 optics), for the fourth bunch in a batch of 24 ion bunches: full-width half-maximum bunch length rescaled to a Gaussian profile (left) and bunch position (right). The red curves correspond to the maximum amplitude of the bunch length and phase. The green vertical line marks the energy 300 $Z_a$GeV/c. The transition crossing occurs at about 41 s cycle time. Other measurements in Ref.[80] show that the third and fourth bunches in the batch are the most unstable, since they remain at flat-bottom for relatively long time without being stabilized by the LLRF phase-loop which is synchronized only with the first two bunches. *Courtesy of A. Lasheen, CERN, 2015.*

Since only integer multiples of the CERN PSB cycle (1.2 s) can be added to the currently used SPS momentum program, the length of the plateau was chosen to be 1.2 s. Figure 6.3 shows the momentum program used in simulations. Out of 1.2 s, 0.8 s were used for MSS, while 0.4 s for filamentation after recapture.

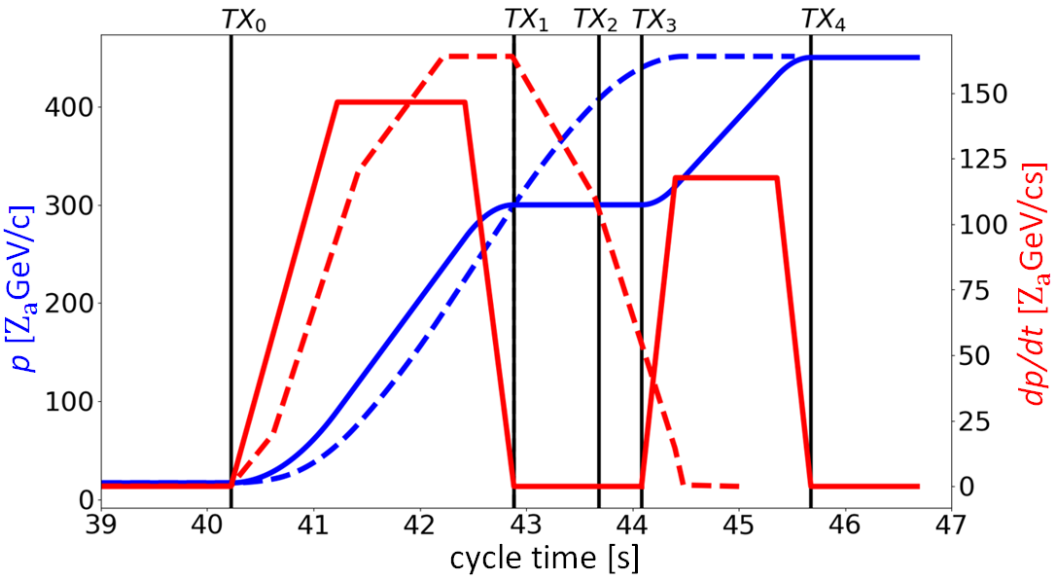


**Figure 6.3.** Operational (dashed line) and used in simulations (continuous line) momentum programs (blue) and their derivatives (red). The label $TX_0$ marks the ramp start, $TX_1$ the start of MSS, $TX_2$ the end of MSS, $TX_3$ and $TX_4$ the start and the end of the second ramp.

### 6.3.2 Initial Beam Conditions

Currently every batch accelerated in the SPS contains 24 bunches. The filling pattern at SPS flat-bottom is the following: 12 mini-batches of two bunches injected from the PS, with a bunch-spacing of 100 ns and a mini-batch spacing of 175 ns. Due to the significant losses at SPS flat-bottom, there is a remarkable variability of bunch emittance and intensity along the batch, see for example the beam measurements in Fig.6.4 showing that emittance and intensity vary respectively by a factor of 2 and 1.5 along the batch at 300 $Z_a$GeV/c [80].

In 2021 operation, the length of the flat-bottom (40 s) will be equal to the current one. However the filling pattern at SPS flat-bottom will be different: there will be 12 mini-batches of 4 bunches coming from the PS, with bunch spacing equal to 100 ns and mini-batch distance of 125 ns or, optimistically, 100 ns (assumed in simulations) [3]. The first six and the second six mini-batches will form the two batches of 24 bunches which will have to be slip-stacked. The distance between these batches has to be established according to the constraints coming from the slip-stacking programs (see next Subsection).

All the simulations shown in this Chapter start at 300 $Z_a$GeV/c, exactly when momentum slip-stacking begins. Considering Fig.6.2, we assume that all the 48 bunches are stable and matched to the RF bucket with intensity effects. Since in operation losses occur continuously along the flat bottom, it is reasonable to suppose that the bunch profiles have strong tails [80]. Therefore the initial longitudinal distribution was chosen to be binomial with relatively high $\mu = 5$, see Eq.(2.63). The beam measurements for 24 bunches in Fig.6.4 are used to extrapolate the values of intensities and emittances for the future 48 bunches: the two additional values

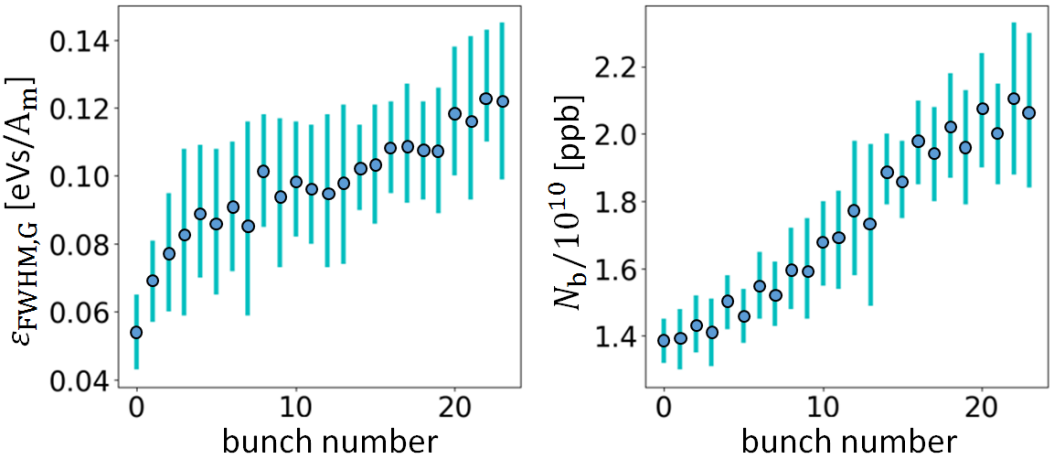


**Figure 6.4.** Measured longitudinal bunch emittance and intensity as a function of the bunch number in one batch at 300 $Z_a$GeV/c in the operational ion cycle of the SPS. Bunch number 0 is the head of the beam, bunch number 23 the tail. The error bars on the measured values are determined by one standard deviation for each side. *Courtesy of A. Lasheen, CERN, 2015.*

needed for each mini-batch of two bunches were obtained by averaging the already two measured values of the mini-batch itself.

### 6.3.3 Effects of RF Perturbations

In order to limit the perturbation of the second RF system on each batch, the two independent groups of 200 MHz cavities are switched on only when the corresponding batch passes by. Figure 6.5 shows cavity voltage measurements for the present TWCs [133]. The rise and decay times are similar and range from about 1 µs for the 4-section to 1.2 µs for the 5-section cavities. In view of the results shown in this Chapter we expect that, after LIU-upgrade, the average time $T_b^{\text{th}}$ needed to switch on and off all the cavities during MSS will be lower than now, since the relatively low required voltage for MSS can be provided only by four new 3-section cavities [134].

In slip-stacking simulations, the value of $T_b^{\text{th}} = 1$ µs is chosen: the peaks of the 4-section RF waveform shown in Fig.6.5 are fitted with a polynomial, then the obtained curve is used in the BLonD code to model the rise and decay laws of the peak RF voltages $V_{\text{rf}}^{(1)}$ and $V_{\text{rf}}^{(2)}$ of the two independent RF systems within one revolution turn, see Fig.6.6. We assumed in simulations that, at each revolution turn, $V_{\text{rf}}^{(1)}$ starts with its maximum value, since the high harmonic number of the machine relative to the amount of buckets occupied during MSS allows sufficient time to rise $V_{\text{rf}}^{(1)}$ from zero to its maximum value at each revolution turn. An analogous reasoning is valid for $V_{\text{rf}}^{(2)}$. From now on, $V_{\text{rf}}^{(1)}$ and $V_{\text{rf}}^{(2)}$ will simply denote, for each revolution turn, only the maximum values of the correspondent, just discussed, peak RF voltage functions.

It is essential that $\alpha \gg 4$ when the distance between the batches $T_b$ is equal to $T_b^{\text{th}}$ in order to minimize the perturbation effects coming from the other RF system. We assumed in simulations a relatively large $T_b = 2.7$ µs at $TX_1$, giving more priority

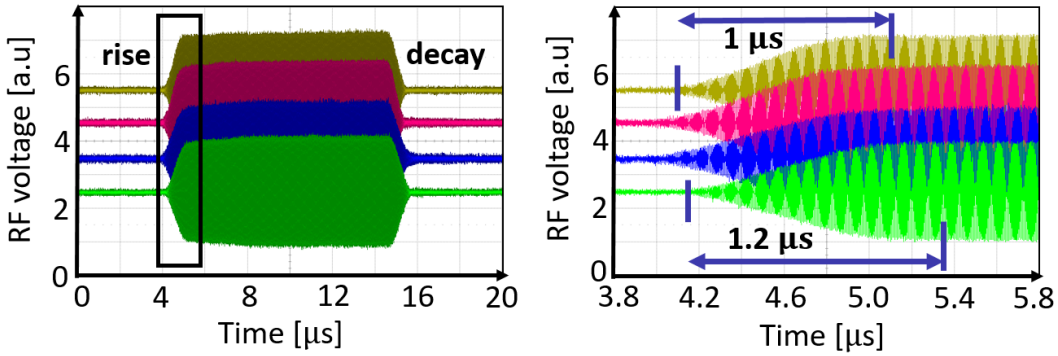


**Figure 6.5.** Left: measurements of RF voltage during batch passage as a function of time for the currently used two 4-section (top) and two 5-section (bottom) SPS traveling-wave cavities. The rise and decay of the RF voltage amplitude are clearly visible. Right: zoom on the rectangular area in the left image highlighting the times needed for the two different cavities to reach their correspondent peak voltages. *Courtesy of T. Bohl, CERN, 2018.*

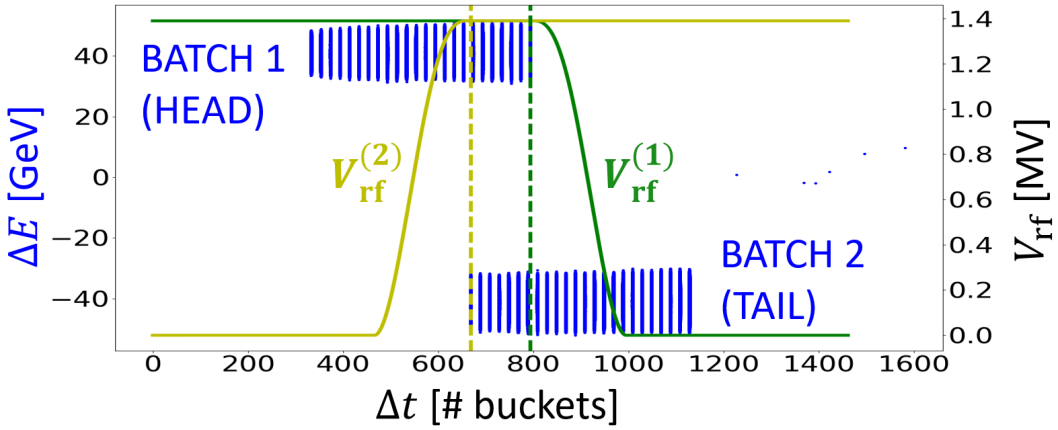


**Figure 6.6.** Example of longitudinal phase space (left axis) in simulation of momentum slip-stacking in the SPS. Two batches of 24 bunches each are shown in blue. The peak voltages of the RF systems synchronized with the head and tail batches are presented in green and yellow respectively (right axis). The rise and decay laws of $V_{\mathrm{rf}}^{(1)}$ and $V_{\mathrm{rf}}^{(2)}$ are derived from cavity voltage measurements, see Fig.6.5.

to the adiabaticity of the MSS manipulation than to the time minimization needed for it. Figure 6.7 shows an example of evolution of parameter $\alpha$ during MSS.

### 6.3.4 RF Voltage Program during MSS

During MSS, we suppose that the RF frequency shift programs of the two 200 MHz RF subsystems have opposite sign relative to $\omega_{\mathrm{rf},0}$ ($\omega_{\mathrm{rf}}^{(1)} + \omega_{\mathrm{rf}}^{(2)} = 2\omega_{\mathrm{rf},0}$) and that the two RF voltage amplitude programs are equal ($V_{\mathrm{rf}}^{(1)} = V_{\mathrm{rf}}^{(2)}$). At recapture time $TX_2$ we have $\omega_{\mathrm{rf}}^{(1)} = \omega_{\mathrm{rf}}^{(2)} = \omega_{\mathrm{rf},0}$ and a common recapture voltage $V_{\mathrm{rf}}^{\mathrm{rc}}$ is used. According to Eq.(6.2) the RF frequency programs determine the momentum programs applied to the two batches. The voltage program during MSS is computed for constant filling

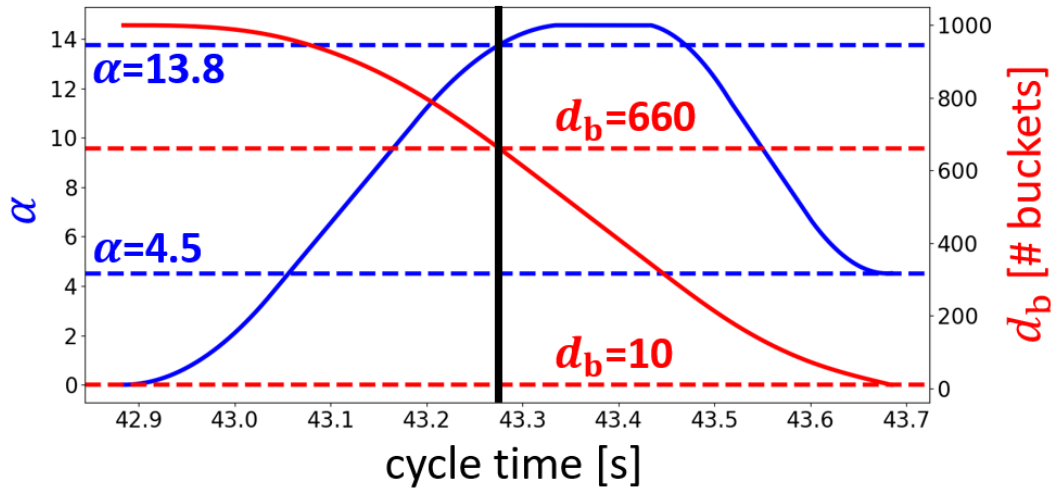


**Figure 6.7.** Example of slip-stacking parameter $\alpha$ (blue) and head-to-head distance between the two batches (red) as a function of the cycle time during momentum slip-stacking (from $TX_1$ to $TX_2$ cycle-times). The black line marks the cycle-time 43.28 s, when $T_b = T_b^{\text{th}} = 1$ µs. At $TX_1$, the shown parameters are $\alpha = 0$ and $d_b = 1000$ buckets (or $T_b = 2.7$ µs), at 43.28 s they are $\alpha = 13.8$ and $d_b = 660$ buckets (the batch length is 460 buckets), at $TX_2$ the parameters are $\alpha = 4.5$ and $d_b = 10$ buckets (bunch spacing at the end of momentum slip-stacking).

factor of bucket in energy $q_e^{\text{MSS}}$ relative to the highest emittance (energy spread) bunch (see Fig.6.8).

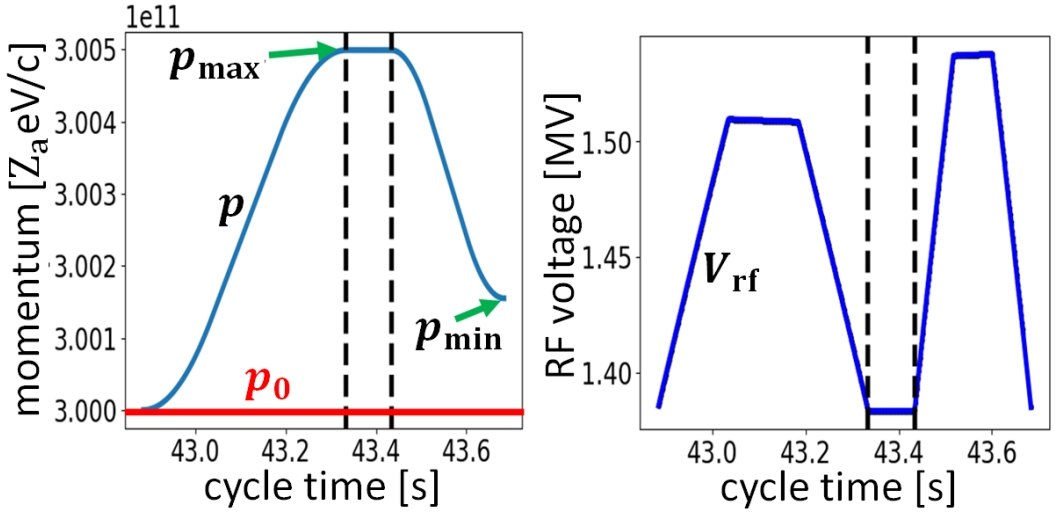


**Figure 6.8.** Example of momentum and RF voltage amplitude programs for one batch during MSS (the same case as in Fig.6.7).

The calculation of the momentum program during MSS can be tedious when parameter scans have to be performed for slip-stacking optimization (see next Section) since proper adjustments should be done case by case to avoid harmful misalignments in phase between the two batches before recapture. Therefore automatic procedures

to obtain alignment between batches (with arbitrary precision) become necessary. Two iterative algorithms have been developed for this purpose, assuming constant longitudinal emittance and filling factor in energy during MSS.

The first iterative algorithm takes $\alpha_{TX_2}^{\text{goal}}$ as input and provides $p_{min}^{\text{goal}}$. Fixing a certain longitudinal emittance and bucket filling factor in energy, the choice of $p_{\text{min}}$ determines $V_{\text{rf},TX_2}$ and therefore $\alpha_{TX_2}$. Thus the iterations are done on $p_{\text{min}}$, until $\alpha_{TX_2}$ is sufficiently close to $\alpha_{TX_2}^{\text{goal}}$.

After having obtained $p_{\text{min}}^{\text{goal}}$, a first estimation $p$ of the desired momentum program during MSS is obtained concatenating a rising, flat and decaying portions, see as an example Fig.6.8 (left). From this momentum program $p$ the accumulated RF phase displacement $\Delta\phi_{\text{rf,tot}}$ with respect to the design RF phase can be computed summing turn by turn the contributions in Eq.(6.3). In general, first-iteration $\Delta\phi_{\text{rf,tot}}$ will be different from the desired $\Delta\phi_{\text{rf,tot}}^{\text{goal}}$ which provides batch alignment. Changing only the value of $p_{\text{max}}$, we can obtain $\Delta\phi_{\text{rf,tot}}$ which is sufficiently close to $\Delta\phi_{\text{rf,tot}}^{\text{goal}}$.

Therefore the second iterative algorithm takes $\Delta\phi_{\text{rf,tot}}^{\text{goal}}$ and the first estimation $p$ as inputs and provides as output a new momentum program which differs from the initial one just by the value for $p_{\text{max}}$ and provides the desired total RF phase displacement. The iterations are done on $p_{\text{max}}$, until the new program gives $\Delta\phi_{\text{rf,tot}} \approx \Delta\phi_{\text{rf,tot}}^{\text{goal}}$.

### 6.3.5 RF Voltage Program after MSS

The recapture voltage $V_{\text{rf}}^{\text{rc}}$ is used during the filamentation process in $[TX_2,\ TX_3]$. Then, the bucket filling factor in energy for the largest emittance bunch is computed at $TX_3$. The RF voltage program for the second ramp is calculated for this filling factor supposing it constant. All along the SPS ion cycle, a maximum RF voltage of 15 MV is assumed, which is expected to be available after RF-upgrade in the framework of the LIU Project [134].

At flat top, with a duration of 1 s, two options of beam manipulations prior to the extraction to the LHC are considered: bunch compression and bunch rotation. During bunch compression, the RF voltage at $TX_4$ is increased linearly and adiabatically for 0.5 s (or about 180 synchrotron periods) up to 15 MV and then is kept constant until extraction. During bunch rotation, the RF voltage at $TX_4$ is applied for 0.8 s, then it is increased non-adiabatically (few turns) to 15 MV and after a quarter of synchrotron period the beam is extracted.

### 6.3.6 SPS Longitudinal Space Charge and Impedance Model

As already mentioned, simulations of momentum slip-stacking were including collective effects. Figure 6.9 shows the calculated longitudinal space charge impedance $|Z_{\text{sc}}|/n$ for the three SPS optics as a function of the design momentum [80] for time after LIU (2021), from slip-stacking to extraction energies. The transverse normalized emittance was assumed to be $\epsilon_{x,y,\text{n}} = 1.2$ µm [3], while $\delta_{\text{rms}} = 1.3 \cdot 10^{-4}$ was selected computing an average of the different fractional rms momentum deviations of the 48 bunches at the beginning of slip-stacking. These two values were used to compute the transverse beam size needed for impedance estimation, similarly to what has been done for the PSB in Chapter 4.

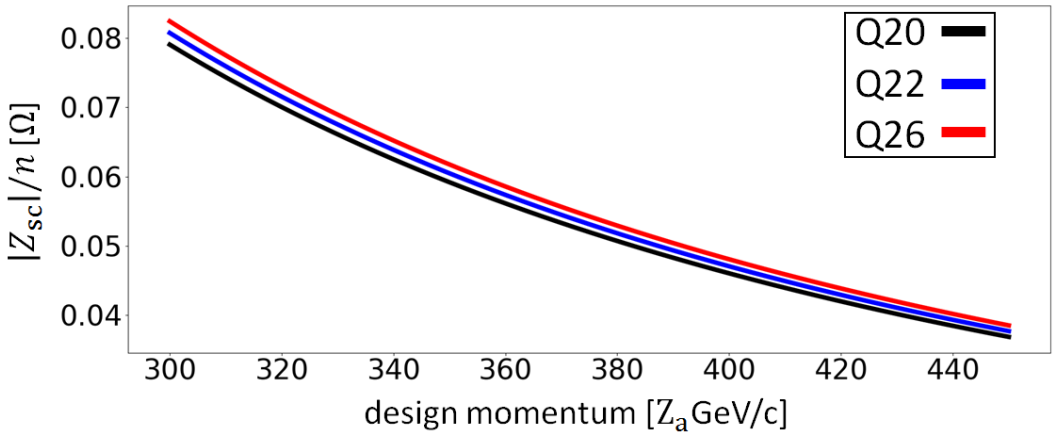


**Figure 6.9.** Estimated longitudinal space charge impedance $|Z_{\mathrm{sc}}|/n$ for the three SPS optics as a function of the design momentum after-LIU, from slip-stacking to extraction energies. The transverse normalized emittance and the relative rms momentum spread are respectively $\epsilon_{x,y,\mathrm{n}} = 1.2$ µm and $\delta_{\mathrm{rms}} = 1.3 \cdot 10^{-4}$. *Courtesy of A. Lasheen, CERN, 2015.*

The after-LIU SPS longitudinal impedance model, which contains narrow and broad-band resonant modes between 50 MHz and 4 GHz, has been studied and simulated for many years, see for example Refs.[19, 16, 135, 136, 137]. A 26 dB reduction on main harmonic (with a few MHz bandwidth) of the 200 MHz TWC impedance through Low Level RF feedbacks is assumed, while the High Order Mode (HOM) at 630 MHz is damped by dedicated RF couplers. The impedance model includes contributions from the 800 MHz TWCs, kicker magnets, vacuum flanges, beam instrumentation devices and resistive wall. Figure 6.10 shows the expected absolute value of the total SPS longitudinal impedance after SPS upgrade.

## 6.4 Constraints on Beam Parameters, Optimization Study and Analysis of Simulation Results

In this Section, unless otherwise specified, simulation results for the currently used Q20 optics are presented. The results for the other two optics Q22 and Q26 are shown in the last Subsection.

Given the significant number of parameters to be determined from the start of slip-stacking until extraction, the first concern was to determine a minimal set of independent parameters able to provide enough variability in the simulated beam dynamics and therefore in the obtained simulation results. Table 6.1 describes the four parameters contained in one of these minimal sets: three of them ($q_{\mathrm{e}}^{\mathrm{MSS}}$, $\alpha_{TX_2}$ and $V_{\mathrm{rf}}^{\mathrm{rc}}$) refer to the slip-stacking and recapture cycle phases, while the remaining one defines the type of RF manipulation used at flat top (bunch compression or rotation). These four parameters have been considered as main inputs for the performed BLonD simulations.

Two constraints on the beam parameters were taken into account in simulations. The first refers to the average and maximum bunch lengths at SPS extraction. These

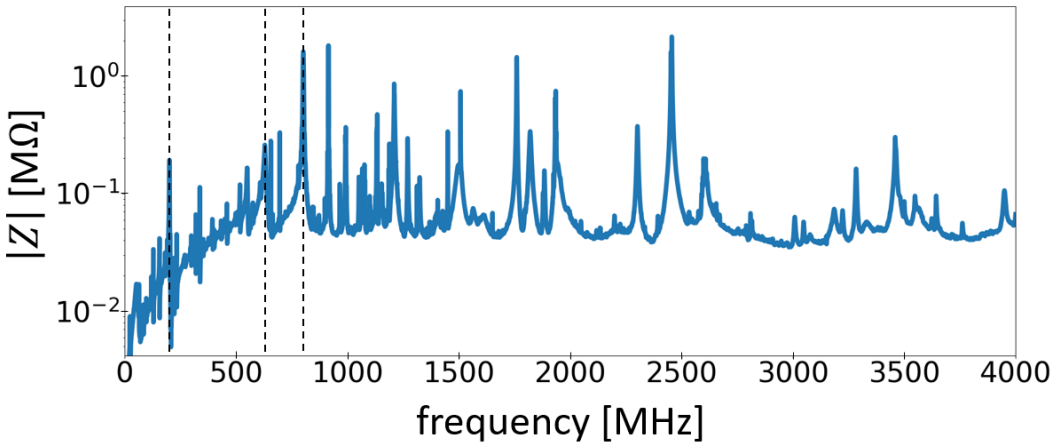


**Figure 6.10.** Expected after-LIU SPS longitudinal impedance model (absolute value). The impedances of the following components are included: 200 MHz TWCs with RF feedback reduction of 26 dB on main harmonic (with a few MHz bandwidth) and HOM at 630 MHz damped via RF couplers, 800 MHz TWCs, kicker magnets, vacuum flanges, beam instrumentation devices and resistive wall. From left to right, the three dashed lines mark 200 MHz, 630 MHz and 800 MHz. *Courtesy of J. Repond, CERN, 2018.*

**Table 6.1.** The four parameters, together with their corresponding options, used in optimization study aimed at finding the best configurations satisfying the constraints on losses and bunch length at SPS extraction.

| | | |
|---|---|---|
| $q_{\mathrm{e}}^{\mathrm{MSS}}$ | bucket filling factor in energy during MSS | from 0.45 to 0.9, step 0.05 |
| $\alpha_{TX_2}$ | slip-stacking parameter at $TX_2$ | from 3.5 to 8, step 0.5 |
| $V_{\mathrm{rf}}^{\mathrm{rc}}$ | recapture RF voltage at $TX_2$ | from 1 to 9, step 0.5 [MV] |
| | RF manipulation at flat top | bunch compression or rotation |

numbers should not be larger than 1.65 ns and 1.80 ns respectively [2], otherwise considerable losses at capture into the 400 MHz LHC RF-buckets are obtained. Since there is a significant variability in bunch length (and emittance) along the two SPS batches at 300 $\mathrm{Z_aGeV/c}$ (see Fig.6.4, left), only the constraint on $\tau_{\mathrm{max}}$, the maximum bunch length at SPS extraction, was considered. However, taking into account that the standard deviation found in measurements for the length of the longest bunch is 7% at 300 $\mathrm{Z_aGeV/c}$, and assuming that this spread is in general preserved until flat-top, it was decided that $\tau_{\mathrm{max}}$ should not be larger than 1.65 ns (instead of 1.80 ns). Note that the maximum bunch-emittance $\epsilon_{\mathrm{max}}$ after filamentation at 300 $\mathrm{Z_aGeV/c}$ should be lower than 0.32 $\mathrm{eVs/A_m}$ in order to have $\tau_{\mathrm{max}} < 1.65$ ns.

The second constraint results from the total losses due to the MSS process. This value as defined by the LIU project should be less than 5% [127]. In the following simulations the total losses $L_{\mathrm{tot}}$ are defined by the sum of the particles lost in the SPS hitting the beam-pipe walls ($L_{\mathrm{SPS}}$) and the particles which will be lost or become satellites in the LHC ($L_{\mathrm{LHC}}$). The quantities $\tau_{\mathrm{max}}$ and $L_{\mathrm{tot}}$,

coming as outputs from a given BLonD simulation after having chosen the four input parameters just discussed, were considered as the principal quantities defining the degree of acceptance of the simulation results.

Figure 6.11 shows an example of particle losses in the SPS due to MSS manipulation. The main parameters $q_{\mathrm{e}}^{\mathrm{MSS}} = 0.9$, $\alpha_{TX_2} = 3.8$ and $V_{\mathrm{rf}}^{\mathrm{rc}} = 7$ MV have been chosen to show an extreme case leading to high amount of particle losses (note in particular that the value of $\alpha_{TX_2}$ is below 4). The current one-sided horizontal aperture limitation in the SPS, coming from the defocusing quadrupoles, is around 20 mm [138]. This value has been used in simulations to identify, through Eq.(6.2), the energy threshold for particles which are close to hit the beam-pipe walls (Fig.6.11, left). Notice that $L_{\mathrm{LHC}}$ contains all the particles in the SPS recaptured into the satellite RF buckets after slip-stacking, in addition to the particles at SPS extraction which are outside the LHC bucket at 450 $\mathrm{Z_aGeV/c}$ (an RF voltage of 8 MV at LHC injection energy was assumed in simulations).

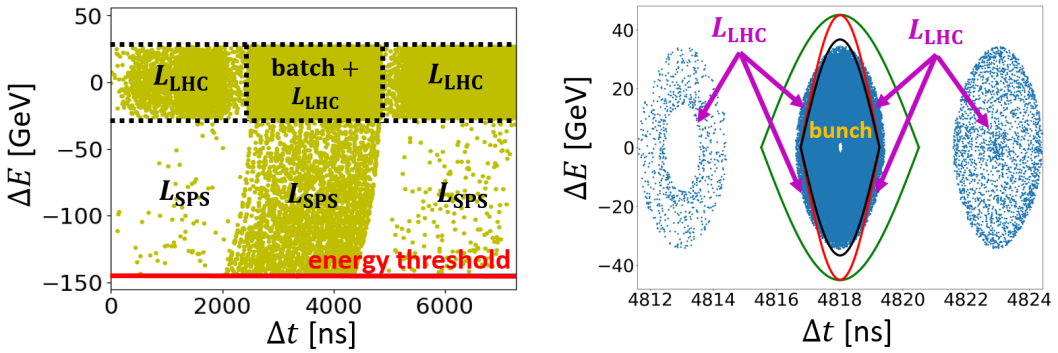


**Figure 6.11.** Example of definition of losses in the SPS ($L_{\mathrm{SPS}}$) and particles which will be lost or become satellites in the LHC ($L_{\mathrm{LHC}}$), due to momentum slip-stacking in the SPS. The main simulation parameters are $q_{\mathrm{e}}^{\mathrm{MSS}} = 0.9$, $\alpha_{TX_2} = 3.8$, $V_{\mathrm{rf}}^{\mathrm{rc}} = 7$ MV with bunch compression at SPS flat-top, see Table 6.1. Left: longitudinal phase space at cycle time 44.2 s, after momentum slip-stacking and filamentation, soon after the start of the second ramp at 44.1 s (see Fig.6.3). The batch, together with inter-bunch satellite particles recaptured by the RF buckets after slip-stacking, is contained in the middle-top rectangular square, other significant portions of satellite particles are on its left and right. Due to acceleration, the energy deviations of the uncaptured particles increase with time. The energy threshold corresponding to the current one-sided SPS horizontal aperture limitation of 20 mm is marked with a red line. Right: zoom onto the last bunch of the batch at SPS extraction. The SPS separatrix with $V_{\mathrm{rf}} = 15$ MV is in green, the LHC separatrices with $V_{\mathrm{rf}} = 8$ MV and $V_{\mathrm{rf}} = 12$ MV are in black and red respectively. The satellite particles on the left and right of the bunch, together with the bunch particles outside of the LHC bucket, contribute to $L_{\mathrm{LHC}}$.

The simulated dynamics, starting from momentum slip-stacking and ending at SPS extraction, is relatively complex, due to the many RF manipulations involved, significant variability of beam parameters along the batches and collective effects. Because of this complexity, in order to avoid the risk of choosing sub-optimal parameter combinations and to be certain that all the possibilities have been examined, scans were performed to find the optimal parameter combinations (see Table 6.1 for the chosen ranges of values). The following criterion for optimality was

adopted: for a given type of RF manipulation at flat top, a combination $A$ of the main parameters $q_e^{MSS}$, $\alpha_{TX_2}$ and $V_{rf}^{rc}$ is optimal if there exists no other combination $B$ for which $L_{tot}^A > L_{tot}^B$ and $\tau_{max}^A > \tau_{max}^B$.

### 6.4.1 Q20 Optics: Bunch Compression

The simulation results for bunch compression are shown in Fig.6.12, together with the optimal solutions. From Fig.6.12 one can see that the real limitation is on $\tau_{max}$ (or $\epsilon_{max}$) rather than on $L_{tot}$. In other words the losses can be considerably reduced by increasing for example $\alpha_{TX_2}$ and $V_{rf}^{rc}$ while decreasing $q_e^{MSS}$, implying a value for $\tau_{max}$ close to 2.05 ns (Fig.6.12, left). However it is more difficult to reduce the emittance after filamentation without having considerable losses, mostly because $\alpha_{TX_2}$ cannot be smaller than 4 (see Section 6.2). Essentially no combination is acceptable, so bunch compression at flat top cannot be adopted in the Q20 optics.

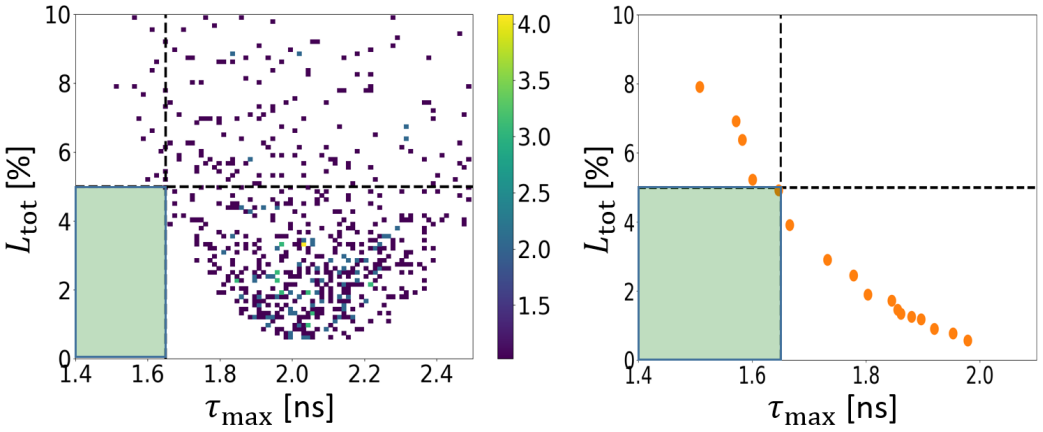


**Figure 6.12.** Left: simulation results in the $L_{tot}$–$\tau_{max}$ plane for the Q20 optics with bunch compression at flat top. The area where the constraints are satisfied is in green. The color bar indicates the percentage of the total number of parameter combinations from Table 6.1 which provides a given $L_{tot}$ and $\tau_{max}$. Right: optimal solutions extracted from the left image.

### 6.4.2 Q20 Optics: Bunch Rotation

Results for the bunch rotation option on flat top are shown in Fig.6.13 (left). It can be seen that the average of the different values for $\tau_{max}$, obtained varying the parameter combinations described in Table 6.1, is reduced from 2.05 ns (as shown in Fig.6.12) to 1.65 ns. As a consequence, numerous parameter combinations satisfy the constraints. Considering the optimal solutions in Fig.6.13 (right), we can identify the "balanced" one as the middle-point of the curve-fit of the optimal solutions which are contained in the area where the constraints are satisfied.

Giving priority to total losses reduction while keeping some safety margin for the maximum bunch length ($\tau_{max} = 1.55$ ns), the blue dot shown in Fig.6.13 (right) marks the proposed solution, associated with $\alpha_{TX_2} = 4.5$, $q_e^{MSS} = 0.65$ and $V_{rf}^{rc} = 8$ MV. The relatively low $q_e^{MSS}$ and a value for $\alpha_{TX_2}$ slightly higher than the stability limit allow to have low losses $L_{tot} = 0.43\%$, $L_{LHC} = 0.13\%$ and $L_{SPS} = 0.30\%$.

Concerning the proposed solution, the maximum radial displacement for the centroid of a generic bunch during MSS was 5.67 mm (Eq.(6.2) was used to convert the MSS RF-frequency program to radial displacement). The maximal standard deviations of the beam transverse distributions along the SPS ring at 300 $Z_a$GeV/c were computed using Eq.(A.31) and assuming zero vertical dispersion. Since $\sigma_{x,\max} = 1.44$ mm and $\sigma_{y,\max} = 1.01$ mm, even assuming a horizontal bunch size of $6\sigma_{x,\max}$ (99.7% of the distribution), the maximum radial displacement for the particles contained in one bunch during MSS was only 10 mm, half the current horizontal aperture limitation of 20 mm.

The maximum difference between the RF frequency of one batch during MSS and the design RF frequency was only 1 kHz for the proposed solution, three orders of magnitude lower than the 200 MHz TWC bandwidth. As for the peak RF voltage, the maximum value during MSS was only 1.54 MV (for one RF subsystem) and during acceleration to flat top it reached 14.6 MV, still inside the limitations (see also Figs.6.7 and 6.8 which refer to this proposed optimal solution).

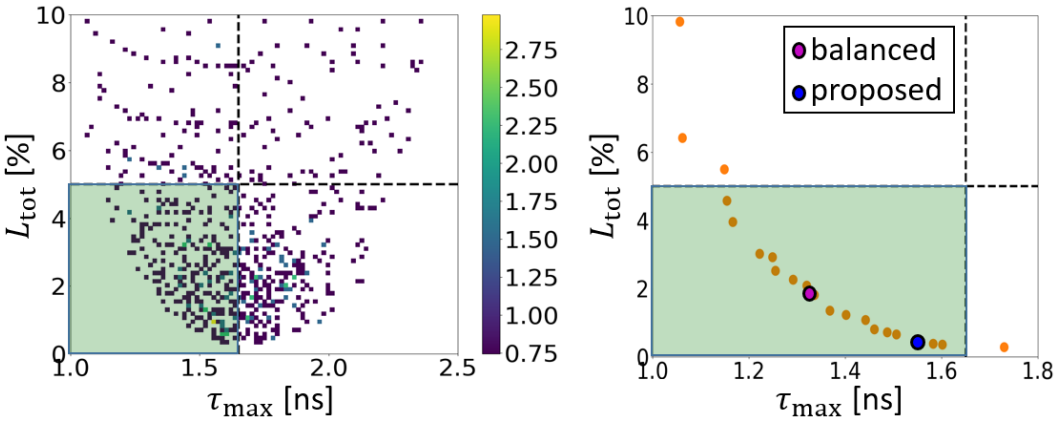


**Figure 6.13.** Left: simulation results in the $L_{\mathrm{tot}}$–$\tau_{\max}$ plane for the Q20 optics with bunch rotation at flat top. The area where the constraints are satisfied is in green. The color bar indicates the percentage of the total number of parameter combinations from Table 6.1 which provides a given $L_{\mathrm{tot}}$ and $\tau_{\max}$. Right: optimal solutions extracted from the left image, the magenta and blue dots mark the balanced and proposed solutions respectively.

Figures 6.14 and 6.15 summarize all the significant parameters associated with the optimal solutions shown in Fig.6.13 (right). The green lines mark the quantities related to the proposed solution. Qualitatively we can see that, as $\tau_{\max}$ increases, $\alpha_{TX_2}$ remains constant, $q_{\mathrm{e}}^{\mathrm{MSS}}$, $L_{\mathrm{tot}}$, $L_{\mathrm{LHC}}$ and $L_{\mathrm{SPS}}$ decrease while $V_{\mathrm{rf}}^{\mathrm{rc}}$ and $\epsilon_{\max}$ increase. In the following, the behaviors of these seven parameters with respect to $\tau_{\max}$ is explained.

As we would expect, all the optimal solutions have $\alpha_{TX_2} \approx 4$, since 4 is the lowest limit for stability. Notice that significantly larger values would make the solutions not optimal anymore, due to the unnecessary space between the two batches at recapture time which would lead to higher recapture voltages and therefore larger emittances and bunch lengths after beam filamentation. Since all the optimal solutions with $q_{\mathrm{e}}^{\mathrm{MSS}} \geq 0.65$ have their highest emittance bunches almost filling the bucket during

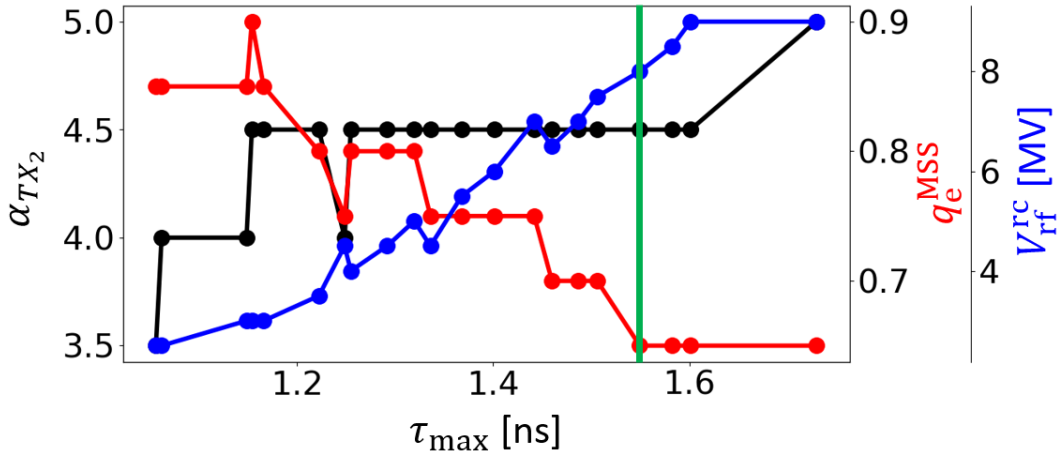


**Figure 6.14.** Scanning parameters $\alpha_{TX_2}$, $q_e^{MSS}$ and $V_{rf}^{rc}$ as a function of $\tau_{max}$ for the optimal solutions shown in Fig.6.13. The green line marks the proposed combination of scanning parameters leading to $\tau_{max} = 1.55$ ns and $L_{tot} = 0.43\%$ (see also Fig.6.15).

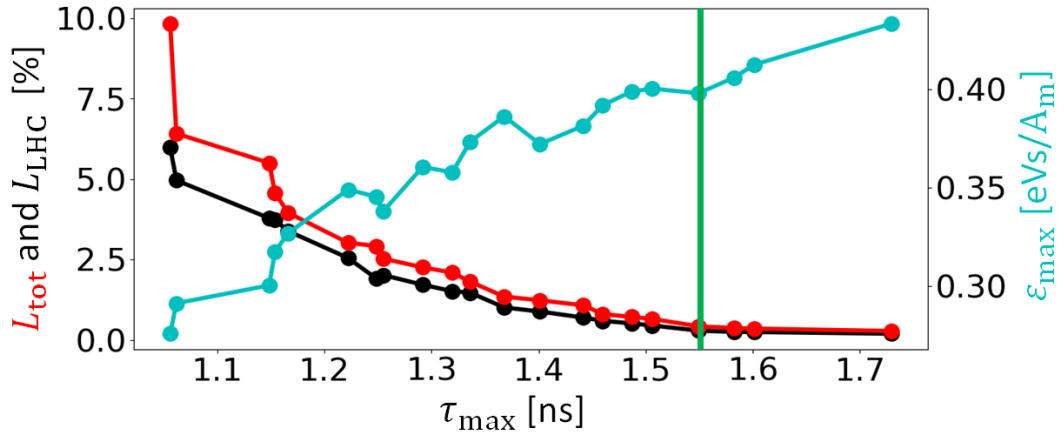


**Figure 6.15.** Total losses $L_{tot}$, LHC satellites and losses $L_{LHC}$, maximum emittance along the SPS batch at extraction $\epsilon_{max}$ as a function of $\tau_{max}$ for the optimal solutions in Fig.6.13. The green line marks the quantities associated to the proposed combination of scanning parameters (see Fig.6.14).

MSS, $\alpha_{TX_2} = 4.5$ gives some safety margin to soften the impact of the chaotic motion close to $\Delta E = 0$.

In order to explain the behavior of the other parameters in Figs.6.14 and 6.15, let us take two general optimal solutions $A$ and $B$ with $\tau_{max}^A < \tau_{max}^B$. It follows immediately that $\epsilon_{max}^A < \epsilon_{max}^B$.

As observed before, higher recapture voltages applied to the unmatched bunches at recapture time lead to larger extracted emittances, since the filamenting bunches tend to cover the increased bucket area. Therefore $V_{rf}^{rc,A} < V_{rf}^{rc,B}$.

At recapture time, a higher recapture voltage for the optimal solution implies a larger $\Delta E_b$, see Fig.6.16. The reason is that the recapture bucket tends to contain the unmatched bunch without leaving any significant margin close to the separatrix: if margin is left then a larger emittance after filamentation is obtained and the

solution would not be optimal anymore. Therefore $\Delta E_b^A < \Delta E_b^B$.

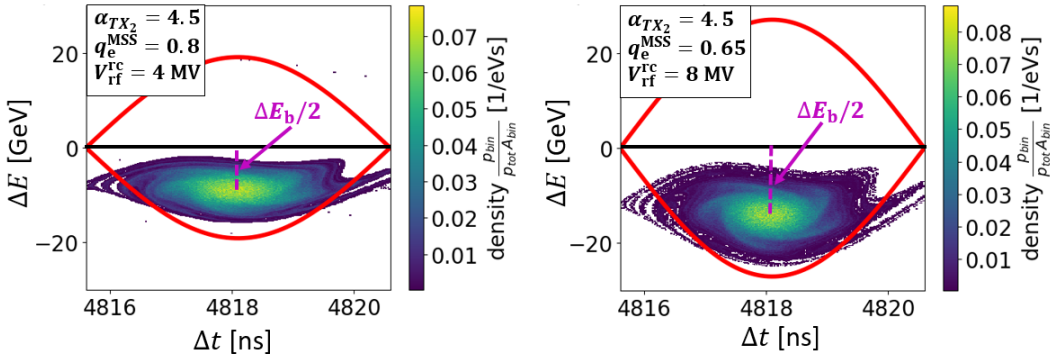


**Figure 6.16.** Zoom onto the last bunch at recapture time for two different optimal combinations of scanning parameters shown in Fig.6.14. The separatrices in red refer to the recapture buckets.

Since $\alpha_{TX_2}$ is constant along the optimal solutions, it follows that $H_b^A < H_b^B$. The half bucket-height scales with $V_{rf}$ of the unperturbed bucket of one of the two RF systems as $H_b \propto V_{rf}^{1/2}$, therefore $V_{rf}^A < V_{rf}^B$. The peak energy spread $\widehat{\Delta E}$ of the bunch inside the unperturbed bucket scales as $\widehat{\Delta E} \propto V_{rf}^{1/4}$. Therefore $q_e^{MSS} \propto V_{rf}^{-1/4}$ and $q_e^{MSS,A} > q_e^{MSS,B}$.

A higher $q_e^{MSS}$ implies larger losses in the SPS due to particles escaping the RF bucket during the MSS manipulation, therefore $L_{SPS}^A > L_{SPS}^B$. A higher $q_e^{MSS}$ leads also to more satellite particles, since the bunch is closer to the $\Delta E = 0$ axis, where the chaotic motion is more significant. Therefore $L_{LHC}^A > L_{LHC}^B$ and $L_{tot}^A > L_{tot}^B$.

Finally, in order to evaluate the impact of collective effects on the parameters $L_{tot}$ and $\tau_{max}$, all the performed simulations were repeated neglecting intensity effects and the optimal solutions are shown in Fig.6.17. No significant difference can be noticed after comparison with Figs.6.12 and 6.13. In addition, if intensity effects are not included, the parameter combinations leading to the optimal solutions are similar to the ones shown in Fig.6.14. Therefore collective effects do not significantly affect the optimal RF manipulations performed along the acceleration cycle. Most importantly, they do not increase the total beam losses and the maximum bunch-length obtained at extraction energy.

### 6.4.3 Simulation Results for the Q22 and Q26 Optics

The MSS in two other optics, Q22 and Q26, was also analyzed. Because of the lower slip factor, a slightly higher $p_{max}$ during MSS was needed (keeping constant the time duration). The radial displacement was still inside the aperture limitations and the process was adiabatic. Fixing all the other parameters (as the RF voltage and emittance), a lower slip factor implies a lower filling factor in energy, $q_e^{MSS} \propto \eta_0^{1/4}$. This helps in reducing $L_{SPS}$ and $L_{LHC}$, especially in the bunch compression case for the Q20 optics where, as observed above, the real limitation comes from $\tau_{max}$ rather than $L_{tot}$. Therefore, in the Q22 and Q26 optics, one can exploit the gained margin for losses bringing the two batches closer to each other and obtaining,

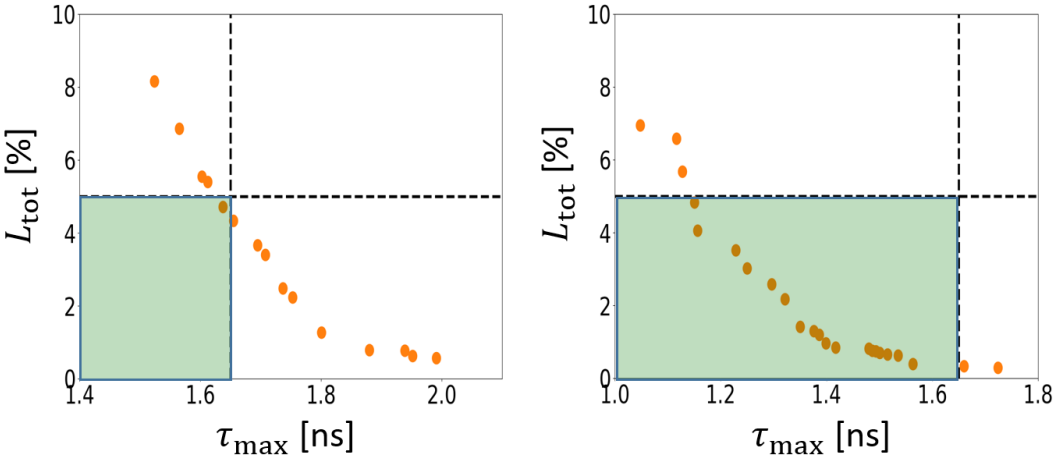


**Figure 6.17.** Optimal combinations in the $L_{tot}$–$\tau_{max}$ plane for the Q20 optics without considering intensity effects. The area where the constraints are satisfied is in green. Left: bunch compression at flat top. Right: bunch rotation at flat top.

as a consequence, lower emittance and $\tau_{max}$. Examining Fig.6.12 for the bunch compression case with the Q20 optics and noticing that some optimal solutions are already on the border of the area where the constraints are satisfied, the expected improvement in results by using the Q22 and Q26 optics should lead to several optimal solutions with $L_{tot}$ and $\tau_{max}$ significantly lower than the corresponding constraint-thresholds.

Figures 6.18 and 6.19 show the simulation results for the Q22 and Q26 optics with bunch compression performed at flat top. As expected, several optimal solutions satisfy the constraints, with the Q26 optics providing the best results. Therefore bunch compression could be adopted if the Q22 and Q26 optics are chosen, however the higher transverse space charge effect for these two optics should also be taken into account in deciding which optics to use for slip-stacking.

As observed in the Q20 optics case, bunch rotation provides in general more acceptable solutions than bunch compression, since $\tau_{max}$ is considerably reduced with no significant change in $L_{tot}$. However bunch rotation could lead to potential issues coming from the transfer of "S-shaped" bunches to the LHC [139]. Therefore the use of this RF manipulation is discouraged if valid alternatives are available, as it is the case for the Q22 and Q26 optics.

Table 6.2 summarizes for each optics the suggested RF manipulation at flat-top and the values of $L_{tot}$ and $\tau_{max}$ for the balanced optimal solution.

## 6.5 Loss of Landau Damping During MSS

It has been shown in the previous Section that for optimal solutions collective effects do not influence the total losses and maximum bunch length at SPS extraction. However, they can cause loss of Landau damping (LLD) for the shortest bunches, as it will be explained below. In what follows, the example of the proposed optimal solution for the Q20 optics is considered (Fig.6.13, right), however the obtained

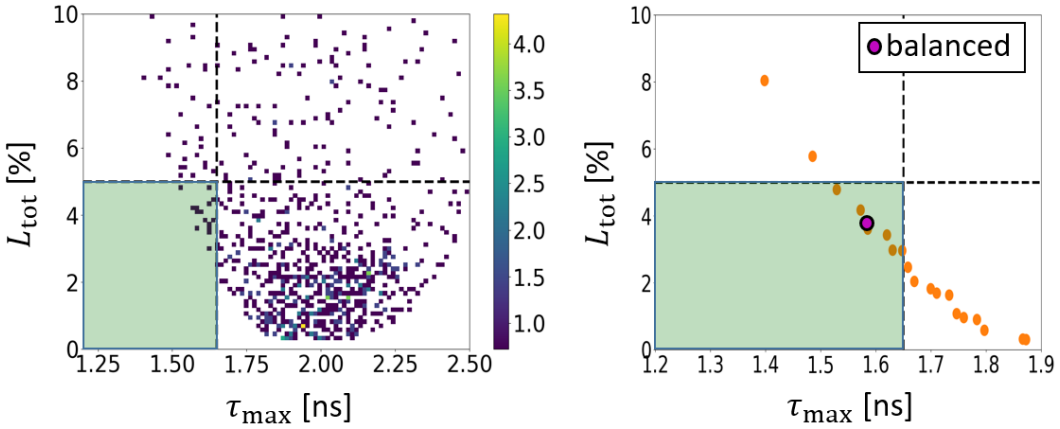


**Figure 6.18.** Left: simulation results in the $L_{\mathrm{tot}}$–$\tau_{\mathrm{max}}$ plane for the Q22 optics with bunch compression at flat top. The area where the constraints are satisfied is in green. The color bar indicates the percentage of the total number of parameter combinations from Table 6.1 which provides a given $L_{\mathrm{tot}}$ and $\tau_{\mathrm{max}}$. Right: optimal solutions extracted from the left image, the magenta dot marks the balanced solution.

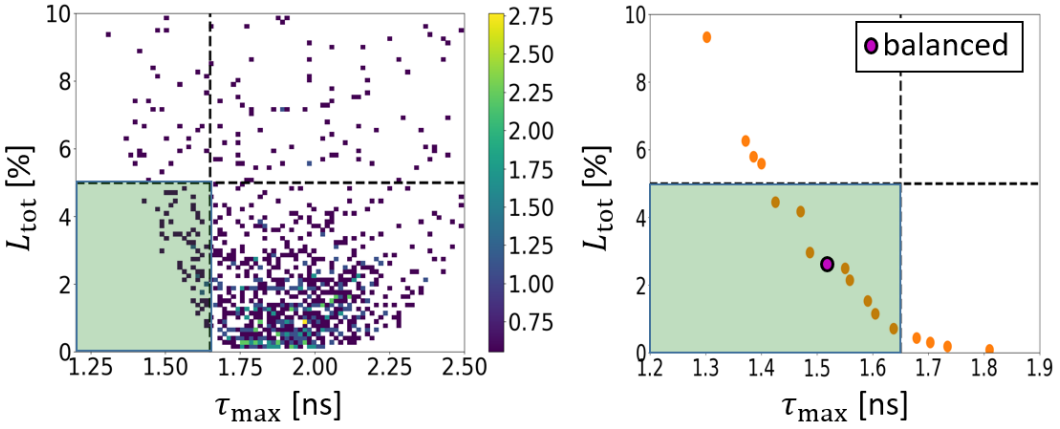


**Figure 6.19.** Left: simulation results in the $L_{\mathrm{tot}}$–$\tau_{\mathrm{max}}$ plane for the Q26 optics with bunch compression at flat top. The area where the constraints are satisfied is in green. The color bar indicates the percentage of the total number of parameter combinations from Table 6.1 which provides a given $L_{\mathrm{tot}}$ and $\tau_{\mathrm{max}}$. Right: optimal solutions extracted from the left image, the magenta dot marks the balanced solution.

**Table 6.2.** Summary of the simulation results for the three SPS optics. The second column indicates the suggested RF manipulation to be performed at flat-top. The third column shows the values of $L_{\mathrm{tot}}$ and $\tau_{\mathrm{max}}$ for the balanced optimal solution.

| SPS Optics | RF manipulation at flat top | Parameters for the balanced solution |
|---|---|---|
| Q20 | bunch rotation | $L_{\mathrm{tot}} = 1.8\%$, $\tau_{\mathrm{max}} = 1.33$ ns |
| Q22 | bunch compression | $L_{\mathrm{tot}} = 3.8\%$, $\tau_{\mathrm{max}} = 1.58$ ns |
| Q26 | bunch compression | $L_{\mathrm{tot}} = 2.6\%$, $\tau_{\mathrm{max}} = 1.52$ ns |

results have more general applications.

At recapture time $TX_2$, the bunch is strongly unmatched, being displaced in energy relatively to the bucket center due to non-zero value of the slip-stacking parameter $\alpha_{TX_2}$, see for example Fig.6.16.

During filamentation a hollow bunch is formed and this bunch shape is preserved up to flat top. While without intensity effects the hollow bunch has a radially symmetric distribution in phase space (Fig.6.20, left), a very dense island appears when intensity effects are taken into account (Fig.6.21, left). This island rotates in longitudinal phase space producing significant dipole oscillations of the bunch centroid, degrading the beam quality. As was found in the optimization study presented in the previous Section, Figs.6.20 and 6.21 show that collective effects do not influence the bunch length $\tau_l$ and emittance $\epsilon_l$. Moreover, Fig.6.21 proves that the bunch-length convention $\tau_{\mathrm{FWHM,G}}$, currently used in the SPS, can lead to meaningless values for bunch length and emittance when intensity effects are included in slip-stacking simulations.

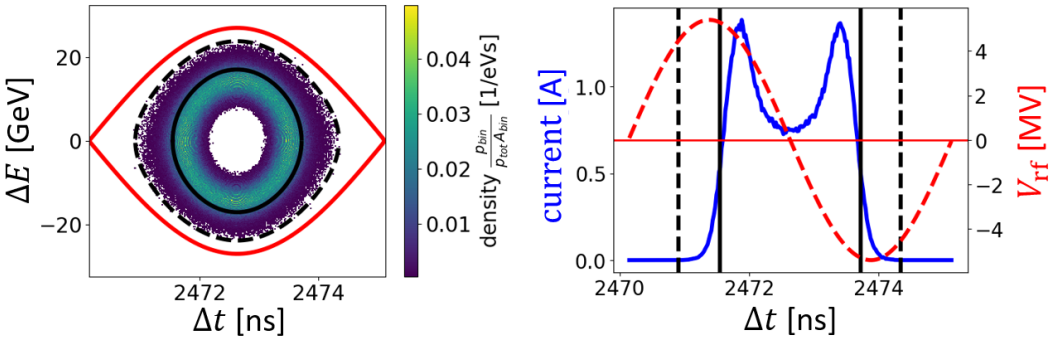


**Figure 6.20.** Simulation of momentum slip-stacking with parameters from the proposed solution in Fig.6.13 (right) without intensity effects. Left: phase space of the first bunch at the beginning of flat top. The black continuous and dashed lines correspond to stable particle-trajectories which determine respectively $\epsilon_{\mathrm{l}} = 0.27$ eVs/A$_{\mathrm{m}}$ and $\epsilon_{\mathrm{FWHM,G}} = 0.58$ eVs/A$_{\mathrm{m}}$, see Section 6.3 for the definitions. Right: bunch profile corresponding to the distribution shown on the left figure. The black continuous and dashed lines determine respectively $\tau_{\mathrm{l}} = 2.16$ ns and $\tau_{\mathrm{FWHM,G}} = 3.43$ ns. The RF voltage curve is in red.

The bunch dipole oscillations produced by the rotating island remain up to flat top, see Fig.6.22 (bottom), where, in order to easily compare the dipole oscillations for the first, middle and last bunches in the batch, $m_\lambda$ in Eq.(2.49) is redefined as the average position of the line density $\lambda$ centered around $t = 0$.

One can see that, relative to the bucket length of 5 ns, the peak-to-peak amplitude of the dipole oscillations with intensity effects is 12% for the shortest (first) bunch and 2% for the longest (last) one. Ignoring intensity effects (Fig.6.22, top), the dipole oscillations become negligible, only 0.1% for all the bunches. Figure 6.22 indicates also that the shortest and longest bunches experience LLD around $TX_2$ and $TX_3$ respectively.

The threshold of LLD can be estimated analytically using Eq.(3.8) in Chapter 3, where we assumed $F = 1$ and $\mathrm{Im}Z/n = 3\,\Omega$ [80]. Figure 6.23 shows the threshold curves for the cases with $V_{\mathrm{rf}} = 1.54$ MV and $V_{\mathrm{rf}} = 8$ MV, which are respectively

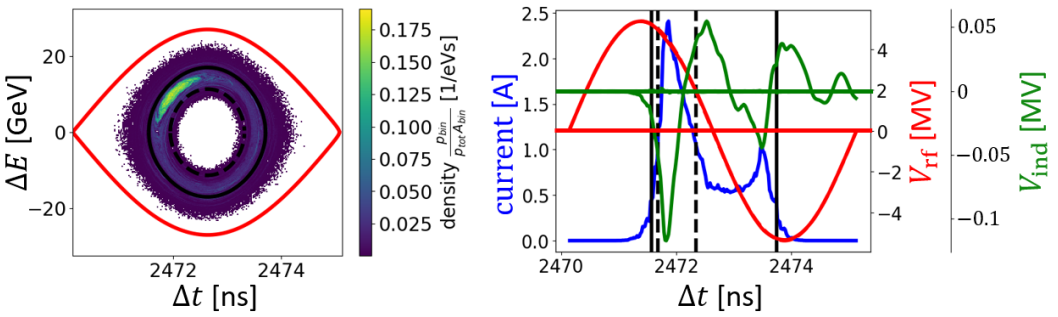


**Figure 6.21.** Simulation for the same conditions as shown in Fig.6.20 but with intensity effects. The emittance and bunch length are determined by the black continuous lines: $\epsilon_l = 0.27$ eVs/A$_m$ (left) and $\tau_l = 2.16$ ns (right). The RF and induced voltage curves are in red and green respectively. Due to the rotating island in longitudinal phase space, the bunch-length convention (black dashed line) of the full-width-half-maximum rescaled to $4\sigma_t$ of a Gaussian profile leads to meaningless values for bunch length and emittance.

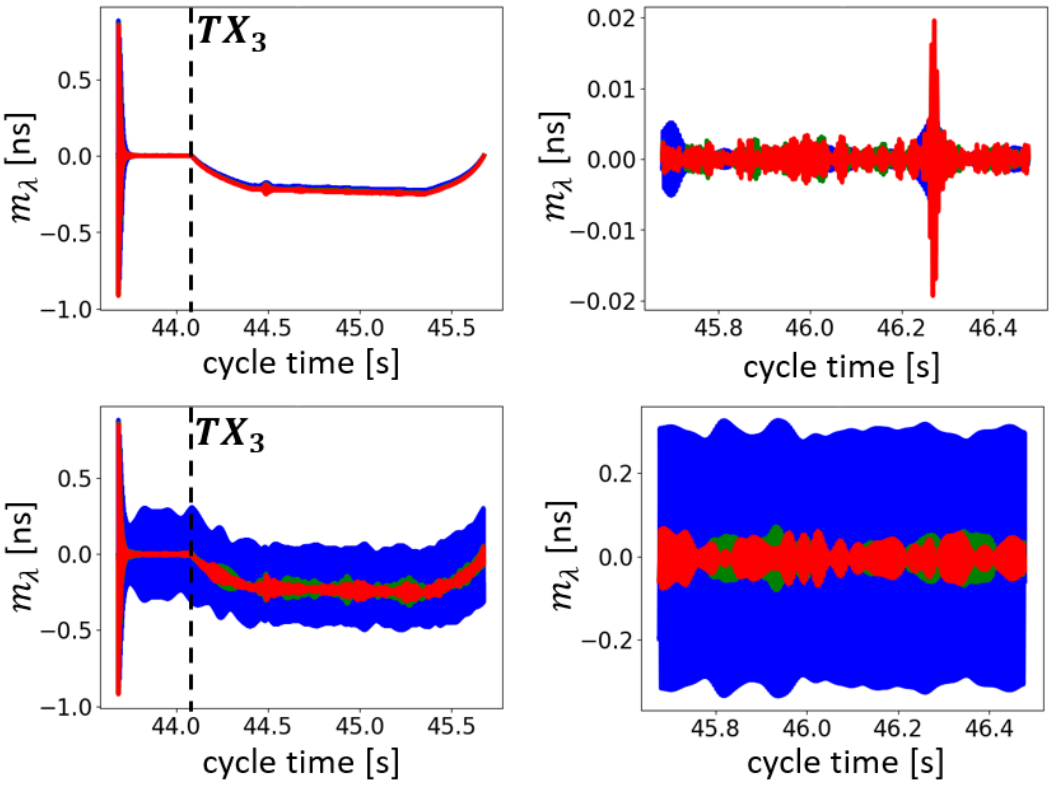


**Figure 6.22.** Simulations for the proposed solution in Fig.6.13. Dipole oscillations as a function of the cycle time for the first (blue), middle (green) and last (red) bunches without (top) and with (bottom) intensity effects between $TX_2$ and $TX_4$ (left) and after $TX_4$ (right).

the maximum RF voltage during MSS and the recapture voltage for the proposed solution with the Q20 optics. One can see that the shortest bunch loses Landau damping during MSS and at recapture, while the longest bunch does not experience

LLD until recapture time. These analytical calculations are in good agreement with the results coming from simulations.

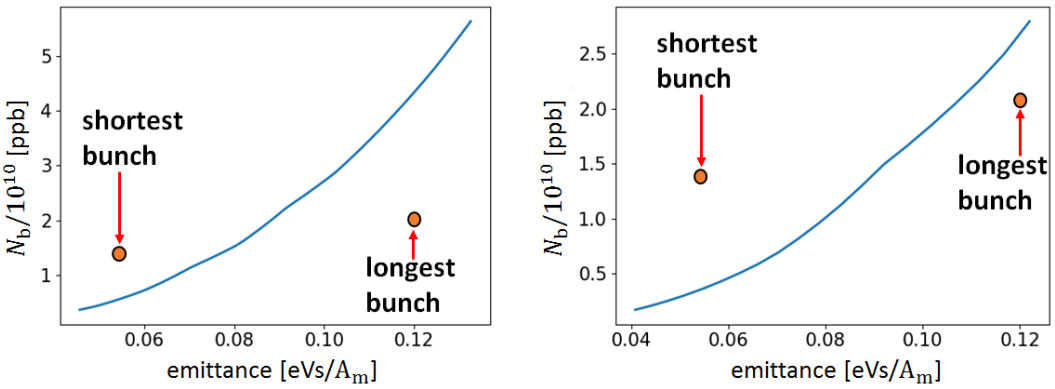


**Figure 6.23.** Analytical LLD thresholds in the bunch emittance–intensity plane for $V_{rf} = 1.54$ MV (left) and $V_{rf} = 8$ MV (right), which are respectively the maximum voltage during MSS and the recapture voltage for the proposed solution in Fig.6.13. The values for the shortest ($\epsilon_l = 0.054$ eVs/A$_m$, $N_b = 1.384 \cdot 10^{10}$ ppb) and longest ($\epsilon_l = 0.122$ eVs/A$_m$, $N_b = 2.067 \cdot 10^{10}$ ppb) bunches are marked by circles.

### 6.5.1 Use of the 800 MHz RF System to Cure LLD

A possible method, applied in different accelerators to increase the LLD threshold, consists in using a higher harmonic RF system in addition to the main one. This increases the synchrotron frequency spread of the particles inside the bunch and therefore makes more effective the damping of coherent motion.

In the SPS there is a fourth harmonic RF system (800 MHz) installed and used in nominal operation for proton beams to increase the longitudinal stability. The 800 MHz RF system is used only in bunch shortening mode with 10%–20% peak voltage with respect to the main RF system. The alternative bunch lengthening mode cannot be used since the instability threshold is significantly reduced in this case [131, 23, 132].

Although the 800 MHz RF system is not currently used for ion beams, this will be possible after LLRF upgrade (2021) and one can consider it for increase of the LLD threshold. In the simulations presented below the proposed solution for the Q20 optics was used, for which the 200 MHz RF voltage at flat top is $V_{rf}^{200} = 5.5$ MV. However, as already mentioned above, the results shown are more general.

We first applied the 800 MHz voltage $V_{rf}^{800}$ at flat top, from $TX_4$ to the start time of the bunch rotation manipulation. The voltage $V_{rf}^{800}$ was increased adiabatically (during 20 synchrotron periods) from zero to the desired value (in the interval 0.5 MV–3.5 MV), and then it was kept constant. Figure 6.24 shows examples of simulation results for the bunch lengthening (top) and shortening (bottom) modes for different values of $V_{rf}^{800}$.

The 800 MHz RF system used in bunch shortening mode starts to significantly reduce the dipole oscillations of the shortest bunch only when $V_{rf}^{800} = 3.5$ MV, while lower values do not provide any substantial damping (to be compared with the

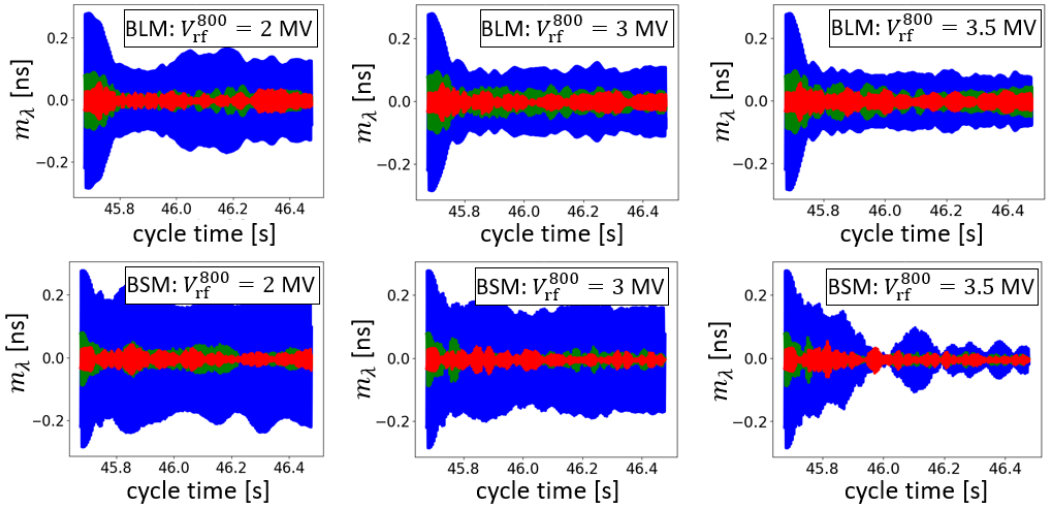


**Figure 6.24.** Dipole oscillations at 450 $Z_a$GeV/c as a function of the cycle time from $TX_4$ to the start time of the bunch rotation manipulation. The 200 MHz RF system has constant $V_{\mathrm{rf}}^{200} = 5.5$ MV. The RF voltage of the 800 MHz RF cavity is increased linearly from zero to the desired $V_{\mathrm{rf}}^{800}$ in the time interval from $TX_4$ to 45.75 s and then kept constant. The 800 MHz RF system is used in different configurations: bunch lengthening (top) and shortening (bottom) modes, with $V_{\mathrm{rf}}^{800} = 2$ MV (left), $V_{\mathrm{rf}}^{800} = 3$ MV (middle) and $V_{\mathrm{rf}}^{800} = 3.5$ MV (right). The blue, green and red curves refer respectively to the first, middle and last bunches.

proton case where in operation $V_{\mathrm{rf}}^{800}$ is only 10%–20% of $V_{\mathrm{rf}}^{200}$). Bunch lengthening mode gives better results than bunch shortening for $V_{\mathrm{rf}}^{800} < 3.5$ MV, however the damping is still not sufficient and, in addition, relatively high 800 MHz voltages are needed. Due to Landau damping, the dipole oscillations of the middle and last bunches in the batch are already relatively small at the beginning of flat top (see also Fig.6.25) and therefore, in these cases, the 800 MHz RF system does not play an important role.

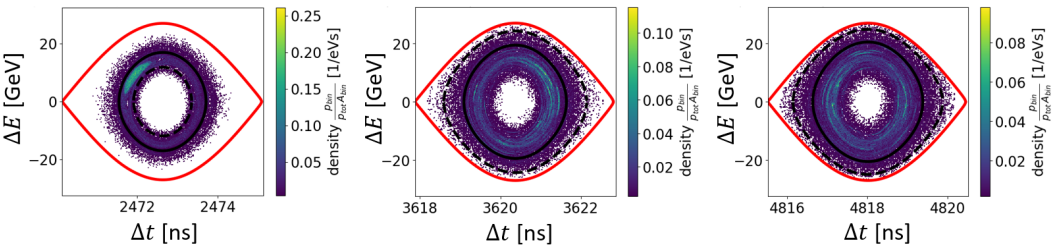


**Figure 6.25.** Phase-space distributions of the first (left), center (middle) and last (right) bunches at the beginning of flat-top, $V_{\mathrm{rf}}^{200} = 5.5$ MV and $V_{\mathrm{rf}}^{800} = 2$ MV in bunch shortening mode (case shown in Fig.6.24, bottom-left). The black continuous lines mark the stable particle-trajectories which determine the emittance $\epsilon_{\mathrm{l}} = 0.27$ eVs/$A_{\mathrm{m}}$ for the first bunch, $\epsilon_{\mathrm{l}} = 0.36$ eVs/$A_{\mathrm{m}}$ for the middle bunch and $\epsilon_{\mathrm{l}} = 0.41$ eVs/$A_{\mathrm{m}}$ for the last bunch in the batch. The black dashed lines mark the stable particle-trajectories which define the emittances $\epsilon_{\mathrm{FWHM,G}}$ for the corresponding bunches. The value for $\epsilon_{\mathrm{FWHM,G}}$ is meaningless when there is a rotating island in phase space (left, see also Fig.6.21).

Using the bunch-shortening and lengthening modes was not sufficient to stabilize the shortest bunch in the batch at flat top. Varying also the phase $\Delta\phi_{800}$ between the two RF systems did not improve the situation, see, for example, Fig.6.26 for $V_{\mathrm{rf}}^{800} = 3.5$ MV. There, $\Delta S$ is defined as the peak-to-peak amplitude of the dipole oscillations of the shortest bunch just before bunch-rotation at flat top starts. One can see that the bunch shortening mode gives the best outcome, however this configuration is highly unstable, since small variations in $\Delta\phi_{800}$ provide large changes in $\Delta S$. Additionally, as seen above, $V_{\mathrm{rf}}^{800}$ should be larger than 3 MV, otherwise the damping is negligible. Figure 6.26 shows also that the bunch lengthening mode is the second optimal solution, which is stable with respect to $\Delta\phi_{800}$ but, as observed above, $V_{\mathrm{rf}}^{800}$ should be at least equal to 3 MV in order to obtain only a mediocre damping.

Note that, when the 800 MHz RF voltage is applied to bunches which are not hollow, the bunch shortening and lengthening modes are respectively stable and unstable with respect to $\Delta\phi_{800}$ [131]. Figure 6.26 shows the opposite, however this discrepancy should not surprise: the results presented in Ref.[131], which determine if a certain operating mode of the 800 MHz RF system is stable or not with respect to $\Delta\phi_{800}$, assume that the particle distribution is not hollow. In case of hollow bunches, dedicated studies have to be done, since the values of the synchrotron-oscillation amplitudes for the different particles are more localized and are relatively far from zero, see for example Fig.6.27.

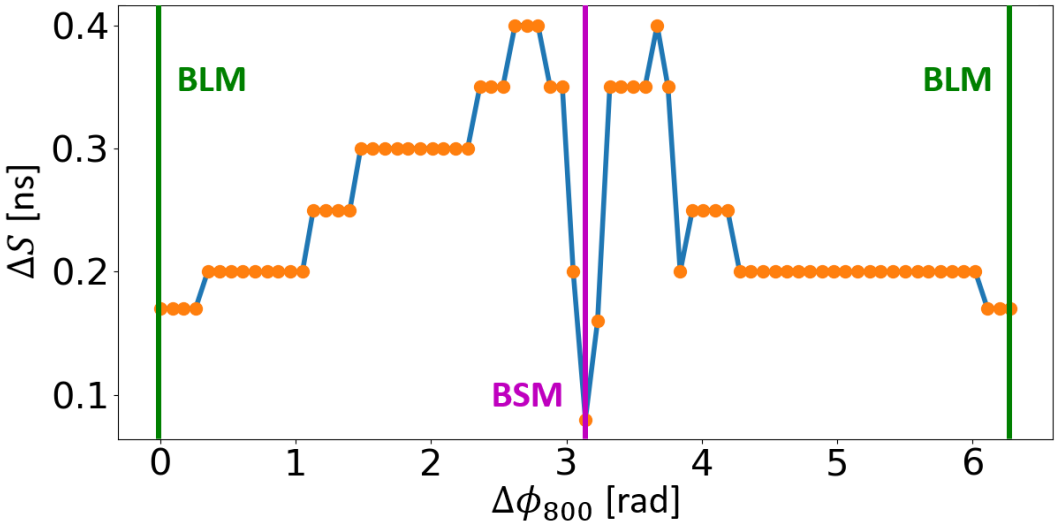


**Figure 6.26.** Peak-to-peak amplitude $\Delta S$ of the dipole oscillations of the shortest bunch as a function of the relative phase $\Delta\phi_{800}$ between the 200 MHz and 800 MHz RF systems, just before bunch-rotation at flat top starts ($V_{\mathrm{rf}}^{200} = 5.5$ MV, $V_{\mathrm{rf}}^{800} = 3.5$ MV). The green and magenta lines mark respectively the relative phases corresponding to the bunch lengthening and shortening modes.

One can explain the LLD for the shortest bunch considering Fig.6.27, where the synchrotron frequency distribution at 450 $Z_a$GeV/c as a function of the emittance is shown for different configurations of the 800 MHz RF system. Focusing on the stable particle-trajectories crossing the center and borders of the rotating island

of the shortest bunch (Fig.6.28, left), one can see that the spread in frequency is relatively small ($\Delta f_s < 25$ Hz) if the 200 MHz RF system is used alone or if the 800 MHz cavity is added with $V_{\mathrm{rf}}^{800} = 0.5$ MV (Fig.6.27, left). Increasing the 800 MHz voltage to $V_{\mathrm{rf}}^{800} = 2$ MV does not help (Fig.6.27, right), since the spread is not significantly higher than before ($\Delta f_s < 40$ Hz) and, most importantly, the synchrotron frequencies of the particles are close to or even cross the flat portion of $f_s$, both in bunch shortening and lengthening modes.

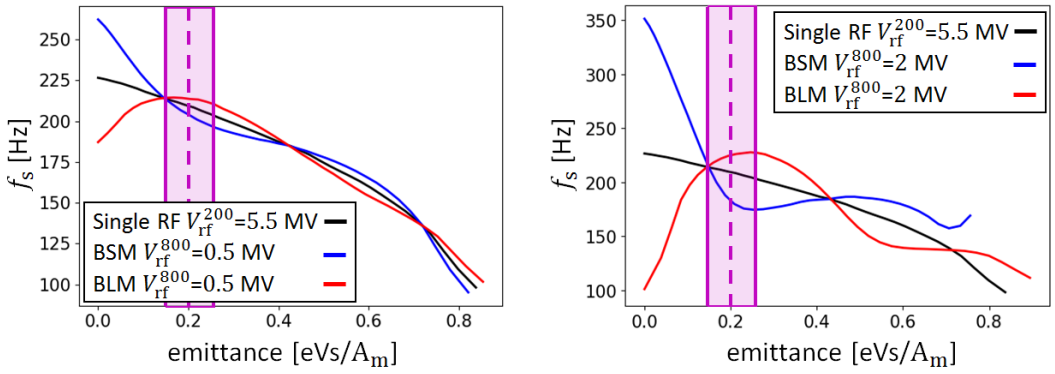


**Figure 6.27.** Synchrotron frequency distribution at 450 $Z_a$GeV/c as a function of emittance using different configurations of the 800 MHz RF system. Left: single RF with $V_{\mathrm{rf}}^{200} = 5.5$ MV (black), double RF with $V_{\mathrm{rf}}^{200} = 5.5$ MV and $V_{\mathrm{rf}}^{800} = 0.5$ MV in bunch shortening (blue) and lengthening (red) modes. Right: the same configurations shown on the left, except that $V_{\mathrm{rf}}^{800} = 2$ MV. The dashed and continuous magenta vertical lines mark the stable particle-trajectories crossing respectively the center and borders of the rotating island, see Fig.6.28 (left).

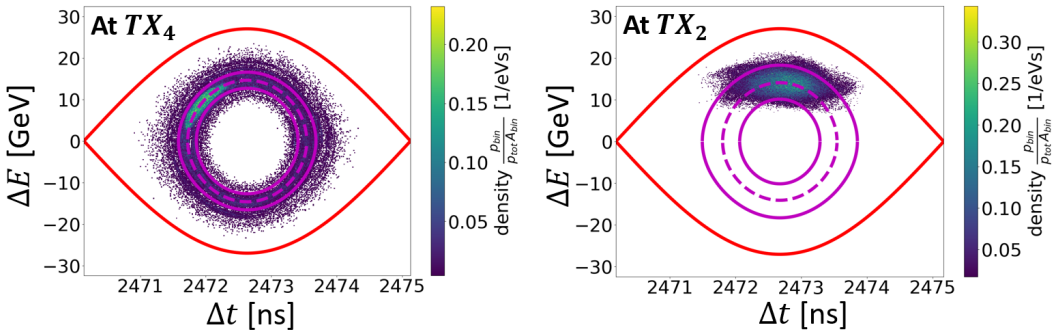


**Figure 6.28.** Left: phase-space distribution of the first bunch at the beginning of flat top with $V_{\mathrm{rf}}^{200} = 5.5$ MV. The dashed and continuous magenta lines mark the stable particle-trajectories crossing respectively the center and borders of the rotating island. In increasing order, the emittances are $\epsilon_{\mathrm{l}} = 0.15$ eVs/A$_m$, $\epsilon_{\mathrm{l}} = 0.20$ eVs/A$_m$ and $\epsilon_{\mathrm{l}} = 0.26$ eVs/A$_m$. Right: phase-space distribution of the first bunch at recapture time with $V_{\mathrm{rf}}^{200} = 8$ MV. The dashed and continuous magenta lines mark the stable particle-trajectories crossing respectively the center and borders of the displaced-bunch core. In increasing order, the emittances are $\epsilon_{\mathrm{l}} = 0.09$ eVs/A$_m$, $\epsilon_{\mathrm{l}} = 0.18$ eVs/A$_m$ and $\epsilon_{\mathrm{l}} = 0.32$ eVs/A$_m$.

This analysis suggests that the hole in the phase-space distribution in Fig.6.25

(left) prevents to exploit the significant energy spread available at relatively low particle amplitudes when the 800 MHz RF system is used. Notice that the holes related to the middle and last bunches (Fig.6.25, center and right) have smaller areas relative to the first bunch. This is mostly due to the fact that, at recapture time, given a certain $\Delta E_b$, larger emittance bunches are closer to the $\Delta E = 0$ axis.

The 800 MHz RF voltage was also applied after MSS at 300 $Z_a$GeV/c, just at the moment of recapture $TX_2$. The goal was to increase the nonlinearities of the bunch before the hollow distribution was formed. In addition, since the LLD threshold is higher at lower energies, the 800 MHz RF system could potentially be more effective there. Notice that, from recapture time until flat-top, the dipole oscillation amplitude does not change (Fig.6.22) since, as already observed above, no instabilities arise after slip-stacking, LLD being the only intensity-effects related phenomenon. Therefore, applying the 800 MHz RF voltage at 300 $Z_a$GeV/c after that the hollow bunch is formed, instead of at flat top, does not provide any advantage in terms of amplitude of dipole oscillations to be damped.

Figure 6.29 shows the simulation results at 300 $Z_a$GeV/c for the bunch lengthening and shortening modes using a $V_{\mathrm{rf}}^{800}$ which is 5%, 10% and 20% of $V_{\mathrm{rf}}^{200}$. While dipole oscillations are significantly enhanced using BLM, remarkable results are obtained in BSM for $V_{\mathrm{rf}}^{800} = 0.8$ MV: dipole oscillations for the shortest bunch are completely damped and become comparable to the ones relative to the other bunches. Note that negative results are obtained using higher voltages for $V_{\mathrm{rf}}^{800}$.

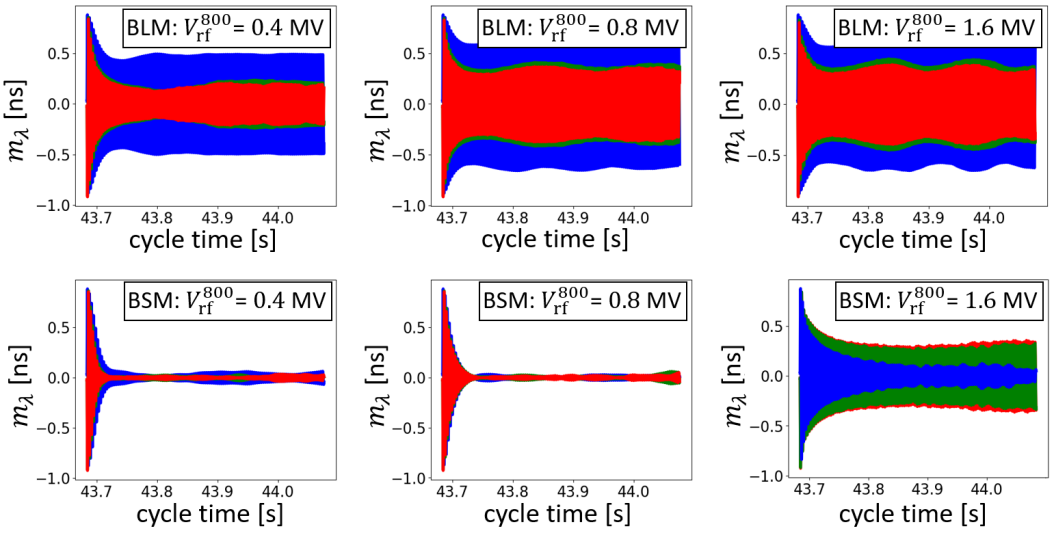


**Figure 6.29.** Dipole oscillations at 300 $Z_a$GeV/c as a function of the cycle time from $TX_2$ to $TX_3$. A constant 800 MHz RF voltage is applied in bunch lengthening (top) and shortening (bottom) modes, with $V_{\mathrm{rf}}^{800} = 0.4$ MV (left), $V_{\mathrm{rf}}^{800} = 0.8$ MV (middle), $V_{\mathrm{rf}}^{800} = 1.6$ MV (right) and always $V_{\mathrm{rf}}^{200} = 8$ MV. The blue, green and red curves refer respectively to the first, middle and last bunches.

All these results match the ones derived from applying the 800 MHz RF system in proton operation [131, 23, 132]: there it has been studied and experimentally tested that BLM does not give satisfying results, while BSM provides the desired cure for LLD only when the applied 800 MHz RF voltage is relatively low.

Following the same reasoning used to explain the proton beam dynamics in a double RF system [132], Fig.6.30 shows the synchrotron frequency distribution at 300 $Z_a$GeV/c as a function of the emittance for different configurations of the 800 MHz RF system. Similarly to what already done for the rotating island at the beginning of flat top (Fig.6.28, left), we focus on the stable particle-trajectories crossing the center and borders of the shortest-bunch core at recapture time (Fig.6.28, right).

One can see that, when $V_{\mathrm{rf}}^{800}$ is 10% of $V_{\mathrm{rf}}^{200}$ and BSM is used (Fig.6.30, left), the spread in frequency is maximum with $\Delta f_s \approx 60$ Hz, which is roughly three times higher than the corresponding value found above for the island at flat top (Fig.6.27, left). In addition, there are no points of $f_s$ with zero derivative when BSM is adopted, therefore damping of dipole oscillations can be expected in this case (Fig.6.29, middle-bottom). On the contrary, when BLM is used with $V_{\mathrm{rf}}^{800} = 0.8$ MV, the frequencies of the particles cover entirely the flat portion of $f_s$, with a spread even lower than the one obtained using only the 200 MHz RF system. This leads to considerable dipole oscillations (Fig.6.29, middle-top), significantly larger than the ones obtained by using only the single RF system (Fig.6.22, bottom-left).

Increasing the voltage of the 800 MHz RF system to 1.6 MV worsens the situation (Fig.6.30, right). The synchrotron frequency distribution for the BLM case has the same shape as above, therefore large dipole oscillations are again obtained (Fig.6.29, top-right). On the contrary, the shape of $f_s$ for the BSM case changes significantly: even if the spread in frequency increases to $\Delta f_s \approx 90$ Hz, the higher amplitude particles have the same synchrotron frequency which corresponds to the flat portion of $f_s$. This explains the less effective damping observed in Fig.6.29 (bottom-right) for the shortest bunch. This plot also shows that even worse results are obtained for the middle and last bunches which, having larger emittances, cover even more the flat portion of $f_s$.

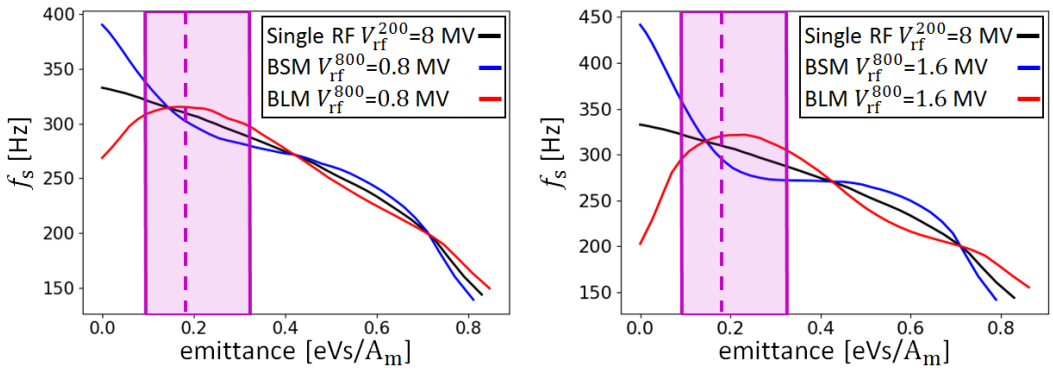


**Figure 6.30.** Synchrotron frequency distribution at 300 $Z_a$GeV/c as a function of emittance using different configurations of the 800 MHz RF system. Left: single RF with $V_{\mathrm{rf}}^{200} =$ 8 MV (black), double RF with $V_{\mathrm{rf}}^{200} = 8$ MV and $V_{\mathrm{rf}}^{800} = 0.8$ MV in bunch shortening (blue) and lengthening (red) modes. Right: the same configurations shown on the left, except that $V_{\mathrm{rf}}^{800} = 1.6$ MV. The dashed and continuous magenta vertical lines mark the stable particle-trajectories crossing respectively the center and borders of the displaced-bunch core, see Fig.6.28 (right).

Finally, the successful RF configuration found at recapture time ($V_{\mathrm{rf}}^{200} = 8$ MV,

$V_{\mathrm{rf}}^{800}$ = 0.8 MV, BSM) was applied at 300 $Z_a$GeV/c after bunch filamentation and formation of the hollow structure, see Fig.6.31. Comparing also with the corresponding single RF case (Fig.6.22, bottom), one can see that the use of the 800 MHz RF system does not lead to any effect. This could have been expected since, similarly to what was observed above at flat top (Fig.6.27, left), the rotating island of the shortest bunch is dense and covers only a small range of amplitudes in phase space, leading to a minimal frequency spread.

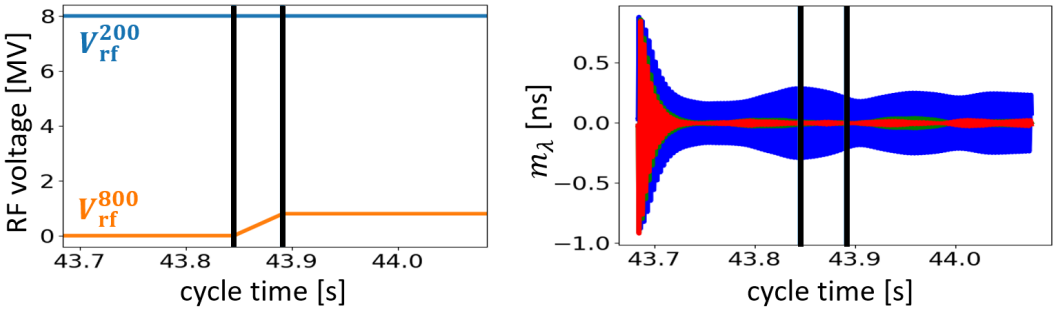


**Figure 6.31.** Left: voltage programs for the 200 MHz and 800 MHz RF systems (BSM mode) as a function of the cycle time from $TX_2$ to $TX_3$ at 300 $Z_a$GeV/c. Right: corresponding dipole oscillations for the first (blue), middle (green) and last (red) bunches. The 800 MHz voltage increases linearly from 0 MV to 0.8 MV during the time interval marked by the two vertical black lines.

The simulation results presented in this Section have shown that the only way to properly cure LLD for the shortest bunches in the batch is to apply the 800 MHz RF voltage in bunch shortening mode and exactly at recapture time, before the hollow-bunch structure is formed.

## 6.6 Conclusions

Momentum slip-stacking of LHC-ion beams in the SPS in framework LIU is fundamental to fulfill the requirements imposed by the High Luminosity LHC Project: halving the bunch spacing in the SPS will allow to increase the peak luminosity in the LHC by a factor of two.

Numerous parameters had to be decided in order to perform a successful slip-stacking. Therefore, after having taken into account the two main constraints dictated by the LIU Project on beam losses and bunch length at extraction energy, the first problem was to determine a minimum set of parameters and conditions able to uniquely characterize a simulation while providing enough flexibility and variety in the simulated beam dynamics. Due to the complexity of the involved RF manipulations and the stringent LIU constraints, a careful optimization study has been performed in order to determine the most desirable beam and machine parameters for the three SPS optics Q20, Q22 and Q26.

Simulations were performed including a reliable SPS impedance model and a careful estimation of the longitudinal space charge. Results indicated that slip-stacking can be applied under certain conditions, providing at extraction the beam parameters required by the LIU project. In particular, it has been emphasized that

bunch compression at flat top, while suitable for the Q22 and Q26 optics, cannot be used for the Q20 optics. In this last case bunch rotation at flat top has to be adopted.

Simulation results also showed that collective effects do not affect the particle losses and maximum bunch-length along the batch at extraction energy. However, intensity effects led to loss of Landau damping for the shortest bunches in the formed batch, severely degrading their quality. More precisely, after recapture time, bunches become hollow and, whenever there is LLD, a relatively small and dense rotating island, which never filaments, is formed in phase space. Analytical calculations confirmed the LLD observed in simulations.

Finally, several studies were done to verify if the 800 MHz RF system could cure LLD. It was shown in simulations that the 800 MHz RF voltage could not help if applied on hollow bunches, either at slip-stacking energy or at flat-top, independently of the relative phase between the main and second RF systems. On the contrary, the 800 MHz cavity could cure LLD if its voltage was applied in bunch-shortening mode exactly at recapture time before hollow bunches were formed. Qualitative explanations have been given to illustrate the reasons why the 800 MHz RF system has proved to be or not successful in all the examined cases.

# Summary and Conclusions

Macro-particle simulations of beam dynamics in accelerators are often used to study numerous cases of interests where analytical studies cannot provide complete understandings. In the more restricted domain of longitudinal beam dynamics the CERN BLonD code for macro-particle simulation is nowadays one of the packages openly available and able to satisfy almost all the accelerator physicists needs. In this thesis, BLonD has been used to study the longitudinal beam dynamics of PSB proton and SPS ion beams in the framework of the CERN LIU Project (post-2021 scenario).

One of the achievements of this thesis has been the validation, through benchmarks and theoretical studies, of the BLonD code [35, 15, 16]. The BLonD project started in 2014 and personal contributions to general improvement and consolidation of the code features (e.g. collective effects, feedbacks) have been presented. Benchmarks with the accelerator simulation code PyORBIT were performed in view of space charge studies at PSB injection for the after-upgrade scenario [82]; good agreements were found also comparing the simulation results with analytical formulas. After a review of the currently available longitudinal beam dynamics codes to study beam instabilities in synchrotrons [29], the present work compared through benchmarks two different approaches for induced voltage calculation [60], namely the ones used in the BLonD and MuSiC codes. Two critical and relatively common types of wakefield were analyzed: the first was generated by a broad-band resonator impedance with a resonant frequency much higher than the Gaussian bunch spectrum cut-off frequency; the second was generated by a narrow-band resonator with resonant frequency much lower than the spectrum cut-off frequency. For the first case just benchmarks between the two codes were performed, since the initial bunch mismatch due to high induced voltage created significant filamentation, losses and later equilibrium in phase space, making the problem difficult to study analytically. Instead for the second case, where the single bunch induced voltage propagate over many turns, simulations were compared with the analytical formula giving the rising time of the Robinson instability. After a careful choice of the simulation parameters, consistency of the MuSiC and BLonD codes was obtained. In addition some computational time considerations were given suggesting which approach to use for a given case. As a by-product of this study, the MuSiC algorithm was included in BLonD to speed-up the benchmarks, allowing the BLonD users to apply both approaches to the same problem depending on their needs.

The second main achievement has been the novel study of the longitudinal beam dynamics in the CERN PSB for after-upgrade time, to evaluate the possible presence of longitudinal beam instabilities [2, 74]. Indeed, the beam performance will be

more demanding than in the current situation: the proton injection from the new Linac4 and the change of the magnet power supplies will increase the injection and extraction energies as well as the acceleration rate, the required beam intensities will be significantly higher than now, and the requested longitudinal emittance to be extracted to CERN PS for nominal-LHC beams will be 3 eVs starting at injection from a 1.4 eVs bunch (currently it increases from 1 eVs to 1.3 eVs). In addition the currently used three narrow-band ferrite RF systems will be replaced by broad-band Finemet® cavities in all four Booster rings. In a future scenario, where many beam parameters will change, and where the momentum program and some impedance contributions (of RF systems and other ring components) will be different, it is vital to predict possible instabilities, which may lead to particle losses and deterioration of beam quality during the acceleration ramp and at extraction.

The BLonD code was used to perform PSB beam simulations for the situation after LIU upgrade [52, 75]. Several features needed for low-energy and $h = 1$ rings were added in BLonD (periodicity, multi-turn wake, relativistic beta less than one). Particular attention has been given to careful estimation of the longitudinal space charge in PSB, very important contribution for all low-energy machines. The value for space charge impedance at injection was carefully estimated dividing the PSB ring into sections and considering, for each of them, the beam pipe cross section and beam transverse size to evaluate the space charge contribution in that part of the ring [83]. An updated longitudinal impedance model has been used, and effort was dedicated to include in simulations the reduction of RF system beam loading through cavity feedbacks at specific revolution harmonics. Low Level RF feedbacks, as phase and radial loops, have been also included in simulations, since they are fundamental for stable acceleration of LHC and high-intensity type beams in PSB.

Controlled longitudinal emittance blow-up, currently achieved using a dedicated high-harmonic RF system, has been studied in simulations for future scenario using an alternative method, applying band-limited phase noise in the main RF system [109]. This method, never considered for fast-cycling PSB but already used operationally in CERN SPS and LHC, allows also to flatten the bunch profile reducing transverse space charge in PSB and likely to reduce complexity of beam operation. It was possible in simulations to blow up by needed factor three the emittance of nominal LHC-type beams in just 100 ms in a single RF system, using an optimal set of configuration parameters for noise. Beam measurements confirmed that noise injection via phase loop in $h = 1$ RF system is able to blow up the beam emittance up to 2.8 eVs in a double RF operation in the bunch lengthening mode, giving confidence for future predictions.

Microwave-like instabilities for high intensity beams in PSB leading to uncontrolled longitudinal emittance blow-up were observed in simulations, and it was proposed that a possible countermeasure could be the increase of the number of revolution harmonics at which the Finemet® impedance is reduced through LLRF feedbacks. Finally comparison of beam measurements and BLonD simulations for the current situation, together with studies for the after-LIU scenario, contributed to the decision to replace in PSB all the ferrite RF systems by Finemet® ones during upgrade [79, 78, 63].

The last contribution of this thesis has been the investigation of the momentum slip-stacking for SPS ion beams, supposed to become operational only after upgrade

in 2021 [140]. The slip-stacking consists in using two RF systems with slightly different rf frequencies between them to interleave two batches in the longitudinal phase space, halving the bunch spacing and allowing to double the peak luminosity in the LHC. Preliminary results were obtained at CERN some years ago [128], but the simulations were done without intensity effects and with average measured beam parameters. In this thesis simulations with a full updated SPS impedance model and detailed (bunch-by-bunch) beam parameters derived from measurements have been performed. Because of the numerous parameters involved and the constraints on the total losses and bunch lengths at SPS extraction, several iterative algorithms were conceived to perform optimization studies. Using them it was possible to suggest the best solutions for the three different SPS optics. Results show that slip-stacking can be applied if specific conditions are fulfilled, providing at extraction energy the beam parameters requested by the LIU Project. Loss of Landau damping for shortest bunches in the batch was observed in simulations and also confirmed by analytical estimations. A possible cure using the 800 MHz RF system in bunch shortening mode was tested successfully in simulations, and the additional voltage has to be applied at recapture time after slip-stacking to obtain stable ion beams.

# Appendix A

# Some Elements of Transverse Beam Dynamics

In this Appendix we present some principles of transverse beam dynamics in a synchrotron. Contents are taken from Refs.[17, 141, 142, 53, 143].

## A.1 Hill's Equation

Let us consider a generic particle circulating in a synchrotron. Its betatron coordinates $x$ and $y$ are functions of the independent variable $s$ in the Frenet-Serret coordinate system, see Fig.2.2.

The radial centrifugal acceleration of a generic particle with an horizontal displacement $x$ relative to the reference trajectory with radius $R_0$ is

$$a_{\mathrm{r}} = \frac{d^2R}{dt^2} - R\left(\frac{d\theta}{dt}\right)^2 = \frac{d^2R}{dt^2} - R\omega^2 = \frac{d^2R}{dt^2} - \frac{v^2}{R} \quad R = R_0 + x, \tag{A.1}$$

where $\theta$ is the angular displacement from a given axis, $\omega$ the angular speed of the particle and $v$ is the cross-radial velocity. Equating the Lorentz and the radial centrifugal force we obtain

$$m\left[\frac{d^2(R_0+x)}{dt^2} - \frac{v^2}{R_0+x}\right] = qBv, \tag{A.2}$$

where $m$ is the mass of the particle, $q$ its charge. Developing for small $x$

$$m\frac{d^2x}{dt^2} - \frac{mv^2}{R_0}\left(1 - \frac{x}{R_0}\right) = qBv. \tag{A.3}$$

The bending magnetic field given by the dipoles is constant and equal to $B_0$, while the focusing magnetic field have components $B_x = gy$ and $B_y = gx$. The constant $g$ is called gradient of the quadrupole while $k = qg/p$ is the focusing strength, where $p$ is the particle momentum. Therefore, in linear approximation,

$$\frac{d^2x}{dt^2} - \frac{v^2}{R_0}\left(1 - \frac{x}{R_0}\right) = \frac{qvB_0}{m} + \frac{gqv}{m}x. \tag{A.4}$$

Changing variable from $t$ to $s$ we have

$$\frac{dx}{dt} = \frac{dx}{ds}\frac{ds}{dt} = x'v \tag{A.5}$$

and

$$\frac{d^2x}{dt^2} = \frac{d}{ds}\left(\frac{ds}{dt}\frac{dx}{ds}\frac{ds}{dt}\right) = \frac{d}{ds}(x'v^2) = x''v^2. \tag{A.6}$$

Substituting and dividing by $v^2$ it follows

$$x'' - \frac{1}{R_0}\left(1 - \frac{x}{R_0}\right) = \frac{qB_0}{mv} + \frac{gq}{mv}x. \tag{A.7}$$

Using the relation $p = mv$ and the magnetic rigidity formula $B_0R_0 = -p/e$ (note that $B_0 < 0$) we obtain

$$x'' + \left(\frac{1}{R_0^2} - k\right)x = 0, \tag{A.8}$$

and, repeating a similar reasoning for the vertical plane, we find

$$y'' + ky = 0. \tag{A.9}$$

Combining Eqs.(A.8) and (A.9), one obtains

$$X''(s) + KX(s) = 0, \tag{A.10}$$

where $X = x$, $K = 1/R_0^2 - k$ or $X = y$, $K = k$. However these equations are not really correct, since the bending and focusing forces depend on $s$. It can pe proven that instead $X(s)$ is solution of the so-called Hill's equation

$$X''(s) + K(s)X(s) = 0, \tag{A.11}$$

where the restoring force $K(s)$ is a periodic function with period $L$, called the lattice period. Only for simplicity of notation, in this Section we consider the solution of Eq.(A.11) in the horizontal plane (the same reasoning applies to the vertical plane). This solution can be written as

$$x(s) = \sqrt{\epsilon_x\beta_x(s)}\cos[\psi_x(s) + \phi_x], \tag{A.12}$$

where $\beta_x$ is called horizontal beta function, has period $L$ and takes into account the focusing properties of the lattice. The constant quantities $\epsilon_x$ and $\phi_x$ depends on the initial conditions associated with Eq.(A.12). It can be proven (Floquet's theorem) that

$$\psi_x(s) = \int_0^s \frac{dz}{\beta_x(z)}. \tag{A.13}$$

The function $\psi(s)$ is called phase advance of the oscillation between the points 0 and $s$ of the lattice. The phase advance for one revolution turn determines the so-called betatron tune $Q_x$

$$Q_x = \frac{1}{2\pi}\oint \frac{ds}{\beta_x(s)}, \tag{A.14}$$

which is the number of horizontal oscillations per revolution turn.

## A.2 Twiss Parameters and Transverse Emittance

It can be proven that the particle trajectory in the phase space $X - X'$ follows an ellipse with equation

$$\epsilon_X = \gamma_X(s)X(s)^2 + 2\alpha_X(s)X(s)X'(s) + \beta_X(s)X'(s)^2, \tag{A.15}$$

where

$$\alpha_X(s) = -\frac{1}{2}\beta'_X(s), \quad \gamma_X(s) = \frac{1+\alpha_X(s)^2}{\beta_X(s)} \tag{A.16}$$

and $\beta_X(s)$ are the so-called Twiss parameters determining the shape and orientation of the ellipse. The maximum amplitude is given by $X_{\max} = \sqrt{\epsilon_X \beta_X}$ and the corresponding angle is $\hat{X}' = -\alpha_X\sqrt{\epsilon_X/\beta_X}$, while the maximum angle is $X'_{\max} = \sqrt{\epsilon_X\gamma_X}$ with the corresponding amplitude $-\alpha_X\sqrt{\epsilon_X/\gamma_X}$. Therefore large values of $\beta_X$ correspond to larger particle displacements from the design orbit and to smaller divergences. The quantity $\epsilon_X$ is a constant of motion called Courant-Snyder invariant and the area $A_X$ of the ellipse is given by $A_X = \pi\epsilon_X$.

If we have an ensemble of particles circulating in a synchrotron, each particle will have its Courant-Snyder invariant $\epsilon_X$ and its displacement will always be $|X(s)| \leq \sqrt{\epsilon_X\beta_X(s)}$, where $\beta_X$ depends on the ring lattice but not on the specific particle. Since in many cases, for every position $s$ along the ring, the horizontal and vertical particle densities follow a Gaussian distribution with standard deviation $\sigma_X(s)$, we can refer to a particle having betatron amplitude $\sigma_X(s)$ and consider its $\epsilon_X$ as a representative of the entire beam. In this sense $\epsilon_X$ is called 1-rms geometrical emittance and therefore

$$\sigma_X = \sqrt{\epsilon_X\beta_X}. \tag{A.17}$$

In practice $\sigma_X$ is found through beam measurements and then Eq.(A.17) is used to find $\epsilon_X$. This definition of geometrical emittance implies that 68.2% of all the particles are included in the area enclosed by the ellipse defined by $\epsilon_X$.

If the beam energy is increased then the geometrical emittance $\epsilon_X$ is not constant anymore. To show it, we introduce the Liouville theorem which states that the area enclosed by a stable trajectory $p_X(X)$ in the phase-space $X - p_X$ does not change with the dynamics. Therefore

$$\oint p_X dX = \text{const}, \tag{A.18}$$

where $p_X$, conjugate variable of $X$, is one of the two transverse components of the total momentum $p = \sqrt{p_x^2 + p_y^2 + p_s^2}$ ($p_s$ is the longitudinal component with usually $p \approx p_s$). Noting that

$$X' = \frac{dX}{ds} = \frac{dX}{dt}\frac{dt}{ds} = \frac{p_X}{p_s} \approx \frac{p_X}{p}, \tag{A.19}$$

it follows that

$$\oint p_X dX = m_0\gamma_0\beta_0 c \oint X' dX = \pi m_0\gamma_0\beta_0 c\epsilon_X = \text{const} \tag{A.20}$$

where $m_0$ is the rest mass of the particle and $\beta_0$ and $\gamma_0$ are the relativistic parameters of the particle. Therefore $\epsilon_X$ scales with the inverse of $\beta_0\gamma_0$ while the so-called normalized emittance $\epsilon_{X,\text{n}} \coloneqq \beta_0\gamma_0\epsilon_X$ remains constant during acceleration.

## A.3 Dispersive Effects

In the derivation of the Hill's equation above we supposed that all the particles go through the central path inside the dipoles following the circular trajectory with radius $R_0$. However this is not realistic since, if we denote by $p_0$ the desired design momentum which is defined for each revolution turn, then a particle with momentum $p \neq p_0$ will go through an arc with radius $R = p/(Bq) \neq p_0/(Bq) = R_0$. In fact the dipole provides an additional contribution $x_\mathrm{i}$ to the transverse displacement $x$

$$x_\mathrm{i}(s) = D_x(s)\frac{\Delta p}{p_0}, \tag{A.21}$$

where the horizontal dispersion function $D_x(s) \geq 0$ can be considered as an intrinsic property of the dipole. Usually the dispersion in the vertical plane is negligible.

Defining $\delta = \Delta p/p_0$ the following implication holds

$$BR = \frac{p}{q} = \frac{p_0(1+\delta)}{q} = BR_0(1+\delta) \quad \Longrightarrow \quad R = R_0(1+\delta). \tag{A.22}$$

We start from Eq.(A.2) and we change variable to $x'$ obtaining

$$x'' - \frac{1}{R_0 + x} = \frac{qB}{p_0(1+\delta)} = -\frac{1}{R_0(1+\delta)} + \frac{kx}{1+\delta}. \tag{A.23}$$

Expanding in Taylor and neglecting terms proportional to $x\delta$ we arrive at

$$x'' + \left(\frac{1}{R_0^2} - k\right)x = \frac{\delta}{R_0}. \tag{A.24}$$

The inhomogeneous Hill's equation is therefore

$$x''(s) + K(s)x(s) = \frac{\delta}{R_0(s)}, \tag{A.25}$$

with $K(s) = 1/R_0^2(s) - k(s)$. The solution of Eq.(A.25) is $x(s) = x_\mathrm{h}(s) + x_\mathrm{i}(s)$, where $x_\mathrm{h}(s)$ solves the corresponding homogeneous Hill's equation while $x_\mathrm{i}(s)$, given by Eq.(A.21), is a particular solution representing the additional deviation of an off-momentum particle relative to the design orbit. It can be proven that

$$x(s) = C(s)x_0 + S(s)x_0' + D_x(s)\delta, \tag{A.26}$$

where $x_0$, $x_0'$ are the initial values of $x_\mathrm{h}(s)$ and $x_\mathrm{h}'(s)$ at $s = 0$ and $C(s)$ and $S(s)$ are two independent solutions of the homogeneous Hill equation, specifically

$$C(s) = \sqrt{\frac{\beta_x(s)}{\beta_x(0)}}[\cos\psi_x(s) + \alpha_x(0)\sin\psi_x(s)], \quad S(s) = \sqrt{\beta_x(s)\beta_x(0)}\sin\psi_x(s), \tag{A.27}$$

while the dispersion function is given by

$$D_x(s) = S(s)\int_0^s \frac{C(t)}{R_0(t)}dt - C(s)\int_0^s \frac{S(t)}{R_0(t)}dt. \tag{A.28}$$

### A.3.1 Beam Size with Dispersive Effects

Let us fix a certain position $s$ along the ring and consider the different $x(s) = x_{\rm h}(s) + x_{\rm i}(s)$ for an ensemble of particles. We can assume that phase advance and betatron amplitude are uncorrelated in Eq.(A.12). In addition we suppose that $\psi_x$ is uniformly distributed in $[0, 2\pi]$. We have therefore

$$\langle x_{\rm h}\rangle = 0, \quad \sigma^2_{x,{\rm h}} = \langle x^2_{\rm h}\rangle = \beta_x\langle\epsilon_x\rangle\langle\cos^2(\psi_x + \phi_x)\rangle = \frac{\beta_x\langle\epsilon_x\rangle}{2}, \tag{A.29}$$

where the angular brackets indicate the average and we used the fact that the integrals of the cosine and squared cosine functions in the interval $[0, 2\pi]$ are equal to 0 and $\pi$ respectively. Assuming that the energy deviation satisfies $\langle\delta\rangle = 0$, then $\langle x\rangle = 0$. If no correlation exists between the betatron phase and energy deviation then

$$\sigma_x = \sqrt{\langle x^2\rangle} = \sqrt{\langle x^2_{\rm h}\rangle + \langle x^2_{\rm i}\rangle + 2\langle x_{\rm h}\rangle\langle x_{\rm i}\rangle} = \sqrt{\frac{\beta_x\langle\epsilon_x\rangle}{2} + D^2_x\langle\delta^2\rangle}. \tag{A.30}$$

If in particular $x_{\rm h}$ follows a Gaussian distribution, then we can use the definition of geometrical emittance in Eq.(A.17) to obtain

$$\sigma_x = \sqrt{\beta_x\epsilon_x + D^2_x\langle\delta^2\rangle}. \tag{A.31}$$

In addition, if $x$ is Gaussian, then $r = \sqrt{\beta_x\epsilon_x}$ and $r^2$ follow respectively a Rayleigh and exponential distributions with probability density functions [144]

$$f_r(z) = \frac{z}{\sigma^2_{x,{\rm h}}} e^{-\frac{z^2}{2\sigma^2_{x,{\rm h}}}}, \quad f_{r^2}(z) = \frac{1}{2\sigma^2_{x,{\rm h}}} e^{-\frac{z}{2\sigma^2_{x,{\rm h}}}}, \quad z \geq 0, \tag{A.32}$$

and, as expected from Eq.(A.29), one finds

$$\beta_x\langle\epsilon_x\rangle = \langle r^2\rangle = 2\sigma^2_{x,{\rm h}}. \tag{A.33}$$

## A.4 Resonances due to Magnet Imperfections

Up to know we have assumed that the design orbit of radius $R_0$ passes through the center of all the quadrupole magnets and that all the dipoles are perfectly designed. The closed orbit in this case, defined as the path around which particles perform betatron oscillations, coincides with the reference orbit.

In reality, however, magnetic field errors can exist, due for example to dipole and quadrupole length errors, dipole rolls producing horizontal dipole field components, errors in dipole and quadrupole power supplies, misalignments of the reference orbit with respect to the dipole and quadrupole centers.

### A.4.1 Dipole Field Errors

As an example, let us suppose to have a thin dipole magnet localized at $s = s_0$. Its field is $B = B_0 + dB$, where $dB$ is the error. The additional force and the consequent kick-angle a particle experiences in the horizontal plane are given by

$$dF_x = mv^2x'' = mv^2\frac{dx'}{ds} = evdB \implies \theta \approx dx' = -\frac{dBds}{B_0R_0} \tag{A.34}$$

where $ds$ is the length of the dipole and $dBds$ is the integrated dipole field error.

The Hill's equation becomes

$$x''(s) + K(s)x(s) = \frac{dB}{B_0 R_0}, \tag{A.35}$$

and it can be proven that the new closed orbit is given by

$$x(s) = \frac{\sqrt{\beta_x(s)\beta_x(s_0)}\theta}{2\sin(\pi Q_x)} \cos(\pi Q_x - |\psi_x(s) - \psi_x(s_0)|). \tag{A.36}$$

Notice that the horizontal tune must not be an integer number to avoid resonances. An analogous reasoning applies to the vertical tune.

### A.4.2 Quadrupole Field Gradient Errors

The Hill's equation with a focusing strength error $\Delta k$ is given by

$$x''(s) + [K(s) + \Delta k(s)]x(s) = 0. \tag{A.37}$$

One effect of this gradient error concerns the modulation of the betatron amplitude function (called beta-beating). For every location $s$ along the ring we have

$$\frac{\Delta\beta_x(s)}{\beta_x(s)} = -\frac{1}{2\sin(2\pi Q_x)} \int_s^{s+C_{\text{ring}}} \Delta k(s_1)\beta_x(s_1)\cos[2\pi Q_x + 2(\psi_x(s) - \psi_x(s_1))]ds_1 \tag{A.38}$$

Note that the horizontal tune should not be an half-integer, and the same holds for the vertical tune.

## A.5 Resonance Diagram and Tune Shift

We have seen in the previous Section that the transverse tunes must not be an integer or half-integer to avoid resonances. More in general the tunes have to fulfill the following equations

$$mQ_x + nQ_y \neq p, \tag{A.39}$$

where $m$, $n$ and $p$ are integers, $p$ being non-negative, and $|m| + |n|$ is the order of the resonance. The strength of the resonance decreases as its order goes higher.

If all the lines in Eq.(A.39) are plotted in the space $Q_x - Q_y$, then the so-called tune or resonance diagram is obtained. The point identified by the chosen tunes, called also working point, must not cross any of these lines. Unfortunately this does not guarantee that resonances are avoided since several mechanisms can create transverse tune shifts inside the beam. Some of these mechanisms are here briefly recalled.

### A.5.1 Tune Shift due to Quadrupole Gradient Errors

Let $\Delta k_X(s)$ be the focusing strength errors in the horizontal and vertical planes. Then the tune shifts are

$$\Delta Q_X = \frac{1}{4\pi} \oint \beta_X(s) \Delta k_X(s) ds \tag{A.40}$$

A peculiar case of quadrupole gradient error derives from the energy spread of the particles inside a beam. A particle with momentum $p = p_0 + \Delta p$ experiences the focusing strength

$$k = \frac{qg}{p_0 + \Delta p} \approx \frac{qg}{p_0} \left(1 - \frac{\Delta p}{p_0}\right) = k_0 + \Delta k, \tag{A.41}$$

where $k_0$ is the design focusing strength and $\Delta k = -k_0 \Delta p / p_0$ is the quadrupole error. Therefore, using Eq.(A.41) we obtain the following tune shift for the particle

$$\Delta Q_X = -\frac{\Delta p}{4\pi p_0} \oint \beta_X(s) k_{0,X}(s) ds = \xi_X \frac{\Delta p}{p_0}, \tag{A.42}$$

where $\xi_X$, always negative, is called natural chromaticity. Notice that the tune shift is different for particles having distinct momenta, therefore chromaticity leads to a tune spread in the resonance diagram. Fixing a certain energy spread inside the beam, the chromaticity determines the size of the tune spot.

### A.5.2 Tune Shift due to Direct Space Charge

Up to now we have assumed that the particles are only influenced by the electric and magnetic fields produced respectively by the RF cavities and magnets. However, being the particles charged, Coulomb interactions have also to be considered, since they induce electromagnetic fields that could lead to beam instability and quality degradation.

The mechanism of one particle interacting directly with the field induced by the other particles is called direct space charge, while the image currents and charges induced by the beam in the vacuum chamber produce wake fields which make the particles interacting among them indirectly.

When a transverse force $F_X$ produced by induced electromagnetic fields is considered, the perturbed Hill's equation becomes

$$X''(s) + K_X(s) X(s) = \frac{F_X}{mv^2} = \frac{F_X}{m_0 \gamma_0 \beta_0^2 c^2}. \tag{A.43}$$

For small amplitudes, and neglecting terms which do not depend on $X$ or $\langle X \rangle$, $F_X$ can be expanded in Taylor series obtaining

$$F_X \approx \left.\frac{\partial F_X}{\partial X}\right|_{\langle X \rangle = 0} X + \left.\frac{\partial F_X}{\partial \langle X \rangle}\right|_{X=0} \langle X \rangle \tag{A.44}$$

Comparing with Eqs.(A.37) and (A.40), the first term in Eq.(A.44) produces a tune shift which depends on the particle amplitude

$$\Delta Q_X^{\text{inc}} = -\frac{1}{4\pi m_0 \gamma_0 \beta_0^2 c^2} \oint \beta_X(s) \left.\frac{\partial F_X}{\partial X}\right|_{\langle X \rangle = 0} ds. \tag{A.45}$$

This tune shift is called incoherent since it can be computed imposing $\langle X \rangle = 0$, that is supposing no displacement of the bunch centroid.

On the other hand, the perturbed Hill's equation for the dynamics of the bunch centroid $\langle X \rangle$ is

$$\langle X \rangle'' + K_X \langle X \rangle = \frac{F_X}{m_0 \gamma_0 \beta_0^2 c^2}, \tag{A.46}$$

and this time the tune shift, dealing with the beam center, is called coherent and is given by

$$\Delta Q_X^{\mathrm{coh}} = -\frac{1}{4\pi m_0 \gamma_0 \beta_0^2 c^2} \oint \beta_X(s) \left( \left. \frac{\partial F_X}{\partial X} \right|_{\langle X \rangle = 0} + \left. \frac{\partial F_X}{\partial \langle X \rangle} \right|_{X=0} \right) ds. \tag{A.47}$$

It can be proven that, when the transverse direct space charge force $F_X$ acts on a transverse bi-Gaussian beam distribution with horizontal and vertical rms beam sizes given respectively by $\sigma_x$ and $\sigma_y$, then, for a given longitudinal coordinate $s$, the maximum tune shift is obtained for particles with zero transverse displacement and is equal to

$$\Delta Q_X^{\mathrm{sc}}(s) = -\frac{r_{\mathrm{p}} \lambda(s)}{2\pi \beta_0^2 \gamma_0^3} \oint \frac{\beta_X(z)}{\sigma_X(z)[\sigma_x(s) + \sigma_y(z)]} dz, \tag{A.48}$$

where $r_{\mathrm{p}} = e^2/(4\pi\epsilon_0 m_0 c^2)$ is the classical particle radius and $\lambda(s)$ is the longitudinal line density. Therefore the maximum tune shift in the bunch is obtained where $\lambda$ reaches its peak value $\hat{\lambda}$. Notice that in general $\sigma_x \neq \sigma_y$, see Eqs.(A.17) and (A.31). However, if we can assume $\sigma_x = \sigma_y$ (round beam cross section) and a negligible product of dispersion and energy spread in Eq.(A.31), then the maximum tune shift for a tri-Gaussian beam distribution with $\hat{\lambda} = N_{\mathrm{b}}/(\sqrt{2\pi}\sigma_{\mathrm{s}})$ is

$$\Delta Q_X^{\mathrm{sc}} \propto -\frac{N_{\mathrm{b}} R_0}{\beta_0^2 \gamma_0^3 \sigma_s \epsilon_X} = -\frac{N_{\mathrm{b}} R_0}{\beta_0 \gamma_0^2 \sigma_s \epsilon_{X,\mathrm{n}}}, \tag{A.49}$$

where $N_{\mathrm{b}}$ is the number of particles per bunch, $\sigma_s$ the longitudinal rms size in meters and $\epsilon_{X,\mathrm{n}}$ the normalized transverse emittance.

Equation (A.48) shows that the direct space charge tune shift increases with the longitudinal line density value. The same applies in the transverse planes, namely particles with smaller betatron amplitudes experience higher tune shifts. Therefore transverse direct space charge leads to a tune spread in the resonance diagram, with the bunch core experiencing the largest tune shift.

# Bibliography

[1] "CERN Official Website." https://home.cern/about/accelerators.

[2] H. Damerau *et al.*, "LHC Injectors Upgrade, Technical Design Report, Vol. I: Protons," Tech. Rep. CERN-ACC-2014-0337, CERN, Geneva, Switzerland, 2014.

[3] J. Coupard *et al.*, "LHC Injectors Upgrade, Technical Design Report, Vol. II: Ions," Tech. Rep. CERN-ACC-2016-0041, CERN, Geneva, 2016.

[4] W. Herr and B. Muratori, "Concept of Luminosity," in *Proc. CAS - CERN Accelerator School: Intermediate Course on Accelerator Physics, Zeuthen, Germany, 15 - 26 Sep 2003*, pp. 361–378.

[5] O. Brüning and S. Myers, *Challenges and Goals for Accelerators in the XXI Century*. World Scientific, 2016.

[6] M. Benedikt *et al.*, "The PS Complex Produces the Nominal LHC Beam," in *Particle accelerator. Proceedings, 7th European Conference, EPAC 2000, Vienna, Austria, June 26-30, 2000. Vol. 1-3*, pp. 527–529.

[7] C. A. Brau, "What Brightness Means," in *Proceedings, Joint ICFA Advanced Accelerator and Beam Dynamics Workshop: The Physics and Applications of High Brightness Electron Beams: Chia Laguna, Sardina, Italy, July 1-6, 2002*, pp. 20–27.

[8] F. M. Velotti, *Higher Brightness Beams from the SPS for the HL-LHC Era*. PhD thesis, Ecole Polytechnique (Lausanne, Switzerland), 2017.

[9] G. Apollinari *et al.*, *High-Luminosity Large Hadron Collider (HL-LHC): Preliminary Design Report*. CERN Yellow Reports: Monographs, Geneva: CERN, 2015.

[10] R. Alemany *et al.*, "LHC Injectors Upgrade (LIU) Project Description," Tech. Rep. EDMS NO. 1448566, CERN, Geneva, Switzerland, 2018.

[11] E. Metral *et al.*, "Update of the HL-LHC Operational Scenarios for Proton Operation," Tech. Rep. CERN-ACC-NOTE-2018-0002, CERN, Geneva, Switzerland, 2018.

[12] "CERN BLonD Code." http://blond.web.cern.ch.

[13] K. Iliakis, D. Soudris, H. Timko, and S. Xydis, "BLonD++: Performance Analysis and Optimizations for Enabling Complex, Accurate and Fast Beam Dynamics Studies," in *International Conference on Embedded Computer Systems: Architectures, Modeling, and Simulation (SAMOS'18), Samos Island, Greece, July 15-19, 2018*.

[14] "CERN BLonD Code Meetings." https://indico.cern.ch/category/6499/.

[15] A. Lasheen *et al.*, "Synchrotron Frequency Shift as a Probe of the CERN SPS Reactive Impedance," in *Proceedings, 54th ICFA Advanced Beam Dynamics Workshop on High-Intensity and High-Brightness Hadron Beams (HB2014): East Lansing, MI, November 10-14, 2014*, p. 409.

[16] J. Campelo *et al.*, "An Extended SPS Longitudinal Impedance Model," in *Proc. 6th International Particle Accelerator Conference (IPAC'15), Richmond, VA, USA, May 3-8, 2015*, pp. 360–362.

[17] S. Y. Lee, *Accelerator Physics*. World Scientific, 3rd ed., 2011.

[18] E. Métral, "Longitudinal Beam Dynamics." Lecture at the Joint Universities Accelerator School (JUAS), Archamps, France, 2011.

[19] G. Dôme, "The SPS Acceleration System Travelling Wave Drift-tube Structure for the CERN SPS," in *Proton Linear Accelerator Conference, Chalk River, Canada, 14 - 17 Sep 1976*, pp. 138–147.

[20] A. Krusche and M. Paoluzzi, "The New Low Frequency Accelerating Systems for the CERN PS Booster," in *Particle accelerator. Proceedings, 6th European conference, EPAC'98, Stockholm, Sweden, June 22-26, 1998. Vol. 1-3*, pp. 1782–1783.

[21] "CERN BLonD Code Documentation." http://blond-admin.github.io/BLonD/.

[22] J. A. MacLachlan, "Difference Equations for Longitudinal Motion in a Synchrotron," Tech. Rep. FERMILAB-FN-529, FERMILAB, Batavia, USA, 1989.

[23] E. Shaposhnikova *et al.*, "Longitudinal Instabilities in the SPS and Beam Dynamics Issues with High Harmonic RF Systems," in *Proceedings of ICFA Advanced Beam Dynamics Workshop on High-Intensity and High-Brightness Hadron Beams (HB'12), Beijing, China, September 17-21, 2012*, pp. 358–362.

[24] J. L. Laclare, "Bunched Beam Coherent Instabilities," in *Proc. CAS - CERN Accelerator School : Accelerator Physics, Oxford, UK, 16 - 27 Sep 1985*, pp. 264–326.

[25] G. Stupakov and G. Penn, *Classical Mechanics and Electromagnetism in Accelerator Physics*. Graduate texts in physics, Springer, 2018.

[26] A. Burov, "Loss of Landau Damping for Bunch Oscillations," Tech. Rep. FERMILAB-PUB-11-174-AD, FERMILAB, Batavia, USA, 2012.

[27] S. Koscielniak and H. J. Tran, "Decoherence of Displaced Beam With Binomial Amplitude Distribution," in *Proceedings of the Fifth European Particle Accelerator Conference (EPAC 96), Sitges (Barcelona), 10-14 June 1996*, p. 1126.

[28] L. Palumbo, V. G. Vaccaro, and M. Zobov, "Wake Fields and Impedance," in *Advanced accelerator physics. Proceedings, 5th Course of the CERN Accelerator School, Rhodos, Greece, September 20-October 1, 1993. Vol. 1, 2*, pp. 331–390.

[29] M. Migliorati and D. Quartullo, "Impedance-induced Beam Instabilities and Damping Mechanisms in Circular Machines – Longitudinal - Simulations," *ICFA Beam Dyn. Newslett.*, vol. 69, pp. 132–141, 2016.

[30] R. H. Siemann, "Computer Models of Instabilities in Electron Storage Rings," in *Proceedings, 3rd Summer School on High-Energy Particle Accelerators: Upton, New York, July 6-16, 1983*, vol. 127, pp. 368–442.

[31] J. MacLachlan and J. Ostiguy, "Enhancements to the Longitudinal Dynamics Code ESME," in *Proceedings of the 1997 Particle Accelerator Conference (Cat. No.97CH36167)*, vol. 2, pp. 2556–2558 vol.2, May 1997.

[32] G. Dattoli *et al.*, "Electron Beam Properties and Impedance Characterization for Storage Rings Used for Free Electron Lasers," *Nucl. Instrum. Met. Phys. Res., Sect. A*, vol. 471, pp. 403–411, 2001.

[33] R. Boni *et al.*, "DAPHNE Accumulator Ring Coupling Impedance Measurements," *Nuclear Instruments and Methods in Physics Research Section A Accelerators Spectrometers Detectors and Associated Equipment*, vol. 418, pp. 241–248, 1998.

[34] D. Alesini *et al.*, "Longitudinal Beam Dynamics in the Frascati DAPhNE e+ e- Collider with a Passive Third Harmonic Cavity in the Lengthening Regime," *Phys. Rev. ST Accel. Beams*, vol. 6, p. 074401, 2003.

[35] H. Timko, J. E. Müller, A. Lasheen, and D. Quartullo, "Benchmarking the Beam Longitudinal Dynamics Code BLonD," in *Proc. of International Particle Accelerator Conference (IPAC'16), Busan, Korea, May 8-13, 2016*, pp. 3094–3097.

[36] M. Migliorati and L. Palumbo, "Multibunch and Multiparticle Simulation Code with an Alternative Approach to Wakefield Effects," *Phys. Rev. ST Accel. Beams*, vol. 18, p. 031001, 2015.

[37] J. F. Ostiguy and V. Lebedev, "A Tool for Small Longitudinal Beam Dynamics in Synchrotrons," in *Proc. of International Particle Accelerator Conference (IPAC'17), Copenhagen, Denmark, 14-19 May, 2017*, pp. 3865–3868.

[38] M. Yamamoto, "Longitudinal Particle Tracking Code for a High Intensity Proton Synchrotron," in *Proc. of ICFA Advanced Beam Dynamics Workshop on High-Intensity and High-Brightness Hadron Beams (HB'16), Malmö, Sweden, July 3-8, 2016*, pp. 110–114.

[39] Y. S. Yuan, N. Wang, S. Y. Xu, and S. Wang, "A Code for the Optimization of RF Voltage Waveform and Longitudinal Beam Dynamics Simulation in an RCS," *Nuclear Instruments and Methods in Physics Research Section A: Accelerators, Spectrometers, Detectors and Associated Equipment*, vol. 729, pp. 864 – 869, 2013.

[40] G. Rumolo and F. Zimmermann, "Practical User Guide for HEADTAIL," Tech. Rep. SL-Note-2002-036-AP, CERN, Geneva, Switzerland, 2002.

[41] N. Mounet, *The LHC Transverse Coupled-Bunch Instability*. PhD thesis, Ecole Polytechnique (Lausanne, Switzerland), 2012.

[42] M. Blaskiewicz, "Fast Head-tail Instability with Space Charge," *Phys. Rev. ST Accel. Beams*, vol. 1, p. 044201, 1998.

[43] G. Bassi, A. Blednykh, and V. Smaluk, "Self-consistent Simulations and Analysis of the Coupled-bunch Instability for Arbitrary Multibunch Configurations," *Phys. Rev. Accel. Beams*, vol. 19, p. 024401, 2016.

[44] R. D. Ryne, "Advanced Computing Tools And Models For Accelerator Physics," in *Proceedings of the Eleventh European Particle Accelerator Conference (EPAC'08), Genoa, Italy, 23-27 June 2008*, p. 2947.

[45] "CERN Future Circular Collider." https://fcc.web.cern.ch/Pages/default.aspx.

[46] M. Ferrario, M. Migliorati, and L. Palumbo, "Wakefields and Instabilities in Linear Accelerators," in *Proc. CAS - CERN Accelerator School: Advanced Accelerator Physics Course: Trondheim, Norway, August 18-29, 2013*, pp. 357–375.

[47] P. B. Wilson and J. E. Griffin, "High Energy Electron Linacs; Application to Storage Ring RF Systems and Linear Colliders," *AIP Conf. Proc.*, vol. 87, pp. 450–555, 1982.

[48] "Computer Simulation Technology (CST) Software." http://www.cst.com.

[49] W. Bruns, "GdfidL: a Finite Difference Program with Reduced Memory and CPU Usage," in *Proceedings of the 1997 Particle Accelerator Conference (Cat. No.97CH36167)*, vol. 2, pp. 2651–2653, 1997.

[50] C. K. Ng *et al.*, "Advances in Parallel Finite Element Code Suite ACE3P," in *Proc. 6th International Particle Accelerator Conference (IPAC'15), Richmond, VA, USA, May 3-8, 2015*, pp. 702–704.

[51] N. Biancacci and M. Migliorati, "Wakefield Approximations." Presentation at the CERN Impedance Meeting, Geneva, Switzerland, 23 Feb 2018. https://indico.cern.ch/event/705548/.

[52] D. Quartullo, S. Albright, E. Shaposhnikova, and H. Timko, "CERN PS Booster Longitudinal Dynamics Simulations for the Post-LS2 Scenario," in *Proc. of ICFA Advanced Beam Dynamics Workshop on High-Intensity and*

*High-Brightness Hadron Beams (HB'16), Malmö, Sweden, July 3-8, 2016*, pp. 140–145.

[53] K. Y. Ng, "Physics of Intensity Dependent Beam Instabilities," Tech. Rep. FERMILAB-FN-0713, FERMILAB, Batavia, USA, 2002.

[54] R. L. Warnock and J. A. Ellison, "A General Method for Propagation of the Phase Space Distribution, with Application to the Sawtooth Instability," in *The physics of high brightness beams. Proceedings, 2nd ICFA Advanced Accelerator Workshop, Los Angeles, USA, November 9-12, 1999*, pp. 322–348.

[55] M. Migliorati, A. Schiavi, and G. Dattoli, "Modeling High-current Instabilities in Particle Accelerators," in *Proc. of International Computational Accelerator Physics Conference (ICAP'06), Chamonix, France, 2-6 October 2006*, pp. 110–113.

[56] R. Warnock, "Study of Bunch Instabilities by the Nonlinear Vlasov–Fokker–Planck Equation," *Nuclear Instruments and Methods in Physics Research Section A: Accelerators, Spectrometers, Detectors and Associated Equipment*, vol. 561, pp. 186–194, 2006.

[57] G. Dattoli, M. Migliorati, and A. Schiavi, "Study of Coherent Synchrotron Radiation Effects by Means of a New Simulation Code Based on the Nonlinear Extension of the Operator Splitting Method," *Nuclear Instruments and Methods in Physics Research Section A: Accelerators, Spectrometers, Detectors and Associated Equipment*, vol. 574, no. 2, pp. 244 – 250, 2007.

[58] A. Hofmann, "Landau Damping," in *Proc. CAS - CERN Accelerator School: Intermediate Course on Accelerator Physics, Zeuthen, Germany, 15 - 26 Sep 2003*, pp. 271–304.

[59] V. I. Balbekov and S. V. Ivanov, "Thresholds of Longitudinal Instability of Bunched Beam in the Presence of Dominant Inductive Impedance," Tech. Rep. IHEP-OUNK–91-14, Institut fiziki vysokikh ėnergiĭ, Protvino , Russia, 1991.

[60] D. Quartullo, M. Migliorati, and J. Repond, "Comparison of Different Methods to Calculate Induced Voltage in Longitudinal Beam Dynamics Codes," in *Proc. of International Particle Accelerator Conference (IPAC'17), Copenhagen, Denmark, 14-19 May, 2017*, pp. 4465–4468.

[61] A. W. Chao, *Physics of Collective Beam Instabilities in High-energy Accelerators.* New York, USA: Wiley (1993) 371 p, 1993.

[62] M. Paoluzzi. CERN, personal communication, 2015.

[63] M. Paoluzzi *et al.*, "Design of the New Wideband RF System for the CERN PS Booster," in *Proc. of International Particle Accelerator Conference (IPAC'16), Busan, Korea, May 8-13, 2016*, pp. 441–443.

[64] S. Hancock, M. Lindroos, and S. Koscielniak, "Longitudinal Phase Space Tomography with Space Charge," *Phys. Rev. ST Accel. Beams*, vol. 3, p. 124202, 2000.

[65] F. Schmidt and H. Bartosik, "LIU Space Charge Studies for the LHC Pre-accelerators," in *Proc. 9th International Particle Accelerator Conference (IPAC'18), Vancouver, BC, Canada, April 29-May 4, 2018*, pp. 810–813.

[66] M. Meddahi and G. Rumolo, "LHC Injectors Upgrade: Ready for Installation." Presentation at the 8th CERN HL-LHC Collaboration Meeting, Geneva, Switzerland, 15-18 Oct 2018. https://indico.cern.ch/event/742082/contributions/3072174/.

[67] H. Bartosik and G. Rumolo, "Review of LIU Beam Parameter Table: Protons." Presentation at the 10th CERN LIU Beam Parameter WG Meeting, Geneva, Switzerland, 26 Aug 2016. https://indico.cern.ch/event/557356/contributions/2246280/.

[68] E. Benedetto *et al.*, "CERN PS Booster Upgrade and LHC Beams Emittance," in *Proc. 6th International Particle Accelerator Conference (IPAC'15), Richmond, VA, USA, May 3-8, 2015*, pp. 3897–3900.

[69] F. Antoniou *et al.*, "The CERN PS Booster: Space Charge Challenges." Presentation at the 2nd CERN Space Charge Collaboration Meeting, Geneva, Switzerland, 12 Mar 2018. https://indico.cern.ch/event/688897/contributions/2851132/.

[70] E. Benedetto, M. Cieslak-Kowalska, V. Forte, and F. Schmidt, "Space Charge Effects and Mitigation in the CERN PS Booster, in View of the Upgrade," in *Proc. of ICFA Advanced Beam Dynamics Workshop on High-Intensity and High-Brightness Hadron Beams (HB'16), Malmö, Sweden, July 3-8, 2016*, pp. 517–522.

[71] V. Forte *et al.*, "The PSB Operational Scenario with Longitudinal Painting Injection in the Post-LIU Era," in *Proc. of International Particle Accelerator Conference (IPAC'17), Copenhagen, Denmark, 14–19 May, 2017*, pp. 3331–3334.

[72] L. Feliciano *et al.*, "A New Hardware Design for PSB Kicker Magnets (KSW) for the 35 mm Transverse Painting in the Horizontal Plane," in *Proc. 6th International Particle Accelerator Conference (IPAC'15), Richmond, VA, USA, May 3-8, 2015*, pp. 3890–3892.

[73] S. Albright, "PS Booster Magnetic Cycles to 1.4 and 2 GeV after LS2," Tech. Rep. EDMS NO. 1770413, CERN, Geneva, Switzerland, 2017.

[74] E. Métral *et al.*, "Beam Instabilities in Hadron Synchrotrons," *IEEE Transactions on Nuclear Science*, vol. 63, no. 2, pp. 1001–1050, 2016.

[75] D. Quartullo, S. Albright, and E. Shaposhnikova, "Studies of Longitudinal Beam Stability in CERN PS Booster After Upgrade," in *Proc. of International Particle Accelerator Conference (IPAC'17), Copenhagen, Denmark, 14–19 May, 2017*, pp. 4469–4472.

[76] "Phase Space Tomography." http://tomograp.web.cern.ch/tomograp/.

[77] A. Savitzky and M. Golay, "Smoothing and Differentiation of Data by Simplified Least Squares Procedures," *Analytical chemistry*, vol. 36, pp. 1627–1639, 1964.

[78] S. Albright, D. Quartullo, and E. Shaposhnikova, "Longitudinal Beam Stability in the PSB: Studies, Simulations and Measurements." Presentation at the 2nd CERN Finemet Review, Geneva, Switzerland, 14-16 Sep 2015. https://indico.cern.ch/event/379027/contributions/901840/.

[79] S. Albright, D. Quartullo, and E. Shaposhnikova, "Preparations for Upgrading the RF Systems of the PS Booster," in *Proc. of International Particle Accelerator Conference (IPAC'16), Busan, Korea, May 8-13, 2016*, pp. 853–855.

[80] A. Lasheen, *Beam Measurements of the Longitudinal Impedance of the CERN Super Proton Synchrotron*. PhD thesis, Université Paris-Saclay (Paris, France), 2017.

[81] P. W. Krempl, "The Abel-type Integral Transformation with the Kernel (t2-x2)-1/2 and its Application to Density Distributions of Particle Beams," 1974. Tech. Rep. CERN Note MPS/Int. BR/74-1.

[82] V. Forte, E. Benedetto, A. Lombardi, and D. Quartullo, "Longitudinal Injection Schemes For the CERN PS Booster at 160 MeV Including Space Charge Effects," in *Proc. 6th International Particle Accelerator Conference (IPAC'15), Richmond, VA, USA, May 3-8, 2015*, pp. 378–381.

[83] D. Quartullo and V. Forte, "Longitudinal Space Charge Simulations with BLonD at Injection in the CERN PS Booster." Presentation at the EuCARD2/XBeams Workshop on Space-Charge, Oxford, UK, 23-27 Mar 2015. https://indico.cern.ch/event/370267/contributions/877425/.

[84] L. Wang and Y. Li, "Analysis of the Longitudinal Space Charge Impedance of a Round Uniform Beam Inside Parallel Plates and Rectangular Chambers," *Phys. Rev. ST Accel. Beams*, vol. 18, no. 2, p. 024201, 2015.

[85] S. Hansen *et al.*, "Effects of Space Charge and Reactive Wall Impedance on Bunched Beams," *IEEE Trans. Nucl. Sci.*, vol. 22, pp. 1381–1384, 1975.

[86] R. Baartman, "Form Factor g In Longitudinal Space Charge Impedance," Tech. Rep. TRI-DN-92-K206, TRIUMF, Vancouver, Canada, 1992.

[87] A. Shishlo, S. Cousineau, J. Holmes, and T. Gorlov, "The Particle Accelerator Simulation Code PyORBIT," *Procedia Computer Science*, vol. 51, pp. 1272 – 1281, 2015. International Conference On Computational Science, ICCS 2015.

[88] V. Forte, *Performance of the CERN PSB at 160 MeV with $H^-$ Charge Exchange Injection*. PhD thesis, Université Blaise-Pascal (Clermont-Ferrand, France), 2016.

[89] R. W. Hockney and J. W. Eastwood, *Computer Simulation Using Particles*. Bristol, PA, USA: Taylor & Francis, Inc., 1988.

[90] P. Moin, *Fundamentals of Engineering Numerical Analysis*. Cambridge University Press, 2010.

[91] J. Wei, *Longitudinal Dynamics of the Nonadiabatic Regime on Alternating Gradient Synchrotrons*. PhD thesis, Stony Brook University (New York, USA), 1990.

[92] I. Kourbanis and K.-Y. Ng, "Main Ring Transition Crossing Simulations," in *Proceedings, Fermilab III Instabilities Workshop, held at Fermilab, USA, June 25-29, 1990*, pp. 151–169.

[93] J. A. MacLachlan, "Particle Tracking in E - $\phi$ Space for Synchrotron Design and Diagnosis," in *Application of accelerators in research and industry '92. Proceedings, 12th International Conference, Denton, USA, November 2-5, 1992*. Report no. FERMILAB-CONF-92-333.

[94] M. Paoluzzi *et al.*, "Beam Tests Using a Wide Band RF System Prototype in the CERN PS Booster," in *Proc. 6th International Particle Accelerator Conference (IPAC'15), Richmond, VA, USA, May 3-8, 2015*, pp. 3134–3137.

[95] M. K. Kazimierczuk, *RF Power Amplifiers*. USA: John Wiley & Sons, Inc., 2015.

[96] C. Zannini, *Electromagnetic Simulation of CERN Accelerator Components and Experimental Applications*. PhD thesis, Ecole Polytechnique (Lausanne, Switzerland), 2013.

[97] C. Zannini and G. Rumolo, "Updated Status of the PSB Impedance Model." Presentation at the CERN LIU-PSB Meeting 125, Geneva, Switzerland, 22 May 2014. https://indico.cern.ch/event/319950/.

[98] N. Esfahani, "Summary of Studies Related to Longitudinal Beam Coupling Impedance of KFA-14L PSB Extraction Kicker." Presentation at the CERN 21st Impedance Working Group Meeting, Geneva, Switzerland, 26 Jun 2018. https://indico.cern.ch/event/738572/.

[99] S. Albright, "ECR 1955075 PSB Extraction Kicker BE.KFA14L1." Presentation at the CERN 23rd Impedance Working Group Meeting, Geneva, Switzerland, 20 Sep 2018. https://indico.cern.ch/event/756863/.

[100] M. E. Angoletta *et al.*, "Experience with the Commissioning and Operation of the New CERN Digital LLRF Family." Presentation at the Low Level Radio Frequency Workshop 2015, Shanghai, China, 3-6 Nov 2015. https://slideplayer.com/slide/10276483/.

[101] "CERN ISOLDE Experiment." http://isolde.web.cern.ch/.

[102] "Highlights of the ISOLDE Facility and the HIE-ISOLDE Project," *Nuclear Instruments and Methods in Physics Research Section B: Beam Interactions with Materials and Atoms*, vol. 376, pp. 408 – 412, 2016.

[103] J. Abelleira *et al.*, "Painting Schemes for CERN PS Booster H- Injection," in *Proc. 6th International Particle Accelerator Conference (IPAC'15), Richmond, VA, USA, May 3-8, 2015*, pp. 3879–3882.

[104] V. Forte *et al.*, "Multi-Particle Simulations of the Future CERN PSB Injection Process with Updated Linac4 Beam Performance," in *Proc. 61st ICFA Advanced Beam Dynamics Workshop (HB'18), Daejeon, Korea, 17-22 June 2018*, pp. 278–283.

[105] H. Bartosik *et al.*, "Can We Ever Reach the HL-LHC Requirements with the Injectors?," in *Proc. RLIUP: Review of LHC and Injector Upgrade Plans, Centre de Convention, Archamps, France, 29 - 31 Oct 2013*, pp. 95–104.

[106] E. Shaposhnikova, "Signatures of Microwaves Instability," Tech. Rep. CERN-SL-99-008-HRF, CERN, Geneva, Switzerland, 1999.

[107] V. Balandin, M. Dyachkov, and E. Shaposhnikova, "The Resonant Theory Of Longitudinal Emittance Blow-up By Phase Modulated High Harmonic Cavities," *Particle Accelerators*, vol. 35, pp. 1–14, 1991.

[108] S. Albright, D. Quartullo, and E. Shaposhnikova, "Longitudinal Emittance Blow-up and Production of Future LHC Beams," in *Proceedings, Injector MD Days 2017: CERN. Geneva, Switzerland, March 23–24, 2017*, pp. 23–26.

[109] D. Quartullo, E. Shaposhnikova, and H. Timko, "Controlled Longitudinal Emittance Blow-up Using Band-limited Phase Noise in CERN PSB," *Journal of Physics: Conference Series*, vol. 874, p. 012066, 2017.

[110] T. Toyama, "Uniform Bunch Formation by RF Voltage Modulation with a Band-limited White Signal," *Nuclear Instruments and Methods in Physics Research Section A: Accelerators, Spectrometers, Detectors and Associated Equipment*, vol. 447, no. 3, pp. 317 – 327, 2000.

[111] P. Baudrenghien *et al.*, "Longitudinal Emittance Blow-up in the LHC," in *Particle accelerator. Proceedings, 2nd International Conference, IPAC 2011, San Sebastian, Spain, September 4-9, 2011*, pp. 1819–1821.

[112] G. Papotti *et al.*, "Study of Controlled Longitudinal Emittance Blow-up for High Intensity LHC Beams in the CERN SPS," Tech. Rep. CERN-LHC-PROJECT-Report-1117, CERN, Geneva, Switzerland, 2008.

[113] J. Tückmantel, "Digital Generation of Noise-signals with Arbitrary Constant or Time-varying Spectra," Tech. Rep. CERN-AB-2008-047, CERN, Geneva, Switzerland, 2008.

[114] G. Dôme, "Diffusion due to RF Noise," in *Proc. CAS - CERN Accelerator School : Accelerator Physics, Oxford, UK, 16 - 27 Sep 1985*, pp. 370–401.

[115] H. Timko, P. Baudrenghien, E. Shaposhnikova, and T. Mastoridis, "Studies on Controlled RF Noise for the LHC," in *Proceedings, 54th ICFA Advanced Beam Dynamics Workshop on High-Intensity and High-Brightness Hadron Beams (HB2014): East Lansing, MI, November 10-14, 2014*, pp. 414–418.

[116] M. E. Angoletta *et al.*, "PS Booster Beam Tests of the New Digital Beam Control System for LEIR," Tech. Rep. CERN-AB-Note-2005-017, CERN, Geneva, Switzerland, 2005.

[117] P. Naidu, *Modern Digital Signal Processing: An Introduction*. Alpha Science International, 2006.

[118] S. V. Vaseghi, *Multimedia Signal Processing: Theory and Applications in Speech, Music and Communications*. USA: John Wiley & Sons, Inc., 2007.

[119] "CERN PSB Beam Docs 2018." https://wikis.cern.ch/display/PSBOP.

[120] R. Garoby, "Multiple Bunch-splitting in the PS: Results and Plans," Tech. Rep. CERN-PS-2001-004-RF, CERN, Geneva, Switzerland, 2001.

[121] G. Rumolo *et al.*, "Expected Performance in the Injectors at 25 ns without and with Linac4," in *Proc. RLIUP: Review of LHC and Injector Upgrade Plans, Centre de Convention, Archamps, France, 29 - 31 Oct 2013*, pp. 17–24.

[122] A. Huschauer *et al.*, "Transverse Beam Splitting Made Operational: Key Features of the Multiturn Extraction at the CERN Proton Synchrotron," *Phys. Rev. Accel. Beams*, vol. 20, p. 061001, 2017.

[123] A. Bazzani, C. Frye, M. Giovannozzi, and C. Hernalsteens, "Analysis of Adiabatic Trapping for Quasi-Integrable Area-preserving Maps," *Phys. Rev. E*, vol. 89, p. 042915, 2014.

[124] K. Hanke *et al.*, "High-Brightness Challenges for the Operation of the CERN Injector Complex," in *Proc. 61st ICFA Advanced Beam Dynamics Workshop (HB'18), Daejeon, Korea, 17-22 June 2018*, pp. 352–356.

[125] Y. Papaphilippou, H. Bartosik, G. Rumolo, and D. Manglunki, "Operational Beams for the LHC," in *Proc. Workshop on LHC Performance, Chamonix, France, 22-25 Sep 2014*, pp. 80–84.

[126] J. Eldred, *Slip-stacking Dynamics for High-power Proton Beams at Fermilab*. PhD thesis, Indiana University (Bloomington, USA), 2015.

[127] A. Saa Hernandez, "Results from Ion Studies in PS and SPS from 2016/2017 and Planning for 2018." Presentation at the CERN LHC Injectors Upgrade MD Day 2018, Geneva, Switzerland, 15 Mar 2018. https://indico.cern.ch/event/706213/contributions/2902802/.

[128] T. Argyropoulos, T. Bohl, and E. Shaposhnikova, "Slip Stacking in the SPS." Presentation at the CERN LIU Day 2014, Geneva, Switzerland, 11 Apr 2014. https://indico.cern.ch/event/299470/contributions/686512/.

[129] F. E. Mills, "Stability of Phase Oscillations Under Two Applied Frequencies," Tech. Rep. BNL-15936, BNL, Brookhaven, USA, 1971.

[130] H. Bartosik, G. Arduini, and Y. Papaphilippou, "Optics Considerations for Lowering Transition Energy in the SPS," Tech. Rep. CERN-ATS-2011-088, CERN, Geneva, Switzerland, 2011.

[131] T. Bohl, T. Linnecar, E. Shaposhnikova, and J. Tückmantel, "Study of Different Operating Modes of the 4th RF Harmonic Landau Damping System in the CERN SPS," Tech. Rep. CERN-SL-98-026-RF, CERN, Geneva, Switzerland, 1998.

[132] T. Argyropoulos, *Longitudinal Beam Instabilities in a Double RF System.* PhD thesis, National Technical University (Athens, Greece), 2015.

[133] T. Bohl. CERN, personal communication, 2018.

[134] E. Shaposhnikova, E. Ciapala, and E. Montesinos, "Upgrade of the 200 MHz RF System in the CERN SPS," in *Proc. 2nd International Particle Accelerator Conference (IPAC'11), San Sebastian, Spain, Sep 4-9, 2011*, pp. 214 – 216.

[135] A. Lasheen, T. Argyropoulos, J. Repond, and E. Shaposhnikova, "Effect of the Various Impedances on Longitudinal Beam Stability in the CERN SPS," in *Proc. of International Particle Accelerator Conference (IPAC'16), Busan, Korea, May 8-13, 2016*, pp. 1666–1669.

[136] P. Kramer and C. Vollinger, "Studies for the SPS Travelling Wave Cavities Upgrade," in *CERN Yellow Reports: Conference Proceedings, 2018*, vol. 1, pp. 57–62.

[137] A. Farricker, M. Beck, J. Repond, and C. Vollinger, "Effect of the Extraction Kickers on the Beam Stability in the CERN SPS," in *Proc. 61st ICFA Advanced Beam Dynamics Workshop (HB'18), Daejeon, Korea, 17-22 June 2018*, pp. 189–194.

[138] V. Kain *et al.*, "Identification and Removal of SPS Aperture Limitations," in *Proc. 9th International Particle Accelerator Conference (IPAC'18), Vancouver, BC, Canada, April 29-May 4, 2018*, pp. 709–712.

[139] H. Timko *et al.*, "Longitudinal Transfer of Rotated Bunches in the CERN Injectors," *Phys. Rev. ST Accel. Beams*, vol. 16, p. 051004, May 2013.

[140] D. Quartullo, T. Argyropoulos, and A. Lasheen, "Momentum Slip-Stacking Simulations for CERN SPS Ion Beams with Collective Effects," in *Proc. 61st ICFA Advanced Beam Dynamics Workshop (HB'18), Daejeon, Korea, 17-22 June 2018*, pp. 174–179.

[141] A. Latina, "Introduction to Transverse Beam Dynamics." Lecture at the Joint Universities Accelerator School (JUAS), Archamps, France, 2015.

[142] A. Wolski, *Introduction to Beam Dynamics in High-Energy Electron Storage Rings.* Morgan & Claypool Publishers, 2018.

[143] H. Bartosik, *Beam Dynamics and Optics Studies for the LHC Injectors Upgrade.* PhD thesis, Technische Universität (Vienna, Austria), 2013.

[144] A. Papoulis and S. U. Pillai, *Probability, Random Variables, and Stochastic Processes.* McGraw-Hill, 2002.